

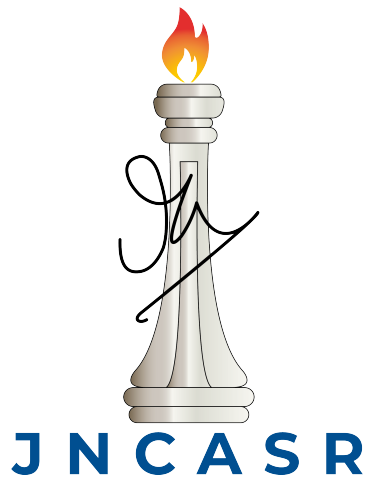
Density Functional Theory Calculations of Doped, Alloyed, and Heterostructure Systems

A Thesis

Submitted to the
Jawaharlal Nehru Centre for Advanced Scientific Research, Bengaluru
for the Degree of DOCTOR OF PHILOSOPHY
in the Faculty of Science

by

Arpan Das



JAWAHARLAL NEHRU CENTRE FOR ADVANCED
SCIENTIFIC RESEARCH, BENGALURU, INDIA.

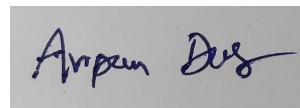
JULY 2023

To my Mother and Father

DECLARATION

I hereby declare that the matter embodied in the thesis entitled “**Density Functional Theory Calculations of Doped, Alloyed, and Heterostructure Systems**” is the result of investigations carried out by me at the Theoretical Sciences Unit, Jawaharlal Nehru Centre for Advanced Scientific Research, Bangalore, India under the supervision of Prof. Shobhana Narasimhan and that it has not been submitted elsewhere for the award of any degree or diploma.

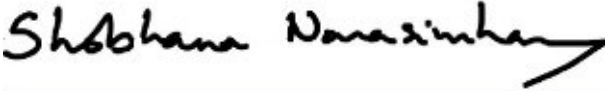
In keeping with the general practice in reporting scientific observations, due acknowledgement has been made whenever the work described is based on the findings of other investigators. Any omission that might have occurred by oversight or error of judgement is regretted.

A rectangular box containing a handwritten signature in black ink. The signature is written in a cursive style and reads "Arpan Das".

Arpan Das

CERTIFICATE

I hereby certify that the matter embodied in this thesis entitled “**Density Functional Theory Calculations of Doped, Alloyed, and Heterostructure Systems**” has been carried out by Mr. Arpan Das at the Theoretical Sciences Unit, Jawaharlal Nehru Centre for Advanced Scientific Research, Bangalore, India under my supervision and that it has not been submitted elsewhere for the award of any degree or diploma.



Prof. Shobhana Narasimhan
(Research Supervisor)

Acknowledgements

First of all, I would like to thank my Ph.D advisor Prof. Shobhana Narasimhan for introducing me to the fascinating world of research. She has helped me in understanding the basics of solid state physics and how I can implement it into daily research for problem solving as well as better understanding of the subject in greater depth. She has introduced me to the fascinating experimental collaborative works I have worked on in this thesis. Compared to when I joined her lab, she has significantly improved my abilities as a researcher. I also learnt a lot from her on ‘how to write a scientific article?’ and ‘How to present a research work in a very simple a way so that everyone can understand it?’ I will be always grateful to her for giving me the opportunity to work internationally at the ICTP, Trieste, Italy for a long two months visit during my Ph.D. Apart from academics, she has opened a completely new and diverse *fields of food* in front of me.

I would like to thank all of my experimental and theoretical collaborators: Prof. Krishnakumar S. R. Menon, Prof. Suvankar Chakraverty, Prof. Ranjani Viswanatha, Prof. Bivas Saha, Dr. Arunava Kar, Dr. Saptarshi Chakrabarty, Dr. Krishna C. Maurya, Ruchi Tomar, Dr. Rajdeep Banerjee and Dr. Depbipto Acharya.

Specially, I want to thank Rajdeep da for helping and supporting in the starting

days of my PhD. He introduced me for the first time in the so called ‘DFT calculations’. I will never forget the long night discussions with Arunava da about our project and later extended to many other topics of science, which finally lead to an excellent friendship. I hope it will last life long. I visited many times to him at SINP, those days will always be remembered. I am very thankful to Saptarshi da, for his always respect towards theorists, which is very rare now a days. I learnt a lot from him.

I am thankful to all of my course instructors for their outstanding teaching: Prof. S. Narasimhan, Prof. N. S. Vidhyadhiraja, Prof. Meher K. Prakash, Prof. Balasubramanian, Prof. Subir K. Das, and Prof. Kavita Jain,

I want to thank all other faculties of TSU: Prof. Umesh V. Waghmare, Prof. Swapan K. Pati, and Prof. Srikant Sastry.

I want to acknowledge the present and past chairpersons of TSU for lot of helps regarding official works: Bindu and Ashrita.

I acknowledge JNCASR for my Ph.D fellowship. I thank ICTP and JNCASR student travel grant for bearing all of my expenses during my visit at ICTP.

I thank everyone in the Academic Section, especially Dr. Princy and Praveen. I want to thank Mr. Joydeep Deb, Mr. Jayachandra, and all others in the Administrative Section for their help with all the administrative procedures. I thank all the Dhanvantari staff for their medical assistance they provided, specially during the terrific Covid time. I am highly grateful to the past & present CCMS staff Suresh, Anoop, Salman and Pandurang for their help and support with computational facilities and cluster related problems. I want to thank all the library staff, all the hostel staff, all the mess staff, all the cleaning staff.

I thank all my past and present labmates: Rajdeep, Debdipto, Sourav, Abhishek, Devina, Nandana, Chiku, Garima, Harshdeep, Shivaranjani, and Ritam for providing a pleasant and joyful research environment in my lab.

Special thanks to Sourav da and Abhishek da for various unforgettable memories during Covid days. I thank Sourav da, I have learnt many things: from cooking to data analysis, the learning spectrum is really wide. This converted into from lab senior to a very close friend. I will always miss him for our 'coffee time'. I am also very thankful to Abhishek da for our outstanding memory in lab and Football matches. I am thankful to Debdipto da for lot of discussions we had together regarding science. I am thankful to Garima for her help in running some calculations and discussion on projects during my thesis pressure time. I am really grateful to have a lab mate like Ritam who was always stood in my side, whatever the situations are.

I thank my friends and batch mates Bidhan, Prasenjit, Soumik, Supriti, Debendra, Sinay, Krishna, Soumen, Oisikha, Anjana, Debattam, Bitan, and Angshuman, for the wonderful time we spent together.

Special thanks to Bidhan, Prasenjit and Ritam for tolerating the ups and downs and being witness of all the events of my Ph.D. I feel lucky to have Bidhan as a friend, who doesn't stay at his comfort zone at all. He made me a better person through out the whole Ph.D journey. I am lucky to have a friend like Prasenjit, who is an outstanding cook, I call him 'Mutton da' as he makes Mutton curry really better than any five-star hotel cook. I am thankful to have a friend (not lab junior!!) Ritam, who has an excellent frequency matching with me. He was the witness of the last part of my Ph.D. We discussed science, quarrelled about 'Mohun Bagan-East Bengal', hurt each other, improved each other, experienced and understood meaning of life in depth. I will never forget our trip to Chennai, a lifetime unforgettable tour!! He took care of me and helped to optimize in some steps of my Ph.D.

My respectful gratitude to Prof. C. N. R. Rao for providing world class research facilities and outstanding scientific environment at JNCASR. He is kind of umbrella to researchers like me.

Finally, I thank my parents, my family, Surajit, Abhijit da, and Indra da for their love, constant support, motivation, and everything through out the whole Ph.D journey and the journey I crossed in my life so far.

Synopsis

In this thesis, we have performed quantum mechanical simulations using density functional theory (DFT) on a rich variety of systems such as: bulk crystals, metal and semiconductor surfaces, surface alloys, pristine and doped halide perovskite materials and heterostructures. We have used spin-polarized DFT for magnetic systems, the DFT+ U method for strongly-correlated systems, and relativistic DFT to study the effects of spin-orbit coupling. This thesis studies the structural, electronic, magnetic, optical and vibrational properties of the above mentioned systems, in great detail.

In Chapter 1, we have provided a very brief introduction to the problems we have studied in this thesis, as well as to the kinds of systems studied. We have discussed the approach of "the rational design of materials", and why this is superior to earlier trial-and-error or brute force approaches.

In Chapter 2, we have summarized the methods we have used in this thesis to perform DFT calculations to find different properties of materials. We have briefly summarized the basics of DFT and the computational approaches used when performing DFT calculations. We have also discussed the mathematical formalism used to calculate different properties throughout the thesis. For example, we have described, in brief, the theory of non spin-polarized and spin-polarized DFT, and

the computational approximations made when using DFT for doing simulations of real materials. We have also described relativistic DFT as we have incorporated spin-orbit coupling in some cases, and the DFT+ U method for strongly correlated systems. We have also described methods used in this thesis to calculate the optical and vibrational properties of materials.

In Chapter 3, we have studied the deposition of Sn atoms on an Ag(001) substrate. This is collaborative work, done together with the experimental group of Prof. K. S. R. Menon, of the Surface Physics and Materials Science Division, SINP, Kolkata. Our theoretical calculations show that when Sn atoms are deposited on an Ag(001) surface, very interestingly, Sn-Ag bimetallic surface alloys are formed for all Sn coverages. This is in contradiction with the naive expectation of Sn atoms forming an overlayer on the Ag(001) surface.

We discuss the reasons why these naive expectations are incorrect. The formation of surface alloys is explained by the fact that, on the Ag(001) surface, the effective size of deposited Sn atoms becomes very large. Thus, when these Sn atoms are intermixed with the smaller Ag atoms, the tensile surface stress on the Ag(001) surface is relieved. The calculated results are compared against the data from low energy electron diffraction (LEED) experiments.

Then we calculate the electronic structure of the lowest energy stable structures at each Sn coverage considered in our calculations. The calculated band structures are compared with the angle-resolved photoemission spectroscopy (ARPES) measurements. Overall, we see very good agreement between theory and experiment. An interesting feature in both the experimentally measured and theoretically computed band structures is the existence of a crossing point between two linearly dispersive bands, similar to the Dirac cone in graphene, and a variation in its energy with the Sn coverage. This variation is explained by a change in the surface electrostatic potential with Sn coverage.

In Chapter 4, we have studied the structural, electronic, vibrational properties of CsPbBr₃, CsPbCl₃, Fe-doped CsPbBr₃ and Fe-doped CsPbCl₃. This work is in collaboration with the experimental group of Prof. Ranjani Viswanatha, New Chemistry Unit, JNCASR, Bangalore. Our experimental collaborators were able to dope Fe atoms successfully into CsPbBr₃ and CsPbCl₃ nanocrystals. They measured the photoluminescence of the Fe-doped systems and compared these results with those obtained from the corresponding pristine systems. They observed that the photoluminescence is considerably quenched or reduced upon Fe doping, compared to the pristine CsPbBr₃ and CsPbCl₃. However, the degree of this quenching was much greater for Fe-doped CsPbCl₃ than for Fe-doped CsPbBr₃.

We have performed DFT calculations to see the effect of Fe doping on the lattice. The electronic structures of the pristine systems and Fe-doped systems are compared. We have found the effects of Fe doping in CsPbBr₃ and CsPbCl₃, and compared the results with the pristine systems. We show that the experimentally observed quenching of photoluminescence upon Fe-doping arises from the presence of mid-gap states in one spin channel that arise from the dopants. We also show that the different degrees of photoluminescence quenching in Fe-doped CsPbCl₃ and Fe-doped CsPbBr₃ can be attributed to the stronger electron-phonon coupling in the former than in the latter.

In Chapter 5, we have calculated the optical properties of CsPbX₃ and Fe-doped CsPbX₃ (X = Br, Cl) perovskite materials. Our experimental collaborators in the groups of Prof. Ranjani Viswanatha and Prof. Bivas Saha, JNCASR, Bangalore, have measured the optical properties of the pristine materials. . Using ellipsometry, our collaborators have measured frequency dependent optical constants (e.g., imaginary part of dielectric function $\epsilon_2(\omega)$) by observing the change in polarization of light when it is reflected from or transmitted through CsPbBr₃ and CsPbCl₃. The peaks found in the spectra of $\epsilon_2(\omega)$ are identified as different transitions from the different

states in the valence band to the states in the conduction band of these materials. We have calculated the electronic structure and optical properties of CsPbBr₃ and CsPbCl₃ using first principles DFT calculations. We have identified the valence states and conduction states involved in the different optical transitions found in the ellipsometry measurements. We have also identified the atomic orbitals involved in these optical transitions. Further, we have calculated the frequency dependent imaginary part of the dielectric function $\epsilon_2(\omega)$ and compared it with the experimental spectra, for both CsPbBr₃ and CsPbCl₃. Further, we have calculated $\epsilon_2(\omega)$ spectra for Fe-doped systems, and found there is a little blue shift (increase in band gap) upon Fe doping with respect to the pristine systems, for both Fe-doped CsPbBr₃ and Fe-doped CsPbCl₃.

In Chapter 6, we have studied the electronic properties of the two-dimensional electron gas (2DEG) formed at the LaVO₃/KTaO₃ (LVO/KTO) heterostructure interface. This work has been performed in collaboration with the experimental group of Prof. Suvankar Chakraverty, INST, Mohali, who formed the LVO/KTO interface by depositing a thin film of LVO on a TaO₂ terminated KTO(001) substrate, using pulsed laser deposition (PLD). They have observed metallicity at the LVO/KTO interface while measuring the 2D resistivity with temperature, above 3 monolayer (ML) LVO thickness. The calculated carrier density and carrier mobility, in their experiment, is very high at the LVO/KTO interface. We have first performed electronic structure calculations of the constituents LVO and KTO which are confirmed to be insulating. However, our calculations of the LVO/KTO interface show a metallic nature, consistent with the experimental observations. The calculated electronic charge is maximum near the interface and decreases away from the interface, which shows the two-dimensional nature of the conduction electrons. We also find that an ‘electronic reconstruction’ is the origin of 2DEG formation at the LVO/KTO interface.

In Chapter 7, we have summarized the main conclusions of each chapter and we raise some open questions that can be addressed in future work. This can lead to diverse directions for each project and possibly reveal even more interesting physics.

List of Publications

1. “Evolution of geometric and electronic structures of oxygen-induced superstructures on Mo(110) surface: A LEED, ARPES, and DFT study”, Arunava Kar, Arpan Das, Smruti Ranjan Mohanty, Shobhana Narasimhan, and Krishnakumar S. R. Menon, *Phys. Rev. B* **106**, 045128 (2022).
2. “Non-Resonant Exciton-Plasmon Interaction in Metal-Chalcogenide Cu_xS /Perovskite (CsPbBr_3) Based Colloidal Heterostructure”, Saptarshi Chakraborty, Gauttam Dash, Subhashri Mannar, Krishna Maurya, Arpan Das, Shobhana Narasimhan, Bivas Saha, Ranjani Viswanatha, (just accepted in *J. Phys. Chem. C.*).
3. “Exciton and Biexciton Decay Dynamics in Fe-doped CsPbBr_3 Quantum Dots: Origin of Photoluminescence Quenching”, Saptarshi Chakraborty, Ayushi Shukla, Gurpreet Kaur, Arpan Das, Debdipto Acharya, Shobhana Narasimhan, Hirendra Ghosh, Ranjani Viswanatha, (manuscript under revision).
4. “Evolution of atomic and electronic structure of Sn-Ag/Ag(001) bimetallic surface alloy systems: A LEED, ARPES and DFT study”, Arunava Kar, Arpan Das*, Suvankar Chakraborty, Rajdeep Banerjee, Shobhana Narasimhan, and Krishnakumar S. R. Menon, (manuscript under preparation).

5. “Electronic properties of two-dimensional electron gas at LVO/KTO interface”, Arpan Das, Ruchi Tomar, Suvankar Chakraverty, Shobhana Narasimhan, (manuscript under preparation).
6. “Photoluminescence Quenching upon Fe doping into CsPbBr₃ and CsPbCl₃: Different Photoluminescence behaviour in Fe-doped CsPbBr₃ and Fe-doped CsPbCl₃”, Arpan Das, Saptarshi Chakraborty, Ranjani Viswanatha, Shobhana Narasimhan, (manuscript under preparation).

* Contributed equally

List of Abbreviations

$\Delta\rho$ Charge density difference

ΔH Enthalpy of Mixing

$\epsilon_2(\omega)$ Frequency dependent imaginary part of Dielectric function

ρ Charge density

C_{ii} Elastic constant

D Deformation potential

E_g Band gap

E_F Fermi Energy

U Hubbard U or onsite Coulomb repulsion energy

1D One Dimensional

2D Two Dimensional

2DEG Two Dimensional Electron Gas

3D Three Dimensional

AFM Antiferromagnetic

ARPES Angle-resolved Photoemission Spectroscopy

BFGS Broyden-Fletcher-Goldfarb-Shanno

BZ Brillouin Zone

CBM Conduction Band Minimum

CDD Charge Density Difference

CN Coordination Number

DFT Density Functional Theory

DOS Density of States

ECN Effective Coordination Number

EPC Electron-phonon Coupling

FBZ First Brillouin Zone

FD Fermi-Dirac

FETs Field Effect Transistors

FFT Fast Fourier Transform

FM Ferromagnetic

GGA Generalized Gradient Approximation

HF Hellmann-Feynman

HK Hohenberg-Kohn

IBZ Irreducible Brillouin Zone

ILDOS Integrated Local Density of States

KS Kohn-Sham

KTO KTaO_3

LDA Local Density Approximation

LDOS Local Density of States

LEED Low Energy Electron Diffraction

LVO LaVO_3

MBE Molecular Beam Epitaxy

ML Monolayer

MP Methfessel-Paxton

MV Marzari-Vanderbilt

NCPP Norm-conserving Pseudopotential

NCs Nanocrystals

PBC Periodic Boundary Conditions

PBE Perdew, Burke and Ernzerhof

PCBZ Primitive Cell Brillouin Zone

PDOS Projected Density of States

PES Potential Energy Surface

PL Photoluminescence

PLQY Photoluminescence Quantum Yield

PPs Pseudopotentials

PW Perdew and Wang

PWs Plane Waves

PWSCF Plane Wave Self-consistent Field

QDs Quantum Dots

QE Quantum ESPRESSO

RT Room Temperature

SCBZ Super Cell Brillouin Zone

SDFT Spin Density Functional Theory

SL Superlattice

SOC Spin-orbit Coupling

SR Scalar Relativistic

Subs Substrate

TFD Thomas-Fermi-Dirac

USPP Ultrasoft Pseudopotential

VBM Valence Band Maximum

VESTA Visualisation for Electronic Structural Analysis

XC Exchange-correlation

XPS X-ray Photoelectron Spectroscopy

XRD X-ray Diffraction

Contents

Acknowledgements	v
Synopsis	ix
List of Publications	xv
List of Abbreviations	xvii
1 Introduction	1
1.1 Rational design of nanomaterials	2
1.2 Outline of the thesis	7
Bibliography	10
2 Methods and Formalism	15
2.1 The many-body problem	15
2.1.1 The Schrödinger equation and many-body problem	16
2.1.2 The Born-Oppenheimer approximation	17
2.2 Density Functional Theory	18
2.2.1 Hohenberg-Kohn (HK) theorems	19
2.2.2 Kohn-Sham ansatz	20

2.2.3	Exchange-correlation functional	23
2.2.4	Plane wave basis sets	28
2.2.5	Pseudopotential approximation	31
2.2.6	Brillouin zone sampling and smearing	35
2.2.7	Calculation of forces: Hellmann-Feynman theorem	38
2.2.8	Stress calculation	39
2.2.9	Spin-polarized density functional theory	40
2.2.10	Modelling aperiodic systems	41
2.3	Relativistic DFT	42
2.3.1	Spin-orbit coupling	44
2.4	Strongly correlated systems: the DFT+ U method	45
2.5	Optical properties of solids: joint density of states and dielectric function calculation	46
2.6	Codes and software used	52
	Bibliography	53

3 Sn Deposited on Ag(001): Formation of Surface Alloy and Evolution of Structural and Electronic Properties **61**

3.1	Introduction	62
3.2	Summary of experiments	67
3.3	Computational details	69
3.3.1	Unfolding and projection of band structure	71
3.4	Systems under study	75
3.5	Results and discussion	75
3.5.1	Surface structure as a function of Sn coverage: results from LEED	76
3.5.2	Structure of Ag(001) and Sn/Ag(001): DFT results	77

3.5.3	Evolution of structure and stability as a function of Sn coverage: DFT results	83
3.5.4	Electronic structure: DFT results and comparison with ARPES data	98
3.5.5	Insights from charge density difference plots	110
3.5.6	Evolution of electrostatic potential with Sn coverage	112
3.5.7	Further discussion	115
3.6	Conclusions	118
	Bibliography	119
4	Structural, Electronic and Vibrational Properties of CsPbX₃ and Fe-doped CsPbX₃ (X = Br, Cl)	131
4.1	Introduction	132
4.2	Experimental motivation	135
4.3	Computational details	136
4.4	Systems under study	138
4.5	Results and discussion	139
4.5.1	Lattice parameters of CsPbX ₃ and Fe-doped CsPbX ₃ (X = Br, Cl)	139
4.5.2	Stability of pristine CsPbX ₃ and Fe-doped CsPbX ₃ (X = Br, Cl)	142
4.5.3	Electronic structure of pristine CsPbBr ₃ and CsPbCl ₃	143
4.5.4	Spin-polarization of Fe-doped CsPbBr ₃ and Fe-doped CsPbCl ₃	146
4.5.5	Electronic structure of Fe-doped CsPbBr ₃ and Fe-doped CsPbCl ₃	148
4.5.6	Vibrational properties of Fe-doped CsPbBr ₃ and Fe-doped CsPbCl ₃	154

4.5.7	Origin of different photoluminescence behaviour in Fe-doped CsPbBr ₃ and Fe-doped CsPbCl ₃ : Explanation from electron-phonon coupling	156
4.6	Summary and conclusions	161
	Bibliography	162
5	Optical properties of CsPbX₃ and Fe-doped CsPbX₃ (X = Br, Cl)	171
5.1	Introduction	172
5.2	Experimental motivation	174
5.3	Computational details	175
5.4	Systems under study	176
5.5	Results and discussion	177
5.5.1	Optical properties of pristine CsPbBr ₃ and CsPbCl ₃	177
5.5.2	Comparison between CsPbBr ₃ and CsPbCl ₃ : Experiment vs. Calculations	182
5.5.3	Comparison of dielectric function: pristine and Fe-doped CsPbX ₃ (X = Br, Cl)	185
5.6	Conclusions	187
	Bibliography	187
6	Electronic Properties of Two Dimensional Electron Gas at LVO/KTO Interface	195
6.1	Introduction	196
6.2	Experimental motivation	204
6.3	Systems studied	206
6.4	Computational details	208
6.5	Results and discussion	210
6.5.1	Constituent: Bulk KTO	211

6.5.2	KTO(001) surface	214
6.5.3	Constituent: Bulk LVO	217
6.5.4	LVO/KTO Interface	225
6.5.5	Conclusions	242
	Bibliography	243
7	Summary and Future Directions	261
	Bibliography	267

List of Figures

1.1	Schematic of procedure of rational design of nanomaterials.	2
2.1	Flow chart showing the self-consistency loop for the iterative solution of the KS equations.	24
3.1	LEED patterns of Sn/Ag(001) for different Sn coverage. (a) Clean Ag(001) with primitive unit cell (yellow square) and (as an example) a $p(2 \times 2)$ surface Brillouin Zone (red square) with high symmetry points. (b) 0.25 ML, (c) 0.50 ML, (d) 0.6 ML, (e) 0.75 ML and (f) 1.0 ML. The energy of the incident electron beam is 55 eV. <i>This Fig. is originally part of Dr. Arunava Kar's (SPMS, SINP) Ph.D thesis and used with permission.</i>	77
3.2	Plot of atomic radius vs effective coordination number (ECN) for (a) Ag atom and (b) for Sn atom. We have considered sc, bcc, fcc and diamond structures of Ag and Sn atoms. The blue lines are the cubic spline fitted curves. The red vertical lines are drawn at ECN values of a surface Ag atom (8.3148) and a Sn atom on Ag(001) (8.2132). The intersection of this vertical red line and blue curves gives the atomic radius of a surface Ag atom (1.360 Å) and a Sn atom on Ag(001) (1.687 Å).	82

3.3	Schematic diagram of five different kinds of structures (top and side views) considered for theoretical calculations. (a) substitutional surface alloy $\text{Sn}_x\text{Ag}_{1-x}/\text{Ag}(001)$, (b) overlayer adsorption of Sn adatoms, (c) a few Sn atoms substitute Ag atoms from the surface layer and a few Sn atoms sit as adatoms, (d) non-psuedomorphic alloy structure in which the atomic density in the surface alloy layer is different from that in an Ag(001) layer, and (e) direct exchange: Sn atoms substitute some Ag atoms, and the substituted Ag atoms sit like overlayer adatoms.	84
3.4	Convergence of $\Delta H/A$ with k-point mesh for $\text{Sn}_x\text{Ag}_{1-x}/\text{Ag}(001)$ systems at (a) $x = 0.6$ and (b) $x = 0.67$, for different possible structures as shown in Figs. 3.11 and 3.12, respectively. In these examples, the structures which were higher in energy at lower k-point density become lower in energy at higher k-point density. This demonstrates the highly sensitive dependence of the enthalpy of formation on the density of the k-point mesh. We see that the $\Delta H/A$ converges at very high k-point density like $36 \times 36 \times 1$ k-point mesh. So, to determine the lowest energy structures at each value of x , we had to consider a very dense k-point mesh.	87
3.5	Enthalpy of formation per unit area, $\Delta H/A$ as a function of Sn coverage x . Different colors of the data points correspond to different surface supercells used in our DFT calculations, as shown in the inset. The red lines show the convex hull drawn through the data. The arrow symbols represent surface alloy structures of Fig. 3.6.	88

3.6	Surface alloy structures (top-views) predicted by DFT calculations and LEED measurements at different Sn coverages x . (a), (b), (c), (d), (e) and (f) are the structures which fall on the convex hull. (c') and (c'') are the 2nd and 3rd lowest energy structure respectively, at $x = 0.5$. c' is seen in the LEED pattern. (d') is the 2nd lowest energy structure at $x = 0.75$, which we have used when computing the band structure. Color code: Green - Sn atoms, Orange - surface Ag atoms and Gray - subsurface Ag atoms.	90
3.7	Different structures considered at $x = 0.2, 0.33$, and 0.4 for energetics calculations. The Sn coverage and surface supercells along with the values of enthalpy of mixing $\Delta H/A$ are written below each figure. Atomic color code: green - Sn, orange - surface Ag and gray - topmost layer of Ag substrate.	92
3.8	Different structures considered at $x = 0.25$ for energetics calculations. The Sn coverage and surface supercells along with the values of enthalpy of mixing $\Delta H/A$ are written below each figure. Atomic color code: green - Sn, orange - surface Ag and gray - topmost layer of Ag substrate.	92
3.9	Different structures considered at $x = 0.5$ having $p(1 \times 10)$ cells for energetics calculations. The Sn coverage and surface supercells along with the values of enthalpy of mixing $\Delta H/A$ are written below each figure. Atomic color code: green - Sn, orange - surface Ag and gray - topmost layer of Ag substrate.	93

3.10	Different structures considered at $x = 0.5$ for energetics calculations. The Sn coverage and surface supercells along with the values of enthalpy of mixing $\Delta H/A$ are written below each figure. Atomic color code: green - Sn, orange - surface Ag and gray - topmost layer of Ag substrate.	94
3.11	Different structures considered at $x = 0.6$ for energetics calculations. The Sn coverage and surface supercells along with the values of enthalpy of mixing $\Delta H/A$ are written below each figure. Atomic color code: green - Sn, orange - surface Ag and gray - topmost layer of Ag substrate.	94
3.12	Different structures considered at $x = 0.67$ for energetics calculations. The Sn coverage and surface supercells along with the values of enthalpy of mixing $\Delta H/A$ are written below each figure. Atomic color code: green - Sn, orange - surface Ag and gray - topmost layer of Ag substrate.	94
3.13	Different structures considered at $x = 0.75$ for energetics calculations. The Sn coverage and surface supercells along with the values of enthalpy of mixing $\Delta H/A$ are written below each figure. Atomic color code: green - Sn, orange - surface Ag and gray - topmost layer of Ag substrate.	95
3.14	Variation of percentage interlayer relaxation for the top two layers with the Sn coverage x . The red circles are results from DFT optimization of the structures, and the blue line is a linear fit to the data. The black dashed line is the zero line of Δ_{12}	96
3.15	Variation of percentage surface stress σ_{XX}^{surf} with the Sn concentration x . The black dashed line is the zero line of σ_{XX}^{surf}	97

- 3.16 (a) Red square represents First Surface Brillouin Zone (FSBZ) of $p(1 \times 1)$ primitive cell in real space, we call it primitive cell Brillouin zone (PCBZ), and light-blue squares represent FSBZ of $p(2 \times 2)$ supercell in real space, we call it supercell Brillouin zone (SCBZ). Primed and unprimed letters represent the high symmetry points of the PCBZ and SCBZ respectively. (b) Projection of bulk band structure onto (001) surface termination. The blue shaded area represents the projection of bulk states while bands computed for the surface slab are shown by red lines. *Fig. is taken from Dr. Arunava Kar's (SINP) Ph.D thesis with permission.* 99
- 3.17 (a) Line profile at \bar{X} as a function of Sn coverage. The inset represents the evolution of the crossing point as a function of Sn coverage. The shaded area represents the projected bulk band [see text for details]. (b) Schematic diagram of the evolution of Sn-induced surface bands on Ag(001) surface at \bar{X} high symmetry point. *Fig. is taken from Dr. Arunava Kar's (SINP) Ph.D thesis with permission.* 100
- 3.18 Position of the crossing point of S_2 and S_3 states at the \bar{X} point as a function of Sn concentration x , from DFT calculated band dispersion. 102
- 3.19 Angle Resolved Photoemission Spectroscopy (ARPES) data along the $\bar{\Gamma} - \bar{X}$ direction measured with $h\nu = 21.2$ eV at RT for (a) a clean Ag(001) surface and (b)-(f) for 0.25 – 1.0 ML of Sn/Ag(001). White and red lines are used to guide our eye. Different surface states and resonances are marked with yellow arrow. *Fig. is taken from Dr. Arunava Kar's (SINP) Ph.D thesis with permission.* 103

3.20	Angle Resolved Photoemission Spectroscopy (ARPES) data along the $\bar{\Gamma} - \bar{M}$ direction measured with $h\nu = 21.2$ eV at RT for (a) a clean Ag(001) surface and (b)-(f) for 0.25 – 1.0 ML of Sn/Ag(001). White and red lines are used to guide our eye. Different surface states and resonances are marked with yellow arrow. <i>Fig. is taken from Dr. Arunava Kar's (SINP) Ph.D thesis with permission.</i>	104
3.21	Theoretically computed electronic band structure of the clean Ag(001) surface along (a) $\bar{\Gamma} - \bar{X} - \bar{\Gamma}$ and (b) $\bar{\Gamma} - \bar{M} - \bar{\Gamma}$ of the PCBZ. Bands are projected onto the atomic orbitals of the top two Ag layers. Value of the projection is represented by the color scale.	105
3.22	Projected density of states (PDOS) of the clean Ag(001) substrate, showing contributions from 4 <i>d</i> and 5 <i>s</i> orbitals of Ag atoms belonging to the top two surface layers. Ag 5 <i>s</i> orbitals have a larger contribution near the Fermi level.	106
3.23	Theoretically computed electronic band structure of $\text{Sn}_x\text{Ag}_{1-x}/\text{Ag}(001)$ for $x = 0.25$ along (a) $\bar{\Gamma} - \bar{X} - \bar{\Gamma}$ and (b) $\bar{\Gamma} - \bar{M} - \bar{\Gamma}$ of the PCBZ. Bands are projected onto the atomic orbitals of the top two Ag layers. Value of the projection is represented by the color scale.	107
3.24	DFT calculated orbital projected band structures of (a)-(e) $x = 0.25$, (f)-(j) $x = 0.5$, (k)-(o) $x = 0.75$, (p)-(t) $x = 1.0$ for $\text{Sn}_x\text{Ag}_{1-x}/\text{Ag}(001)$ systems. Here we have projected the Kohn-Sham orbitals on individual orbitals of Ag- <i>sp</i> , Sn-5 <i>s</i> , Sn-5 <i>p_x</i> , Sn-5 <i>p_y</i> , Sn-5 <i>p_z</i> , respectively. . . .	107
3.25	Theoretically computed electronic band structure of $\text{Sn}_x\text{Ag}_{1-x}/\text{Ag}(001)$ for $x = 0.5$ along (a) $\bar{\Gamma} - \bar{X} - \bar{\Gamma}$ and (b) $\bar{\Gamma} - \bar{M} - \bar{\Gamma}$ of the PCBZ. Bands are projected onto the atomic orbitals of the top two Ag layers. Value of the projection is represented by the color scale.	108

- 3.26 Theoretically computed electronic band structure of $\text{Sn}_x\text{Ag}_{1-x}/\text{Ag}(001)$ for $x = 0.75$ along (a) $\bar{\Gamma} - \bar{X} - \bar{\Gamma}$ and (b) $\bar{\Gamma} - \bar{M} - \bar{\Gamma}$ of the PCBZ. Bands are projected onto the atomic orbitals of the top two Ag layers. Value of the projection is represented by the color scale. 109
- 3.27 Theoretically computed electronic band structure of the 1 ML $\text{Sn}/\text{Ag}(001)$ (i.e., $x = 1.0$) along (a) $\bar{\Gamma} - \bar{X} - \bar{\Gamma}$ and (b) $\bar{\Gamma} - \bar{M} - \bar{\Gamma}$ of the PCBZ. Bands are projected onto the atomic orbitals of the top two Ag layers. Value of the projection is represented by the color scale. 110
- 3.28 3D charge density difference (CDD) plots $\Delta\rho$ (right Figs. along with side and top views) and planar-averaged CDD plots (left Figs.) for (a) $x = 0.25, p(2 \times 2)$ cell, (b) $x = 0.5, p(2 \times 1)$ cell, (c) $x = 0.75, p(2 \times 2)$ cell, and (d) $x = 1.0, p(1 \times 1)$ cell. Color scheme of the atoms: Sn – green, surface Ag atom – orange, below Ag atom – light gray. Isosurface value for the CDD plots = $\pm 0.001 \text{ e/bohr}^3$. Accumulation and depletion of electrons are represented by the red and blue colors, respectively. The horizontal blue lines in each case correspond to the average heights of the top two layers. 112
- 3.29 Electrostatic potential $V_{bare} + V_{Hartree}$ as a function of z-coordinates of the slabs for (a) clean $\text{Ag}(001)$, $p(1 \times 1)$ cell, (b) $x = 0.25, p(2 \times 2)$ cell, (c) $x = 0.5, p(2 \times 2)$ cell, (d) $x = 0.75, p(2 \times 2)$ cell, and (e) $x = 1.0, p(1 \times 1)$ cell. The vertical black dotted line represent average height of the top layer in each case. The change in the potential is clearly observed in the Sn/Ag interface region; the potential is decreasing as Sn concentration x is increasing. 113

3.30	Variation of the crossing point below the Fermi level with surface electrostatic potential for different Sn concentration x . Blue filled squares are for the structures for which band structures are calculated, and green filled circle is for $x = 0.5$, $p(1 \times 10)$ cell.	114
4.1	Experimental photoluminescence (PL) spectra of pristine CsPbX_3 and Fe-doped CsPbX_3 systems ($X = \text{Br}, \text{Cl}$). (a) and (c) show the change in the PL intensity and absorbance with increasing Fe concentration for Fe-doped CsPbBr_3 and Fe-doped CsPbCl_3 , respectively. (b) and (d) show change in the area under the PL curve with Fe concentration. <i>This figure is taken from Saptarshi Chakraborty's (NCU, JNCASR) Ph.D thesis and used with permission.</i>	135
4.2	Systems studied in our DFT calculations: (a) 12.5% Fe-doped CsPbBr_3 , (b) 25% Fe-doped CsPbBr_3 , (c) 12.5% Fe-doped CsPbCl_3 , and (d) 25% Fe-doped CsPbCl_3 . A $2 \times 2 \times 2$ supercell contains 8 Cs, 7(6) Pb, 1(2) Fe and 24 Br/Cl atoms for 12.5%(25%) Fe concentrations. Only the lowest energy structures are shown at 25% Fe concentration in which two Fe atoms are 2nd NN or face-diagonal. Atomic color code: Cyan – Cs, Gray – Pb, Green – Br, Yellow – Cl, Red – Fe.	138
4.3	Lattice constants of pristine CsPbBr_3 and Fe-doped CsPbBr_3 (black circles), and of CsPbCl_3 and Fe-doped CsPbCl_3 (red circles). Black and red lines are linear fits to the data.	140

4.4	Electronic structure of pristine CsPbBr ₃ . Panels (a) and (b) show the orbital-projected band structure and projected density of states(PDOS), respectively, of CsPbBr ₃ , without spin-orbit coupling (SOC). Panels (c) and (d) show the orbital-projected band structure and PDOS, respectively, of CsPbBr ₃ , with SOC. The PDOS confirms that the main contributions come from Pb-6 <i>p</i> and Br-4 <i>p</i> orbitals, we have projected the band structures onto these orbitals and shown the relative contributions from these two orbitals according to the color scale. Orbital contributions in the band structure plots: Green - Pb-6 <i>p</i> and Blue - Br-4 <i>p</i>	144
4.5	Electronic structure of pristine CsPbCl ₃ . (a) and (b) are projected band structure and PDOS, respectively, of CsPbCl ₃ , without spin-orbit coupling (SOC). (c) and (d) are the same of CsPbCl ₃ , with SOC. PDOS confirms that the main contributions come from Pb-6 <i>p</i> and Cl-3 <i>p</i> orbitals, we have projected the band structures onto these orbitals and shown a comparison according to the color scale. Orbital contributions in the band structures plots: Green - Pb-6 <i>p</i> and Blue - Cl-3 <i>p</i>	145
4.6	Isosurfaces of the spin-polarization density or magnetization density [$m(\mathbf{r}) = n^\uparrow(\mathbf{r}) - n^\downarrow(\mathbf{r})$] of Fe-doped CsPbBr ₃ for (a) 12.5% and (b) 25% Fe concentration, and of Fe-doped CsPbCl ₃ for (c) 12.5% and (d) 25% Fe concentration. Red and blue lobes represent $m(\mathbf{r}) > 0$ and $m(\mathbf{r}) < 0$, respectively. We note strong magnetic moments on Fe atoms, plus small magnetic moments on the Br/Cl atoms adjacent to the Fe atoms. Isovalue used = ± 0.001 e/bohr ³ . We do not see any blue lobes at this isovalue.	147

- 4.7 Orbital projected density of states (PDOS) of Fe-doped CsPbBr₃ and comparison with the PDOS of pristine CsPbBr₃. (a) and (d) are PDOS of pristine CsPbBr₃ without SOC and with SOC, respectively. PDOS of 12.5% Fe-doped CsPbBr₃ is shown in (b) without SOC, for spin up and down, and (c) with SOC. PDOS of 25% Fe-doped CsPbBr₃ is shown in (e) without SOC, for spin up and down, and (f) with SOC. The main contributions come from three orbitals: Fe-3*d*, Br-4*p* and Pb-6*p*. 149
- 4.8 Orbital projected band structure of Fe-doped CsPbBr₃. At 12.5% Fe concentration, (a), (b) are without SOC, for spin up and down, respectively, and (c) is with SOC. At 25% Fe concentration, (d), (e) are without SOC, for spin up and down, respectively, and (f) is with SOC. The bands are projected onto three atomic orbitals, which have the most contributions near the Fermi level, as shown in the three-color triangle - red: Fe-3*d*, blue: Br-4*p* and green: Pb-6*p*. The intermediate colors indicate the extent of mixing of these orbital contributions. . . 150
- 4.9 Orbital projected density of states (PDOS) of Fe-doped CsPbCl₃ and comparison with the PDOS of pristine CsPbCl₃. (a) and (d) are PDOS of pristine CsPbCl₃ without SOC and with SOC, respectively. PDOS of 12.5% Fe-doped CsPbCl₃ is shown in (b) without SOC, for spin up and down, and (c) with SOC. PDOS of 25% Fe-doped CsPbCl₃ is shown in (e) without SOC, for spin up and down, and (f) with SOC. The main contributions come from three orbitals: Fe-3*d*, Cl-3*p* and Pb-6*p*. 151

- 4.10 Orbital projected band structure of Fe-doped CsPbCl₃. At 12.5% Fe concentration, (a), (b) are without SOC, for spin up and down, respectively, and (c) is with SOC. At 25% Fe concentration, (d), (e) are without SOC, for spin up and down, respectively, and (f) is with SOC. The bands are projected onto 3 atomic orbitals, which have the most contributions near the Fermi level, as shown in the three-color triangle - red: Fe-3*d*, blue: Cl-3*p* and green: Pb-6*p*. The intermediate colors correspond to mixing of the orbital contributions. 152
- 4.11 Phonon dispersion along with atomic contributions, calculated without SOC for 12.5% Fe-doped systems. (a) and (b) are for Fe-doped CsPbBr₃ and Fe-doped CsPbCl₃, respectively. The phonon branches are colored according to the weights of the atomic contributions. Color code: Red – Fe, Blue – Br/Cl and Green – Pb, as shown in the triangle. The intermediate colors correspond to the mixing of the atomic contributions. 155
- 4.12 Phonon or vibrational density of states along with atomic contributions, calculated without SOC for 12.5% Fe-doped systems. (a) and (b) are for Fe-doped CsPbBr₃ and Fe-doped CsPbCl₃, respectively. Color code: Magenta – Fe, Blue – Br/Cl and Green – Pb. 155
- 4.13 Electronic band structure of (a) 12.5% Fe-doped CsPbBr₃ and (b) 12.5% Fe-doped CsPbCl₃, with different applied strains. For comparison, all the band structures with three different strain values are shown in the same plot. Black, red and blue lines correspond to bands due to 0%, +1% and –1% strain. 158

5.1	All-inorganic perovskite NCs show emission throughout the whole visible region. Used with permission from Ref. 1. Further permission related to the material excerpted should be directed to the ACS. . . .	173
5.2	(a) Calculated band structure of CsPbBr ₃ . Scissor correction of 0.76 eV has been applied to the conduction bands. The vertical blue arrows indicate direct transitions that have been identified with the peaks in the dotted blue curves in (b). (b) Imaginary part of the dielectric function ϵ_2 from ellipsometry measurements (red curve) and DFT calculations (blue and green curves) for CsPbBr ₃ . The dotted blue and solid green curves were computed using broadening parameters $\Gamma = 0.2$ eV and 0.4 eV, respectively.	178
5.3	(a) Calculated band structure of CsPbCl ₃ . Scissor correction of 0.88 eV has been applied to the conduction bands. The vertical blue arrows indicate direct transitions that have been identified with the peaks in the dotted blue curves in (b). (b) Imaginary part of the dielectric function ϵ_2 from ellipsometry measurements (red curve) and DFT calculations (blue and green curves) for CsPbCl ₃ . The dotted blue and solid green curves were computed using broadening parameters $\Gamma = 0.2$ eV and 0.4 eV, respectively.	180
5.4	Calculated band structure of (a) CsPbBr ₃ and (b) CsPbCl ₃ for -1% (blue bands), 0% (black bands) and +1% (red bands) strain.	183
5.5	Calculated imaginary part (ϵ_2) of frequency dependent dielectric function for (a) CsPbBr ₃ , 12.5% Fe-doped CsPbBr ₃ and (b) CsPbCl ₃ , 12.5% Fe-doped CsPbCl ₃ . Color code of curves: magenta – pristine systems and blue – Fe-doped systems. Green vertical lines and black arrows represent the first peak in ϵ_2 spectra for all the systems. . . .	186

6.1	(a) The unreconstructed interface has neutral (001) planes in SrTiO ₃ , but the (001) planes in LaAlO ₃ have alternating net charges (ρ). If the interface plane is LaO/TiO ₂ , this produces a non-negative electric field (E), leading in turn to an electric potential (V) that diverges with thickness. (c) The divergence catastrophe at the LaO/TiO ₂ interface can be avoided if half an electron is added to the last Ti layer. This produces an interface dipole that causes the electric field to oscillate about zero and the potential remains finite. The upper free surface is not shown, but in this simple model the uppermost AlO ₂ layer would be missing half an electron, which would bring the electric field and potential back to zero at the upper surface. Reprinted with permission from Ref. 15.	198
6.2	Principle of modulation doping. Electrons from the donors in the material with the higher-conduction band edge transfer into the conduction band of the semiconductor on the other side of the interface, creating a 2DEG. The electrons are spatially separated from their donors, and ionized impurity scattering is thus reduced. E_C and E_V denote the conduction band edge and valence band edge, respectively, and E_F denotes the Fermi level. Reprinted with permission from Ref. 38.	200
6.3	Measured two-dimensional resistivity vs temperature for LVO/KTO interface using four-probe method. Reprinted with permission from Ref. 62.	205

6.4	Cubic crystal structure of bulk KTaO_3 . It has the perovskite structure in which each Ta atom is surrounded by six O atoms forming an TaO_6 Octahedron. Here, a $2 \times 2 \times 2$ supercell is shown. The primitive unit cell contains five atoms: one K, one Ta and three O atoms. Atomic color code: magenta: K, blue: Ta, red: O.	206
6.5	Structure of bulk LaVO_3 : (a) orthorhombic and (b) tetragonal. The orthorhombic structure can be derived from the cubic structure by introducing a pattern of alternating distortions in the VO_6 octahedra. The primitive unit cell of (a) contains a total of 20 atoms: four La, four V and twelve O atoms. The primitive unit cell of (b) contains five atoms: one La, one V and three O. Atomic color code: green: La, brown: V, red: O.	207
6.6	Optimized structure of (a) 9-layers KTO(001) slab with TaO_2 termination, (b) LVO/KTO interface in the superlattice model, and (c) LVO/KTO interface with vacuum. The horizontal red dashed lines indicate the locations of the interfaces. (b) contains two interfaces per unit cell and (c) contains only one interface per unit cell. Atomic color code: green: La, brown: V, red: O, magenta: K, blue: Ta. . . .	209
6.7	(a) Electronic band structure and (b) projected density of states (PDOS) of bulk KTO without spin-orbit coupling (SOC). (c) Electronic band structure and (d) PDOS of bulk KTO with SOC. The corresponding colors of the orbital projected DOS are shown in the insets of (b) and (d). The calculated $R - \Gamma$ indirect band gap is = 2.18 eV without SOC, and 2.04 eV with SOC. In each case, the Fermi level is set at the valence band maximum (VBM) and is indicated by the red dashed lines.	212

6.8	Electronic band structure of the KTO(001) surface (a) without SOC and (b) with SOC. The horizontal red dashed line represents the Fermi level in each case.	216
6.9	PDOS of KTO(001) surface, calculated without SOC. Orbitals on which the wavefunctions are projected are shown in the inset. The horizontal red dashed line represents the Fermi level.	216
6.10	Bands are projected on to all atomic orbitals of (a) top TaO ₂ , (b) 3rd TaO ₂ , (c) 5th TaO ₂ and (d) 7th TaO ₂ layer of KTO(001) surface, without SOC. The color scales represent the amount of orbital projection. The horizontal black dashed line represents the Fermi level in each case. The color scales represent the amount of orbital projection, for each layer.	217
6.11	(a) Schematic representation of a 2×2×2 standard perovskite (RVO ₃) structure. Each vanadium atom is surrounded by an oxygen octahedron (for simplicity only one oxygen octahedron is shown). Orthorhombic RVO ₃ structure is derived from the above 2×2×2 standard perovskite structure as shown by thick red line. (b) Orthorhombic crystal structure of RVO ₃ . Reprinted with permission from Ref. 101.	218
6.12	Electronic band structure of bulk orthorhombic LVO with DFT+ <i>U</i> calculations. Two types of DFT+ <i>U</i> calculations are used, as implemented in QE: (i) C-dG method ⁷⁹ , and (ii) L method ⁸⁰ . Used different combinations of values of <i>U</i> and <i>J</i> parameters to match the experimental band gap of 1.1 eV. The method, values of <i>U</i> and <i>J</i> , and <i>E_g</i> are written at the top of each figure.	220

6.13 PDOS of bulk orthorhombic LVO without SOC. Here we have used DFT+ U with kind = 1 of QE, ortho-atomic projection, $U = 5.65$ eV, $J = 0.65$ eV. The orbitals on which the wave functions are projected on are shown in the inset. The Fermi level is represented by the red dashed line.	221
6.14 Electronic band structure of bulk orthorhombic LVO (a) without SOC and (b) with SOC. Here we have used DFT+ U with kind = 1 of QE, ortho-atomic projection, $U = 5.65$ eV, $J = 0.65$ eV. The Fermi level is set at the VBM and is represented by the red dashed line in each case.	221
6.15 Different types of anti ferromagnetic (AFM) orderings. C-AFM means ferromagnetic stacking of antiferromagnetic layers, A-AFM means antiferromagnetic stacking of ferromagnetic layers, and G-AFM means antiferromagnetic stacking of antiferromagnetic layers. Reprinted with permission from Ref. 101.	224
6.16 (a) Electronic band structure and (b) PDOS of bulk tetragonal LVO calculated without SOC. The atomic orbitals on which the wave functions are projected on are shown in the inset of (b). Black dashed line represents the Fermi level in each case.	225
6.17 Structure of $(\text{LVO})_{4.5}/(\text{KTO})_{8.5}$ superlattice model. The red dashed lines represent the locations of the interfaces. Atomic color code: green: La, brown: V, red: O, magenta: K, blue: Ta.	226
6.18 (a) Percentage interlayer relaxations $\Delta_{ij}(\%)$ and (b) relative displacement or polar distortion between cations and anions for each layer of $(\text{LVO})_{4.5}/(\text{KTO})_{8.5}$ superlattice. The black dashed line represent the location of the interface.	227

- 6.19 Magnetization density of $(\text{LVO})_{4.5}/(\text{KTO})_{4.5}$ superlattice model for A-AFM ordering. Red and blue lobes correspond to excess of spin-up and spin-down electron densities, respectively. Isosurface value = $0.003 \text{ e}/\text{bohr}^3$. Atomic color code: green: La, brown: V, red: O, magenta: K, blue: Ta. 229
- 6.20 Electronic band structure of (a) $(\text{LVO})_{4.5}/(\text{KTO})_{4.5}$ superlattice and (b) $(\text{LVO})_{4.5}/(\text{KTO})_{8.5}$ superlattice. Both are calculated for A-AFM ordering, without SOC. Red lines represent spin up bands and blue dashed lines represent spin down bands. The Fermi level is represented by the black dashed line in each case. 230
- 6.21 (a) Layer-resolved and spin-resolved PDOS of $(\text{LVO})_{4.5}/(\text{KTO})_{8.5}$ superlattice. (b) shows the corresponding structure from the middle of the KTO part to the middle of the LVO part. Color code in (a): magenta - Ta-5*d*, blue - V-3*d*, red - O-2*p*, cyan - La-5*d*. The full lines represent spin up and the dashed lines represent spin down states. . . 232
- 6.22 (a) Bands are projected on to Ta-5*d* states of each layer of $(\text{LVO})_{4.5}/(\text{KTO})_{8.5}$ superlattice. (a)-(e) are for spin up and (f)-(j) are for spin down bands. Color scales represent the amount of orbital projection. . . . 234
- 6.23 (a) Bands are projected on to V-3*d* states of each layer of $(\text{LVO})_{4.5}/(\text{KTO})_{8.5}$ superlattice. (a)-(b) are for spin up and (c)-(d) are for spin down bands. Color scales represent the amount of orbital projection. . . . 235
- 6.24 Layer-resolved and spin-resolved electronic charge for $(\text{LVO})_{4.5}/(\text{KTO})_{8.5}$ superlattice. Being mirror symmetric, only the layers around the middle interface are shown. Black dashed line represents the position of the middle interface. Counting of layers starts from the interface and represented by positive and negative integers for LVO and KTO part, respectively. 236

6.25	Planar-averaged ILDOS for $(\text{LVO})_{4.5}/(\text{KTO})_{8.5}$ superlattice. Black dashed lines represent the position of the interfacial TaO_2 and LaO layers. Structure is also aligned to better understand the peak positions along the z -axis. Atomic color code: green: La, brown: V, red: O, magenta: K, blue: Ta.	238
6.26	Planar-averaged charge density difference $\Delta\tilde{\rho}(z)$ in units of e/bohr^3 for $(\text{LVO})_{4.5}/(\text{KTO})_{8.5}$ superlattice. The vertical black dashed lines represent the interfacial TaO_2 and LaO layers, at the middle and end interfaces of the supercell. The structure is also aligned with the z -coordinates for better understanding. Atomic color code: green: La, brown: V, red: O, magenta: K, blue: Ta.	240
6.27	Magnetic moments on atoms of each layer for $(\text{LVO})_{4.5}/(\text{KTO})_{8.5}$ superlattice. Red and blue represent spin up and down moments, respectively. Being mirror symmetric, only the layers around the middle interface are shown. Black dashed line represents the position of the middle interface. Counting of layers starts from the interface and represented by positive and negative integers for LVO and KTO part, respectively.	241

List of Tables

- 3.1 Energetics of different geometries considered for the 1 ML Sn/Ag(001), as obtained from DFT calculations. ΔE_{ads} denotes the energy of a given configuration with respect to the lowest energy configuration i.e., hollow site adsorption. The number in boldface indicates the highest value of adsorption energy, and hence corresponds to the most stable adsorption geometry. **78**
- 4.1 DFT energetics of different structures of Fe-doped CsPbBr₃, for 25% Fe concentration. In the different structures, the two Fe atoms in the unit cells are at different distances from each other; they also differ in their relative magnetic ordering. ΔE_{ads} denotes the energy of a given configuration with respect to the lowest energy configuration. **141**
- 4.2 DFT energetics of different structures of Fe-doped CsPbCl₃, for 25% Fe concentration. In the different structures, the two Fe atoms in the unit cells are at different distances from each other; they also differ in their relative magnetic ordering. ΔE_{ads} denotes the energy of a given configuration with respect to the lowest energy configuration. **141**
- 4.3 Calculated formation energies of pristine and Fe-doped systems. . . . **143**

5.1	Band gap E_g of CsPbBr ₃ and CsPbCl ₃ . Comparison between our calculated values, previously calculated values and experimentally measured values.	177
5.2	Identified optical transitions from calculation for CsPbBr ₃ and comparison with ellipsometry measurements. The values of the transitions energies are written and compared between calculation and experiment. The orbitals involved in the transitions are also mentioned. All the theoretical values are shifted up with 0.76 eV.	179
5.3	Identified optical transitions from calculation for CsPbCl ₃ and comparison with ellipsometry measurements. The values of the transitions energies are written and compared between calculation and experiment. The orbitals involved in the transitions are also mentioned. All the theoretical values are shifted up with 0.88 eV.	181
5.4	Variation in the transition energies corresponding to the band edge (ω_{BE}) and peak (ω_{pk}) in $\epsilon_2(\omega)$ with applied strain, for both CsPbBr ₃ and CsPbCl ₃ . W is the difference in energy between the peak and band edge transitions, and δ (defined in the text) is a measure of electron-phonon coupling.	184
6.1	Our PBE-GGA calculated optimized lattice constant (a_0) and bulk modulus (B_0) of bulk KTO. The values are compared against previous calculations with different functionals and with experiments.	211
6.2	Our PBE-GGA calculated band gap of bulk KTaO ₃ . The value is compared against other calculated values with different functionals and methods, and also with the experiment. As usual, GGA underestimates the band gap.	213

6.3	Table of lattice parameters of orthorhombic LVO. Our PBE-GGA calculated optimized lattice parameters (here, $U = J = 0$) are compared against previous calculations with different functionals and with experiments.	218
6.4	Comparison of total energy of different magnetic configurations of tetragonal bulk LVO. ΔE is the total energy difference with respect to the lowest energy configuration A-AFM. It is taken per formula unit of LVO to compare the total energies.	224
6.5	Comparison of total energy of different magnetic orderings of V atoms in $(\text{LVO})_{4.5}/(\text{KTO})_{4.5}$ superlattice. ΔE is the total energy difference with respect to the lowest energy configuration A-AFM. It is taken per formula unit of LVO/KTO to compare the total energies.	228

Chapter 1

Introduction

To be a scientist is to be naive. We are so focused on our search for truth, we fail to consider how few actually want us to find it. But it is always there, whether we see it or not, whether we choose to or not. The truth doesn't care about our needs or wants. It doesn't care about our governments, our ideologies, our religions. It will lie in wait for all time. Where I once would fear the cost of truth, now I only ask: "what is the cost of lies?"

Chernobyl

In this chapter, we give a very brief summary of 'rational design' of nanomaterials, its historical importance, technological applications and how we do rational design using computer simulations and predict the properties of materials. We also summarize the essence of each chapter of this thesis.

1.1 Rational design of nanomaterials

Humans have used improved materials for better civilization from ancient ages. Examples of this are the Stone age, the Bronze age and the Iron age. The study of materials is not new; humans have been manipulating and utilizing materials since ancient times. However, materials science as a distinct scientific discipline emerged in the mid 20th century, driven by the need to understand and engineer materials with specific properties for various applications. Humans have also (unknowingly) used nanomaterials from ancient times, for diverse applications. For example, humans used asbestos nanofibers to reinforce ceramic mixtures about four thousand years ago.¹ Also, about four thousand years ago, the ancient Egyptians knew about PbS nanoparticles and used them for hair-dyeing.^{2;3} Another ancient example of the use of nanomaterials is the Lycurgus Cup, made by the Romans in the fourth century CE. It is a dichroic cup whose color changes based on the nature of the incoming light. This color change is due to the presence of Au and Ag nanoparticles.⁴

The field of materials science has witnessed remarkable advances in recent years, enabling the development of novel materials with extraordinary properties. From high-performance alloys and flexible electronics to drug-delivery systems and energy storage devices, the quest for designing materials with tailored functionalities has become increasingly significant. A key part of this scientific pursuit is the concept of rational design, which represents a paradigm shift from the traditional trial-and-error approach to materials development.

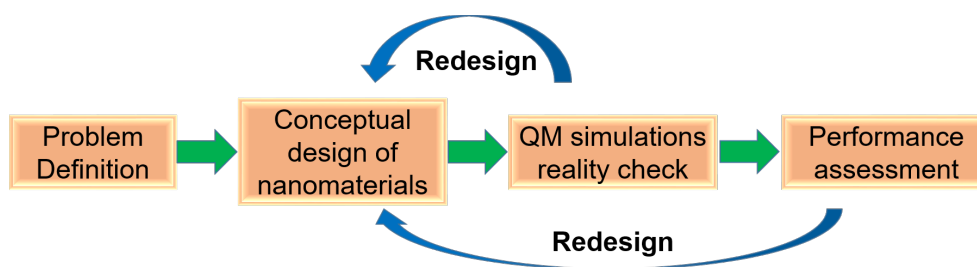


Figure 1.1: Schematic of procedure of rational design of nanomaterials.

The ‘rational design’ of materials is based on the concept of ‘design on purpose’,⁵ and refers to a deliberate and systematic approach toward designing new materials with desired properties and functionalities based on a fundamental understanding of their structure-property relationships. It involves using scientific principles, computational modeling, and experimental techniques to guide the design process.

Traditionally, materials development relied heavily on trial-and-error approaches, where researchers would explore various compositions and fabrication methods in the hope of discovering new materials with desired properties. However, this approach can be time-consuming, costly, and inefficient.

Rational design aims to overcome these challenges by leveraging our knowledge of material properties at the atomic and molecular level. Fig. 1.1 shows the schematic of steps followed in rational design of nanomaterials. It involves understanding how the arrangement of atoms or molecules influences the material’s properties, and then using this knowledge to design and synthesize materials with specific characteristics. Advances in computational modeling, such as quantum mechanical simulations and materials informatics, play a crucial role in rational design. These tools enable researchers to predict material properties, simulate material behavior under different conditions, and screen large databases of materials to identify promising candidates. The problem is well defined first [see Fig. 1.1], then one does conceptual design of the nanomaterials and verifies whether the material is suitable for the defined problem, using theoretical calculations at the atomic scale. After the design phase, experimentalists synthesize the predicted material and do measurements on it. If the theoretically predicted properties match well with the experimental observations, then it is fine. If they do not match, theoreticians try to understand the reason, at the atomic level, for these deviations, and come up with better solutions based on the insights gained. In this way, one does not have to synthesize *all* the nanomaterials considered and measure their properties. Rather, theoretical calculations filter out

most candidates until one is left with only a few nanomaterials which have to be synthesized and studied by experimentalists. This saves an extremely huge amount of time and effort.

By employing rational design strategies, scientists can develop materials with enhanced properties such as strength, conductivity, durability, magnetism, catalytic activity, or specific optical properties. This approach has applications in various fields, including electronics, energy storage, catalysis, biomaterials, and more, leading to the development of innovative and tailored materials for specific applications.

Nanomaterials possess unique characteristics due to their nanoscale dimensions, which typically range from 1 to 100 nanometers (nm). At this scale, materials exhibit intriguing properties such as enhanced surface-to-volume ratio, quantum confinement effects, and distinctive mechanical, electronic, optical, and catalytic behavior. Rational design enables researchers to leverage these inherent nanoscale properties and precisely engineer materials with desired attributes for specific applications.

Richard Feynman introduced the concept of ‘nanotechnology’ for the first time in 1959 at the American Physical Society’s annual meeting; this is considered as the first academic talk in nanotechnology. He said - “There is plenty of room at the bottom” and “why can’t we write the entire 24 volumes of the Encyclopedia Britannica on the head of a pin?” The broad vision was to create smaller materials or nanomaterials, even at the atomic scale, to store extremely large amounts of information.⁶

The research in the field of nanotechnology has advanced by some breakthrough discoveries and inventions, such as the scanning tunneling microscope (STM) in 1982 by Gerd Binnig and Heinrich Rohrer.⁷ Using STM, one can obtain images at the single atom level, of systems such as atoms on surfaces. Shortly thereafter, the atomic force microscope (AFM) was invented in 1986.⁸ Advances such as these, and

the knowledge gained, ultimately helped to create hard disks with huge storage capacity. Research in the field of nanotechnology is evolving every day and nowadays very powerful methods are available to tune different properties at the nanoscale. Several applications of nanomaterials have already been reached at the commercial level such as surface coatings, electronics, scratch-free paints, environmental remediation, cosmetics, energy-storage devices, sports equipment, and sensors.⁹

Experimentalists use two main schemes for the synthesis of nanomaterials: (i) top-down approach and (ii) bottom-up approach. In top-down approaches, bulk materials are divided to produce nanomaterials. Top-down methods include sputtering, laser ablation, mechanical milling, etching, and electro-explosion. In bottom-up approaches, individual atoms are assembled to form larger nanoparticles. Some bottom-up approaches are chemical vapor deposition, spinning, solvothermal and hydrothermal methods, sol-gel method, molecular condensation, soft and hard templating methods, reverse micelle methods, etc.

Nanomaterials have diverse emergent properties which are very different from their bulk counterparts. The properties varies with the size, shape and composition of the nanoparticles forming the nanomaterials.^{10;11} For example, a solution of large Au particles is yellow in color, whereas a solution of Au nanoparticles is purple or red in color, depending on the size of the nanoparticles. Electronic properties change drastically at the nanoscale, compared to the corresponding bulk. e.g., boron in its bulk structure is an insulator, whereas a two dimensional (2D) network of boron atoms, i.e., borophene, shows a metallic nature. Mechanical properties are improved at the nanoscale due to the enhancement of crystal perfection.¹² Optical properties of nanomaterials such as zero dimensional quantum dots depend on their size and shape.¹³

Nanomaterials can have the following properties which are very different from their bulk counterparts: (i) large surface area – nanomaterials have very large surface

to volume ratio, compared to their bulk counterparts,¹⁴ (ii) magnetism – emergence of magnetism at the nanoscale even when the bulk is non-magnetic.¹¹, (iii) quantum effects – these depend on the nature of the nanomaterials,¹⁵, (iv) enhanced electrical and thermal conductivity. One example is graphene, obtained from graphite by exfoliating a single layer of carbon atoms.¹⁶, (v) better mechanical properties,¹⁷, (vi) better support for catalysts – increases the catalytic performance.^{18;19}, (vii) some nanomaterials have antiviral, antibacterial, and anti-fungal properties and hence they have medical applications.^{20;21}

One of the key aspects of rational design is the utilization of computational modeling and simulation techniques. These tools provide invaluable insights into the behavior of materials by elucidating the interplay between their atomic or molecular arrangements and their macroscopic properties. Through the integration of computer-aided design, data-driven approaches, and machine learning algorithms, scientists can efficiently explore vast design spaces, accelerating the discovery and optimization of new materials.

In this thesis, we have followed the path of rational design of materials by which we can tune the structural, electronic, magnetic and optical properties of materials at the nanoscale, to make them better suited for technological applications. Nanomaterials can have zero dimensions (e.g., single atom, molecule, quantum dot, nanocluster of particles etc.), one dimension (nanowires, nanotubes, one-dimensional (1D) coordination polymers etc.), two dimensions (graphene, surfaces, thin films, etc.) or three dimensions (bulk crystals). When the size of material or the size in one of the dimension is in the range of 1 to 100 nm, then they are usually defined to be nanomaterials. This thesis presents atomistic modelling of bulk crystals, surfaces and heterostructure interfaces, and density functional theory (DFT) calculations of the structural, electronic, magnetic and optical properties of these systems.

Materials properties can be calculated using different ab initio computational

techniques such as density functional theory (DFT),^{22;23} molecular dynamics,²⁴ Monte Carlo simulations,²⁵ etc. The meaning of ‘ab initio’ or ‘first-principles’ methods is that you need almost zero input from experiment; in DFT calculations the only experimental inputs are, in principle, atomic masses and atomic numbers. This has represented a huge step forward in the search for new materials and the rational design of nanomaterials, and the goal of finding their properties. DFT has become very popular nowadays due to huge improvements in computational power and resources, and one is now in a position to tackle challenging calculations for very complex systems.

In this thesis, we have performed DFT calculations to find structural, electronic, magnetic and optical properties. The range of systems studied in this thesis cover a broad spectrum such as bulk crystals, metal and semiconductor surfaces, alloyed surfaces, bulk perovskite materials, transition metal doped perovskite systems, and heterostructures of perovskite oxide materials.

1.2 Outline of the thesis

In Chapter 1, we provide a very brief introduction to the projects and problems we have studied in this thesis. In this thesis, we have considered different kinds of systems, such as bulk crystals, the surfaces of bulk crystals, and interfaces between two materials. Specifically, we have considered metal surfaces, alloy formation on metal surfaces, bulk perovskite structures, transition metal atom doped bulk perovskites, and heterostructure interfaces between two perovskite oxide materials.

In Chapter 2, we have summarized the methods we have used in this thesis to perform density functional theory (DFT) calculations to find different properties of nanomaterials. We have briefly summarized the basics of DFT and the computational approaches used when performing DFT calculations. We have also discussed

the mathematical formalism used to calculate different properties throughout the thesis. For example, we have described, in brief, the theory of non spin-polarized and spin-polarized DFT, the computational approximations made when using DFT for doing simulations of real materials. We have also described relativistic DFT as we have incorporated spin-orbit coupling in some cases, and the DFT+ U method for strongly correlated systems, optical properties of materials and so on.

In Chapter 3, we have studied the deposition of Sn atoms on an Ag(001) substrate. This is collaborative work, done together with the experimental group of Prof. K. S. R. Menon, of the Surface Physics and Materials Science Division, SINP, Kolkata. Our theoretical calculations show that when Sn atoms are deposited on an Ag(001) surface, very interestingly Sn-Ag bimetallic surface alloys are formed for all Sn coverages. This is in contradiction with the naive expectation of Sn atoms forming an overlayer on the Ag(001) surface. We discuss the reasons why these naive expectations are incorrect. The calculated results are compared against the data from low energy electron diffraction (LEED) experiments. Then we calculate the electronic structure of the lowest energy stable structures at each Sn concentration considered in our calculations. The calculated band structures are compared with the angle-resolved photoemission spectroscopy (ARPES) measurements. Overall, we see very good agreement between theory and experiment. An interesting feature in both the experimentally measured and theoretically computed band structure is the existence of a crossing point between two linearly dispersive bands, similar to the Dirac cone in graphene, and a variation in its energy with the Sn concentration. We have also analyzed the electrostatic potential and charge density difference, to gain insights into the origins of surface states and surface resonances.

In Chapter 4, we have studied the structural, electronic, photoluminescence and optical properties of CsPbBr₃, CsPbCl₃, Fe-doped CsPbBr₃ and Fe-doped CsPbCl₃. This work is in collaboration with the experimental group of Prof. Ranjani Viswanatha,

New Chemistry Unit, JNCASR, Bangalore. They were able to dope Fe atoms successfully into CsPbBr₃ and CsPbCl₃ nanocrystals. They measured the photoluminescence of the Fe-doped systems and compared these results with those obtained from the corresponding pristine systems. They observed that the photoluminescence is considerably quenched or reduced upon Fe doping, compared to the pristine CsPbBr₃ and CsPbCl₃. We have performed DFT calculations to see the effect of Fe doping on the lattice. The electronic structures of the pristine systems and Fe-doped systems are compared. We have found the effects of Fe doping in CsPbBr₃ and CsPbCl₃, and compared the results with the pristine systems. We are able to explain the fundamental origin of photoluminescence quenching in the Fe-doped systems. Finally, we calculated the vibrational properties of Fe-doped CsPbBr₃ and Fe-doped CsPbCl₃ and give an explanation of different degrees of photoluminescence quenching in these materials.

In Chapter 5, we calculate the optical properties of CsPbBr₃ and CsPbCl₃ perovskite materials. Our experimental collaborators in the group of Prof. Ranjani Viswanatha, JNCASR, Bangalore, have done some optical measurements. Other experimental collaborators, in the group of Prof. Bivas Saha, JNCASR, Bangalore, were trying to find the possible optical transitions occurring in CsPbBr₃ and CsPbCl₃ perovskites, using ellipsometry measurements. They measured the band edge transition, as well as other excited state transitions. Using ellipsometry, our collaborators have measured frequency dependent optical constants (e.g., imaginary part of dielectric function $\epsilon_2(\omega)$) by observing the change in polarization of light when it reflects or transmits from CsPbBr₃ and CsPbCl₃. The peaks found in the spectra of $\epsilon_2(\omega)$ are identified as different transitions from the different states in the valence band to the states in the conduction band of these materials. We have calculated the electronic structure and optical properties of CsPbBr₃ and CsPbCl₃ using first principles DFT calculations. We have identified the valence states and

conduction states involved in the different optical transitions found in the ellipsometry measurements. We have also identified the atomic orbitals involved in these optical transitions. Further, we have calculated the frequency dependent imaginary part of the dielectric function $\epsilon_2(\omega)$ and compared it with the experimental spectra, for both CsPbBr₃ and CsPbCl₃.

In Chapter 6, we have studied the electronic properties of the two-dimensional electron gas (2DEG) formed at the LaVO₃/KTaO₃ (LVO/KTO) heterostructure interface. This work has been performed in collaboration with the experimental group of Prof. Suvankar Chakraverty, INST, Mohali, who formed the LVO/KTO interface by depositing a thin film of LVO on a TaO₂ terminated KTO(001) substrate, using pulsed laser deposition (PLD). They have observed metallicity at the LVO/KTO interface while measuring the two dimensional (2D) resistivity as a function of temperature, above 3 monolayer (ML) LVO thickness. The calculated carrier density and carrier mobility, in their experiment, is very high at the LVO/KTO interface.

We have first performed electronic structure calculations of the constituents LVO and KTO which are confirmed to be insulating. However, our calculations of the LVO/KTO interface show a metallic nature, consistent with the experimental observations. The calculated electronic charge is maximum near the interface and decreases rapidly away from the interface, which shows the two-dimensional nature of the conduction electrons. We also find that an ‘electronic reconstruction’ is the origin of 2DEG formation at the LVO/KTO interface.

In Chapter 7, we have summarized the main conclusions of each chapter and we raise some open questions that can be addressed in future work. This can lead to diverse directions for each project and possibly reveal even more interesting physics.

Bibliography

- [1] F. J. Heiligtag and M. Niederberger, “The fascinating world of nanoparticle research,” *Mater. Today.*, vol. 16, no. 7-8, pp. 262–271, 2013.
- [2] P. Walter, E. Welcomme, P. Hallégot, N. J. Zaluzec, C. Deeb, J. Castaing, P. Veyssi ere, R. Br eniaux, J.-L. L ev eque, and G. Tsoucaris, “Early use of PbS nanotechnology for an ancient hair dyeing formula,” *Nano Lett.*, vol. 6, no. 10, pp. 2215–2219, 2006.
- [3] J. Jeevanandam, A. Barhoum, Y. S. Chan, A. Dufresne, and M. K. Danquah, “Review on nanoparticles and nanostructured materials: history, sources, toxicity and regulations,” *Beilstein J. Nanotechnol.*, vol. 9, no. 1, pp. 1050–1074, 2018.
- [4] I. Freestone, N. Meeks, M. Sax, and C. Higgitt, “The Lycurgus cup – a Roman nanotechnology,” *Gold Bull.*, vol. 40, pp. 270–277, 2007.
- [5] R. Li, L. Zhang, and P. Wang, “Rational design of nanomaterials for water treatment,” *Nanoscale*, vol. 7, no. 41, pp. 17167–17194, 2015.
- [6] R. Feynman, “There’s plenty of room at the bottom,” in *Feynman and Computation*, pp. 63–76, CRC Press, 2018.

-
- [7] G. Binnig, H. Rohrer, C. Gerber, and E. Weibel, "Surface studies by scanning tunneling microscopy," *Phys. Rev. Lett.*, vol. 49, no. 1, p. 57, 1982.
- [8] G. Binnig, C. F. Quate, and C. Gerber, "Atomic force microscope," *Phys. Rev. Lett.*, vol. 56, no. 9, p. 930, 1986.
- [9] S. Sharifi, S. Behzadi, S. Laurent, M. L. Forrest, P. Stroeve, and M. Mahmoudi, "Toxicity of nanomaterials," *Chem. Soc. Rev.*, vol. 41, no. 6, pp. 2323–2343, 2012.
- [10] R. J. Varghese, S. Parani, S. Thomas, O. S. Oluwafemi, J. Wu, *et al.*, "Introduction to nanomaterials: synthesis and applications," in *Nanomaterials for Solar Cell Applications*, pp. 75–95, Elsevier, 2019.
- [11] E. Roduner, "Size matters: why nanomaterials are different," *Chem. Soc. Rev.*, vol. 35, no. 7, pp. 583–592, 2006.
- [12] R. S. Tomar, A. Jyoti, and S. Kaushik, "Nanobiotechnology: Concepts and applications in health, agriculture, and environment," 2020.
- [13] A. P. Alivisatos, "Semiconductor clusters, nanocrystals, and quantum dots," *Science*, vol. 271, no. 5251, pp. 933–937, 1996.
- [14] R. Tomar, A. A. Abdala, R. Chaudhary, and N. Singh, "Photocatalytic degradation of dyes by nanomaterials," *Mater. Today: Proc.*, vol. 29, pp. 967–973, 2020.
- [15] L. D. Geoffrion and G. Guisbiers, "Quantum confinement: size on the grill!," *J. Phys. Chem. Solids*, vol. 140, p. 109320, 2020.
- [16] S. K. Krishnan, E. Singh, P. Singh, M. Meyyappan, and H. S. Nalwa, "A review on graphene-based nanocomposites for electrochemical and fluorescent biosensors," *RSC Adv.*, vol. 9, no. 16, pp. 8778–8881, 2019.

-
- [17] Q. Wu, W.-s. Miao, Y.-d. Zhang, H.-j. Gao, and D. Hui, “Mechanical properties of nanomaterials: A review,” *Nanotechnol. Rev.*, vol. 9, no. 1, pp. 259–273, 2020.
- [18] W. Zhu, Y. Guo, B. Ma, X. Yang, Y. Li, P. Li, Y. Zhou, and M. Shuai, “Fabrication of highly dispersed Pd nanoparticles supported on reduced graphene oxide for solid phase catalytic hydrogenation of 1, 4-bis (phenylethynyl) benzene,” *Int. J. Hydrog. Energy*, vol. 45, no. 15, pp. 8385–8395, 2020.
- [19] X. Liu, M. Xu, L. Wan, H. Zhu, K. Yao, R. Linguerri, G. Chambaud, Y. Han, and C. Meng, “Superior catalytic performance of atomically dispersed palladium on graphene in CO oxidation,” *ACS Catal.*, vol. 10, no. 5, pp. 3084–3093, 2020.
- [20] P. Makvandi, C.-y. Wang, E. N. Zare, A. Borzacchiello, L.-n. Niu, and F. R. Tay, “Metal-based nanomaterials in biomedical applications: Antimicrobial activity and cytotoxicity aspects,” *Adv. Funct. Mater.*, vol. 30, no. 22, p. 1910021, 2020.
- [21] E. Castro, A. H. Garcia, G. Zavala, and L. Echevoyen, “Fullerenes in biology and medicine,” *J. Mater. Chem. B*, vol. 5, no. 32, pp. 6523–6535, 2017.
- [22] P. Hohenberg and W. Kohn, “Inhomogeneous electron gas,” *Phys. Rev.*, vol. 136, no. 3B, p. B864, 1964.
- [23] W. Kohn and L. J. Sham, “Self-consistent equations including exchange and correlation effects,” *Phys. Rev.*, vol. 140, no. 4A, p. A1133, 1965.
- [24] A. Rahman, “Correlations in the motion of atoms in liquid argon,” *Phys. Rev.*, vol. 136, no. 2A, p. A405, 1964.
- [25] N. Metropolis and S. Ulam, “The Monte Carlo method,” *J. Am. Stat. Assoc.*, vol. 44, no. 247, pp. 335–341, 1949.

Chapter 2

Methods and Formalism

The important thing in science is not so much to obtain new facts as to discover new ways of thinking about them.

W. L. Bragg

2.1 The many-body problem

A material, whether it is an atom, molecule, cluster, bulk solid, surface or nanowire, and whether it is in the solid, liquid, or gas phase, and whether it be homogeneous or heterogeneous, can be described as a set of interacting atomic nuclei and electrons. Density Functional Theory (DFT) is a highly successful theory to describe the electronic structure of such many-particle systems. In this thesis, we use DFT to solve a variety of problems concerning many-electron systems. In this chapter, I will give a brief overview of some of the formalism of DFT, and associated techniques needed to perform DFT calculations on a computer.

2.1.1 The Schrödinger equation and many-body problem

The quantum mechanical time-independent Schrödinger equation is given by:

$$\hat{H}\Psi(\mathbf{R}, \mathbf{r}) = E\Psi(\mathbf{R}, \mathbf{r}). \quad (2.1)$$

Here, $\Psi(\mathbf{R}, \mathbf{r})$ is the wavefunction of all the particles, i.e, electrons and nuclei, in the system; it is a function of $\{\mathbf{R}, \mathbf{r}\}$, where $\mathbf{R} = \{\mathbf{R}_I, I = 1, 2, \dots, P\}$, is a set of P nuclear coordinates and $\mathbf{r} = \{\mathbf{r}_i, i = 1, 2, \dots, N\}$, is a set of N electronic coordinates. This wavefunction must be antisymmetric with respect to exchange of electronic coordinates in \mathbf{r} , and symmetric or antisymmetric with respect to exchange of nuclear coordinates in \mathbf{R} . The many-particle Hamiltonian operator \hat{H} can be written as:¹

$$\begin{aligned} \hat{H} = & - \sum_{I=1}^P \frac{\hbar^2}{2M_I} \nabla_I^2 - \sum_{i=1}^N \frac{\hbar^2}{2m_e} \nabla_i^2 + \frac{e^2}{2} \sum_{I=1}^P \sum_{J \neq I}^P \frac{Z_I Z_J}{|\mathbf{R}_I - \mathbf{R}_J|} \\ & + \frac{e^2}{2} \sum_{i=1}^N \sum_{j \neq i}^N \frac{1}{|\mathbf{r}_i - \mathbf{r}_j|} - e^2 \sum_{I=1}^P \sum_{i=1}^N \frac{Z_I}{|\mathbf{R}_I - \mathbf{r}_i|}, \end{aligned} \quad (2.2)$$

where \mathbf{R}_I , M_I and Z_I are the position, mass and the atomic number of the I^{th} nucleus, and \mathbf{r}_i is the coordinate of the i^{th} electron. m_e is the mass of electron, \hbar is Planck's constant divided by 2π , e is the electronic charge. One can express Eq. (2.2) as:

$$\hat{H} = \hat{T}_n + \hat{T}_e + \hat{V}_{nn} + \hat{V}_{ne} + \hat{V}_{ee}, \quad (2.3)$$

where \hat{T}_n and \hat{T}_e are the kinetic energy operators for the nuclei and electrons, respectively. \hat{V}_{nn} , \hat{V}_{ne} and \hat{V}_{ee} are the potential energy operators for the nucleus–nucleus interaction, nucleus–electron interaction and electron–electron interaction, respectively. It is almost impossible to solve the above equation, analytic solutions and

exact numerical solutions are available only in a few cases (e.g., hydrogenoid atoms, H_2^+ molecule). The separation of variables is very hard for the Coulomb interaction term in the above Schrödinger equation and cannot be done analytically for many-electronic systems. Hence, to solve the many-body Hamiltonian many approximations need to be made. I will discuss a few of them in the sections below.

2.1.2 The Born-Oppenheimer approximation

In an atom, the mass of the nucleus is much greater than the sum of masses of the electrons (a proton is 1836 times heavier than a electron). Therefore, the time scale associated with the motion of the nucleus is much slower than the time scale associated with the electrons. Born and Oppenheimer showed² in 1927 that the effect of the nuclear motion on the electronic wavefunctions becomes negligible and as a result the electronic motion becomes decoupled from the nuclear motion. That is, the electrons do not undergo transitions between stationary states due to the interaction with the nuclei. Also, if the nuclear mass is set to infinity, the kinetic energy of the nuclei can be neglected. This is called the *adiabatic* or *Born-Oppenheimer approximation*. As the nuclei change their coordinates, the electrons instantaneously adjust their wavefunctions. Hence it helps to separate out the electronic Hamiltonian from the nuclear Hamiltonian:

$$\Psi(\mathbf{R}, \mathbf{r}) = \Psi_{nuc}(\mathbf{R})\Psi_e(\mathbf{R}, \mathbf{r}). \quad (2.4)$$

where $\Psi_{nuc}(\mathbf{R})$ is the nuclear wavefunction. $\Psi_e(\mathbf{R}, \mathbf{r})$, which is the many-electron wavefunction corresponding to a particular nuclear configuration, satisfies the time-independent Schrödinger equation:

$$\hat{h}_e\Psi_e(\mathbf{R}, \mathbf{r}) = \epsilon(\mathbf{R})\Psi_e(\mathbf{R}, \mathbf{r}), \quad (2.5)$$

and the electronic Hamiltonian is,

$$\hat{h}_e = \hat{T}_e + \hat{V}_{ee} + \hat{V}_{ne} = \hat{H} - \hat{T}_n - \hat{V}_{nn}. \quad (2.6)$$

In the electronic Hamiltonian, the nuclear coordinates act as parameters. Now, the main aim is to solve Eq. (2.5) to find the many-electron wavefunction $\Psi_e(\mathbf{R}, \mathbf{r})$ and the total energy of the system.

2.2 Density Functional Theory

As the electrons interact via Coulomb two-body interactions, the probability of finding an electron at a position in space depends on the positions of the other electrons. This is called *correlation*. Hence, the many-electron wave function $\Psi_e(\mathbf{R}, \mathbf{r})$ cannot be simply written as the product of the wavefunctions of the individual electrons. Also, the many-electron wavefunction has to be antisymmetric i.e., if two electrons are exchanged, the wavefunction must change sign. Two famous approaches were first made to solve the many-electron problem: the Hartree approximation and the Hartree-Fock approximation. The Hartree approximation includes neither exchange nor correlation. The Hartree-Fock approximation includes exchange but not correlation. It captures the Pauli exclusion principle and the antisymmetric nature of the wavefunction. Also the wavefunctions are described by a single Slater determinant, which is not sufficient. Other, more sophisticated, methods like Configuration Interaction have also been subsequently developed to solve the problem.

A different idea was conceived by L.H. Thomas and E. Fermi at the same time as Hartree (1927-28). They proposed, for the first time, the electron density as the fundamental variable of the many-electron system. This Thomas-Fermi approximation set up a basis for the later development of the density functional theory (DFT), which has become the most successful theory for electronic structure calculations

in the last few decades. Dirac (in 1930) added exchange and correlation to the Thomas-Fermi theory. In this Thomas-Fermi-Dirac (TFD) theory, for the very first time, the total energy of a many-electron system was written as a functional of the electron density. This idea was intuitive at that time; one had to wait more than thirty years for a mathematical justification of this procedure. In 1964, Hohenberg and Kohn proved two theorems that justified that the total energy in the ground state can be expressed as a functional of the density; this expression of the total energy in terms of the electron density remarkably simplified the problem from depending on $3N$ degrees of freedom for N electrons to depending on only 3 variables for the density.

2.2.1 Hohenberg-Kohn (HK) theorems

DFT is based on two fundamental theorems given by Hohenberg and Kohn (1964).³

Theorem I:⁴ For any system of interacting particles in an external potential $V_{ext}(\mathbf{r})$, the potential $V_{ext}(\mathbf{r})$ is determined uniquely, up to an additive constant, by the ground state particle density $n_0(\mathbf{r})$.

Corollary: Once the ground state electron density is known, then we know V_{ext} and the full Hamiltonian operator. Then, solving the Schrödinger equation gives us the N -electron ground state wavefunction. Therefore all the properties of the interacting system are completely determined, given only the ground state electron density $n_0(\mathbf{r})$.

Theorem II: A universal functional for the energy $E[n]$ in terms of $n(\mathbf{r})$ can be defined, valid for any external potential $V_{ext}(\mathbf{r})$. For any particular $V_{ext}(\mathbf{r})$, the exact ground state energy of the system is the global minimum value of this functional, and the density $n(\mathbf{r})$ that minimizes the functional is the exact ground state density $n_0(\mathbf{r})$.⁴

The second HK theorem states that the total energy $E[n]$ of an interacting system

can be written as a functional of the electron density $n(\mathbf{r})$. This can be written as:¹

$$E[n] = F[n] + \int d^3r V_{ext}(\mathbf{r})n(\mathbf{r}), \quad (2.7)$$

where:

$$F[n] = \langle \Psi_e[n] | \hat{T}_e + \hat{V}_{ee} | \Psi_e[n] \rangle. \quad (2.8)$$

$F[n]$ is a “universal” functional i.e., it is valid for any external potential $V_{ext}(\mathbf{r})$. $F[n]$ includes all the internal energies: kinetic and potential energy of the interacting electron system. It does not depend on the external environment, hence it is a universal functional. Minimizing Eq. (2.7) with respect to $n(\mathbf{r})$ calculates the ground state total energy of the system and the ground state electron density. These two theorems establish the mathematical foundation of DFT.

However, now a problem arises: the exact form of $F[n]$ in terms of the density is not known. The HK theorems only tell us how to calculate the ground state energy and ground state density, but they do not tell us the form of $F[n]$. To address this, in 1965, W. Kohn and L.J. Sham⁵ proposed an ansatz that enables us to deal with this problem.

2.2.2 Kohn-Sham ansatz

The Kohn-Sham approach is to replace the original many-body problem by an auxiliary independent particle problem. Kohn-Sham’s main idea was: if one can find a system of non-interacting electrons which produces the same electron density as that of the true interacting system, the kinetic energy of the auxiliary non-interacting system can be calculated exactly. This remarkably simplifies the interacting many-body problem to independent-particle equations of the non-interacting system which can be solvable exactly, except for the fact that all the unknowns are

thrown into an exchange-correlation functional $E_{xc}[n(\mathbf{r})]$. The ground state density and ground state energy of the original interacting system can be found by solving the independent-particle equations with an accuracy limited by the approximations made in the expression of $E_{xc}[n(\mathbf{r})]$.

So, now consider a system of N non-interacting electrons whose ground state density is the same as that of the interacting system. We call this non-interacting system the *non-interacting reference system*, and it is described by the following Hamiltonian:

$$\hat{H}_R = \sum_{i=1}^N \left[-\frac{\hbar^2}{2m} \nabla_i^2 + V_R(\mathbf{r}_i) \right], \quad (2.9)$$

where $V_R(\mathbf{r})$ is the *reference potential* and the density obtained from this Hamiltonian is the same as the density of the true interacting system. Therefore, the HK theorem confirms that the ground state energy of this Hamiltonian is equal to the ground state energy of the true interacting system.

Let us first consider the spin-independent case. The single-particle orbitals or the one-electron orbitals $\phi_i(\mathbf{r})$ are the $N/2$ lowest energy eigenstates of the one-electron Hamiltonian:

$$\hat{H}_{KS} = -\frac{\hbar^2}{2m} \nabla^2 + V_R(\mathbf{r}). \quad (2.10)$$

The one-electron orbitals $\phi_i(\mathbf{r})$, also known as the Kohn-Sham orbitals, can be obtained by solving one-electron Schrödinger equations, known as Kohn-Sham equations:

$$\hat{H}_{KS} \phi_i(\mathbf{r}) = \epsilon_i \phi_i(\mathbf{r}). \quad (2.11)$$

In this scenario, the electron density is given by:

$$n(\mathbf{r}) = 2 \sum_{i=1}^{N/2} |\phi_i(\mathbf{r})|^2, \quad (2.12)$$

and the kinetic energy of the non-interacting reference system is expressed as:

$$T_R[n(\mathbf{r})] = -2 \frac{\hbar^2}{2m} \sum_{i=1}^{N/2} \langle \phi_i(\mathbf{r}) | \nabla^2 | \phi_i(\mathbf{r}) \rangle. \quad (2.13)$$

Now, the Kohn-Sham total energy functional can be written as:

$$E_{KS}[n] = T_R[n] + \int V_{ext}(\mathbf{r})n(\mathbf{r})d\mathbf{r} + \frac{1}{2} \iint \frac{n(\mathbf{r})n(\mathbf{r}')}{|\mathbf{r} - \mathbf{r}'|} d\mathbf{r}d\mathbf{r}' + E_{xc}[n]. \quad (2.14)$$

Remember that in this expression, the kinetic correlation neglected in $T_R[n]$, i.e., the difference in the kinetic energy of the interacting system and the non-interacting reference system, viz., $T_e[n] - T_R[n]$, is included in the exchange-correlation energy functional $E_{xc}[n]$. In the equation above, the second term on the right-hand-side is the external potential, i.e., the interaction between nuclei and electrons. The third term is the classical electrostatic interaction energy between electronic densities at different points in space, known as the Hartree term. The fourth term is the exchange-correlation energy that contains all the unknowns of the many-body problem.

Now, applying the variational principle and minimizing the Kohn-Sham functional under the constraint of particle conservation,

$$\frac{\delta}{\delta n(\mathbf{r})} (E_{KS}[n] - \mu \int n(\mathbf{r})d\mathbf{r}) = 0, \quad (2.15)$$

we get,

$$\frac{\delta T_R[n]}{\delta n(\mathbf{r})} + V_{ext}(\mathbf{r}) + \int \frac{n(\mathbf{r}')}{|\mathbf{r} - \mathbf{r}'|} d\mathbf{r}' + \frac{\delta E_{xc}[n]}{\delta n(\mathbf{r})} = \mu. \quad (2.16)$$

Comparing Eq. (2.10) and Eq. (2.16), we conclude that the reference potential or the Kohn-Sham potential consists of three terms:

$$V_{KS}(\mathbf{r}) = V_R(\mathbf{r}) = V_{ext}(\mathbf{r}) + V_H(\mathbf{r}) + V_{xc}(\mathbf{r}), \quad (2.17)$$

with the Hartree potential $V_H(\mathbf{r}) = \int \frac{n(\mathbf{r}')}{|\mathbf{r}-\mathbf{r}'|} d\mathbf{r}'$, and the exchange-correlation potential $V_{xc}(\mathbf{r}) = \frac{\delta E_{xc}[n]}{\delta n(\mathbf{r})}$.

Notice that the Kohn-Sham potential depends on the electron density, which however has to be calculated from the solution of the one-electron Kohn-Sham equations (by Eq. (2.12)). Therefore, this equation has to be solved self-consistently.

A flowchart describing the self-consistent procedure has been shown in Fig. 2.1.

2.2.3 Exchange-correlation functional

The total energy of a many-electron system is given by Eq. (2.14):

$$E[n] = T_R + V_{ext} + E_H + E_X + E_C, \quad (2.18)$$

where T_R is the kinetic energy of the non-interacting electrons, V_{ext} is the interaction energy of the electrons with external potentials, in particular with the atomic nuclei, E_H is the classical density-density electrostatic energy known as the Hartree energy, E_X is the exchange and E_C is the correlation energy. Here, the second and the third terms are the explicit functionals of the electron density. The first and fourth terms are functionals of the single-particle orbitals which are again functionals of the density. The last term i.e., the correlation energy is the big unknown. Among E_H , E_X and E_C , the contributions come in order of decreasing energy: Hartree, exchange and correlation.

Electrons being fermions obey Pauli's exclusion principle, therefore two same-spin electrons repel each other. The exchange term lowers the energy by keeping

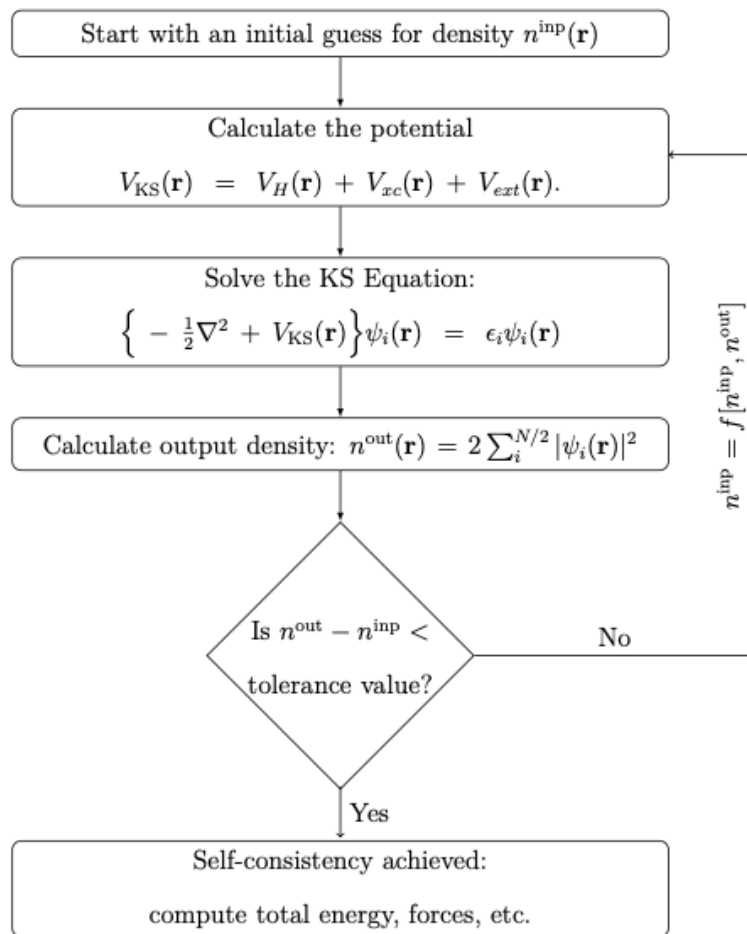


Figure 2.1: Flow chart showing the self-consistency loop for the iterative solution of the KS equations.

electrons of the same spin away from each other, thus reducing the Coulomb repulsion, and provides extra stabilization to the system. The correlation energy is defined as the difference between the exact energy of the many-body system and its energy as calculated by the Hartree-Fock approximation (remember that Hartree-Fock theory counts for the exchange but not the correlation). Correlation is a result of the collective behaviour of electrons to screen and reduce Coulombic interaction. Unlike the exchange term, the correlation becomes more important for opposite spins as they are more likely to occupy nearby locations.

So, the form of the exchange-correlation energy is not known. Many approximations have been made so far for E_{XC} . I will now discuss the two most widely used approximations for E_{XC} , namely the local density approximation and the generalized gradient approximation.

The local density approximation (LDA)

The local density approximation (LDA)⁶⁻⁹ has been the most extensively used approximation for the exchange-correlation energy for a long time. The philosophy of considering "inhomogeneous system as locally homogeneous" was first given by Thomas-Fermi-Dirac (1930). According to this approximation, the exchange-correlation energy can be written as:

$$E_{XC}^{LDA}[n] = \int n(\mathbf{r}) \epsilon_{XC}^{hom}[n(\mathbf{r})] d\mathbf{r}, \quad (2.19)$$

where $\epsilon_{XC}^{hom}[n]$ is the exchange-correlation energy density of the homogeneous electron gas, calculated locally by the density at every point in space. For the homogeneous electron gas, the exact expression of the exchange energy was given by Dirac.¹⁰ Various approximations have been made for the correlation term.⁶⁻⁹ The most accurate results are from the Quantum Monte Carlo simulations of Ceperley and Alder (1980).⁷ Perdew and Zunger (1981)⁹ parameterized these results for the correlation.

In practice, the exchange-correlation energy is calculated using Eq. (2.19) with $\epsilon_{XC}^{hom}[n] = \epsilon_X^{LDA}[n] + \epsilon_C^{LDA}[n]$, where the exchange energy density is given by:

$$\epsilon_X^{LDA}[n] = \epsilon_X^{Dirac}[n] = -\frac{3}{4} \left(\frac{3}{\pi}\right)^{1/3} n^{1/3} = -\frac{3}{4} \left(\frac{9}{4\pi^2}\right)^{1/3} \frac{1}{r_s}, \quad (2.20)$$

where $r_s = (3/4\pi n)^{1/3}$ is the mean interelectronic distance, and the correlation energy density is calculated by:⁹

$$\begin{aligned} \epsilon_C^{PZ}[n] &= A \ln r_s + B + C r_s \ln r_s + D r_s, \quad r_s \leq 1 \\ &= \gamma / (1 + \beta_1 \sqrt{r_s} + \beta_2 r_s), \quad r_s > 1, \end{aligned} \quad (2.21)$$

where $A, B, C, D, \beta_1, \beta_2$ are constants and fitted to the Monte Carlo simulations of Ceperley and Alder. The LDA is especially successful for the bulk metals where the electron density is reasonably uniform, and also for less uniform density systems like molecules and ionic crystals. However, the LDA has several limitations: (i) it underestimates bond lengths due to over-binding nature, (ii) it fails to cancel the self-interaction for localized electrons, i.e., for strongly correlated systems (e.g., transition metal oxides), LDA fails to reproduce the band gap near the Fermi level, (iii) the exchange-correlation potential decays exponentially instead of the correct $-e^2/r$ behaviour in the vacuum region.

The generalized gradient approximations (GGA)

The electron density is not always homogeneous in real systems. In fact, in most of the cases it is inhomogeneous. To deal with the issue of inhomogeneities in the density, the natural way is to do expansion of the electron density in terms of the gradient, Laplacian and higher order derivatives.

The exchange correlation energy for a GGA functional can be written as:¹¹

$$E_{XC}^{GGA} = \int n(\mathbf{r}) \epsilon_{XC}[n(\mathbf{r}), |\nabla n(\mathbf{r})|] d\mathbf{r}, \quad (2.22)$$

where $\epsilon_{XC}[n(\mathbf{r}), |\nabla n(\mathbf{r})|]$ is the exchange-correlation energy per electron, which depends on the local electron density $n(\mathbf{r})$ at point \mathbf{r} in space, as well as on the gradient of the density $|\nabla n(\mathbf{r})|$ in the vicinity of \mathbf{r} . The Laplacian term $\nabla^2 n$ and also the higher order derivative terms can also be incorporated into ϵ_{XC} .

One of the important things about the GGA is that the gradient expansion has to be carried out very carefully, such that it retains all the important contributions to the desired order. Another important point is that this expansion may violate some exact conditions of the exchange-correlation holes, like normalization condition, negativity of the exchange density and the self-interaction cancellation. Perdew showed that imposing these conditions on the functionals that originally do not satisfy them results in a remarkable improvement (1986)¹². Many gradient expansions have been suggested between 1986 and 1996. The three most widely used GGAs are Becke (B88),¹³ Perdew and Wang (PW91),¹⁴ and Perdew, Burke and Ernzerhof (PBE 1996).¹¹ The PBE functional is very satisfactory in the sense that it satisfies many of the exact conditions of the exchange-correlation (XC) hole and it does not have any fitting parameters.

GGAs have several successes compared to the LDA: they improve binding and atomic energies, improve bond lengths and angles, and improve the computed energetics and dynamical properties of, for example, ice, water and water clusters. However, the GGAs overestimate lattice constant of noble metals (Ag, Au, Pt). Moreover, GGAs do not satisfy some known asymptotic behaviour, e.g., for isolated atoms, the exchange-correlation potential: $V_{XC}(\mathbf{r}) \sim -e^2/r$ as $\mathbf{r} \rightarrow \infty$, whereas $V_{XC}^{LDA/GGA}(\mathbf{r})$ decays exponentially as $\mathbf{r} \rightarrow \infty$. Further, $V_{XC}(\mathbf{r}) \rightarrow \text{constant}$ as $\mathbf{r} \rightarrow 0$, whereas $V_{XC}^{LDA}(\mathbf{r}) \rightarrow \text{constant}$, $V_{XC}^{GGA}(\mathbf{r}) \rightarrow -\infty$ as $\mathbf{r} \rightarrow 0$.

These drawbacks arise due to several factors: the non-locality of the exchange is not fully taken into account, and the GGAs do not cancel the self-interaction present in the Hartree term, and hence produce wrong results for strongly-correlated systems.

2.2.4 Plane wave basis sets

In order to carry out electronic structure calculations using the Kohn-Sham equations, we usually expand the Kohn-Sham one-electron orbitals, $\phi_i(\mathbf{r})$, in a general basis set described by a set of functions $\{f_\alpha(\mathbf{r})\}$ in the Hilbert space. The Kohn-Sham orbitals can then be written as a linear combination of these basis functions:

$$\phi_j(\mathbf{r}) = \sum_{\alpha=1}^M c_{j\alpha} f_\alpha(\mathbf{r}), \quad (2.23)$$

where j labels the Kohn-Sham orbitals (band index), the sum runs over all the basis functions up to the dimension or size of the basis set M , $c_{j\alpha}$ are the expansion coefficients for the orbital j .

The basis set $\{f_\alpha(\mathbf{r})\}$ can be of different types, such as plane waves,^{15;16} localized atomic orbitals,¹⁷ Muffin Tin Orbitals,¹⁸ mixed (localized + extended), augmented basis, etc. In all the work presented in this thesis, I have used plane waves as the basis set. Plane waves are delocalized, independent of the nuclear positions, and extended over the whole system. Hence they are particularly useful for extended solid or liquid materials.

Crystalline solids are periodic. So, electrons must obey Bloch's theorem in the sense that the solution of the Schrödinger equation follows the translational periodicity of the supercell. Considering this,

$$\phi_j^{(\mathbf{k})}(\mathbf{r}) = e^{i\mathbf{k}\cdot\mathbf{r}} \sum_{\alpha=1}^M c_{j\alpha}^{(\mathbf{k})} f_\alpha(\mathbf{r}) = \sum_{\alpha=1}^M c_{j\alpha}^{(\mathbf{k})} f_\alpha^{(\mathbf{k})}(\mathbf{r}), \quad (2.24)$$

where \mathbf{k} is the Bloch's wave vector in the Brillouin zone and the modified basis functions are:

$$f_{\alpha}^{(\mathbf{k})}(\mathbf{r}) = e^{i\mathbf{k}\cdot\mathbf{r}} f_{\alpha}(\mathbf{r}). \quad (2.25)$$

According to Bloch's theorem, $f_{\alpha}(\mathbf{r})$ should be a periodic function with the same periodicity as that of the crystal. In general, any function in real space (\mathbf{r}) can be expressed as the Fourier transform of a function in reciprocal space (\mathbf{g}). However, it can be shown that if the function in real space is periodic, the \mathbf{g} vectors are restricted only to the reciprocal lattice vectors $\mathbf{G} = n_1\mathbf{b}_1 + n_2\mathbf{b}_2 + n_3\mathbf{b}_3$, where \mathbf{b}_i 's are the primitive reciprocal lattice vectors and n_i 's are integers. In that case, the Fourier transform becomes a Fourier series and the restriction that \mathbf{g} 's can only be \mathbf{G} 's confirms that periodic boundary conditions (PBCs) are automatically satisfied. Now, let's define the plane wave basis functions as:

$$f_{\alpha}(\mathbf{r}) = f_{\mathbf{G}}(\mathbf{r}) = \frac{1}{\sqrt{\Omega}} e^{i\mathbf{G}\cdot\mathbf{r}}. \quad (2.26)$$

where Ω is the volume of the unit cell in real space and the factor $\frac{1}{\sqrt{\Omega}}$ is introduced as the normalization constant such that the above basis functions become orthonormal to each other. Substituting Eqs. (2.25) and (2.26) into Eq. (2.24) we get,

$$\phi_j^{(\mathbf{k})}(\mathbf{r}) = e^{i\mathbf{k}\cdot\mathbf{r}} \sum_{\mathbf{G}=0}^{\infty} c_{j\mathbf{k}}(\mathbf{G}) f_{\mathbf{G}}(\mathbf{r}). \quad (2.27)$$

Inserting the phase factor into the definition of the basis functions:

$$f_{\mathbf{G}}^{(\mathbf{k})}(\mathbf{r}) = \frac{1}{\sqrt{\Omega}} e^{i(\mathbf{k}+\mathbf{G})\cdot\mathbf{r}}, \quad (2.28)$$

we get,

$$\phi_j^{(\mathbf{k})}(\mathbf{r}) = \sum_{\mathbf{G}=0}^{\infty} c_{j\mathbf{k}}(\mathbf{G}) f_{\mathbf{G}}^{(\mathbf{k})}(\mathbf{r}). \quad (2.29)$$

These are the Kohn-Sham one-electron orbitals, where the basis functions $f_{\mathbf{G}}^{(\mathbf{k})}(\mathbf{r})$ are given by Eq. (2.28). Notice that, now we have one-electron orbitals for each band j and for each k-point \mathbf{k} . The \mathbf{k} vectors belong to the first Brillouin zone (FBZ), and all the \mathbf{G} vectors, except $\mathbf{G} = 0$, always reside outside of the FBZ.

So far, we have seen that Bloch's theorem confirms that the wavefunction of an electron in an external periodic potential can be naturally expanded in a plane wave basis set. In principle, an infinite number of plane waves, i.e., an infinite number of \mathbf{G} 's, are needed to represent the Kohn-Sham orbitals with complete accuracy. In practice, however, the Fourier coefficients $c_{\mathbf{k}}(\mathbf{G})$ decay with increasing $|(\mathbf{k} + \mathbf{G})|$. So the plane wave expansion can be truncated after a finite number of terms, i.e., taking into account all the plane waves with kinetic energy lower than some cutoff E_{cut} :

$$\frac{\hbar^2}{2m_e} |\mathbf{k} + \mathbf{G}|^2 \leq E_{cut}. \quad (2.30)$$

Thus, only those plane waves $e^{i(\mathbf{k}+\mathbf{G})\cdot\mathbf{r}}$ which have kinetic energy $\leq E_{cut}$ are taken into account for the computational calculations of the Kohn-Sham orbitals. One big advantage of using a plane wave basis set is that a single parameter, E_{cut} , controls the convergence of the basis set. Actually the Kohn-Sham orbitals are defined in real space on a grid of points separated by $\Delta x = \frac{|\mathbf{a}_i|}{n_i}$, where \mathbf{a}_i 's are the primitive lattice vectors in real space. If some operations are done in reciprocal space, Fast Fourier Transforms (FFTs) can be used to convert terms to real space.

If the true nuclear potential Z/r is retained, the true all-electron wavefunction of a core electron has sharp peaks near the core region, while that of a valence electron has many nodes in the core region. In both cases, the spatial variation of

the wavefunction in the core region is very fast, so a large number of plane waves are needed to expand the Kohn-Sham wavefunctions. This increase in the number of plane waves increases the computational time hugely. This problem is solved by the introduction of pseudopotentials, as described in greater detail in the next section below. Instead of doing all-electron plane wave calculations, we consider only the valence electrons, freezing the core electrons; moreover, the bare nuclear potential is replaced by a smooth pseudopotential. The valence states are pseudized and made nodeless inside the core region. The wavefunctions now become smooth enough that decreasing the grid spacing, i.e., equivalently increasing the energy cut-off E_{cut} , does not carry any additional information. Then it is said that the system is *converged* with respect to the size of the plane wave basis. The cut-off can be calculated from the pseudopotentials, but in general E_{cut} is computed for a specific property and specific system. When the electron density, in terms of the sum of the square of the Kohn-Sham orbitals, is written as a convolution in Fourier space, it becomes clear that there should be a cut-off for the density equal to $4E_{cut}$ (except for the special case of ultrasoft pseudopotentials, which have an additional augmentation charge). Next, I will discuss the pseudopotential approximation.

2.2.5 Pseudopotential approximation

According to Bloch's theorem, the Kohn-Sham wavefunctions for a periodic system can be expanded as a linear combination of plane waves. If the true nuclear potential Z/r is retained, the true all-electron wavefunction of a core electron is sharply peaked in the core region, while the wavefunction of a valence electron has nodes in the core region. So, the plane wave expansion of both core and valence wavefunctions requires a large number of plane waves to adequately represent the wavefunction. This increases the computational time and memory storage requirements hugely, making DFT calculations very very expensive.

The electronic states of an atom consist of (i) core states which are highly localized and do not participate in chemical bonding, (ii) valence states which are extended and do participate in chemical bonding, (iii) semi-core states which are localized and polarizable and generally do not contribute directly to the chemical bonding. Based on the observations that, (i) core states are not essential for the description of the chemical bonding, and (ii) a good description of the valence states inside the core region is not strongly necessary, there is no lack of crucial information if the true all-electron wavefunction inside the core region (within some cut-off radius) is replaced by a pseudo wavefunction which is smooth and nodeless. This pseudo wavefunction is the solution of the Schrödinger equation in the presence of a pseudopotential, and can be determined from the inverse Schrödinger equation. Since the pseudo wavefunction is smooth and nodeless, its spatial variation is comparatively weak, and requires much fewer plane wave components in an expansion than the true all-electron wave function. This is known as the pseudopotential approximation.¹⁹⁻²¹ So, in this approximation, the core electrons are removed from the calculations, and the interaction of the valence electrons with the ionic core is replaced by an effective, screened potential. Due to the orthogonality conditions, this screened potential depends on the angular momentum l of the valence electrons. The computational expense is reduced hugely upon the use of pseudopotentials.

A good pseudopotential should have the following properties:

1. *Smoothness*: The pseudo wavefunctions and their first and second derivatives should match smoothly with the true all-electron wave functions at the cutoff radius which separates the core region from the valence region.
2. *Transferability*: The flexibility of using a pseudopotential generated for an atom to use in a different chemical and structural environment.
3. *Softness*: To reduce the computational cost, a pseudopotential should have a

low energy cutoff for the expansion of the wavefunctions using plane waves. The lower the cutoff, the softer it is.

I have used two different kind of pseudopotentials in my calculations, namely *norm-conserving* and *ultrasoft* pseudopotentials. I will very briefly discuss about them now.

Norm-conserving pseudopotentials (NCP)

This type of pseudopotential was first introduced by Hamann, Schlüter and Chiang (1979).²⁰ The norm-conserving pseudopotentials follow four properties:

(i) For a particular electronic configuration of an atom, the eigenvalues of the pseudo-wavefunctions are exactly equal to the eigenvalues of the all-electron wave functions.

(ii) The radial part of the pseudo-wavefunction R_{PS} is nodeless, and it is exactly equal to the all-electron wavefunction outside the chosen cutoff radius:

$$\begin{aligned} R_{PS}(r) &= R_{PS}(r), r < r_c \\ &= R_{AE}(r), r \geq r_c. \end{aligned} \quad (2.31)$$

(iii) The norm conservation condition is that the norm of the true all-electron wave functions and pseudo-wavefunctions are the same inside the core region ($r < r_c$):

$$\int_0^{r_c} r^2 |R_{PS}(r)|^2 dr = \int_0^{r_c} r^2 |R_{AE}(r)|^2 dr. \quad (2.32)$$

(iv) The logarithmic derivatives of the pseudo-wave function and all-electron wave function match for $r \geq r_c$.

A lot of the success of norm-conserving pseudopotentials is due to the fact that

the constraint of norm-conservation also automatically improves transferability, due to the existence of a mathematical identity connecting norms to logarithmic derivatives. However, norm-conserving pseudopotentials are "hard" in the sense that they require a very large number of plane waves, especially for those valence states which are nodeless and have no corresponding core states, with the same angular momentum, with which they must be orthogonal. For instance, p -states of the first row elements and d -states of the second row transition metals (e.g., C- $2p$ and Cu- $3d$ states). To avoid this problem D.H. Vanderbilt introduced the concept of ultrasoft pseudopotentials (1990)²¹ which reduces the plane wave cut off and hence the computational time, hugely.

Ultrasoft pseudopotentials (USPP)

D.H. Vanderbilt relaxed the norm conservation constraint²¹ and developed a method of using much smoother (softer) pseudopotentials, having larger cutoff radius r_c and still with high transferability. The logarithmic derivatives of the all-electron and pseudo-wavefunctions still match for $r \geq r_c$. r_c can be chosen very large, well beyond the maximum of the radial wavefunction. At larger cutoff the derivative of the wavefunction is smaller, also sharp peaks in the wavefunction can be neglected since the norm conservation constraint is released; this results in a smoother wavefunction, and it require much fewer plane waves in the expansion, compared to the norm-conserving pseudopotentials. Thus ultrasoft pseudopotentials reduce computational time hugely. In this scheme, though the pseudo-wavefunction is the same as the all-electron wavefunction outside the core region, the charge enclosed by the pseudo-wavefunction inside the core region is different from that of the all-electron wavefunction. Again, in the Kohn-Sham approach, the potential is unique for a charge density. So, if the charge density is calculated using the pseudo-wavefunction, then the lack of charge inside the pseudized region (or the core region) will produce

an incorrect Kohn-Sham potential. This problem is solved by adding some “augmentation charge” to the charge density of the pseudo-wavefunction. This method has been remarkably successful for the last three decades, and substantially reduces the plane wave cutoff. For example, for the same level of accuracy, the kinetic energy cutoff for an oxygen atom can be reduced from 150 Ry for a NCPP to only 40 Ry for USPP. It is important to note that in most DFT codes (including Quantum ESPRESSO) one can use NCPP for some elements and USPP for other elements in a given system.

2.2.6 Brillouin zone sampling and smearing

It can be shown, using Bloch’s theorem, that it is not necessary to calculate the electronic wavefunctions throughout the whole space, it is sufficient to calculate them in a unit cell. The wavefunctions in the neighbouring unit cells are the same except for a phase factor $e^{i\mathbf{k}\cdot\mathbf{R}}$. The calculation of the wavefunction for *all* the electrons in an infinite crystal is replaced – via Bloch’s theorem – by the calculation of the wavefunction for a *finite* number of electrons in the unit cell, at, in principle, an infinite number of \mathbf{k} -vectors in the first Brillouin zone (FBZ). However, to solve for the Kohn-Sham orbitals at an infinite number of \mathbf{k} -points is not possible in a computational approach, and the larger the number of \mathbf{k} -points, the greater the computational time. \mathbf{k} -points which are close to one another carry almost similar information. Therefore, there will not be a large error in calculating the desired physical properties (such as charge density, total energy, density of states, magnetic moment, etc., which require an integration over the \mathbf{k} -points in the FBZ), within some numerical accuracy, by using the Kohn-Sham orbitals at a small and finite number of \mathbf{k} -points in the FBZ. This approximation of the full BZ integral with a summation over some finite and discrete \mathbf{k} -points of the FBZ is known as *Brillouin zone sampling*. Numerically the integration can be replaced by summation over

finite number of \mathbf{k} -points in the FBZ. The most widely used \mathbf{k} -points grid or mesh is that defined by Monkhorst and Pack,²² using the following formula:

$$\mathbf{k}_{n_1, n_2, n_3} = \sum_{\beta=1}^3 \frac{2n_\beta - N_\beta - 1}{2N_\beta} \mathbf{b}_\beta, \quad (n_\beta = 1, 2, 3, \dots, N_\beta), \quad (2.33)$$

where N_β is an integer and gives the number of \mathbf{k} -points in FBZ in reciprocal space along the β th direction ($\beta = 1, 2, 3$), and $\mathbf{b}_1, \mathbf{b}_2$ and \mathbf{b}_3 are the primitive lattice vectors in reciprocal space. It can also be shown that the total number of \mathbf{k} -points in the FBZ, i.e., $N_1 N_2 N_3$ is equal to the total number of unit cells in the crystal. The number of \mathbf{k} -points corresponds to the number of unit cells involved in the calculations.

If the crystal possesses some kind of symmetry, the calculation of the Kohn-Sham one-electron wavefunctions further reduces to do calculations only for those \mathbf{k} -points which lie inside the irreducible part of the Brillouin zone (IBZ). In that case, the general expression of the electron density, for an arbitrary number of replicas along the direction of the three direct lattice vectors, is as follows:

$$n(\mathbf{r}) = \sum_{\mathbf{k} \in \text{IBZ}} w_{\mathbf{k}} |\phi_{n\mathbf{k}}(\mathbf{r})|^2, \quad (2.34)$$

where the sum runs over all the \mathbf{k} -points in the IBZ, $w_{\mathbf{k}}$'s are the weight factors corresponding to a particular \mathbf{k} -point, and it depends on the symmetry of the unit cell. The IBZ contains all the symmetry-inequivalent \mathbf{k} -points and all the information of the whole FBZ can be found within the IBZ. Usually metallic systems having no band gap require very dense \mathbf{k} -points mesh to capture the properties around the Fermi level. For semiconductors and insulators having band gaps, a coarse \mathbf{k} -point mesh is sufficient to capture all the properties.

So, for DFT calculations of crystalline solids, we have to solve the Kohn-Sham equations at each \mathbf{k} -point in the IBZ, and we get Kohn-Sham orbitals and eigenvalues

for each \mathbf{k} -point and each band:

$$\left\{ -\frac{\hbar^2}{2m} \nabla^2 + V_{ext}(\mathbf{r}) + \int \frac{n(\mathbf{r}')}{|\mathbf{r} - \mathbf{r}'|} d\mathbf{r}' + V_{XC}[n] \right\} \phi_{i\mathbf{k}}(\mathbf{r}) = \epsilon_{i\mathbf{k}} \phi_{i\mathbf{k}}(\mathbf{r}). \quad (2.35)$$

The electron density is given by:

$$n(\mathbf{r}) = \sum_{\mathbf{k} \in IBZ} w_{\mathbf{k}} \sum_{i=1}^{N_{\mathbf{k}}} f_{i\mathbf{k}} |\phi_{i\mathbf{k}}(\mathbf{r})|^2, \quad (2.36)$$

where $N_{\mathbf{k}}$ is the number of occupied Kohn-Sham orbitals at each \mathbf{k} -point, and $f_{i\mathbf{k}}$ is the occupation number of band i at wave vector \mathbf{k} . If the system is an insulator or semiconductor, the Fermi level lies in between the valence band maximum and conduction band minimum; for this, $f_{i\mathbf{k}} = 1$ independent of i and \mathbf{k} and $N_{\mathbf{k}} = N$, the total number of electrons involved in the calculation (or, rather $N/2$ if one accounts for spin degeneracy). However, for metallic systems, there is no gap, and the valence and conduction bands overlap. It can happen that at a particular \mathbf{k} -point a certain band is occupied and at *just the next* \mathbf{k} -point the same band is empty. Therefore, the occupation function changes discontinuously from non-zero value to zero value, at the Fermi level. Thus, the calculation of the Fermi level for the metallic systems requires a very dense \mathbf{k} -point mesh. The Fermi level is given by the highest occupied Kohn-Sham eigenvalue. The Fermi level is calculated self-consistently, and a slightly different choice of the \mathbf{k} -points can lead to bands entering or exiting the above sum, depending on whether $\epsilon_{i\mathbf{k}}$ is below or above the Fermi energy ϵ_F . So, the accurate determination of the Fermi level requires a highly dense \mathbf{k} -point mesh, which increases the computational cost hugely. To computationally deal with the discontinuity of the occupation function $f_{i\mathbf{k}}$ at the Fermi level, different "smearing" techniques have been introduced. The main idea of the "smearing" technique is to replace the occupation function to be integrated

by a smooth and continuous function, hence “smearing out” the discontinuity. Some widely used smearing functions are Gaussian smearing,²³ Fermi-Dirac smearing, Methfessel-Paxton smearing,²⁴ and Marzari-Vanderbilt cold smearing.²⁵ After the introduction of the smooth and continuous smearing function, the integration can be done using standard methods. The larger the smearing width, the faster is the convergence with respect to \mathbf{k} -points, but the lower is the accuracy.

2.2.7 Calculation of forces: Hellmann-Feynman theorem

To find out the ground state geometry or equilibrium nuclear configuration, the forces and stresses acting on the atoms should ideally be zero. Forces also need to be computed if one wants to perform an ab initio molecular dynamics calculation. The force acting on an ion I with coordinate \mathbf{R}_I can be calculated by computing the first derivative of the total energy E with respect to the ionic position \mathbf{R}_I :

$$\mathbf{F}_I = -\frac{\partial E}{\partial \mathbf{R}_I} = -\nabla_{\mathbf{R}_I} E. \quad (2.37)$$

To compute forces in this way requires the calculation of the total energy at different nuclear positions, i.e., one has to compute the total energy using DFT for more than one set of positions. The Hellmann-Feynman (HF) force theorem provides an alternative way of calculating the force on an atom without any need for performing total energy calculations for different nuclear positions. The forces acting on each nucleus of a system can be calculated using the Hellmann-Feynman (HF) force theorem²⁶ which states that the force acting on a nucleus can be expressed as the expectation value of the derivative of the Hamiltonian operator \hat{H} with respect to the nuclear coordinate. The HF theorem shows that total energy calculation at a single configuration would be sufficient to compute the force. Mathematically,

$$\mathbf{F}_I = -\frac{\partial E}{\partial \mathbf{R}_I} = -\langle \Psi | \frac{\partial \hat{H}}{\partial \mathbf{R}_I} | \Psi \rangle, \quad (2.38)$$

where E is the total energy for a given set of nuclear co-ordinates $\{\mathbf{R}_I\}$ and Ψ is the eigenfunction of the Hamiltonian \hat{H} . Eq. (2.38) holds only when the basis set is complete or position-independent, as is true in the case of a plane wave basis set, and when the electronic wavefunction Ψ is an exact eigenstate of the Hamiltonian \hat{H} . If the basis set is not complete or is position-dependent, e.g., for atom-centered orbitals like a Gaussian basis, additional contributions, known as Pulay forces, have to be calculated.

2.2.8 Stress calculation

Stress is an intrinsic property of a material in a given structural configuration. It results from internal forces acting between neighbouring atoms when the system is under external force. Strain is the deformation of a material that results in displacement of a point. In solid state systems, the state of the system is given by the forces on each atom and the stress which is an independent variable. The conditions for equilibrium are: (i) total force vanishes on each atom, and (ii) the macroscopic stress is equal to the externally applied stress. The stress tensor $\sigma_{\alpha\beta}$ is defined as the derivative of the total energy with respect to the strain tensor $\epsilon_{\alpha\beta}$:

$$\sigma_{\alpha\beta} = -\frac{1}{V} \frac{\partial E}{\partial \epsilon_{\alpha\beta}}, \quad (2.39)$$

where V is the volume of the system, E is the total energy and $\epsilon_{\alpha\beta}$ is the strain tensor, where α, β are the Cartesian indices. In analogy with the HF theorem, Nielsen and Martin²⁷ derived the stress theorem; the derivative of the total energy with respect to strain can be written as the expectation value of the derivative of the Hamiltonian with respect to strain:

$$\sigma_{\alpha\beta} = -\frac{1}{V} \langle \Psi | \frac{\partial H}{\partial \epsilon_{\alpha\beta}} | \Psi \rangle. \quad (2.40)$$

Similar to the force calculations the truncation of the basis set can lead to an error in the stress calculation. The stress converges usually at a higher kinetic energy cutoff E_{cut} for plane waves than the total energy.

2.2.9 Spin-polarized density functional theory

In order to extend Kohn-Sham theory to spin-polarized or magnetic systems, we have to consider that the total electron density is comprised of two spin densities: $n(\mathbf{r}) = n_{\uparrow}(\mathbf{r}) + n_{\downarrow}(\mathbf{r})$, where $n_{\uparrow}(\mathbf{r})$ and $n_{\downarrow}(\mathbf{r})$ are the up and down spin densities, respectively. The spin-polarization or the magnetization density is given by: $m(\mathbf{r}) = n_{\uparrow}(\mathbf{r}) - n_{\downarrow}(\mathbf{r})$. The up and down spin densities are calculated from the Kohn-Sham spin orbitals, which satisfy the following Kohn-Sham equations self-consistently:

$$\left\{ -\frac{\hbar^2}{2m} \nabla^2 + V_{R,s}(\mathbf{r}) \right\} \phi_{i,s}(\mathbf{r}) = \epsilon_{i,s} \phi_{i,s}(\mathbf{r}), \quad (2.41)$$

where the subscript s indicates the spin component \uparrow or \downarrow . The reference or Kohn-Sham potential is given by:

$$V_{KS,s}(\mathbf{r}) = V_{R,s}(\mathbf{r}) = V_{ext}(\mathbf{r}) + V_H(\mathbf{r}) + V_{XC,s}[n_{\uparrow}, n_{\downarrow}](\mathbf{r}), \quad (2.42)$$

where the exchange-correlation potential is given by,

$$V_{XC,s}[n_{\uparrow}, n_{\downarrow}](\mathbf{r}) = \frac{\delta E_{XC}[n_{\uparrow}, n_{\downarrow}]}{\delta n_s(\mathbf{r})}. \quad (2.43)$$

Only the exchange-correlation energy depends on the spin densities which are computed from the Kohn-Sham spin orbitals:

$$n_s(\mathbf{r}) = \sum_{i=1}^{N_s} |\phi_{i,s}(\mathbf{r})|^2, \quad (2.44)$$

where N_s is the number of occupied one-electron spin orbitals with spin projection s . For spin-polarized systems, $N_\uparrow \neq N_\downarrow$. For non-spin-polarized systems, $n_\uparrow(\mathbf{r}) = n_\downarrow(\mathbf{r})$, in this case the spin density functional theory (SDFT) reduces to the normal density functional theory with double occupancy of the one-electron orbitals. In SDFT, the expression of the total energy is as follows:

$$\begin{aligned} E_{KS}[n_\uparrow, n_\downarrow] &= T_R[n_\uparrow, n_\downarrow] + \int n(\mathbf{r}) V_{ext}(\mathbf{r}) d\mathbf{r} \\ &+ \frac{1}{2} \iint \frac{n(\mathbf{r})n(\mathbf{r}')}{|\mathbf{r} - \mathbf{r}'|} d\mathbf{r}d\mathbf{r}' + E_{XC}[n_\uparrow, n_\downarrow], \end{aligned} \quad (2.45)$$

with the kinetic energy of the reference system given by,

$$T_R[n(\mathbf{r})] = -\frac{\hbar^2}{2m} \sum_{s=1}^2 \sum_{i=1}^{N_s} \langle \phi_{i,s}(\mathbf{r}) | \nabla^2 | \phi_{i,s}(\mathbf{r}) \rangle. \quad (2.46)$$

Eqs. (2.45) and (2.46) are very similar to the corresponding equations (2.14) and 2.13 of the unpolarized system.

2.2.10 Modelling aperiodic systems

Some systems are periodic in all the three spatial directions (e.g., bulk crystals), some are periodic in only two dimensions (e.g., surfaces of crystals, graphene, etc.), some systems are periodic in only one dimension (e.g., carbon nanotubes, one-dimensional chain of a coordination polymer), some systems are zero dimensional (e.g., an isolated atom, a molecule, cluster of atoms, quantum dots etc.). The use of a plane wave basis set requires periodic boundary conditions in all the three spatial directions. For three-dimensional (3D) systems, this will not pose a problem.

However, when modeling the two-dimensional (2D) surfaces which I have used in my thesis, we need to introduce a large vacuum region in the unit cell considered, along the direction of aperiodicity (e.g., a surface extended in xy plane is not periodic along the z -direction) such that, along the aperiodic direction the periodic images of the unit cells will have a large separation which diminishes the artificially introduced interactions along this direction between atoms of the periodic images of the unit cells.

2.3 Relativistic DFT

Relativistic effects become important for heavier elements. Relativistic effects are introduced in quantum mechanics through the Dirac equation. A. K. Rajagopal and J. Callaway²⁸ first formulated the extension of the HK theorem for the inhomogeneous electron gas to the relativistic domain using four component current density as the basic variable. The corresponding Kohn-Sham equations have been formulated by Rajagopal,²⁹ and independently by MacDonald and Vosko.³⁰ Starting from the Dirac equation the relativistic Kohn-Sham equations, also known as Dirac-Kohn-Sham equations, are given by:²⁸

$$\{c\boldsymbol{\alpha} \cdot \mathbf{p} + \beta m_e c^2 + \alpha_\mu V_s^\mu(\mathbf{r})\} \psi_\nu(\mathbf{r}) = \epsilon_\nu \psi_\nu(\mathbf{r}), \quad (2.47)$$

where c is the speed of light in vacuum, $\mathbf{p} = -i\hbar\nabla$ is the momentum operator, m_e is the mass of the electron, $\mu = \{0, x, y, z\}$, $\psi_\nu(\mathbf{r})$ and ϵ_ν are the one-electron orbitals and eigenvalues, α and β are the 4×4 matrices:

$$\alpha = \begin{pmatrix} 0 & \boldsymbol{\sigma} \\ \boldsymbol{\sigma} & 0 \end{pmatrix}, \quad (2.48)$$

where $\boldsymbol{\sigma}$ denotes the 2×2 Pauli spin matrices, and

$$\beta = \begin{pmatrix} \mathbf{I}_2 & 0 \\ 0 & -\mathbf{I}_2 \end{pmatrix}, \quad (2.49)$$

where \mathbf{I}_2 is the 2×2 identity matrix.

The 4-component single-particle wave function is written as,

$$\psi_\nu(\mathbf{r}) = \begin{pmatrix} \phi_\nu^\uparrow(\mathbf{r}) \\ \phi_\nu^\downarrow(\mathbf{r}) \\ \chi_\nu^\uparrow(\mathbf{r}) \\ \chi_\nu^\downarrow(\mathbf{r}) \end{pmatrix}, \quad (2.50)$$

where $\phi_\nu(\mathbf{r})$ and $\chi_\nu(\mathbf{r})$ are two-component spinors. For electrons (positive energy solutions) ϕ is the large component and χ is the small component.

In Eq. (2.47), V_s^μ is the effective four potential:

$$V_s^\mu(\mathbf{r}) = V_{ext}^\mu(\mathbf{r}) + V_H^\mu([j], \mathbf{r}) + V_{XC}^\mu([j], \mathbf{r}), \quad (2.51)$$

where the 4-component Hartree potential is given by,

$$V_H^\mu(\mathbf{r}) = \int \frac{j^\mu(\mathbf{r}')}{|\mathbf{r} - \mathbf{r}'|} d\mathbf{r}', \quad (2.52)$$

and the 4-component exchange-correlation potential is given by,

$$V_{XC}^\mu(\mathbf{r}) = \frac{\delta E_{XC}[j^\mu]}{\delta j_\mu(\mathbf{r})}, \quad (2.53)$$

and the 4-current is given by,

$$j^\mu(\mathbf{r}) = \sum_{-mc^2 < \epsilon_\nu \leq \epsilon_F} \bar{\phi}_\nu(\mathbf{r}) \alpha^\mu \phi_\nu(\mathbf{r}). \quad (2.54)$$

Eq. (2.47) has to be solved self-consistently.

The relativistic corrections to the Dirac Hamiltonian of Eq. (2.47) produce a relativistic correction to the kinetic energy (also known as the mass-velocity term), the Darwin term and the spin-orbit coupling (SOC) term. For scalar-relativistic (SR) calculations, only the relativistic correction to the kinetic energy and the Darwin term are considered. When the SOC is included in the calculation it is referred to as a fully relativistic calculation.

2.3.1 Spin-orbit coupling

The spin-orbit coupling (SOC) is a relativistic effect. An electron in its rest frame sees the nucleus moving in an orbit around it, generating a magnetic field proportional to the orbital angular momentum, which in turn interacts with the spin magnetic moment of the electron. So, SOC is basically the effective magnetic field ‘seen’ by the spin of the electron in its rest frame. This is the origin of spin-orbit coupling, which results in a splitting of electronic energy levels. The energy level splitting due to SOC is directly proportional to the fourth power of the atomic number Z . Therefore, for heavier elements in the periodic table, the effect of SOC is significant. The expression of the SOC term is given by,

$$H_{SOC} = -\frac{e\hbar}{4m^2c^2}\boldsymbol{\sigma} \cdot (\mathbf{E} \times \mathbf{p}). \quad (2.55)$$

For an electron in an electromagnetic field (\mathbf{E} is the electric field), force = $e\mathbf{E} = -\nabla V$, for the spherically symmetric potential,

$$H_{SOC} = \frac{e\hbar}{4m^2c^2}\boldsymbol{\sigma} \cdot (\nabla V \times \mathbf{p}) = \frac{1}{2m^2c^2} \frac{1}{r} \frac{dV(r)}{dr} \mathbf{L} \cdot \mathbf{S}, \quad (2.56)$$

where orbital angular momentum $\mathbf{L} = \mathbf{r} \times \mathbf{p}$ and the spin angular momentum $\mathbf{S} = \frac{\hbar}{2}\boldsymbol{\sigma}$. Here \mathbf{p} is the momentum operator and $\boldsymbol{\sigma}$ denotes the Pauli spin matrices. Upon the introduction of SOC in the Hamiltonian, orbital angular momentum l and

spin angular momentum s are no longer good quantum number, the total angular momentum j is now a good quantum number.

In my thesis, the SOC is introduced through fully relativistic pseudopotentials.³¹

2.4 Strongly correlated systems: the DFT+ U method

Transition metal and rare earth elements are characterized by well-localized d or f orbitals. This localization results in strong on-site correlations, such that if an electron is occupying a state localized at a particular site, placing a second electron in the same site is penalized with an additional energy U . These types of systems are called strongly correlated systems. This type of systems are studied under the Hubbard model (1965) Hamiltonian. In computational DFT calculations, if we introduce the Hubbard onsite term, depending on whether we have combined it with LDA or GGA, the calculational method is known as LDA+ U or GGA+ U , respectively.³²⁻³⁴

In this scheme, the total energy³² of the system is given by,

$$E_{DFT+U} = E_{DFT} + \frac{1}{2}U \sum_{i \neq j} f_i f_j - \frac{1}{2}UN(N-1), \quad (2.57)$$

where E_{DFT} is total energy calculated from normal DFT calculation, f_i are orbital occupancies for the localized d and f electrons. The second term on the right hand side of the equation is the Hubbard correction, the third term is the double counting term and hence it is subtracted. Here $\sum_i f_i = N$, the total number of electrons. In this thesis, I have used GGA+ U .

The above model of Eq. (2.57) splits the energy level into lower and upper Hubbard sub-bands, with eigenvalues that are given by:

$$\epsilon_i = \frac{\partial E_{DFT+U}}{\partial f_i} = \epsilon_{DFT} + U \left(\frac{1}{2} - f_i \right), \quad (2.58)$$

such that the separation between the sub-bands is U . For Mott-Hubbard insulators, the valence and conduction bands overlap, having no gap, according to the conventional band theories. However, when the strong electron-electron correlations of the localized d and f electrons are taken into consideration, they turn out to be insulators, which is the correct description.

The value of the Hubbard parameter U can either be calculated or it can be determined empirically, by fitting it to the experimental data. The U parameter mainly affects the electronic structure, it moves the states away from the Fermi level and thus creates a gap. The experimental gap of the Mott-Hubbard insulators can then be compared with the calculated results to choose the U value. The value of U can also be computed theoretically using density functional perturbation theory.³⁵

2.5 Optical properties of solids: joint density of states and dielectric function calculation

The optical properties of solids carry important insights on energy band structures, lattice vibrations, impurity levels, localized defects, excitons and certain magnetic excitations. Some observables like reflectivity, transmission coefficient, absorption coefficient, light scattering etc., are experimentally measured. From these measurements we deduce the frequency dependent complex dielectric function $\epsilon(\omega)$ or complex optical conductivity $\sigma(\omega)$, which are directly related to the energy band structures of solids.

Consider a solid material subjected to electromagnetic radiation. It can be shown, using the famous Maxwell's electromagnetic equations, that when there is

loss of the amplitude of the incident electromagnetic radiation within a material, the dielectric function and the optical conductivity become complex quantities. There can then occur intraband or interband processes. *Intraband processes* are basically electronic conduction due to free carriers. Hence these are important for metals and semimetals. These processes can be understood using the classical Drude theory or classical Boltzmann equation or by the quantum mechanical density matrix technique. *Interband processes* are basically the absorption of electromagnetic radiation by an electron in an occupied state below the Fermi level, thereby making a transition to an unoccupied state in the conduction bands. Interband processes are purely quantum mechanical. They occur in semiconductors and insulators. The interband transitions can be *direct* or *indirect*. In direct transitions, the crystal momentum is conserved i.e., $E_v(\mathbf{k}) \rightarrow E_c(\mathbf{k})$. Since the momentum of the photon involved in an indirect transition is much less than the Brillouin zone dimension (10^5 and 10^8 cm^{-1} respectively), in direct optical transitions the wave vector of the electron does not change significantly in going from the valence to conduction band. In indirect transitions, as the wave vectors of the involved valence and conduction band states are not the same, a third particle, namely a phonon, enters into the picture and conserves momentum: $\mathbf{k}_{valence} = \mathbf{k}_{conduction} \pm \mathbf{q}_{phonon}$. In my calculations, I have only considered direct interband transitions.

The Hamiltonian of an electron in a crystalline solid interacting with electromagnetic radiation is given by:³⁶

$$H = \frac{(\mathbf{p} - e\mathbf{A})^2}{2m} + V(\mathbf{r}) = \frac{p^2}{2m} + V(\mathbf{r}) - \frac{e}{m}\mathbf{A} \cdot \mathbf{p} + \frac{e^2 A^2}{2m}, \quad (2.59)$$

where \mathbf{p} is the conjugate variable to position (the kinetic momentum is given by, $m\mathbf{v} = \mathbf{p} - e\mathbf{A}$), $V(\mathbf{r})$ is the periodic potential of the crystal, \mathbf{A} is the vector potential of the electromagnetic radiation, e and m are the electronic charge and mass,

respectively. The one-electron Hamiltonian in the absence of the electromagnetic radiation is,

$$H = \frac{p^2}{2m} + V(\mathbf{r}), \quad (2.60)$$

We can treat the electromagnetic radiation field as a perturbation term, which is given by,

$$H' = -\frac{e}{m} \mathbf{A} \cdot \mathbf{p} + \frac{e^2 A^2}{2m}. \quad (2.61)$$

Optical fields are generally weak (if not generated by powerful lasers) and hence we can consider only the term linear in \mathbf{A} , the linear response regime. In that case, from this perturbation theory, it is now clearly understandable why the interband transitions depend on momentum matrix elements $\langle v | \mathbf{p} | c \rangle$, which couple the valence band state v and the conduction band state c , and determine the strength of the optical transitions.

In order to get information about the optical transitions, we need Fermi's golden rule which gives the *transition probability per unit time* from an initial state $|i\rangle$ to a final state $|f\rangle$,

$$W = \frac{2\pi}{\hbar} |\langle i | H' | f \rangle|^2 \rho(E_f), \quad (2.62)$$

where $|\langle i | H' | f \rangle|$ is the matrix element of the perturbation given by the linear term of Eq. (2.61): $H' = -\frac{e}{m} \mathbf{A} \cdot \mathbf{p}$, $|i\rangle$ and $|f\rangle$ are two eigenstates of the unperturbed Hamiltonian H_0 , and $\rho(E_f)$ is the density of final states at the energy E_f . When the initial and final states are separated by quantum of energy $\hbar\omega$ of the incident electromagnetic radiation, the above equation can be written as,

$$W = \frac{2\pi}{\hbar} \sum_{\sigma} \sum_{n \in V} \sum_{n' \in C} \frac{\Omega}{(2\pi)^3} \int d^3k |\langle i | H' | f \rangle|^2 \delta(E_{\mathbf{k},n'} - E_{\mathbf{k},n} - \hbar\omega). \quad (2.63)$$

Clearly, the eigenstates of the unperturbed Hamiltonian are Bloch states, and in the above expression all the Bloch states of the valence and conduction bands (n and n' index belong to the valence bands V and conduction bands C , respectively) separated by energy value $\hbar\omega$, at all the wave vectors of the Brillouin zone are considered. $E_{\mathbf{k},n}$ and $E_{\mathbf{k},n'}$ are the eigenvalues of the unperturbed Hamiltonian; they are Kohn-Sham eigenvalues in DFT calculations. σ is the spin-multiplicity. For simplicity assuming the perturbation matrix elements $|\langle i | H' | f \rangle|^2$ to be \mathbf{k} -independent, the remaining integral is defined as *joint density of states* between valence and conduction bands,

$$\rho_{cv}(\hbar\omega) = \sum_{n \in V} \sum_{n' \in C} \frac{2}{(2\pi)^3} \int d^3k \delta(E_{\mathbf{k},n'} - E_{\mathbf{k},n} - \hbar\omega). \quad (2.64)$$

Here, $\rho_{cv}(\hbar\omega)$ actually gives the number of states per unit volume, per unit energy range, which occur with an energy difference between the conduction and valence bands equal to the photon energy $\hbar\omega$. For two-dimensions (2D) and one dimension (1D), we replace $d^3k/(2\pi)^3$ by $d^2k/(2\pi)^2$ and $dk/(2\pi)$, respectively. Considering the interband transitions at finite temperature, we have to include Fermi functions to represent the occupation of the bands at finite temperature; in that case the joint density of states is expressed as,

$$\rho_{cv}(\hbar\omega) = \sum_{n \in V} \sum_{n' \in C} \frac{2}{(2\pi)^3} \int d^3k \delta(E_{\mathbf{k},n'} - E_{\mathbf{k},n} - \hbar\omega) [f(E_{\mathbf{k},n}) - f(E_{\mathbf{k},n'})], \quad (2.65)$$

where $f(E_{\mathbf{k},n})$ is the Fermi distribution function that accounts for the occupation

of the bands. For numerical calculations, the Dirac delta function is implemented using a Gaussian function normalized to unity,

$$G(\hbar\omega) = \frac{1}{\Gamma\sqrt{\pi}} e^{-\frac{(E_{\mathbf{k},n'} - E_{\mathbf{k},n} - \hbar\omega)^2}{\Gamma^2}}, \quad (2.66)$$

and the integration over \mathbf{k} -vectors is replaced by a simple sum over \mathbf{k} -points.

The imaginary part of the dielectric function $\epsilon_{\alpha,\beta}^{(2)}(\omega)$ is given by the following equation:^{37–39}

$$\epsilon_{\alpha,\beta}^{(2)}(\omega) = \frac{4\pi e^2}{m\omega^2} \sum_{n,n'} \int_k d^3k \langle \psi_{\mathbf{k},n} | \hat{\mathbf{P}}_\alpha | \psi_{\mathbf{k},n'} \rangle \langle \psi_{\mathbf{k},n'} | \hat{\mathbf{P}}_\beta^\dagger | \psi_{\mathbf{k},n} \rangle f_i(1-f_i) \delta(E_{\mathbf{k},n'} - E_{\mathbf{k},n} - \hbar\omega) \quad (2.67)$$

and we define square of the momentum matrix elements as,

$$\hat{\mathbf{M}}_{\alpha\beta} = \langle \psi_{\mathbf{k},n} | \hat{\mathbf{P}}_\alpha | \psi_{\mathbf{k},n'} \rangle \langle \psi_{\mathbf{k},n'} | \hat{\mathbf{P}}_\beta^\dagger | \psi_{\mathbf{k},n} \rangle \quad (2.68)$$

where $\langle \psi_{\mathbf{k},n} | \hat{\mathbf{P}}_\alpha | \psi_{\mathbf{k},n'} \rangle$ are the momentum matrix elements, $|\mathbf{k}, n\rangle$ and $|\mathbf{k}, n'\rangle$ represent the initial and final states involved in the optical transitions, f_i is the Fermi distribution representing the electronic occupation function in the initial states, e and m are the electronic charge and mass, respectively. n, n' are the valence band and conduction band indices. \mathbf{k} is a wave vector in the FBZ. ω represents the energy or frequency of the incoming electromagnetic wave. The Dirac delta function conserves the energy during optical transitions.

The imaginary part of the frequency dependent dielectric function $\epsilon_{\alpha,\beta}^{(2)}(\omega)$ can be viewed as a response function that comes from a perturbation expansion with adiabatic turning on,^{40;41}

$$\begin{aligned} \epsilon_{\alpha,\beta}^{(2)}(\omega) &= \frac{4\pi e^2}{\Omega N_{\mathbf{k}} m^2} \sum_{n,\mathbf{k}} \frac{df(E_{\mathbf{k},n})}{dE_{\mathbf{k},n}} \frac{\eta\omega \hat{\mathbf{M}}_{\alpha\beta}}{\omega^4 + \eta^2\omega^2} \\ &+ \frac{8\pi e^2}{\Omega N_{\mathbf{k}} m^2} \sum_{n \neq n'} \sum_{\mathbf{k}} \frac{\hat{\mathbf{M}}_{\alpha\beta}}{E_{\mathbf{k},n'} - E_{\mathbf{k},n}} \frac{\Gamma\omega f(E_{\mathbf{k},n})}{[(\omega_{\mathbf{k},n'} - \omega_{\mathbf{k},n})^2 - \omega^2]^2 + \Gamma^2\omega^2}, \end{aligned} \quad (2.69)$$

where Γ and η are *intersmear* and *intrasmear*, respectively (broadening parameter for interband and intraband transitions), Ω is the volume of the unit cell, ω is frequency, $N_{\mathbf{k}}$ number of \mathbf{k} -points in the FBZ, α, β correspond to Cartesian coordinates (the double indices make it clear that the dielectric function is a tensor quantity), e and m are electronic charge and mass, respectively. $E_{\mathbf{k},n'} - E_{\mathbf{k},n}$ correspond to the transition energy, and the square of the momentum matrix elements are give by,

$$\begin{aligned} \hat{\mathbf{M}}_{\alpha\beta} &= \langle u_{\mathbf{k},n'} | \hat{\mathbf{p}}_{\alpha} | u_{\mathbf{k},n} \rangle \langle u_{\mathbf{k},n} | \hat{\mathbf{p}}_{\beta}^{\dagger} | u_{\mathbf{k},n'} \rangle \\ &\propto u_{\mathbf{k},n'}^*(\mathbf{r}) \frac{d}{dx_{\alpha}} u_{\mathbf{k},n}(\mathbf{r}) u_{\mathbf{k},n}^*(\mathbf{r}) \frac{d}{dx_{\beta}} u_{\mathbf{k},n'}(\mathbf{r}), \end{aligned} \quad (2.70)$$

where $\hat{\mathbf{p}}_{\alpha}$ is one component of the momentum operator is and is represented as $-i\hbar \frac{d}{dx_{\alpha}}$. $|u_{\mathbf{k},n}\rangle$ is the periodic part of the one-electron Bloch wave function for the plane wave DFT calculations. For the plane wave basis set, I have already written the Kohn-Sham orbitals in Eq. (2.29), having similar form of the Bloch wave functions. In this case the square of the momentum matrix elements become,

$$\hat{\mathbf{M}}_{\alpha\beta} = \left(\sum_{\mathbf{G}} c_{j\mathbf{k}}^*(\mathbf{G}) c_{j'\mathbf{k}}(\mathbf{G}) G_{\alpha} \right) \left(\sum_{\mathbf{G}} c_{j\mathbf{k}}^*(\mathbf{G}) c_{j'\mathbf{k}}(\mathbf{G}) G_{\beta} \right). \quad (2.71)$$

Note that here we have only considered direct interband transitions in which crystal momentum \mathbf{k} is conserved, we have not accounted for indirect interband transitions. j is the band index here. In standard optics, the contribution to the dielectric tensor coming from the intraband transitions is negligible due to very low

momentum transferred by the incoming/outgoing photon.

Once we know the imaginary part of the dielectric function $\epsilon_{\alpha,\beta}^{(2)}(\omega)$, many things can be calculated from it. The real part of the dielectric function can be found using the Kramers-Kronig transformation relation:

$$\epsilon_{\alpha,\beta}^{(1)}(\omega) = 1 + \frac{2}{\pi} \int_0^\infty \frac{\omega' \epsilon_{\alpha,\beta}^{(2)}(\omega')}{\omega'^2 - \omega^2} d\omega'. \quad (2.72)$$

Operating a London transformation on $\epsilon_{\alpha,\beta}^{(2)}(\omega)$, the dielectric function can be calculated on the imaginary axis,

$$\epsilon_{\alpha,\beta}(i\omega) = 1 + \frac{2}{\pi} \int_0^\infty \frac{\omega' \epsilon_{\alpha,\beta}^{(2)}(\omega')}{\omega'^2 + \omega^2} d\omega'. \quad (2.73)$$

From this expression, the electron energy loss spectrum can be calculated as the imaginary part of the inverse dielectric tensor on the imaginary axis,

$$Im \left\{ \frac{1}{\epsilon_{\alpha,\beta}(i\omega)} \right\} = \frac{\epsilon_{\alpha,\beta}^{(2)}(\omega)}{\epsilon_{\alpha,\beta}^{(2)2}(\omega) + \epsilon_{\alpha,\beta}^{(1)2}(\omega)}. \quad (2.74)$$

The absorption coefficient is an important quantity for the optical performance of a material and it can easily be calculated from the real and imaginary part of the dielectric function,

$$\alpha(\omega) = \sqrt{2\omega} \sqrt{\sqrt{\epsilon_1^2(\omega) + \epsilon_2^2(\omega)} - \epsilon_1(\omega)}. \quad (2.75)$$

2.6 Codes and software used

I have performed quantum mechanical density functional theory (DFT) calculations using the Quantum ESPRESSO (PWSCF) software package^{15;42} for structural, electronic, magnetic, chemical, and vibrational properties of solid state materials.

The atomic scale modelling of materials, charge density and redistribution plots,

magnetization density etc. reported in this thesis, are obtained using the software packages XCrySDen⁴³ and VESTA.⁴⁴ All two and three-dimensional graphs used in the thesis are either plotted using the Xmgrace software package or obtained using gnuplot.

Bibliography

- [1] J. Kohanoff, *Electronic Structure Calculations for Solids and Molecules: Theory and Computational Methods*. Cambridge University Press, 2006.
- [2] M. Born and R. Oppenheimer, “Zur quantentheorie der molekeln,” *Annalen der physik*, vol. 389, p. 457, 1927.
- [3] P. Hohenberg and W. Kohn, “Inhomogeneous electron gas,” *Phys. Rev.*, vol. 136, p. B864, 1964.
- [4] R. M. Martin, *Electronic structure: basic theory and practical methods*. Cambridge University Press, 2004.
- [5] W. Kohn and L. J. Sham, “Self-consistent equations including exchange and correlation effects,” *Phys. Rev.*, vol. 140, p. A1133, 1965.
- [6] U. Von Barth and L. Hedin, “A local exchange-correlation potential for the spin polarized case. i,” *J. of Phys. C: Solid State Phys.*, vol. 5, no. 13, p. 1629, 1972.
- [7] D. M. Ceperley and B. J. Alder, “Ground state of the electron gas by a stochastic method,” *Phys. Rev. Lett.*, vol. 45, no. 7, p. 566, 1980.

-
- [8] S. H. Vosko, L. Wilk, and M. Nusair, “Accurate spin-dependent electron liquid correlation energies for local spin density calculations: a critical analysis,” *Canadian Journal of physics*, vol. 58, no. 8, pp. 1200–1211, 1980.
- [9] J. P. Perdew and A. Zunger, “Self-interaction correction to density-functional approximations for many-electron systems,” *Phys. Rev. B*, vol. 23, no. 10, p. 5048, 1981.
- [10] P. A. M. Dirac, “Note on Exchange Phenomena in the Thomas Atom,” *Mathematical Proceedings of the Cambridge Philosophical Society*, vol. 26, no. 3, p. 376–385, 1930.
- [11] J. P. Perdew, K. Burke, and M. Ernzerhof, “Generalized gradient approximation made simple,” *Phys. Rev. Lett.*, vol. 77, no. 18, p. 3865, 1996.
- [12] J. P. Perdew and W. Yue, “Accurate and simple density functional for the electronic exchange energy: Generalized gradient approximation,” *Phys. Rev. B*, vol. 33, no. 12, p. 8800, 1986.
- [13] A. D. Becke, “Density-functional exchange-energy approximation with correct asymptotic behavior,” *Phys. Rev. A*, vol. 38, no. 6, p. 3098, 1988.
- [14] J. P. Perdew and Y. Wang, “Accurate and simple analytic representation of the electron-gas correlation energy,” *Phys. Rev. B*, vol. 45, no. 23, p. 13244, 1992.
- [15] P. Giannozzi, S. Baroni, N. Bonini, M. Calandra, R. Car, C. Cavazzoni, D. Ceresoli, G. L. Chiarotti, M. Cococcioni, I. Dabo, *et al.*, “QUANTUM ESPRESSO: a modular and open-source software project for quantum simulations of materials,” *Journal of physics: Condensed matter*, vol. 21, no. 39, p. 395502, 2009.

-
- [16] X. Gonze, J.-M. Beuken, R. Caracas, F. Detraux, M. Fuchs, G.-M. Rignanese, L. Sindic, M. Verstraete, G. Zerah, F. Jollet, *et al.*, “First-principles computation of material properties: the ABINIT software project,” *Comput. Mater. Sci.*, vol. 25, pp. 478–492, 2002.
- [17] J. M. Soler, E. Artacho, J. D. Gale, A. García, J. Junquera, P. Ordejón, and D. Sánchez-Portal, “The SIESTA method for ab initio order-N materials simulation,” *J. Phys. Condens. Matter*, vol. 14, p. 2745, 2002.
- [18] H. Dreyssé, *Electronic structure and physical properties of solids*. Springer, 2000.
- [19] W. E. Pickett, “Pseudopotential methods in condensed matter applications,” *Comput. Phys. Commun.*, vol. 9, p. 115, 1989.
- [20] D. Hamann, M. Schlüter, and C. Chiang, “Norm-conserving pseudopotentials,” *Physical Review Letters*, vol. 43, no. 20, p. 1494, 1979.
- [21] D. Vanderbilt, “Soft self-consistent pseudopotentials in a generalized eigenvalue formalism,” *Physical Review B*, vol. 41, no. 11, p. 7892, 1990.
- [22] H. J. Monkhorst and J. D. Pack, “Special points for Brillouin-zone integrations,” *Physical Review B*, vol. 13, no. 12, p. 5188, 1976.
- [23] C.-L. Fu and K.-M. Ho, “First-principles calculation of the equilibrium ground-state properties of transition metals: Applications to Nb and Mo,” *Phys. Rev. B*, vol. 28, p. 5480, 1983.
- [24] M. Methfessel and A. Paxton, “High-precision sampling for Brillouin-zone integration in metals,” *Phys. Rev. B*, vol. 40, p. 3616, 1989.
- [25] N. Marzari, D. Vanderbilt, A. De Vita, and M. Payne, “Thermal contraction and disordering of the Al(110) surface,” *Phys. Rev. Lett.*, vol. 82, p. 3296, 1999.

-
- [26] R. P. Feynman, "Forces in molecules," *Physical Review*, vol. 56, no. 4, p. 340, 1939.
- [27] O. Nielsen and R. M. Martin, "First-principles calculation of stress," *Physical Review Letters*, vol. 50, no. 9, p. 697, 1983.
- [28] A. Rajagopal and J. Callaway, "Inhomogeneous electron gas," *Physical Review B*, vol. 7, no. 5, p. 1912, 1973.
- [29] A. Rajagopal, "Inhomogeneous relativistic electron gas," *Journal of Physics C: Solid State Physics*, vol. 11, no. 24, p. L943, 1978.
- [30] A. H. MacDonald and S. Vosko, "A relativistic density functional formalism," *Journal of Physics C: Solid State Physics*, vol. 12, no. 15, p. 2977, 1979.
- [31] A. Dal Corso and A. M. Conte, "Spin-orbit coupling with ultrasoft pseudopotentials: Application to Au and Pt," *Physical Review B*, vol. 71, no. 11, p. 115106, 2005.
- [32] V. I. Anisimov, J. Zaanen, and O. K. Andersen, "Band theory and Mott insulators: Hubbard U instead of Stoner I," *Physical Review B*, vol. 44, no. 3, p. 943, 1991.
- [33] V. I. Anisimov, I. Solovyev, M. Korotin, M. Czyżyk, and G. Sawatzky, "Density-functional theory and NiO photoemission spectra," *Physical Review B*, vol. 48, no. 23, p. 16929, 1993.
- [34] A. Liechtenstein, V. I. Anisimov, and J. Zaanen, "Density-functional theory and strong interactions: Orbital ordering in Mott-Hubbard insulators," *Physical Review B*, vol. 52, no. 8, p. R5467, 1995.

-
- [35] I. Timrov, N. Marzari, and M. Cococcioni, “HP–A code for the calculation of Hubbard parameters using density-functional perturbation theory,” *arXiv preprint arXiv:2203.15684*, 2022.
- [36] M. S. Dresselhaus, *Solid state physics part ii optical properties of solids*. Cite-seer, 2001.
- [37] N. V. Smith, “Photoelectron energy spectra and the band structures of the noble metals,” *Physical Review B*, vol. 3, no. 6, p. 1862, 1971.
- [38] C. Ambrosch-Draxl and J. O. Sofo, “Linear optical properties of solids within the full-potential linearized augmented planewave method,” *Computer physics communications*, vol. 175, no. 1, pp. 1–14, 2006.
- [39] Z. Xu, “The determination of the momentum matrix elements involved in calculating the dielectric constants of superlattices using the tight-binding method,” *Solid state communications*, vol. 76, no. 9, pp. 1143–1147, 1990.
- [40] G. Wysin, “Quantum Theory for Dielectric Properties of Conductors A. Response to Optical Electric Field Only,” 2012.
- [41] A. Benassi, A. Feretti, and C. Carlo, “PWSCF’S epsilon.x user’s manual,” 2001.
- [42] P. Giannozzi, O. Andreussi, T. Brumme, O. Bunau, M. B. Nardelli, M. Calandra, R. Car, C. Cavazzoni, D. Ceresoli, M. Cococcioni, *et al.*, “Advanced capabilities for materials modelling with quantum espresso,” *Journal of Physics: Condensed matter*, vol. 29, no. 46, p. 465901, 2017.
- [43] A. Kokalj, “XCrySDen:(X-Window) CRYstalline Structures and DENsities,” *Comp. Mater. Sci.*, vol. 28, p. 155, 2003.

-
- [44] K. Momma and F. Izumi, “VESTA 3 for three-dimensional visualization of crystal, volumetric and morphology data,” *J. Appl. Crystallogr.*, vol. 44, p. 1272, 2011.

Sn Deposited on Ag(001): Formation of Surface Alloy and Evolution of Structural and Electronic Properties

The highest education is that which does not merely give us information but makes our life in harmony with all existence.

Rabindranath Tagore

In this chapter, we study the structural and electronic properties of Sn atoms deposited on an Ag(001) substrate. This work was done in collaboration with the experimental group of Prof. Krishnakumar S. R. Menon, Surface Physics and Materials Science Division, SINP, Kolkata, and his student Arunava Kar. In their experiments, they deposited Sn atoms on an Ag(001) surface. Low energy electron diffraction (LEED) experiments showed the existence of different superstructures as a function of Sn coverage. They also measured the electronic structure of these

systems using Angle Resolved Photoemission Spectroscopy (ARPES). We have performed density functional theory (DFT) calculations to interpret and shed insight on the experimental data. Somewhat counterintuitively, we find that an ordered Sn-Ag surface alloy is formed in the topmost layer, with a structural configuration and periodicity that changes with Sn coverage.

3.1 Introduction

The epitaxial growth of metal atoms on different metal substrates is a fantastic way to control the structural, electronic, chemical, magnetic and topological properties of the overlayer and/or substrate.¹ The properties change significantly when the deposited atoms form a thin epitaxial film that is only a single or a few atoms layer thick on the substrate, and thus essentially confined to two dimensions. In such systems, orbital hybridization between the states of the overlayer and substrate can result in a drastic change in the electronic structure, compared to that of either the clean substrate or the thin film deposited on it.

These properties depend crucially on the growth pattern and structure of the overlayer. Even when the growth is pseudomorphic (i.e., the lattice constant of the overlayer is the same as that of the underlying substrate), many kinds of structures are possible for metal-on-metal pseudomorphic growth: (i) normal overlayer adsorption, (ii) sub-surface adsorption, where the deposited ('guest') atoms get buried under one or more layers of the single crystal substrate, (iii) the guest atoms can substitute the host atoms from different layers of the clean surface and form an ordered bimetallic surface alloy, etc. For example, when Cr is deposited on Ag(001), the Cr atoms prefer to get buried under one Ag layer and form a 1Ag/Cr/Ag(001) structure.^{2;3} In contrast, when Sn is deposited on an Ag(111) substrate, Sn atoms substitute every third Ag atom from the surface layer, and form a surface alloy on

Ag(111) at 0.33 ML Sn coverage.^{4;5} The study of such surface alloys is of great interest because of their possible applications in multiple fields such as heterogeneous catalysis, corrosion-resistance, spintronic devices, surface hardening, etc.^{6;7} Recently, the study of surface alloys has gained added attention because of the Rashba spin splitting in systems such as Bi/Ag(111), and its application to spintronics.⁸

When atoms of one metallic species are deposited on atoms of another metal substrate, the two atomic species need not always be confined to different atomic layers. Instead the two atomic species can get mixed in layers at or near the surface, resulting in the formation of a surface alloy.^{9;10} The formation of surface alloys can stabilize alloy phases and structures that are not energetically favorable in the bulk, i.e., one can get surface alloys out of bulk-immiscible constituents.^{11–15} Surface alloys may possess superior and emergent properties which were not present in the constituent elements. In surface alloys, one expensive metal can be ‘diluted’ with a less expensive elements, and thus cost can be reduced.

One can ask the question: why might two bulk-immiscible atoms mix on the surface and form a surface alloy? Two possible driving forces have been reported in the literature: the possible reduction of surface stress,⁹ and (in spin-polarized systems) the possible lowering of exchange energy by increase of magnetic moments.¹¹ An atom in the bulk (metal) crystal can be viewed as sitting at an optimal electron density arising from its neighbors. An atom on the surface has a lower coordination number compared to an atom in the bulk. For example, a bulk atom in the face centered cubic (FCC) crystal structure has coordination number 12; however an atom on the FCC(001) surface has coordination number 8. So, a surface atom would like to come closer to its neighbouring atoms to regain the optimal electron density; this can happen either through surface reconstruction or interlayer relaxation. However, in many cases, surface reconstruction does not occur because this

would result in the surface losing registry with the bulk, which costs energy. As a result, if we imagine a spring connecting two surface atoms, the spring will be under tension. This causes the very well known tensile surface stress of unreconstructed metal surfaces.¹⁶ Equivalently, one can say that the effective size of a surface atom is *reduces* compared to that of a bulk atom of the same species.

Now, if *bigger* atoms of another species are deposited on the metal surface, instead of sitting as overlayer on the surface, the deposited (bigger) atoms can get embedded into the surface layer by substituting some of the surface atoms of the metal surface, thus forming a surface alloy. The formation of this surface alloy relieves the tensile surface stress of the metal surface explained in the previous paragraph. The effective ‘size’ of a surface atom can be calculated.¹⁷ In most previous work, the effective size of atoms deposited on a metal surface of the same or different species were always found to be *smaller* compared to the size of corresponding bulk atoms. However, in this chapter, we will see that this need not be the case always.

The p-block metals (In, Sn, Sb, Tl, Pb and Bi) do not form bulk alloys with other metals easily.¹⁸ This low bulk miscibility arises due to some factors such as the two atoms having very different sizes, crystal structures or chemical affinities.^{19–21} Moreover, most of these p-block metals have low surface energies. Therefore, when these atoms are deposited on the surface of another metal with a higher surface energy, they tend to form an overlayer and wet the surface, instead of forming a surface alloy.^{2;22} However, one would still like to explore the formation of surface alloys from these p-block metals, motivated by various possible applications, e.g., as catalysts.

Previous studies on surface alloys have primarily focused on structural properties; understanding the electronic structure and its evolution with composition is still incomplete for many of the systems. Although many interesting electronic properties

induced by the p-block metals on metal substrates, like strong Fermi surface nesting,²³ Peierls-type charge-density-wave phase transitions,²³ effects of the large spin-orbit coupling,^{24;25} Dirac-like band dispersions,²⁶ order-disorder structural phase transitions,²⁷ etc., have been studied, only a few reports of the evolution of electronic structure of their surface alloys are found in the literature.^{28;29} We note that the study of electronic structure is difficult due to the presence of substrate states near the Fermi level and their hybridization with the surface states and overlayer states. However, there exists a projected bulk band gap at the zone edges, which helps to separate out the substrate states from the surface states. This helps one to study the evolution of the surface states with changing composition and surface structures.

For the reasons stated above, in this work, we consider the case of Sn and Ag, by studying what happens when Sn atoms are deposited on an Ag(001) surface. One might naïvely expect that Sn and Ag will mix in the bulk, because they satisfy two of the Hume-Rothéry rules³⁰ that determine bulk miscibility: Sn and Ag have almost identical atomic sizes in the bulk (diameters of 2.81 Å and 2.88 Å for Sn and Ag, respectively)^{31;32}, and they have almost identical electronegativities (1.96 and 1.93 for Sn and Ag, respectively, in the Pauling scale.^{33;34}) However, the bulk phase diagram³⁵ of Sn and Ag shows eutectic behaviour at 3.5 wt. % Sn with a eutectic temperature of 221 °C with solid solubility of about 0.05 wt. % of Ag. Moreover, Sn and Ag form only a single intermetallic compound, Ag₃Sn, in a narrow range of composition in the phase diagram.³⁶

However, will Sn and Ag atoms mix in surface to form surface alloy? A naïve expectation is that they will not form any surface alloy for two reasons: (i) The first Hume-Rothéry rule does not apply in the case of *surface* alloys.³⁷ Rather, (binary) surface alloys generally form when the two atomic species have very *different* sizes. Therefore, one might expect that Sn and Ag atoms, having very similar (bulk) sizes,

are unlikely to form a surface alloy. (ii) The surface energy of Sn(001) (0.709 J/m^2)³⁸ is lower than that of Ag(001) (1.27 J/m^2).³⁹ So, one might expect that deposited Sn atoms will form an overlayer i.e., wet the Ag(001) surface, instead of forming a surface alloy. However, in this work, in contrast to these naïve expectations, we will see that when Sn atoms are deposited on an Ag(001) surface, Sn-Ag surface alloys are formed at all values of the Sn coverage x , where $0 < x < 1$. The reason for this counter-intuitive behavior is very interesting: we find that while the effective size of surface Ag atoms is smaller than that of bulk Ag atoms, the effective size of surface Sn atoms is found to be *larger* than that of bulk Sn atoms. Moreover, Sn atoms become *larger* than both surface and bulk Ag atoms on the Ag(001) surface.

We now briefly summarize some earlier studies of Sn deposition on different metal surfaces. Previous studies of Sn deposition on metal substrates have mostly focused on the (111) surfaces of FCC metals such as Pt, Ni, Cu and Au.^{4;40;41} It is found that Sn forms stable two-dimensional surface alloy phases with a $p(\sqrt{3} \times \sqrt{3})\text{-}R30^\circ$ structure at Sn coverage of $x = \frac{1}{3}$ monolayer (ML), beyond which dealloying sets in.⁴⁰ However, when deposited on Ag(111), Sn atoms were found to form a surface alloy, with no dealloying observed even for higher coverages.⁴ Surface alloys of Sn on FCC(001) metal surfaces have been observed on Ni(001) and Pt(001),^{42;43} with an ordered $c(2 \times 2)$ structure for $x = 0.5$ ML. A surface alloy was also observed for the initial growth stage of Sn on Au(001).⁴⁴ In experiments on Sn on Cu(001), the structure of the system was seen to evolve with Sn coverage.⁴⁵ Density functional theory (DFT) calculations on this system suggest that Sn deposition on Cu(001) results in the formation of substitutional surface alloys, with complex alloy structures for high coverages of Sn.^{46;47} We note that Menon's group had earlier performed a preliminary study of Sn/Ag(001).⁴⁸ The results of this earlier study indicated that there may be continuous formation of substitutional surface alloys with Sn coverage x . In this chapter, we return to this system and study its structure in greater depth, along

with further low energy electron diffraction (LEED) experiments, as well as angle resolved photoemission spectroscopy (ARPES) experiments, again performed by the Menon group. Importantly, we have now performed DFT calculations to investigate this system. The LEED data is interpreted by structural studies using DFT. The electronic structure of the system is measured using ARPES, and computed using DFT.

In the present chapter, we have systematically studied the evolution of the structural and electronic properties of ordered Sn-Ag substitutional surface alloys, upon deposition on the Ag(001) surface of Sn atoms up to a monolayer coverage. With some hints of possible unit cells from the LEED experiments, we have considered several possible structures (including, but not limited to, surface alloys) for the Sn/Ag(001) system for different Sn coverages x for our first-principles DFT calculations.

3.2 Summary of experiments

Our experimental collaborators in the group of Prof. Krishnakumar S. R. Menon, Surface Physics and Materials Science Division, SINP, Kolkata have performed low energy electron diffraction (LEED) and angle-resolved photoemission spectroscopy (ARPES) experiments for clean Ag(001) surface and for the systems of Sn deposited on the Ag(001) surface. LEED gives the reciprocal space image of a surface structure. In the LEED experiments, a beam of electrons (typical energy 20 – 200 eV having wavelengths 2.7 Å – 0.87 Å) is incident on a single crystal sample having well-defined surface structure. The electrons get scattered elastically by the surface atoms and by looking at the diffraction spots one gets information on the size and symmetry of the surface unit cell, along with the size, symmetry and rotational alignment of the adsorbate unit cell with respect to the surface unit cell (qualitative

analysis). One could also, in principle, get information about the exact atomic positions (quantitative analysis), though we have not carried out such an analysis. ARPES is an experimental technique which directly extracts the band structure of a crystalline solid. The most distinctive advantage of this technique is that it can measure the energies and wave vectors of electrons simultaneously. ARPES is a "photon in, electron out" process (similar to that occurring in the photoelectric effect). If a crystal is illuminated by light of appropriate frequency (such that the energy of these photons is greater than the work function of the material) the electrons inside the material get enough energy to escape its potential barrier and come out of the material. These electrons, called "photoelectrons", are then forced to bend in a circular trajectory using an electric field. The radius of the circular path taken by an electron depends on the initial kinetic energy of the electron, from which one can calculate the binding energy of the electron in a band. Also, the take-off angle with respect to the surface normal is directly related to the component of the electron momentum parallel to the surface of the sample. So, from the radius and take-off angle, we get information about the binding energy related to the energy and wavevector simultaneously.

A clean and well-ordered Ag(001) surface was prepared by repeated cycles of Ar⁺ ion sputtering (at 600 eV, 1 μ A) for 15 min, followed by annealing to 823 K for 30 min, until a sharp $p(1 \times 1)$ LEED pattern was observed. High purity Sn (99.999%) was deposited from a homemade resistive evaporator at a rate of 0.2 $\text{\AA}/\text{min}$ calibrated with a water-cooled quartz crystal thickness monitor. Here, coverage of 1 monolayer (ML) is defined as the atomic density in the topmost layer of the bulk-truncated Ag(001) surface, $\sim 2 \times 10^{19}$ atom/m². The ultrahigh vacuum (UHV) chamber base pressure was maintained at $\leq 2 \times 10^{-10}$ mbar during the Sn deposition. LEED measurements were performed using a four-grid LEED apparatus (OCI Vacuum Microengineering), to determine the crystalline quality of the deposited film, as

well as the crystallographic symmetry directions. A highly-sensitive Peltier-cooled 12-bit CCD camera was used to collect the LEED images.

ARPES measurements were performed in an analysis chamber with base pressure $\leq 8 \times 10^{-11}$ mbar attached to the growth chamber, using a VG SCIENTA-R4000WAL electron energy analyzer and a high-flux GAMMADATA VUV He lamp with VUV monochromator.⁴⁹ All the ARPES measurements were performed at room temperature (RT) using He I $_{\alpha}$ (21.2 eV) and He II $_{\alpha}$ (40.8 eV) resonance lines. The overall energy resolution of the analyzer, including thermal broadening at room temperature, near the Fermi energy E_F was 100 meV, while the angular resolution was set to 1° with an acceptance angle of $\pm 15^\circ$. The appearance of a sharp and intense Tamm-like surface state (SS) at the \bar{M} symmetry point in the ARPES measurements directly confirmed the cleanliness and surface ordering quality of the Ag(001) substrate.⁵⁰

3.3 Computational details

DFT calculations were performed using the Quantum ESPRESSO package.⁵¹ The Kohn-Sham wavefunctions and the corresponding charge densities were expanded in plane-wave basis sets having cutoffs of 45 Ry and 450 Ry, respectively. Exchange-correlation interactions were treated using the Perdew-Burke-Ernzerhof form of the Generalized Gradient Approximation (PBE-GGA).⁵² The interactions between valence electrons and ionic cores were described by ultrasoft pseudopotentials.⁵³

The clean Ag(001) surface was modeled using an eight-atomic-layer thick asymmetric slab having a (1×1) surface unit cell. For Sn/Ag(001) systems, we have considered a topmost Sn $_x$ Ag $_{1-x}$ alloy layer (or other possible structures as described in Section 5.3), deposited over a substrate consisting of either four Ag layers (when determining structures and energetics) or seven Ag layers (when computing band

structures).

The following coverages (x) of Sn were considered: 0.2, 0.25, 0.33, 0.4, 0.5, 0.6, 0.67, 0.714, 0.75, 0.8 and 1.0 (all in units of ML). In general, at a given x , more than one surface unit cell was considered; further, for a given x and surface unit cell, all possible pseudomorphic configurations of surface Ag and Sn atoms within the cell were studied. Details of the surface unit cells and configurations are given in the Supporting Information (SI). Periodic images along the z direction (normal to the surfaces of the slabs) were separated by a vacuum region of width ~ 16 Å, which sufficed to eliminate interactions between artificially periodic images. A ‘dipole correction’ was introduced to offset the artificial electric field originating from the asymmetric nature of the slab.⁵⁴ Except for atoms belonging to the bottommost two/three Ag layers (for energetics/band structure calculations), all atoms were allowed to relax using the Broyden-Fletcher-Goldfarb-Shanno (BFGS) algorithm⁵⁵, until all components of the forces on all atoms were less than 0.001 Ry/Bohr.

Brillouin zone sampling was done using a Monkhorst-Pack mesh⁵⁶ commensurate with a $36 \times 36 \times 1$ sampling of the primitive 1×1 surface cell of the Ag(001) substrate. We note that we found that such a relatively dense sampling was necessary in order to get converged values of ΔH , the enthalpy of mixing of the surface alloy. Convergence was aided by using Marzari-Vanderbilt cold smearing⁵⁷ with a width of 0.001 Ry.

When using a supercell, the computed band structure needs to be ‘unfolded’ from the supercell Brillouin zone (SCBZ) to the Brillouin zone of the surface primitive cell (PCBZ), to enable a direct comparison of experimentally measured and theoretically computed band structures.⁵⁸ Further details of the band unfolding procedure can be found in a previous publication,³ and are also described further below.

The bulk lattice constant of Ag is calculated to be 4.16 Å. This value is in good agreement with previously reported theoretical values^{3;59} and with the experimental value of 4.09 Å.⁶⁰ This leads to an in-plane lattice constant on the Ag(001) surface

of $4.16/\sqrt{2} = 2.94$ Å, and a metallic radius of 1.47 Å. The bulk lattice constant of Sn (in the α -Sn structure) is found to be 6.66 Å, leading to $r_m = 1.44$ Å. We will use these these theoretically computed values of r_m in discussions further below. Note that this leads to a theoretically computed lattice mismatch of 2.04%, compared to the experimental lattice mismatch of 2.78%.

In order to understand the nature of bonding at overlayer-substrate interfaces and the charge redistribution upon forming the interface, we examine the charge redistribution $\Delta\rho$, where

$$\Delta\rho = \rho[\text{Ovr}/\text{Ag}(001)] - \rho[\text{Ovr}] - \rho[\text{Ag}(001)]. \quad (3.1)$$

Here, the first term on the right-hand-side of the equation is the charge density of the system consisting of the overlayer on Ag(001), and the second and third terms are the charge densities of the overlayer alone and the clean Ag(001) surface slab, respectively (all calculated at the relaxed geometries of the combined system). We also calculated the corresponding planar-averaged charge density difference $\Delta\rho_{\text{avg}}(z)$, given by

$$\Delta\rho_{\text{avg}}(z) = \int dx dy \Delta\rho(x, y, z). \quad (3.2)$$

3.3.1 Unfolding and projection of band structure

The energy bands calculated theoretically by DFT differ from ARPES data in three aspects:⁶¹

(i) For a band structure calculation corresponding to a supercell, bands are *folded* into the supercell Brillouin zone (SCBZ) while the ARPES measurements always span over the primitive cell Brillouin zone (PCBZ).

(ii) DFT calculations usually provide the electronic energy dispersion $E(\mathbf{k})$. ARPES spectra are related to the spectral function $S(\mathbf{k}, \epsilon)$ which is reduced to $E(\mathbf{k})$ only within the picture of the single particle Green's function.

(iii) The DFT calculated bands consist of all electronic states of the slab under computation including contributions from surface layers and deep bulk layers. By contrast, ARPES is a surface sensitive technique and hence probes only the electronic states near the surface.

So we need to unfold the theoretically calculated band structure from the SCBZ corresponding to the $p(2 \times 2)$ supercell in real space to the PCBZ corresponding to the $p(1 \times 1)$ primitive cell in real space for direct comparison between experiment and theory. The theoretical formulation used for such an unfolding of bands has previously been given in Refs. 58;62;63. Here we present a summary of these for the calculation of projection and unfolding of band structure in a plane wave basis set DFT formulation.

Suppose \mathbf{k} and \mathbf{K} are the wave vectors in the PCBZ [of two-dimensional (2D) area Ω_{PCBZ}] and SCBZ (of 2D area Ω_{SCBZ}) respectively. Clearly $\{\mathbf{K}\} \subset \{\mathbf{k}\}$. There are $N_{\mathbf{K}}$ number of reciprocal lattice vectors \mathbf{G}^{SCBZ} corresponding to the $p(2 \times 2)$ cell, which satisfy the following equation:⁶⁴

$$\mathbf{k}_i = \mathbf{K} + \mathbf{G}_i^{SCBZ}, \quad i = 1, 2, \dots, N_{\mathbf{K}}, \quad (3.3)$$

where \mathbf{k}_i is any wave vector in the PCBZ and $N_{\mathbf{K}} = \Omega_{PCBZ}/\Omega_{SCBZ}$

Now, by solving the Kohn-Sham (KS) equations self-consistently using a supercell, we obtain single-particle KS wave functions for the supercell $|\psi_{\mathbf{K}, m}^{SC}\rangle$. Expanding these in a plane wave basis set,

$$|\psi_{\mathbf{K}, m}^{SC}\rangle = \sum_{\{\mathbf{G}^{SCBZ}\}} c_{\mathbf{K}-\mathbf{G}^{SCBZ}, m} |\mathbf{K} - \mathbf{G}^{SCBZ}\rangle, \quad (3.4)$$

where m is a band index, $|\mathbf{K} - \mathbf{G}^{SCBZ}\rangle$ are the plane wave basis functions and $c_{\mathbf{K} - \mathbf{G}^{SCBZ}, m}$ are the plane wave expansion coefficients. In a similar way, the KS wave functions corresponding to the primitive cell $|\psi_{\mathbf{k}, \nu}^{PC}\rangle$ can be written as:

$$|\psi_{\mathbf{k}, \nu}^{PC}\rangle = \sum_{\{\mathbf{G}^{PCBZ}\}} c_{\mathbf{k} - \mathbf{G}^{PCBZ}, \nu} |\mathbf{k} - \mathbf{G}^{PCBZ}\rangle, \quad (3.5)$$

where ν is the band index in the primitive cell. Note that the set of reciprocal lattice vectors $\{\mathbf{G}^{PCBZ}\}$ is a subset of $\{\mathbf{G}^{SCBZ}\}$. Thus Eq. 3.5 can be decomposed as:

$$|\psi_{\mathbf{K}, m}^{SC}\rangle = \sum_{\{\mathbf{G}^{PCBZ}\}} c_{\mathbf{K} - \mathbf{G}^{PCBZ}, m} |\mathbf{K} - \mathbf{G}^{PCBZ}\rangle + \sum_{\{\mathbf{G}^{SCBZ}\} \neq \{\mathbf{G}^{PCBZ}\}} c_{\mathbf{K} - \mathbf{G}^{SCBZ}, m} |\mathbf{K} - \mathbf{G}^{SCBZ}\rangle. \quad (3.6)$$

To obtain the set of reciprocal lattice vectors $\{\mathbf{G}^{PCBZ}\}$ from the set $\{\mathbf{G}^{SCBZ}\}$ we have the following condition:

$$\mathbf{G}^{SCBZ} \cdot \mathbf{R} = 2\pi M, \quad \forall \{\mathbf{G}^{SCBZ}\}, \quad (3.7)$$

where M is an integer and \mathbf{R} is a Bravais lattice vector of the chemical structure corresponding to the primitive cell in real space. Eq. 3.7 gives nonzero contributions only if $\mathbf{G}^{SCBZ} \in \{\mathbf{G}^{PCBZ}\}$.

Now we define a quantity, the *spectral weight* $S_{\mathbf{K}, m}(\mathbf{k})$, which is the probability of supercell KS states having the same character as primitive cell KS states:⁶⁴

$$S_{\mathbf{K}, m}(\mathbf{k}) = \sum_{\nu} |\langle \psi_{\mathbf{K}, m}^{SC} | \psi_{\mathbf{k}, \nu}^{PC} \rangle|^2. \quad (3.8)$$

Since ARPES always probes the band structure in the PCBZ, we need to calculate the band dispersion in the PCBZ only. So we can ignore the second term on

the right hand side of Eq. 3.6, and using Eqs. 3.5 and 3.6 we get,

$$S_{\mathbf{k}, m}(\mathbf{k}) = \sum_{\{\mathbf{G}^{PCBZ}\}, \nu} |c_{\mathbf{k}-\mathbf{G}^{PCBZ}, m}|^4 \delta_{m\nu}. \quad (3.9)$$

Now, expanding $\psi_{\mathbf{k}, m}^{SC}$ in the basis of atomic orbitals,

$$\psi_{\mathbf{k}, m}^{SC} = \sum_q A_q \phi_q, \quad (3.10)$$

where $\{q\}$ is the set of good quantum numbers, ϕ_q is the atomic orbital corresponding to the state q and the A_q 's are the corresponding coefficients. The probability of $\psi_{\mathbf{k}, m}^{SC}$ having the same character as an orbital ϕ_q is:

$$|\langle \phi_q | \psi_{\mathbf{k}, m}^{SC} \rangle|^2 = |A_q|^2. \quad (3.11)$$

In all of our calculations, when carrying out such a projection, we have only considered atomic orbitals belonging to the top two surface layers. By projecting the supercell wave function ($\psi_{\mathbf{k}, m}^{SC}$) onto different atomic orbitals (ϕ_q) of a varying number of layers, we can control the surface sensitivity, i.e., the ability to probe bands arising from different layers, and can compare our computed band dispersion with ARPES probed band structure.

We have already mentioned that ARPES always probes bands in the PCBZ, which is possible after unfolding the band dispersion from the SCBZ to PCBZ. So, we have to calculate the probability of the primitive cell wave function having the same character as an atomic orbital ϕ_q i.e., *projected spectral weight* P , which we can write as:

$$P = |\langle \phi_q | \psi_{\mathbf{k}, \nu}^{PC} \rangle|^2 = |\langle \phi_q | \psi_{\mathbf{k}, m}^{SC} \rangle \langle \psi_{\mathbf{k}, m}^{SC} | \psi_{\mathbf{k}, \nu}^{PC} \rangle|^2 = |A_q|^2 S_{\mathbf{k}, \nu}(\mathbf{k}). \quad (3.12)$$

This P is an important quantity and is used to plot the amount of orbital projection in theoretically calculated band structures to compare with the ARPES data of Sn/Ag(001). Note that for the clean Ag(001) surface ($x = 0$) and 1 ML Sn/Ag(001) ($x = 1.0$), as no supercell is used for these systems, unfolding is not required. So P indicates only the projected band structures in these cases.

3.4 Systems under study

We have first modelled the clean Ag(001) surface having a $p(1 \times 1)$ surface unit cell. For Sn/Ag(001) systems, for $x = 0$ and $x = 1$, we have taken $p(1 \times 1)$ surface cells for our theoretical calculations. For $0 < x < 1$, we have considered different kinds of surface structures, with different possible surface supercells at each particular value of x to find out the most favourable geometry at the considered values of x . The following coverages (x) of Sn were considered: 0.2, 0.25, 0.33, 0.4, 0.5, 0.6, 0.67, 0.714, 0.75, 0.8 and 1.0 (all in units of ML). For energetics calculations we have considered an Ag(001) slab consisting of 4 Ag layers and for electronic structure calculations we have considered an Ag(001) slab consisting of 8 Ag layers.

3.5 Results and discussion

We asked the questions: (i) whether Sn atoms form an overlayer on the Ag(001) surface, or prefer to go subsurface, or form a surface alloy with the surface Ag atoms of the Ag(001) surface, (ii) what factors favour the formation of the lowest-energy structures? (iii) how the surface geometry changes with increasing Sn coverage on Ag(001) surface, and (iv) what is the electronic structure of Ag(001) surface, how is it modified upon Sn deposition and also what is the evolution of electronic structure with Sn coverage?

We first look into the energetics and structural properties of Sn/Ag(001) systems at different Sn coverages x . We first try to find the most favourable surface structures at each x considered, among different types of atomic arrangements and different supercells. We compare these results with the LEED experiment. Next we make some insights from electronic structures for the stable surface geometries of Sn/Ag(001). We compare our results with measured ARPES data.

3.5.1 Surface structure as a function of Sn coverage: results from LEED

During the deposition of Sn atoms on Ag(001) surface at room temperature (RT), our experimental collaborators have found some ordered surface superstructures as the Sn coverage x changes [see Figs. 3.1(a)-(f)]. In some places we will use the term coverage in ML unit and in some places we will use the term concentration x ; they are basically the same. The $p(1 \times 1)$ LEED pattern of the clean Ag(001) surface [Fig. 3.1(a)] changes, upon increasing the Sn coverage, to a $p(2 \times 2)$ pattern [Fig. 3.1(b)] at nearly 0.25 ML ($x = 0.25$) Sn coverage. This pattern is observed up to ~ 0.4 ML, but its intensity gradually decreases with increasing Sn coverage. At 0.5 ML, a pattern corresponding to two orthogonal domains of a $p(1 \times 10)$ structure is observed [Fig. 3.1(c)], which changes to a $p(1 \times 5)$ twin domain pattern [Fig. 3.1(d)] at a coverage of 0.6 ML. At 0.75 ML, a complex $p(1 \times 6)$ pattern with fractional diffraction spots [Fig. 3.1(e)] is seen. Finally, at 1 ML coverage, the complex superstructure spots disappear, and a well ordered $p(1 \times 1)$ LEED pattern [Fig. 3.1(f)] is again seen, suggesting pseudomorphic growth of a Sn layer on the Ag(001) substrate.

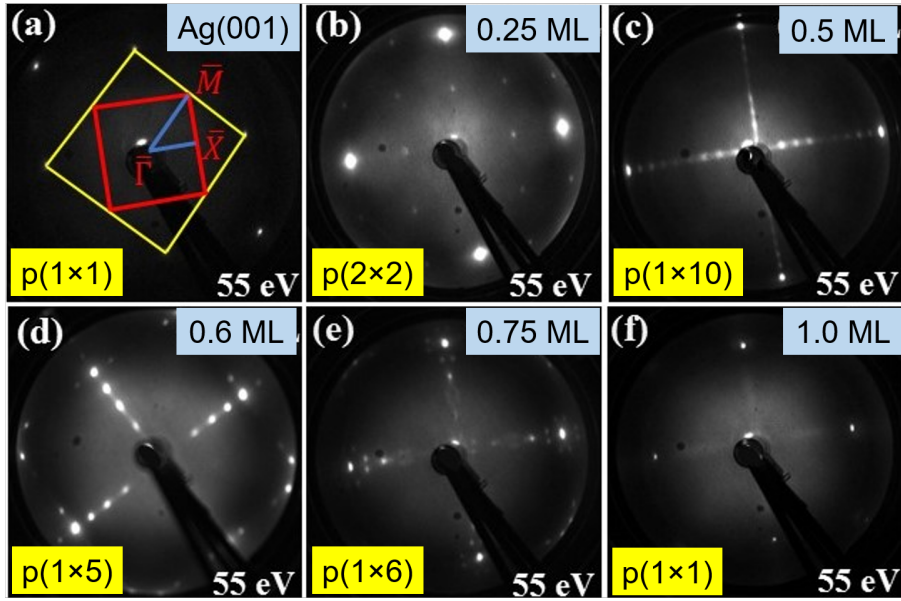


Figure 3.1: LEED patterns of Sn/Ag(001) for different Sn coverage. (a) Clean Ag(001) with primitive unit cell (yellow square) and (as an example) a $p(2 \times 2)$ surface Brillouin Zone (red square) with high symmetry points. (b) 0.25 ML, (c) 0.50 ML, (d) 0.6 ML, (e) 0.75 ML and (f) 1.0 ML. The energy of the incident electron beam is 55 eV. *This Fig. is originally part of Dr. Arunava Kar's (SPMS, SINP) Ph.D thesis and used with permission.*

3.5.2 Structure of Ag(001) and Sn/Ag(001): DFT results

In this subsection, we will first discuss the structure for $x = 0.0$ and $x = 1.0$ which corresponds to clean Ag(001) and 1 ML Sn/Ag(001) systems, respectively.

At first, as a benchmark, we check our results for the clean Ag(001) surface. The optimized lattice constant of bulk Ag having FCC crystal structure is found to be 4.16 Å in our calculations. So, while modelling the Ag(001) surface, the surface unit cell is square and the in-plane lattice constant is $4.16/\sqrt{2} = 2.94$ Å. We have also calculated the *percentage interlayer spacing* Δ_{ij} between the i^{th} and j^{th} layers, which is given by:

$$\Delta_{ij} = \frac{d_{ij} - d_B}{d_B} \times 100, \quad (3.13)$$

where d_{ij} is the separation between i^{th} and j^{th} layers upon relaxation and d_B is the

bulk separation between layers. We find that d_{12} is contracted with respect to d_B by -1.85% , and d_{23} and d_{34} are expanded by $+0.74\%$ and $+0.15\%$, respectively. These values are in good agreement with previous theoretical and experimental values.^{65;66} The calculated surface energy is 0.81 J/m^2 which is in excellent agreement with a previous theoretical value⁶⁵ of 0.78 J/m^2 and in reasonable agreement with an experimental value of 1.27 J/m^2 .³⁹ We further calculate the surface stress. The surface stress of clean Ag(001) is found to be -1.07 J/m^2 , where a minus sign corresponds to a tensile surface stress. This value falls in between two previously reported values in the literature.^{67;68}

We next consider the structure at full monolayer of Sn ($x = 1.0$) on Ag(001). We have considered four types of structures; three of them correspond overlayer adsorption of Sn atoms on the surface, with Sn atoms sitting at different sites, viz., hollow, atop and bridge. The fourth configuration is the sub-surface adsorption i.e., Sn monolayer is buried under an Ag layer, while maintaining the face centered cubic (fcc) stacking.

Adsorption geometry	E_{ads} (eV)	ΔE_{ads} (eV)
Atop site	-3.79	0.19
Bridge site	-3.91	0.07
Hollow site	-3.98	0.00
Subsurface adsorption	-3.52	0.46

Table 3.1: Energetics of different geometries considered for the 1 ML Sn/Ag(001), as obtained from DFT calculations. ΔE_{ads} denotes the energy of a given configuration with respect to the lowest energy configuration i.e., hollow site adsorption. The number in boldface indicates the highest value of adsorption energy, and hence corresponds to the most stable adsorption geometry.

We have shown the adsorption energy values for the above mentioned four configurations in Table 3.1. The *adsorption energy per adatom* is calculated using the following formula:

$$E_{ads} = \frac{1}{n} (E_{Sn/Ag(001)} - E_{Ag(001)} - nE_{Sn-atom}), \quad (3.14)$$

where $E_{Sn/Ag(001)}$ is the total energy from DFT of the Ag slab with Sn atoms adsorbed on the surface, $E_{Ag(001)}$ is the total energy of the clean Ag(001) substrate, $E_{Sn-atom}$ is the total energy of isolated Sn atom and n is the number of Sn atoms in the unit cell of the Sn/Ag(001) system.

DFT energetics calculations show (see Tab. 3.1) Sn atoms like to sit at the hollow sites on the surface over any other sites. This result is expected and can be explained in terms of surface energies. We note that the surface energy of Sn(001) [experimental value³⁸ = 0.709 J/m² and theoretical value⁶⁹ = 0.611 J/m²] is much lower than that of Ag(001) [experimental value^{38;39} = 1.24 J/m², 1.27 J/m² and theoretical value⁶⁵ = 0.78 J/m²]. This indicates that it is unfavourable for Sn atoms to get buried sub-surface under an Ag layer.

Next we attempt to calculate the effective "sizes" of the Sn and Ag atoms on Ag(001), using three different methods:

Method 1 for Estimating Sizes of Ag and Sn Atoms on Ag(001): Looking at Surface Stress

As noted above, if we consider bulk metallic radii, there is a very small size mismatch between Ag and Sn atoms, with the latter being slightly smaller. However, the effective sizes of surface Sn and Ag atoms that are deposited on an Ag(001) substrate may be expected to be different from these values. We can get an idea of this by examining the surface stress of the Ag(001) and Sn/Ag(001) systems. We find that the computed surface stress on the relaxed Sn/Ag(001) system is +2.42 J/m². This may be compared to the value of -1.07 J/m² obtained on the Ag(001) system.

The results for surface stress presented above suggest that the effective diameter

of surface Ag atoms on the Ag(001) surface is less than 2.94 Å (which is an expected result); however, the effective diameter of the surface Sn atoms on the Sn/Ag(001) system is *larger* than 2.94 Å (since this system has a compressive surface stress). This latter finding may initially seem like a surprising and counter-intuitive result. However, this result can be justified using a relatively simple explanation. The basic idea is similar to that of effective medium theory or the embedded atom method,⁷⁰ i.e., that a metal atom in its bulk structure is sitting at an optimal electron density from its neighbors; when the number of neighbors is changed, the atom would ideally like to change the geometry so as to regain this optimal value of ambient electron density. Let us first consider the case of Ag(001). Ag atoms in the bulk have a (nominal) coordination number (CN) of 12, whereas a surface Ag atom has a CN of 8. To compensate for the reduced coordination (and hence reduction in electron density), a surface Ag atom would like, in principle, to come closer to its neighbors, i.e., its effective size is reduced at the surface relative to the bulk. However, the situation is quite different for Sn atoms in the Sn/Ag(001) system. A Sn atom in the bulk has a CN of either 4 (in α -Sn) or 6 (in β -Sn). When a pseudomorphic Sn overlayer is deposited on Ag(001), the Sn atoms in the overlayer now have a CN of 8. Thus, to compensate for the increase in CN (and hence increase in electron density), the Sn atoms would ideally like to increase their separation from neighboring atoms, i.e., the effective size of the Sn atoms is increased. Further below, we will quantify this argument by moving from the nominal CN to the effective coordination number (ECN).

Above, we have qualitatively determined that on the Ag(001) surface, Ag (Sn) atoms have sizes that are smaller (larger) than Ag bulk atoms. While it is possible to quantify this result by computing the surface stress as a function of lattice constant,³⁷ the procedure is rather tedious, and involves various other approximations. Below, we therefore will use two other approaches to numerically estimate the sizes

of surface Sn and Ag atoms.

Method 2 for Estimating Sizes of Ag and Sn Atoms on Ag(001): Looking at Interlayer Relaxations

The conclusions of the previous paragraph can be supported and also further quantified by examining the geometries of the Ag(001) and Sn/Ag(001) systems. As already mentioned above, for Ag(001), the first interlayer spacing d_{12} is *contracted* by 1.85% with respect to d_B , the bulk interlayer spacing in Ag(001) (the value of d_{12} is 2.04 Å, while the value of d_B is 2.08 Å). This confirms that surface Ag atoms are smaller in size than bulk Ag atoms. However, for Sn/Ag(001), d_{12} is hugely *expanded* by 12.91% (the value of d_{12} is 2.35 Å while the value of d_B is 2.08 Å). This confirms that the surface Sn atoms [when deposited on Ag(001)] are larger in size than bulk Ag atoms, and hence also larger than both surface Ag atoms and bulk Sn atoms. On feeding these data into a simple hard-sphere model, where we assume that Ag atoms everywhere except in the topmost layer have a radius = $r_b^{\text{Ag}} = 1.47$ Å, we obtain $r_s^{\text{Ag}} = 1.44$ Å and $r_s^{\text{Sn}} = 1.71$ Å, where r_s^{Ag} is the radius of an atom in the surface layer of Ag(001), and r_s^{Sn} is the radius of an atom in a Sn overlayer on Ag(001). Once again, we see that $r_s^{\text{Ag}} < r_b^{\text{Ag}} < r_s^{\text{Sn}}$.

Method 3 for Estimating Sizes of Ag and Sn Atoms on Ag(001): Looking at Effective Coordination Number (ECN)

We now use a third method to gauge the sizes of Sn and Ag atoms at the surface, where we will put on a firmer footing the arguments stated above regarding number of neighbors, expanding them to account for the fact that not just the number of neighboring atoms, but also their chemical species, is changed. We define the effective coordination number (ECN) n_e^i of an atom i in a given system, as:^{71;72}

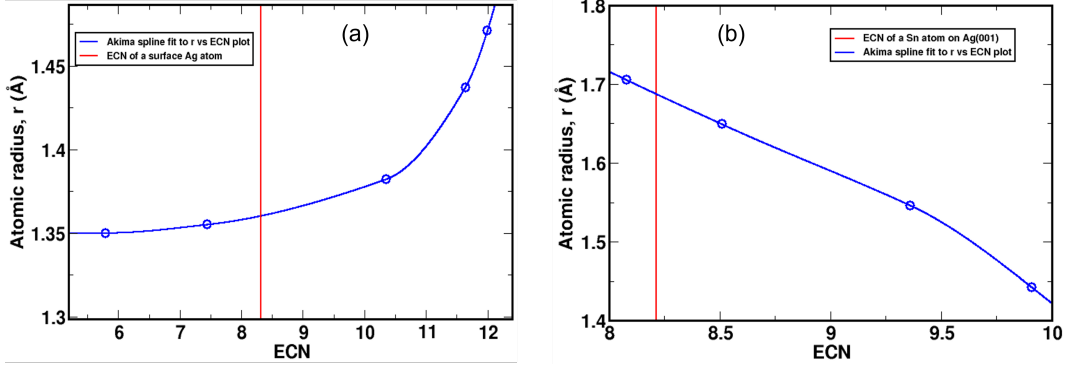


Figure 3.2: Plot of atomic radius vs effective coordination number (ECN) for (a) Ag atom and (b) for Sn atom. We have considered sc, bcc, fcc and diamond structures of Ag and Sn atoms. The blue lines are the cubic spline fitted curves. The red vertical lines are drawn at ECN values of a surface Ag atom (8.3148) and a Sn atom on Ag(001) (8.2132). The intersection of this vertical red line and blue curves gives the atomic radius of a surface Ag atom (1.360 Å) and a Sn atom on Ag(001) (1.687 Å).

$$n_e^i = \frac{\sum_j \rho_j^{at(j)}(R_{ij})}{\rho^{at(i)}(R_{\text{bulk}})}, \quad (3.15)$$

where the sum runs over all neighbors j of the i th atom. Here, $\rho_j^{at(j)}(R)$ is the charge density of an isolated atom, of species j , at a distance R away from the nucleus. R_{bulk} is the nearest-neighbor distance for the bulk of the element corresponding to the i th atom, and R_{ij} is the distance separating the atoms i and j in the system under consideration. Note that when this expression is computed for the bulk systems (either Ag in the FCC structure or Sn in the α -Sn diamond structure), Eq. (3.15) will return values of 12 and 4, respectively. However, for a different system, if, e.g., the ambient electron density at the site of an Ag (Sn) atom is less than in the corresponding bulk, we will get a value less than 12 (4), etc. The advantage of the ECN over the usual definition of coordination number (where one just counts the number of nearest-neighbor atoms) is that it accounts not just for how many neighbors an atom has, but how far away they are, and what element they are.

We next calculate how the atomic size changes with ECN. To do this, we consider

the following three-dimensional (hypothetical) periodic structures: simple cubic, body centered cubic, diamond, and face centered cubic. In each of these structures, we optimize the lattice constant for both Ag and Sn, and compute the corresponding values of ECN. Note that to do this, while evaluating Eq. (3.15), we use values of R_{bulk} corresponding to FCC for Ag and diamond structure for Sn.

Fig. 3.2 shows how the atomic size changes with ECN for (a) Ag and (b) Sn. It is extremely interesting to note that the shape of the two curves is markedly different, with the atomic size increasing with ECN for Ag, but (counter-intuitively) decreasing with ECN for Sn. Indeed, for Sn, as we go from the diamond structure to the FCC structure, the ECN actually decreases, emphasizing that the information contained in the ECN is quite different from that contained in the nominal coordination number. However, the fact that the nearest-neighbor distance is larger in the FCC than in the diamond structure still holds.

The vertical red lines in Figs. 3.2 (a) and (b) are drawn at values of ECN corresponding to those of a surface atom on Ag(001) and Sn/Ag(001) respectively, i.e., 8.31 and 8.21, respectively. By reading the corresponding values of ordinate, we obtain $r_s^{\text{Ag}} = 1.36 \text{ \AA}$ and $r_s^{\text{Sn}} = 1.69 \text{ \AA}$. Once again, we obtain $r_s^{\text{Ag}} < r_B^{\text{Ag}} < r_s^{\text{Sn}}$.

3.5.3 Evolution of structure and stability as a function of Sn coverage: DFT results

Next, we consider intermediate Sn coverages, that is, $0 < x < 1$.

In general, we consider five kinds of structures [see Fig. 3.3]:

(a) Structures where the deposited Sn atoms form a Sn-Ag pseudomorphic surface alloy overlayer $\text{Sn}_x\text{Ag}_{1-x}$ on the Ag(001) substrate. For a schematic depiction, see Fig. 3.3(a).

(b) Structures where the deposited Sn atoms form an ordered array of adatoms

with coverage x on the Ag(001) substrate. For a schematic depiction, see Fig. 3.3(b).

(c) Structures where a non-pseudomorphic array of Sn adatoms sits atop a monolayer of pseudomorphic Sn-Ag surface alloy below which there is the Ag(001) substrate. For a schematic depiction, see Fig. 3.3(c)]. This is consistent with our conclusion, in the previous subsection, that Sn atoms deposited on Ag(001) have an effective size that is larger than that of Ag atoms.

(d) Structures consisting of a non-pseudomorphic surface alloy with a lower density of surface atoms than is found on Ag(001). For an example, see the schematic figure in Fig. 3.3(d).

(e) Direct exchange configurations,⁷³ where the Ag atoms that have been replaced by substituting Sn atoms now sit as adatoms over the Sn-Ag surface alloy layer, occupying four-fold hollow sites [see Fig. 3.3(e)].

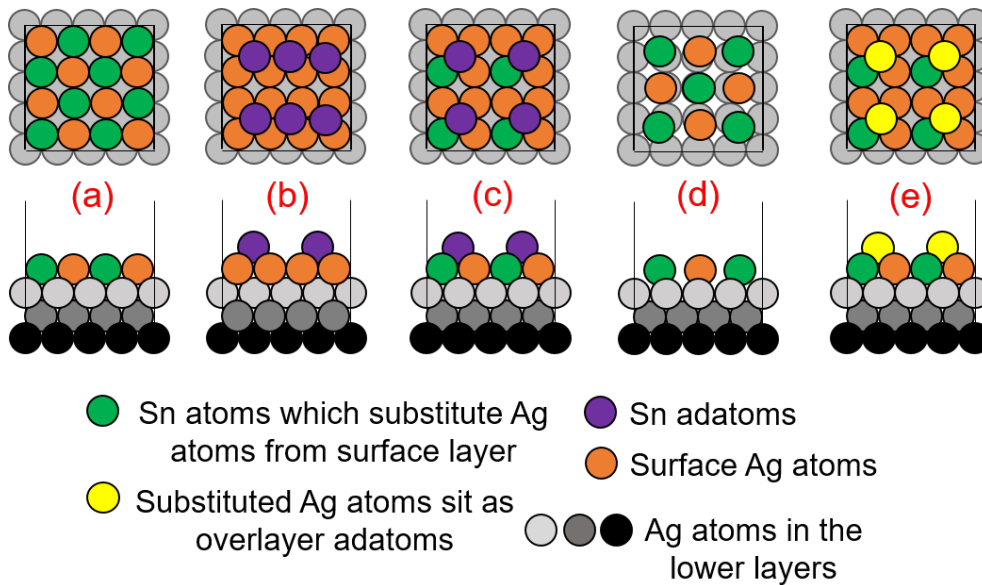


Figure 3.3: Schematic diagram of five different kinds of structures (top and side views) considered for theoretical calculations. (a) substitutional surface alloy $\text{Sn}_x\text{Ag}_{1-x}/\text{Ag}(001)$, (b) overlayer adsorption of Sn adatoms, (c) a few Sn atoms substitute Ag atoms from the surface layer and a few Sn atoms sit as adatoms, (d) non-pseudomorphic alloy structure in which the atomic density in the surface alloy layer is different from that in an Ag(001) layer, and (e) direct exchange: Sn atoms substitute some Ag atoms, and the substituted Ag atoms sit like overlayer adatoms.

To determine the most stable structure at each value of x considered, as well as to determine the values of x correspond to the phases that are stable against phase segregation, we calculate ΔH , the enthalpy of mixing. To normalize for the different surface supercells we get enthalpy of mixing per unit area. For the particular case of a pseudomorphic surface alloy $\text{Sn}_x\text{Ag}_{1-x}$ in the topmost layer [Case (a) above] this is computed as:

$$\begin{aligned} \frac{\Delta H}{A} = \frac{1}{A} \{ & [E[\text{Sn}_x\text{Ag}_{1-x}/\text{Ag}(001)] \\ & - xE[\text{Sn}/\text{Ag}(001)] - (1-x)E[\text{Ag}(001)] \}. \end{aligned} \quad (3.16)$$

Here, A is the area of the $(m \times n)$ cell used to compute all three total energy terms on the right-hand-side of the above equation; $E[\text{Sn}_x\text{Ag}_{1-x}/\text{Ag}(001)]$ is the total energy of the system with a $\text{Sn}_x\text{Ag}_{1-x}$ surface alloy on a l -layer $\text{Ag}(001)$ substrate, $E[\text{Sn}/\text{Ag}(001)]$ is the total energy of a system consisting of a Sn overlayer on a l -layer $\text{Ag}(001)$ substrate, and $E[\text{Ag}(001)]$ is the total energy of a $(l+1)$ -layer $\text{Ag}(001)$ surface slab; all these total energies are computed from DFT for the corresponding relaxed configurations.

For Case (b) above, where the deposited Sn atoms form an ordered array of adatoms with coverage x , ΔH is computed as:

$$\begin{aligned} \frac{\Delta H}{A} = \frac{1}{A} \{ & E[\text{Sn}_x/\text{Ag}(001)] \\ & - E[\text{Ag}(001)] - x \times (m \times n) \times \mu(\text{Sn}) \}. \end{aligned} \quad (3.17)$$

Here, $E[\text{Sn}_x/\text{Ag}(001)]$ is the total energy of a system consisting of adatoms of Sn, with coverage x , on a l -layer $\text{Ag}(001)$ substrate and $E[\text{Ag}(001)]$ is the total energy of a l -layer $\text{Ag}(001)$ surface slab. $\mu(\text{Sn})$ is the chemical potential of Sn, calculated as the energy of a Sn atom in the α -Sn bulk crystal. All other terms are as before.

For Case (c) above, where Sn adatoms of coverage z sit above a pseudomorphic $\text{Sn}_y\text{Ag}_{1-y}$ surface alloy which in turn is on an Ag(001) substrate, ΔH is given by:

$$\begin{aligned} \frac{\Delta H}{A} = \frac{1}{A} \{ & E[\text{Sn}_z/\text{Sn}_y\text{Ag}_{1-y}/\text{Ag}(001)] \\ & - yE[\text{Sn}/\text{Ag}(001)] - (1-y)E[\text{Ag}(001)] \\ & - z \times (m \times n) \times \mu(\text{Sn}) \}. \end{aligned} \quad (3.18)$$

Here, $E[\text{Sn}_z/\text{Sn}_y\text{Ag}_{1-y}/\text{Ag}(001)]$ is the total energy of a system consisting of Sn adatoms of coverage z sitting above a $\text{Sn}_y\text{Ag}_{1-y}$ surface alloy which in turn is on an l -layer Ag(001) substrate; we note that in this system, the total deposited coverage of Sn is $x = (y + z)$. $E[\text{Ag}(001)]$ is the total energy of an $(l + 1)$ -layer Ag(001) surface slab; all other terms are as before.

For Case(d) above, where the overlayer is comprised of a low density non-pseudomorphic surface alloy Sn_xAg_y , we have:

$$\begin{aligned} \frac{\Delta H}{A} = \frac{1}{A} \{ & E[\text{Sn}_x\text{Ag}_y/\text{Ag}(001)] \\ & + (1 - (x + y)) \times (m \times n) \times \mu(\text{Ag}) \\ & - xE[\text{Sn}/\text{Ag}(001)] - xE[\text{Ag}(001)] \}. \end{aligned} \quad (3.19)$$

Here, $E[\text{Sn}_x\text{Ag}_y/\text{Ag}(001)]$ is the total energy of a system consisting of a non-pseudomorphic Sn_xAg_y surface alloy on a l -layer Ag(001) substrate, the other terms are as before. We note that in this case, $(x + y) < 1$ as the density of atoms in the surface alloy layer is lower than the density of the clean Ag(001) surface layer. Some substituted Ag atoms, with coverage $[1 - (x + y)]$, are completely removed from the surface as the bigger Sn atoms take their space.

Finally, for Case (e) above, where Ag adatoms of coverage x sit above a pseudomorphic $\text{Sn}_x\text{Ag}_{1-x}$ surface alloy which in turn is on an Ag(001) substrate, ΔH is

given by:

$$\begin{aligned} \frac{\Delta H}{A} = \frac{1}{A} \{ & E[\text{Ag}_x/\text{Sn}_x\text{Ag}_{1-x}/\text{Ag}(001)] \\ & - xE[\text{Sn}/\text{Ag}(001)] - (1-x)E[\text{Ag}(001)] \\ & - x \times (m \times n) \times \mu(\text{Ag}) \}. \end{aligned} \quad (3.20)$$

Here $E[\text{Ag}_x/\text{Sn}_x\text{Ag}_{1-x}/\text{Ag}(001)]$ is the energy of a system where Sn atoms of coverage x have substituted Ag atoms in the surface layer, and these displaced Ag atoms now occupy adatom sites over the surface alloy layer, and $\mu(\text{Ag})$ is the chemical potential of Ag, defined as the energy of a bulk Ag atom; all other terms have been previously defined.

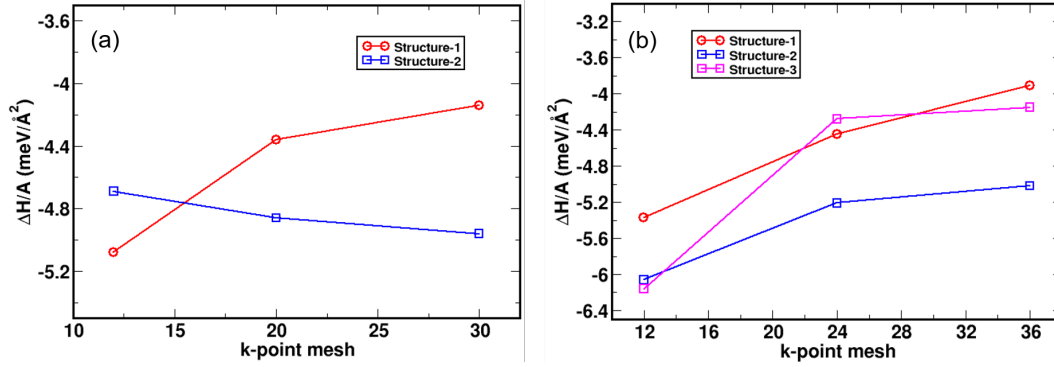


Figure 3.4: Convergence of $\Delta H/A$ with k-point mesh for $\text{Sn}_x\text{Ag}_{1-x}/\text{Ag}(001)$ systems at (a) $x = 0.6$ and (b) $x = 0.67$, for different possible structures as shown in Figs. 3.11 and 3.12, respectively. In these examples, the structures which were higher in energy at lower k-point density become lower in energy at higher k-point density. This demonstrates the highly sensitive dependence of the enthalpy of formation on the density of the k-point mesh. We see that the $\Delta H/A$ converges at very high k-point density like $36 \times 36 \times 1$ k-point mesh. So, to determine the lowest energy structures at each value of x , we had to consider a very dense k-point mesh.

Fig. 3.4 shows how the computed value of the enthalpy of formation depends on k-point density used, i.e., the density of the Brillouin zone sampling. For illustrative purposes, we have only shown the results for two different x -values of 0.6 and 0.67 in Fig. 3.4(a) and (b), respectively. Here we plot the enthalpy of formation per unit area, $\Delta H/A$, as a function of the k-point density, with the x -axis representing

equivalent number of k-points along each direction in the PCBZ. For Fig. 3.4(a) we have taken the structures shown in Fig. 3.11(a)-(b), with $x = 0.6$ in $p(1 \times 5)$ supercells. For Fig. 3.4(b) we have considered the structures shown in Fig. 3.12(b)-(d), with $x = 0.67$ in $p(1 \times 6)$ supercells. We see in both panels that structures having higher energy at lower k-point density become lower in energy at higher k-point density. This shows that the enthalpy of formation ΔH is very sensitive to the k-point density. This leads us to consider very high k-point density for all of the energetics calculations at all x -values for all structures.

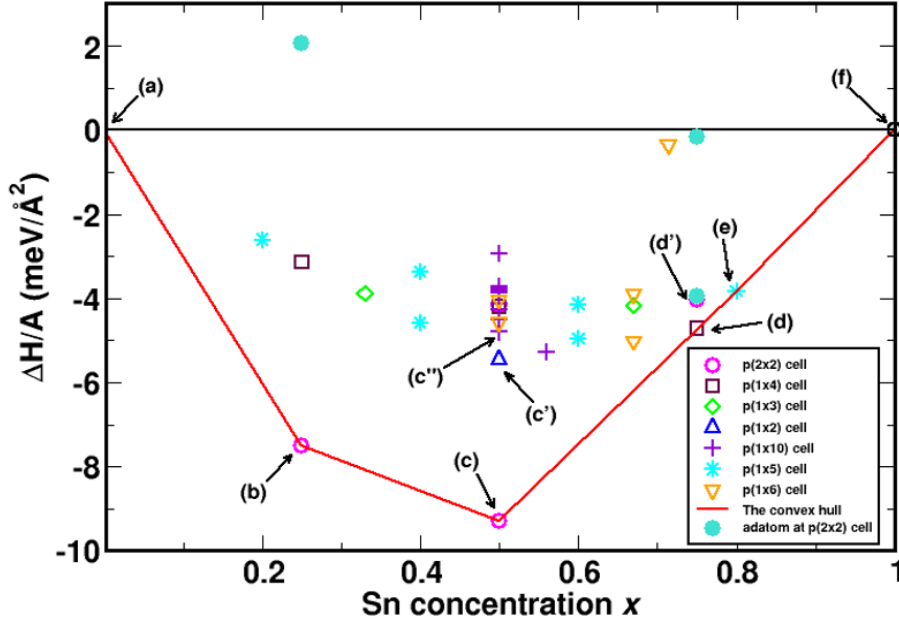


Figure 3.5: Enthalpy of formation per unit area, $\Delta H/A$ as a function of Sn coverage x . Different colors of the data points correspond to different surface supercells used in our DFT calculations, as shown in the inset. The red lines show the convex hull drawn through the data. The arrow symbols represent surface alloy structures of Fig. 3.6.

We want to mention one important thing here: that in evaluating Eqs. (3.16) - (3.20), very dense k-points grids have been used in the DFT calculations, to make sure that the results are converged with respect to Brillouin zone sampling; this point has already been discussed above. We have also used the same (or equivalent) grids for all systems on the right-hand-sides of these equations, to maximize the

likelihood of k-point errors cancelling out.

In Fig. 3.5 we plot our results, from DFT calculations, for the enthalpy of mixing, $\Delta H/A$, versus the Sn coverage x . When $\Delta H/A$ is positive, this means that these structures are energetically unfavorable with respect to clean Ag(100) and 1 ML of Sn on Ag(100), the system will phase segregate into these two phases, instead of forming the mixed phase. At each value of x , the lowest-lying point indicates the most stable configuration, for that coverage, among the structures examined by us. The different colors of the different data points in this graph correspond to different surface supercells used in our calculations as mentioned in the inset. The red line is the convex hull obtained from this data; the configurations which fall on this convex hull are the phases and structures that are stable against phase segregation to other mixed phases. We found that many structures of type (b) have a very high positive value of $\Delta H/A$; these points are not plotted in Fig. 3.5. We also note that in general, for a given x , among the above described structures, structures of types (b), (c), (d) and (e) tend to lie much higher in energy than structures of type (a).

Fig. 3.6 shows top views of the structures found to lie on the convex hull, as well as a few other low-energy structures of interest. At $x = 0.0$ and $x = 1.0$, the favored configurations correspond to a pseudomorphic monolayer of Ag and Sn atoms, respectively.

At intermediate values of x , the following configurations are found to fall on the convex hull. We will discuss them in order of increasing values of x :

(i) At $x = 0.25$, a $p(2 \times 2)$ structure, in which one out of four surface Ag atoms is substituted by a Sn atom to form a structure of type (a). This agrees with the LEED result that upon increasing coverage from $x = 0$, the first pattern seen corresponds to $p(2 \times 2)$, at $x = 0.25$. The structure of this configuration (top view) is shown in Fig. 3.6(b). In this configuration, Sn atoms in the surface layer get eight-fold coordination - four from the in-plane layer and four from the layer below. This is

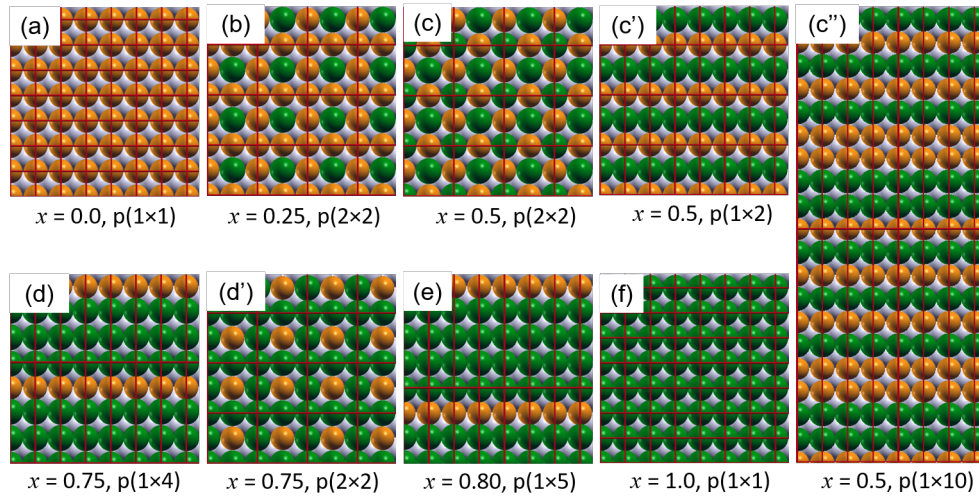


Figure 3.6: Surface alloy structures (top-views) predicted by DFT calculations and LEED measurements at different Sn coverages x . (a), (b), (c), (d), (e) and (f) are the structures which fall on the convex hull. (c') and (c'') are the 2nd and 3rd lowest energy structure respectively, at $x = 0.5$. c' is seen in the LEED pattern. (d') is the 2nd lowest energy structure at $x = 0.75$, which we have used when computing the band structure. Color code: Green - Sn atoms, Orange - surface Ag atoms and Gray - subsurface Ag atoms.

energetically more favorable than Sn atoms occupying four-fold coordinated hollow adatom sites. The value of the surface stress of this structure is -0.90 J/m^2 , which is in between the values at $x = 0.0$ and $x = 1.0$. This configuration is similar to that seen earlier for Sn/Ni(001)^{74;75} and Sn/Cu(001).^{76;77}

(ii) At $x = 0.5$, a $p(2 \times 2)$ configuration, in which out of four surface Ag atoms, two Ag atoms are substituted by two Sn atoms. Two diagonal surface Ag atoms are substituted in this case. This is again type (a). The structure of this is shown in Fig. 3.6(c). This partly agrees with LEED, in that the next stable pattern is indeed observed at $x = 0.5$. However, experiments observed a $p(1 \times 10)$ pattern. The configurations considered by us include all possible configurations with $x = 0.5$ and a $p(1 \times 10)$ unit cell; however, our calculations find that all of these lie somewhat higher in energy (by $> 4 \text{ meV/\AA}^2$) than the $p(2 \times 2)$ configuration. After the $p(2 \times 2)$ structure, the two lowest-lying structures are the $p(1 \times 2)$ configuration shown in

Fig. 3.6(c') and one of the $p(1 \times 10)$ configurations shown in Fig. 3.6(c'').

(iii) At $x = 0.75$, a $p(1 \times 4)$ configuration, in which three out of four surface Ag atoms are substituted by three Sn atoms. This is again type (a). This configuration is shown in Fig. 3.6(d). However, almost degenerate with this (lying higher in energy by $< 1 \text{ meV}/\text{\AA}^2$), DFT also predicts two $p(2 \times 2)$ configurations: one is a surface alloy structure of type (a), shown in Fig. 3.6(d'), and the other is a structure of type (c). LEED observed an ordered superstructure around $x = 0.75$, but with a $p(1 \times 6)$ pattern. We note that it is not possible to have a pseudomorphic configuration with $x = 0.75$ and a $p(1 \times 6)$ unit cell. However, we can consider structures having $p(1 \times 6)$ unit cells at some values of x which are close to 0.75. In particular, we can have such pseudomorphic configurations at $x = 0.67$ with $p(1 \times 6)$ unit cells, the lowest energy structures among these is found to lie only slightly above the convex hull, and may correspond to the structure seen in LEED experiments at around 0.75 ML. We have also considered some non-pseudomorphic structures. For example, a non-pseudomorphic Sn-Ag surface alloy structure at $x = 0.714$ with a $p(1 \times 6)$ unit cell which contains seven atoms (five Sn atoms and two Ag atoms) in the surface layer instead of the ideal six atoms per layer. After relaxation, we found that one Sn adatom sits on top of a pseudomorphic (i.e., total six atoms in the surface layer) surface alloy with four Sn atoms and two Ag atoms in the $p(1 \times 6)$ unit cell. This structure lies very high in energy. One Sn atom sits as an adatom because we know that size of the Sn atoms is larger on the surface. This also implies that the size of the Sn atoms on Ag(001) is larger than the size of the surface Ag atoms.

(iv) Finally, our calculations predict one stable structure that is not clearly observed in the LEED experiment: a $p(1 \times 5)$ structure at $x = 0.8$; this is shown in Fig. 3.6(e). However, it only just lies on the straight line connecting the points at $x = 0.75$ and $x = 1.0$.

We also note that in addition to the structures mentioned above, a $p(1 \times 5)$

structure at $x = 0.6$ is observed in the LEED experiment; our calculations find that the lowest energy such structure lies above the convex hull by ~ 1.5 meV/Å².

Now we show the other structures we have considered in our DFT energetics calculations, in Fig. 3.7–3.13. These structures are not the lowest energy structures at each x -values and hence not falling on the convex hull.

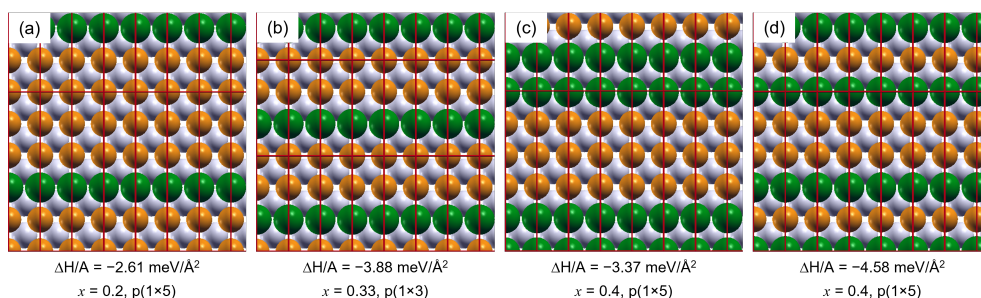


Figure 3.7: Different structures considered at $x = 0.2, 0.33$, and 0.4 for energetics calculations. The Sn coverage and surface supercells along with the values of enthalpy of mixing $\Delta H/A$ are written below each figure. Atomic color code: green - Sn, orange - surface Ag and gray - topmost layer of Ag substrate.

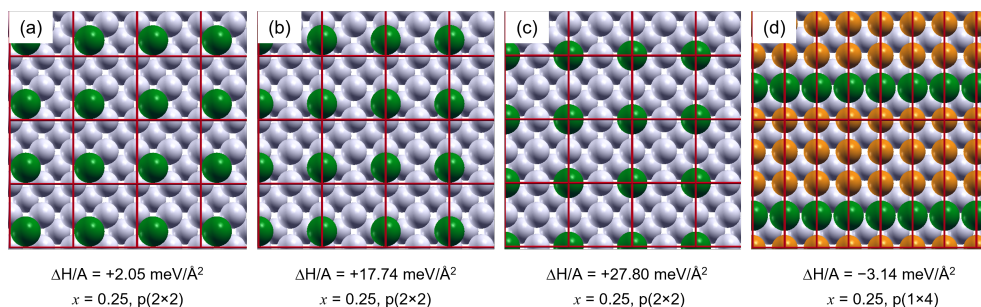


Figure 3.8: Different structures considered at $x = 0.25$ for energetics calculations. The Sn coverage and surface supercells along with the values of enthalpy of mixing $\Delta H/A$ are written below each figure. Atomic color code: green - Sn, orange - surface Ag and gray - topmost layer of Ag substrate.



Figure 3.9: Different structures considered at $x = 0.5$ having $p(1 \times 10)$ cells for energetics calculations. The Sn coverage and surface supercells along with the values of enthalpy of mixing $\Delta H/A$ are written below each figure. Atomic color code: green - Sn, orange - surface Ag and gray - topmost layer of Ag substrate.

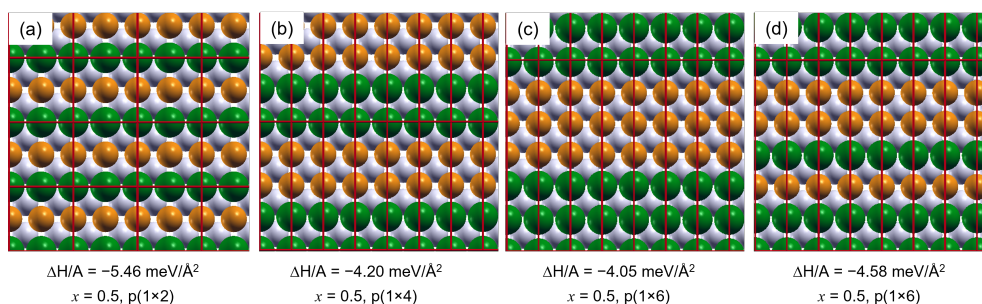


Figure 3.10: Different structures considered at $x = 0.5$ for energetics calculations. The Sn coverage and surface supercells along with the values of enthalpy of mixing $\Delta H/A$ are written below each figure. Atomic color code: green - Sn, orange - surface Ag and gray - topmost layer of Ag substrate.

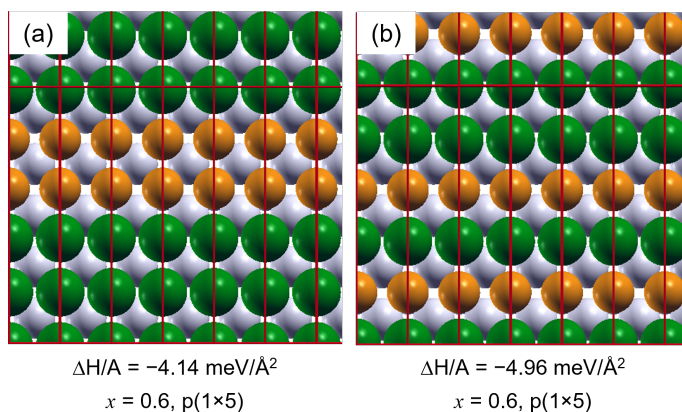


Figure 3.11: Different structures considered at $x = 0.6$ for energetics calculations. The Sn coverage and surface supercells along with the values of enthalpy of mixing $\Delta H/A$ are written below each figure. Atomic color code: green - Sn, orange - surface Ag and gray - topmost layer of Ag substrate.

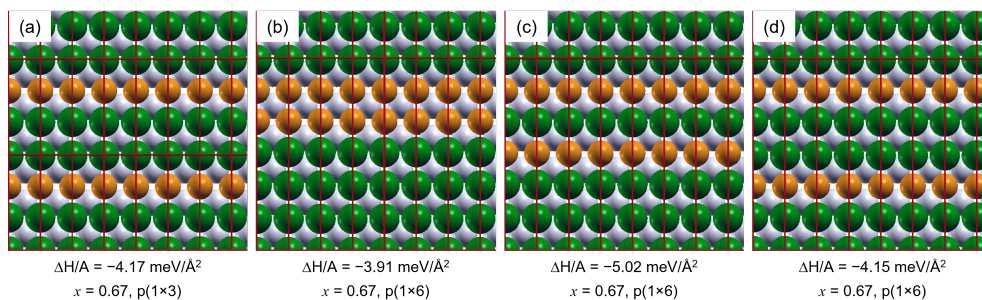


Figure 3.12: Different structures considered at $x = 0.67$ for energetics calculations. The Sn coverage and surface supercells along with the values of enthalpy of mixing $\Delta H/A$ are written below each figure. Atomic color code: green - Sn, orange - surface Ag and gray - topmost layer of Ag substrate.

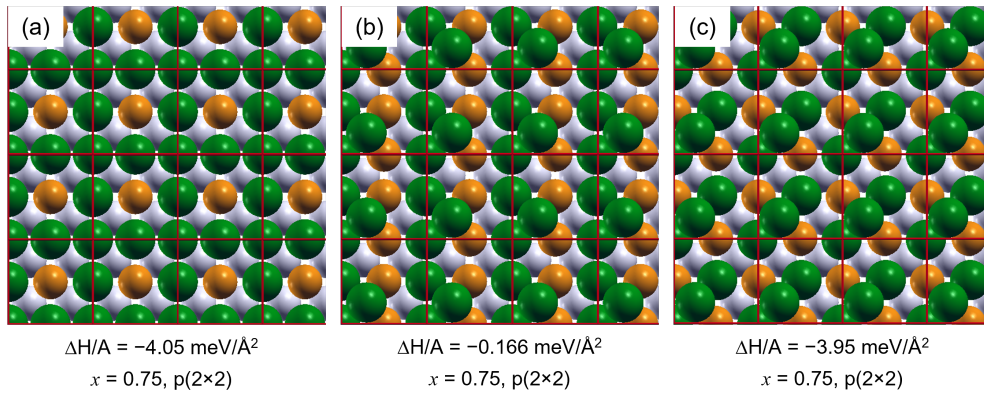


Figure 3.13: Different structures considered at $x = 0.75$ for energetics calculations. The Sn coverage and surface supercells along with the values of enthalpy of mixing $\Delta H/A$ are written below each figure. Atomic color code: green - Sn, orange - surface Ag and gray - topmost layer of Ag substrate.

For all Sn-Ag surface alloy phases, we see a significant buckling of surface atoms along the z -direction (normal to the surface). In all of these, the Sn atoms in the surface alloy layer are found to be raised higher than the Ag atoms in this layer; this is consistent with our earlier conclusion that on the Ag(001) surface, Sn atoms have a larger effective size than do Ag atoms. This is because when there is denser packing of atoms on the surface the bigger atoms will always move out of the layer to reduce the surface stress. Comparing the average z -coordinates of Sn atoms with respect to the average z -coordinates of Ag atoms in the surface layer, we see that, Sn atoms are found to be buckled outward; Sn atoms are sitting 2.72% higher for $x = 0.25$, 2.62% higher for $x = 0.5$ and 4.66% higher for $x = 0.75$.

We also calculate the value of Δ_{12} using Eq. 6.1 for $x = 0.25, 0.5$ and 0.75 . For cases where there is more than one atom per layer per unit cell, we take the average z -coordinates of the atoms in that layer, after relaxation. We see that d_{12} is expanded for all the Sn-Ag surface alloys (with respect to d_B for bulk Ag) and this expansion increases with the Sn coverage x as shown in Fig. 3.14. The corresponding values of d_{12} are 1.50%, 6.20% and 10.58% for $x = 0.25, 0.5$ and 0.75 , respectively, followed by the already mentioned value of 12.91% at $x = 1$. This further confirms

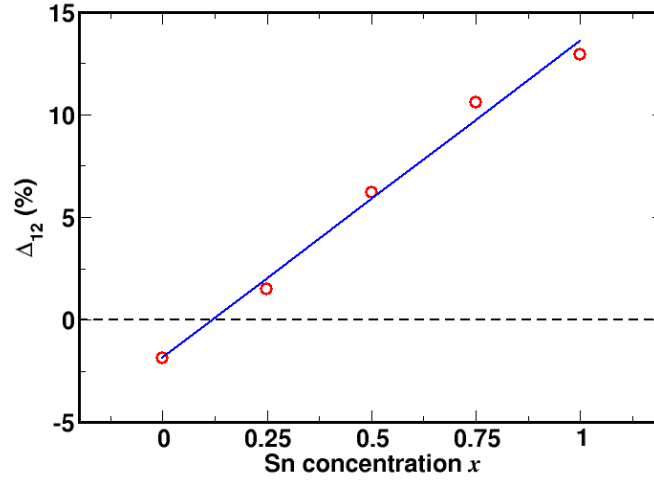


Figure 3.14: Variation of percentage interlayer relaxation for the top two layers with the Sn coverage x . The red circles are results from DFT optimization of the structures, and the blue line is a linear fit to the data. The black dashed line is the zero line of Δ_{12} .

that the *size* of the Sn atoms on the Ag(001) surface is *larger* than that of the Ag atoms.

Fig. 3.15 shows the surface stress as a function of the Sn concentration x . The surface stress σ_{XX}^{surf} is given by,

$$\sigma_{XX}^{surf} = \frac{\sigma_{XX}^{SC} \times L_z}{2}, \quad (3.21)$$

where σ_{XX}^{SC} is the XX component of the stress tensor of the corresponding slab supercell used for $x = 0.0, 0.25, 0.5, 0.75$ and 1.0 , and L_z is the length of the slab supercell along the z -direction, including vacuum. We note that calculations of surface stress were performed using symmetric slabs (with the surface alloy on both the top and bottom surfaces of the Ag slab), which is why we have to divide by 2. We have already mentioned that for clean Ag(001) ($x = 0.0$) and 1 ML Sn/Ag(001) ($x = 1.0$) $\sigma_{XX}^{surf} = -1.07 \text{ J/m}^2$ and $+2.42 \text{ J/m}^2$, respectively. For $x = 0.25, 0.5$ and 0.75 the calculated value of $\sigma_{XX}^{surf} = -0.90 \text{ J/m}^2, -0.64 \text{ J/m}^2$ and $+0.71 \text{ J/m}^2$,

respectively [see Fig. 3.15]. The value of σ_{XX}^{surf} increases as x increases. We see that the surface stress is negative for $x = 0.0, 0.25$ and 0.5 and positive for $x = 0.75$ and 1.0 . Here negative surface stress corresponds to the tensile surface stress and positive surface stress corresponds to the compressive surface stress. Initially at low Sn concentrations, though the Sn atoms become bigger on the surface, the overall surface stress is still tensile because of the greater number of smaller-sized Ag atoms in the surface layer. However, as x increases, the effect of the larger size of the Sn atoms starts to dominate and overcome the tensile surface stress effect caused by the smaller surface Ag atoms. That is why σ_{XX}^{surf} increases as x increases and finally becomes positive i.e., compressive at $x = 0.75$.

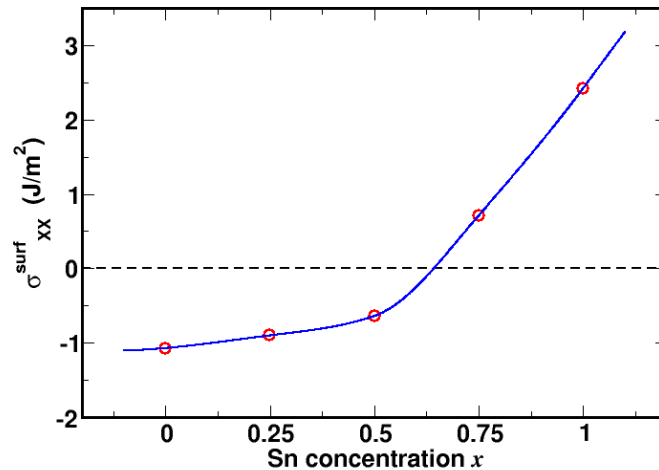


Figure 3.15: Variation of percentage surface stress σ_{XX}^{surf} with the Sn concentration x . The black dashed line is the zero line of σ_{XX}^{surf} .

To summarize and discuss the results in this section, we find that at all values of x , the lowest energy configuration corresponds to a pseudomorphic Sn-Ag surface alloy. The driving force for the formation of such a surface alloy is the relief of tensile stress on the Ag(001) surface, as has pointed out by Tersoff.⁹ As the Sn atoms become bigger on Ag(001), these bigger atoms get embedded into the surface

layer and relieve the tensile surface stress of the metal surface. Regarding the favored structures in the phase diagram, the agreement between theoretically and experimentally observed phases is reasonably good, but not perfect. There are some phases observed in experiment that lie slightly above the theoretically obtained convex hull. The most notable disagreement is at $x = 0.5$, where calculations predict a $p(2 \times 2)$ structure to be favored, but actually a $p(1 \times 10)$ structure is observed in the experiment. It is possible that these discrepancies (of the order of few meV/Å²) are due to DFT errors, though we have taken good care of the convergences. Another possible source of error may be due to the fact that the lattice mismatch in DFT is slightly different from that in experiment.

3.5.4 Electronic structure: DFT results and comparison with ARPES data

To obtain further insight into the electronic structure of the system, we used DFT to compute the electronic band structure for a few values of Sn coverage x . Fig. 3.16(a) shows the schematics of the PCBZ and SCBZ. The red square represents the PCBZ i.e., the BZ corresponding to the $p(1 \times 1)$ cell in real space, the cyan squares represent BZ corresponding to the $p(2 \times 2)$ cell in real space. The unprimed symbols are used for the high symmetry points of the PCBZ and primed symbols are used for the high symmetry points of the SCBZ corresponding to the $p(2 \times 2)$ cell. Fig. 3.16(b) shows the projected bulk band structure of Ag along (001) direction of the BZ. The blue shaded region corresponds to the projection onto the surface of the bulk states, and the red lines correspond to the surface bands. We see that all the surface bands fall within the bulk band region. We note that for $x = 0$, i.e., Ag(001), and $x = 1$, i.e., Sn/Ag(001), our calculations were performed using a (1×1) surface unit cell, shown in Figs. 3.6(a) and (f); the resulting band structures did not therefore require

any unfolding. However, at intermediate coverages x , where supercells were used, the unfolding procedure was carried out from the relevant SCBZ to the primitive cell Brillouin zone (PCBZ) [see Fig. 3.16(a)]. The results presented in this section for $x \neq 0$ were obtained from calculations on the structures shown in Fig. 3.6(b),(c) and (d'), all of which have a $p(2 \times 2)$ primitive unit cell. We recall that for $x = 0.25$, both LEED and DFT results agree that this is the most energetically favored configuration, for $x = 0.5$, DFT (but not LEED) suggests that this is the most energetically favored configuration, and for $x = 0.75$, this configuration, though low in energy, is not found to be the most favored one. Nevertheless, for reasons of computational feasibility (the unfolding procedure becomes very expensive when working with large supercells), we computed the unfolded band structure obtained from these configurations, and found very good agreement with the experimental ARPES data, as shown below.

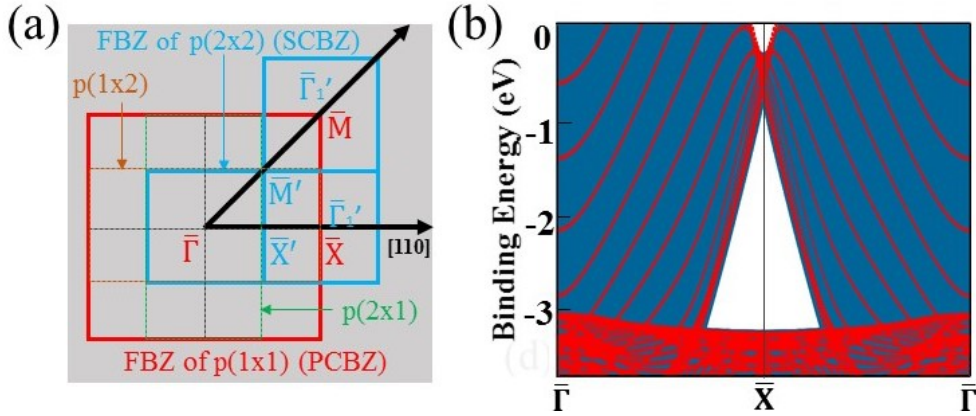


Figure 3.16: (a) Red square represents First Surface Brillouin Zone (FSBZ) of $p(1 \times 1)$ primitive cell in real space, we call it primitive cell Brillouin zone (PCBZ), and light-blue squares represent FSBZ of $p(2 \times 2)$ supercell in real space, we call it supercell Brillouin zone (SCBZ). Primed and un-primed letters represent the high symmetry points of the PCBZ and SCBZ respectively. (b) Projection of bulk band structure onto (001) surface termination. The blue shaded area represents the projection of bulk states while bands computed for the surface slab are shown by red lines. *Fig. is taken from Dr. Arunava Kar's (SINP) Ph.D thesis with permission.*

Fig. 3.17(a) shows the coverage-dependent evolution of the crossing point of a

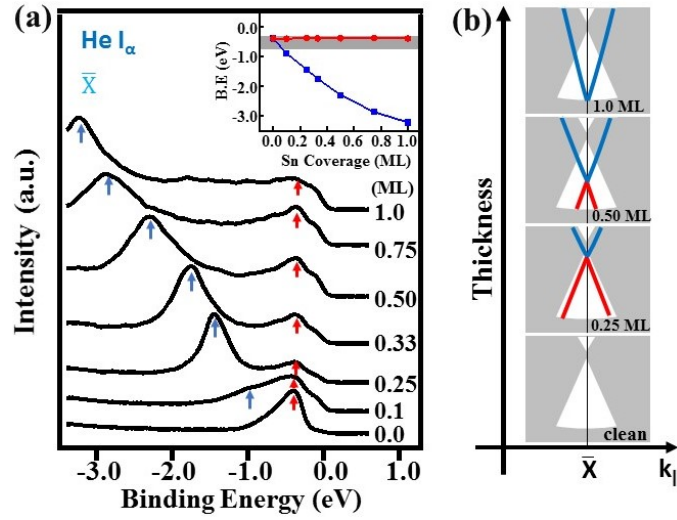


Figure 3.17: (a) Line profile at \bar{X} as a function of Sn coverage. The inset represents the evolution of the crossing point as a function of Sn coverage. The shaded area represents the projected bulk band [see text for details]. (b) Schematic diagram of the evolution of Sn-induced surface bands on Ag(001) surface at \bar{X} high symmetry point. *Fig. is taken from Dr. Arunava Kar's (SINP) Ph.D thesis with permission.*

surface state and a surface resonance, observed through a line scan at the \bar{X} point. For clean Ag(001), an Ag-s peak is observed (marked with a red arrow) at around -0.4 eV. Upon deposition of Sn atoms on Ag(001), another peak (marked with a blue arrow) is observed at Sn coverage $x = 0.1$. This corresponds to the crossing point of two two linearly dispersive bands, as discussed further below. At $x = 0.25$, this new peak is very prominent and observed till $x = 1.0$. This peak shifts downward in energy with increasing x . The change in energy of the crossing point with x is shown in the inset of Fig. 3.17(a), and this variation is shown schematically in Fig. 3.17(b), in which a band arising from a surface state (red line) and another band arising from a surface resonance (blue line) cross each other. The crossing point shifts downward in energy with increasing x . Also the peak width increases with increasing x , which can be attributed to the enhanced Sn-Sn interaction. The Ag-s peak remains inside the projected band region, but gets slightly shifted to higher binding energies with increasing Sn deposition. This can be explained by the suppression of the indirect

photoemission channel due to a reduction of the dielectric mismatch between the Ag surface and vacuum after deposition of Sn.⁷⁸

In the following figures of DFT calculated band structures, the orange bands show the computed band structure for $\text{Sn}_x\text{Ag}_{1-x}/\text{Ag}(001)$ along the $\bar{\Gamma}-\bar{X}-\bar{\Gamma}$ and $\bar{\Gamma}-\bar{M}-\bar{\Gamma}$ directions of the PCBZ [see Fig. 3.16(a)], for $x = 0.0, 0.25, 0.50, 0.75$ and 1.0 . In these figures, the ‘white stars’ and ‘red triangles’ show experimentally obtained data points from ARPES using He I_α and He II_α , respectively. As ARPES probes states in the surface region, we have projected our theoretically computed bands onto the atomic orbitals belong to atoms in the two outermost layers, and the size and color of each orange dot in the figures indicate the value of this calculated projection, as is indicated in the color scale to the right of each graph. The magnitude of this projection is expected to correlate with the ARPES intensity. We note that in addition to certain bright features, the computed spectra show dimmer discrete bands in the energy range between -3 eV and 0 eV. These are projections of bulk bands, which form a continuum in the experimental case, but show up as discrete bands in the computational results because of the finite thickness of the slabs used for DFT calculations. As was observed in the experimental ARPES data, the calculated bands also show a Dirac cone-like crossing at the \bar{X} point, with the energy at which this occurs lowering with increasing x . As one goes from $x = 0$ to $x = 1$, this energy changes from 0.42 eV to 3.04 eV below the Fermi level. Fig. 3.18 shows the variation of the crossing point of S_2 and S_3 states at the \bar{X} point with the Sn concentration x . We see that the crossing point shifts downward in energy with increasing x , which is similar to the schematic shown in the inset of Fig. 3.17(a).

The ARPES data are shown in Fig. 3.19 and 3.20 along the $\bar{\Gamma}-\bar{X}$ and $\bar{\Gamma}-\bar{M}$ direction of the PCBZ, respectively. The experimental band dispersions obtained from the ARPES spectra for both He I_α and He II_α are displayed on top of the calculated spectra with the “white stars” and “red triangles”, respectively for comparison.

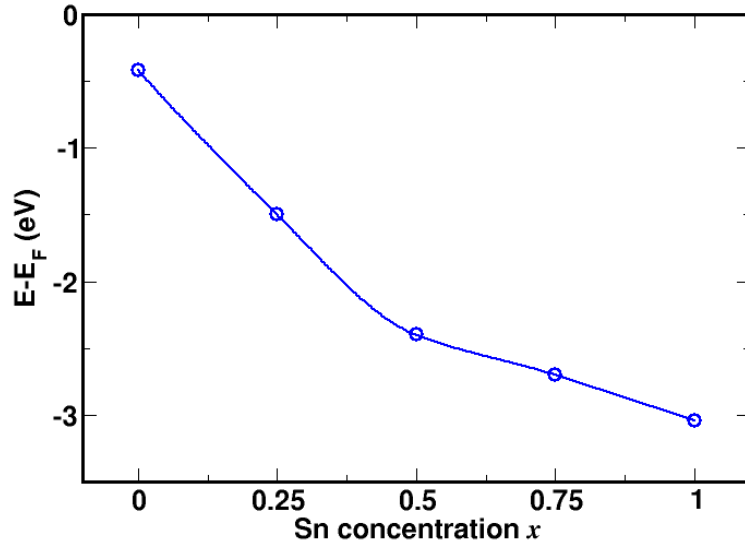


Figure 3.18: Position of the crossing point of S_2 and S_3 states at the \bar{X} point as a function of Sn concentration x , from DFT calculated band dispersion.

We now discuss separately the results at the five values of x .

$x = 0$: Fig. 3.21(a) and 3.21(b) represents calculated band structure of clean Ag(001) substrate along the $\bar{\Gamma} - \bar{X}$ and $\bar{\Gamma} - \bar{M}$ directions of the PCBZ, respectively. ARPES data indicated by the ‘white stars’ and ‘red triangles’ are superposed on the calculated spectra. We see excellent agreement between calculated band structure and the ARPES data, both in energy and momentum, as well as with the previously reported band structure.³ In particular the S_1 state around the $\bar{\Gamma}$ point of Fig. 3.19(a) matches extremely well with the computed bands. As ARPES probes extreme surface states, we have projected our calculated band structure onto the atomic orbitals belonging to the two outermost layers of the asymmetric slab. In Fig. 3.21, the colour scale represents the amount of orbital contribution to the bands, or it is the summation of the overlap between the Kohn-Sham states and the atomic orbitals of the top two layers.

The computed bands also match very well with experiment near the \bar{X} point, in binding energy (BE) as well as in intensity [Fig. 3.21(a)]. Due to the finite thickness of the slab used in our calculations, we observe the presence of a finite number of

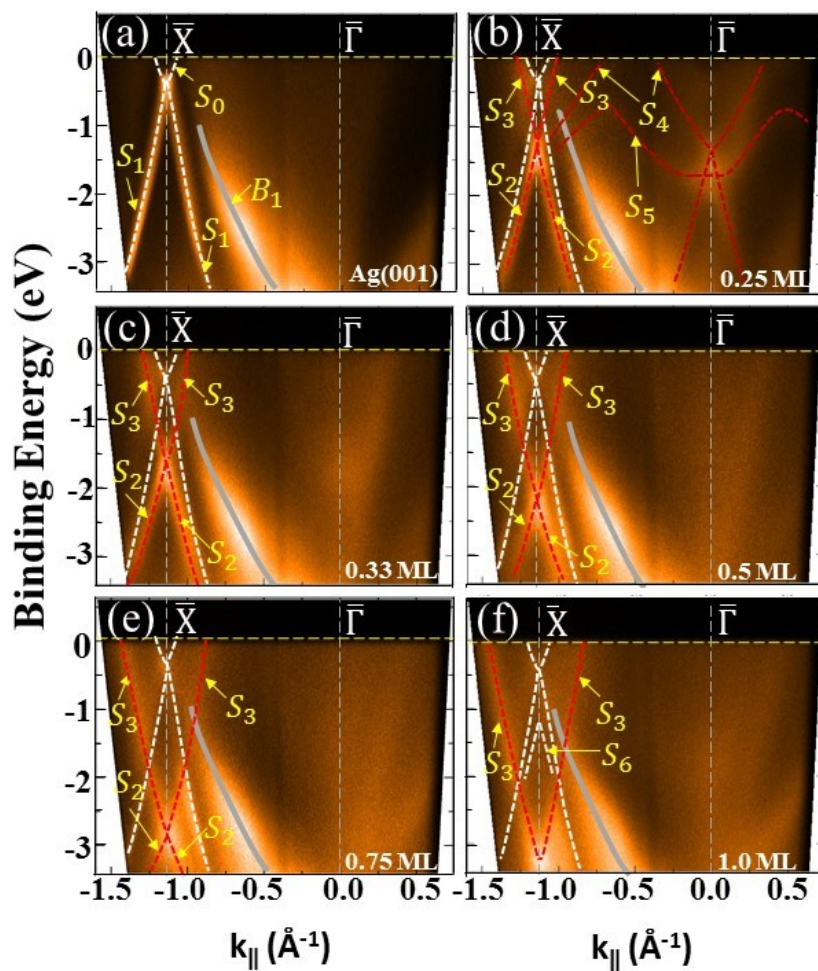


Figure 3.19: Angle Resolved Photoemission Spectroscopy (ARPES) data along the $\bar{\Gamma} - \bar{X}$ direction measured with $h\nu = 21.2$ eV at RT for (a) a clean Ag(001) surface and (b)-(f) for 0.25 – 1.0 ML of Sn/Ag(001). White and red lines are used to guide our eye. Different surface states and resonances are marked with yellow arrow. *Fig. is taken from Dr. Arunava Kar's (SINP) Ph.D thesis with permission.*

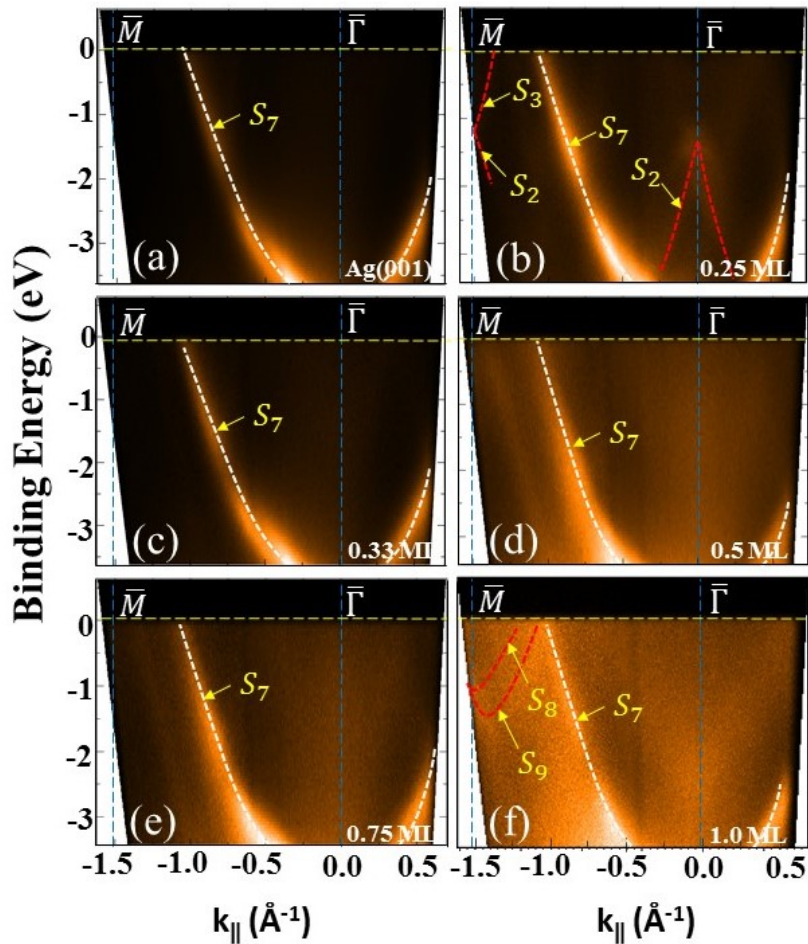


Figure 3.20: Angle Resolved Photoemission Spectroscopy (ARPES) data along the $\bar{\Gamma} - \bar{M}$ direction measured with $h\nu = 21.2$ eV at RT for (a) a clean Ag(001) surface and (b)-(f) for 0.25 – 1.0 ML of Sn/Ag(001). White and red lines are used to guide our eye. Different surface states and resonances are marked with yellow arrow. *Fig. is taken from Dr. Arunava Kar's (SINP) Ph.D thesis with permission.*

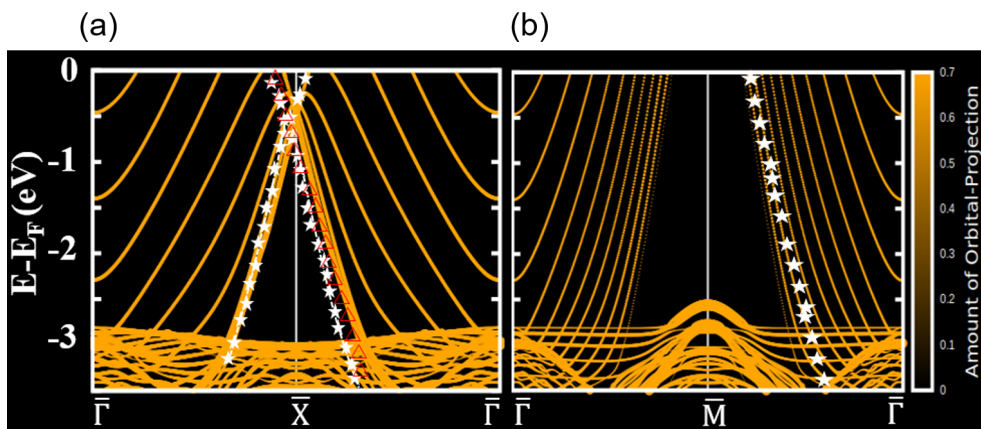


Figure 3.21: Theoretically computed electronic band structure of the clean Ag(001) surface along (a) $\bar{\Gamma} - \bar{X} - \bar{\Gamma}$ and (b) $\bar{\Gamma} - \bar{M} - \bar{\Gamma}$ of the PCBZ. Bands are projected onto the atomic orbitals of the top two Ag layers. Value of the projection is represented by the color scale.

discrete states with non-zero orbital contributions in our calculated band dispersion, away from the \bar{X} point. In a real experimental scenario, because of the very large thickness of the slab, we will have a diffuse continuum of states in this energy range. In our theoretical plot, in the energy range $-2.5 \text{ eV} \leq E - E_F \leq 0 \text{ eV}$, surface states appear at -0.41 eV and -1.84 eV at the $\bar{\Gamma}$ point and at -0.28 eV , -0.42 eV and -0.51 eV at the \bar{X} point.

The theoretically computed and experimentally measured bands also match well near the \bar{M} point, in particular [Fig. 3.21(b)]. Due to the reason already mentioned above, we again see some discrete states with non-zero orbital contributions in the theoretically computed band structure. The high intensity and the spatial localization in the ARPES spectra (S_7 state of Fig. 3.20(a)) can be obtained by combining all the bands located between \bar{M} and $\bar{\Gamma}$ points of the calculated band dispersion. In this case no states appear at the \bar{M} point in the energy range $-2.5 \text{ eV} \leq E - E_F \leq 0 \text{ eV}$, where E_F is the Fermi energy. From the orbital projected density of states (PDOS) calculation of clean Ag(001) [see Fig. 3.22], we observe, above -2.5 eV up to the Fermi level, the dominant contribution is from Ag-5s orbitals,

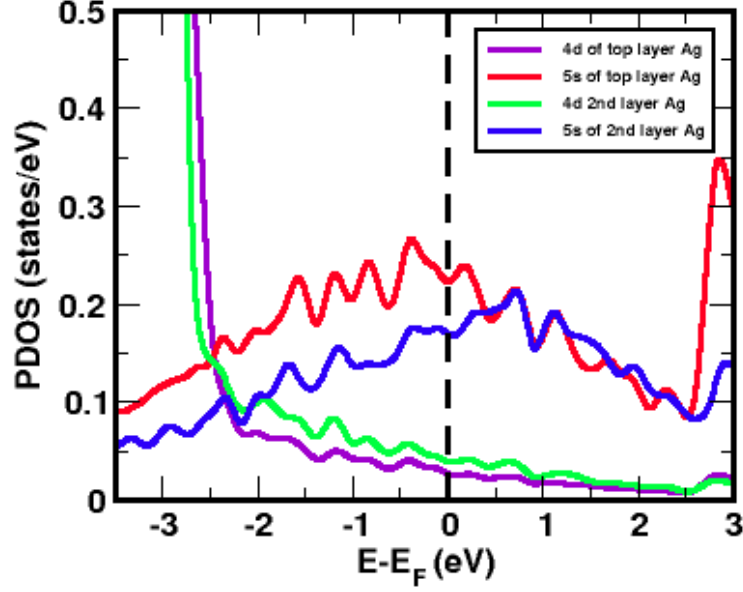


Figure 3.22: Projected density of states (PDOS) of the clean Ag(001) substrate, showing contributions from 4*d* and 5*s* orbitals of Ag atoms belonging to the top two surface layers. Ag 5*s* orbitals have a larger contribution near the Fermi level.

and below -2.5 eV the Ag-4*d* states contribute more.

$x = 0.25$: In Figs. 3.23(a) and (b), we compare the experimentally measured and theoretically computed band structures for $x = 0.25$. Several new surface states now appear: S_2, S_3, S_4 and S_5 along $\bar{\Gamma} - \bar{X}$ and S_7 along $\bar{\Gamma} - \bar{M}$. Once again, the agreement between experiment and theory is excellent. In particular, we note very good agreement for the dispersion of the S_2 surface state and S_5 surface resonance [see Fig. 3.19(b)] along the $\bar{\Gamma} - \bar{X}$ direction, and the S_2 surface state and S_7 surface resonance [see Fig. 3.20(b)] along $\bar{\Gamma} - \bar{M}$. We note that for some of these surface states, the calculations show a set of discrete features instead of one continuous band, due to the use of a relatively thin slab in the computations. Intense surface states appear at the $\bar{\Gamma}$ point at around -1.1 eV, -1.5 eV and -2.5 eV. [see Fig. 3.23(b)].

To gain further insight, in Figs. 3.24(a)–(e), we once again plot the band structure for $x = 0.25$, but this time with the contributions from different orbitals (surface Ag-5*s*, Sn-5*s*, Sn-5*p_x*, Sn-5*p_y* and Sn-5*p_z*) plotted separately. (Note that, for simplicity,

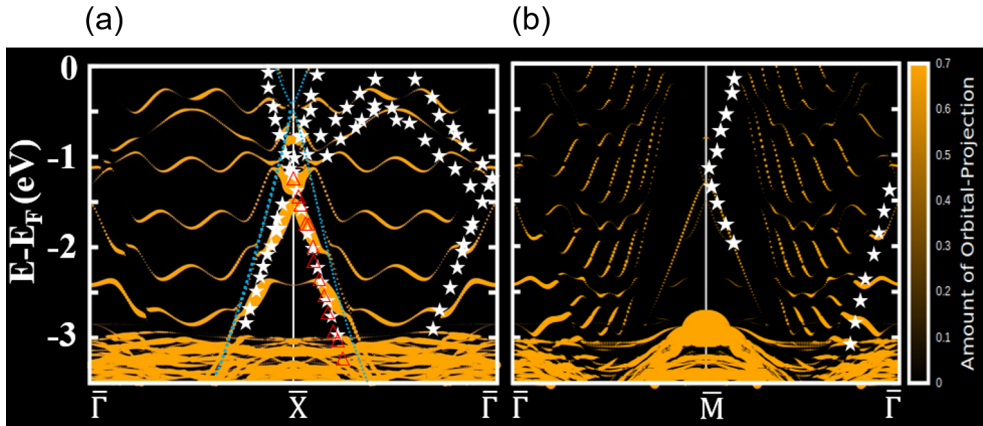


Figure 3.23: Theoretically computed electronic band structure of $\text{Sn}_x\text{Ag}_{1-x}/\text{Ag}(001)$ for $x = 0.25$ along (a) $\bar{\Gamma} - \bar{X} - \bar{\Gamma}$ and (b) $\bar{\Gamma} - \bar{M} - \bar{\Gamma}$ of the PCBZ. Bands are projected onto the atomic orbitals of the top two Ag layers. Value of the projection is represented by the color scale.

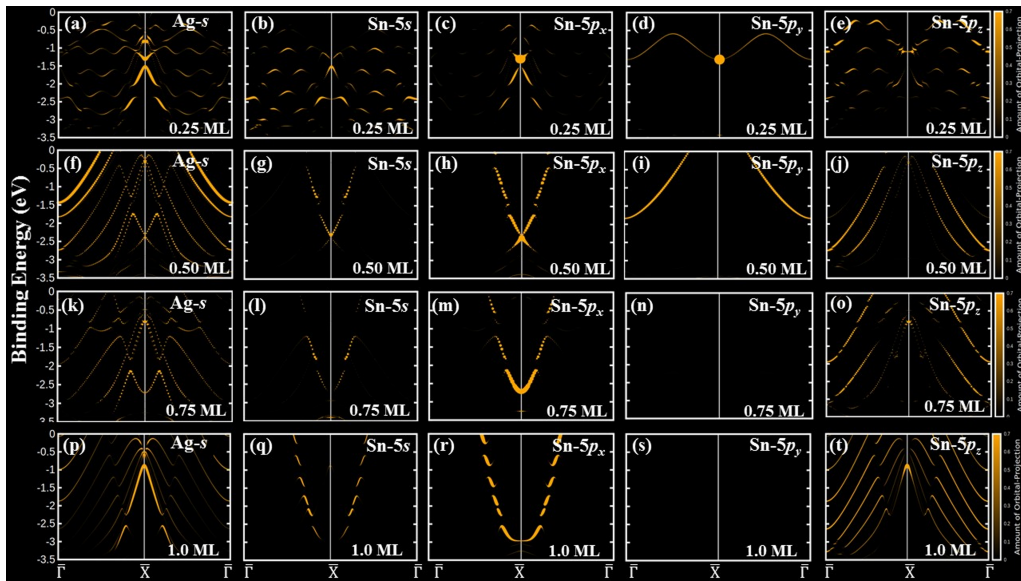


Figure 3.24: DFT calculated orbital projected band structures of (a)-(e) $x = 0.25$, (f)-(j) $x = 0.5$, (k)-(o) $x = 0.75$, (p)-(t) $x = 1.0$ for $\text{Sn}_x\text{Ag}_{1-x}/\text{Ag}(001)$ systems. Here we have projected the Kohn-Sham orbitals on individual orbitals of Ag- sp , Sn- $5s$, Sn- $5p_x$, Sn- $5p_y$, Sn- $5p_z$, respectively.

in Fig. 3.24, we have only plotted bands along the $\bar{\Gamma} - \bar{X}$ direction.) By comparing Figs. 3.24(a)–(e) with Fig. 3.23(a), we can conclude that the S_2 surface state arises primarily from hybridization of the Ag- $5s$ orbitals with the Sn- $5p_x$ orbitals, with a small contribution from Sn- $5s$. The S_4 and S_5 surface resonances arise from Sn- $5p_z$

and Sn-5 p_y orbitals, respectively.

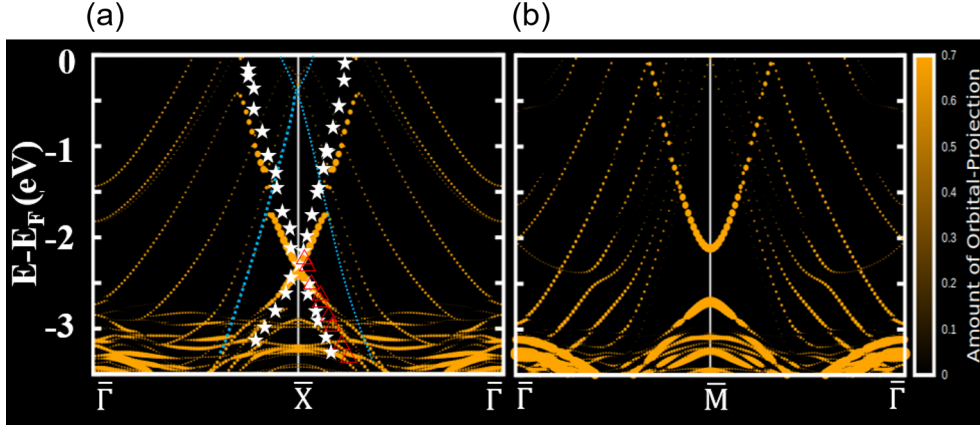


Figure 3.25: Theoretically computed electronic band structure of $\text{Sn}_x\text{Ag}_{1-x}/\text{Ag}(001)$ for $x = 0.5$ along (a) $\bar{\Gamma} - \bar{X} - \bar{\Gamma}$ and (b) $\bar{\Gamma} - \bar{M} - \bar{\Gamma}$ of the PCBZ. Bands are projected onto the atomic orbitals of the top two Ag layers. Value of the projection is represented by the color scale.

$x = 0.5$: Figs. 3.25(a) and (b) show the comparison between the calculated and experimentally measured bands at $x = 0.5$ structure with the ARPES measurements. The most prominent features along $\bar{\Gamma} - \bar{X}$ are the S_2 surface state and S_3 surface resonance, which match excellently in calculation and experiment. As already noted above, the crossing point between S_2 and S_3 is shifted downward, compared to $x = 0.25$.

Along $\bar{\Gamma} - \bar{M}$, the calculations show a prominent surface resonant state with a parabolic dispersion centered at \bar{M} ; this band does not show up in the ARPES data.

Figs. 3.24(f)-(j) show the individual orbital contributions to the bands, along the $\bar{\Gamma} - \bar{X}$ direction. We see that the S_2 state mainly comes from the Ag-5s and Sn-5 p_x orbitals, whereas the S_3 resonance mainly comes from the Sn-5s and Sn-5 p_x orbitals.

$x = 0.75$: In Figs. 3.26(a) and (b) we compare the calculated band structure and experimentally observed ARPES data. We see that there is good agreement between theory and experiment, specially along the $\bar{\Gamma} - \bar{X}$ direction. The crossing

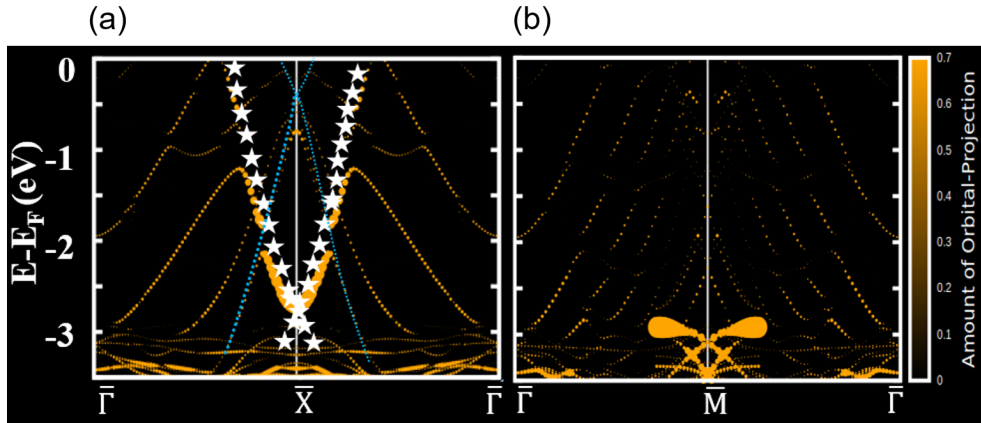


Figure 3.26: Theoretically computed electronic band structure of $\text{Sn}_x\text{Ag}_{1-x}/\text{Ag}(001)$ for $x = 0.75$ along (a) $\bar{\Gamma} - \bar{X} - \bar{\Gamma}$ and (b) $\bar{\Gamma} - \bar{M} - \bar{\Gamma}$ of the PCBZ. Bands are projected onto the atomic orbitals of the top two Ag layers. Value of the projection is represented by the color scale.

point of the linearly dispersive states S_2 and S_3 further shifts downward in energy. The S_3 state becomes more intense while the S_2 state becomes more unclear. On further decomposing in Figs. 3.24(k)-(o), we see that the S_3 state is mostly coming from the Sn- $5p_x$ orbital, with very little contribution from the Sn- $5s$ orbital. Ag- $5s$ contribution has become less as Sn concentration x increases.

$x = 1.0$: Figs. 3.27(a) and (b) show the comparison between the computed band structure and ARPES data. Here, the most intense feature is the linearly dispersive (or ‘V’-shaped) band i.e., the S_3 state around the \bar{X} point, where we find excellent agreement between calculation and experiment. The S_2 state gets suppressed by the core Ag- $4d$ states, and the crossing point is located at -3.1 eV. The crossing point is also visible at the \bar{M} point due to BZ periodicity but the band intensity is quite low [Fig. 3.27(b)] in comparison with $\bar{\Gamma}$ - \bar{X} direction; the symmetry of the Brillouin zone is reflected in the band dispersion characteristics. Around the \bar{X} point, we also see the S_6 state which has an inverted ‘V’-shape. Two nearly parabolic bands around the \bar{M} point are observed with the same vertex point at the \bar{M} at around -1.19 eV. These bands match with the experimental S_8 and S_9 states of Fig. 3.20(f).

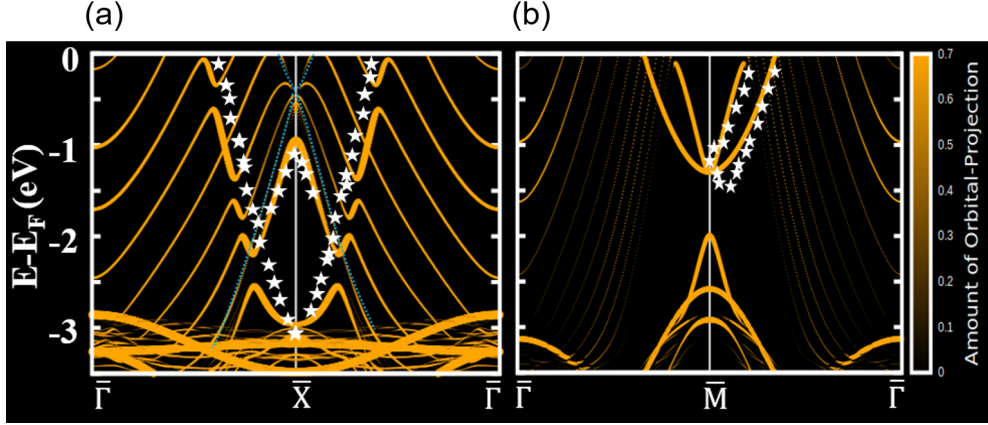


Figure 3.27: Theoretically computed electronic band structure of the 1 ML Sn/Ag(001) (i.e., $x = 1.0$) along (a) $\bar{\Gamma} - \bar{X} - \bar{\Gamma}$ and (b) $\bar{\Gamma} - \bar{M} - \bar{\Gamma}$ of the PCBZ. Bands are projected onto the atomic orbitals of the top two Ag layers. Value of the projection is represented by the color scale.

Calculation also shows some bands around the \bar{M} point below -2 eV, which are missing in the ARPES data.

On further decomposing, along the $\bar{\Gamma} - \bar{X}$ direction, the contributions of different orbitals are shown in Fig. 3.24(p)-(t). It is clear that the most intense linearly dispersive or ‘V-shape’ feature is mainly coming from Sn- $5p_x$ orbitals, with little contribution from Sn- $5s$ orbitals; so this has now purely Sn character. Sn- $5p_z$ orbitals contribute to the bands away from the \bar{X} point. The S_6 state is mainly coming from the Ag- $5s$ orbitals. We note that, as expected, the Sn- $5p_x$ orbitals mainly contribute in the $\bar{\Gamma} - \bar{X}$ direction and Sn- $5p_y$ orbitals mainly contribute in the $\bar{\Gamma} - \bar{M}$ direction.

3.5.5 Insights from charge density difference plots

In order to understand the nature of the bonding at Sn $_x$ Ag $_{1-x}$ /Ag(001) interface and the charge redistribution upon forming the interface, we examine the charge density difference (CDD) $\Delta\rho$, where

$$\Delta\rho = \rho[\text{Sn}_x\text{Ag}_{1-x}/\text{Ag}(001)] - \rho[\text{Sn}/\text{Ag}(001)] - \rho[\text{Ag}(001)]. \quad (3.22)$$

Here, the first term on the right-hand-side of the equation is the charge density of the $\text{Sn}_x\text{Ag}_{1-x}/\text{Ag}(001)$ surface alloy system, and the second and third terms are the charge densities of the full coverage $\text{Sn}/\text{Ag}(001)$ system and the clean $\text{Ag}(001)$ surface slab, respectively (all calculated at the relaxed geometries of the combined system). We also calculated the corresponding planar-averaged charge density difference $\Delta\rho_{\text{avg}}(z)$, given by

$$\Delta\rho_{\text{avg}}(z) = \int dx dy \Delta\rho(x, y, z). \quad (3.23)$$

We now examine the charge density difference (CDD) $\Delta\rho$ plots and planar-averaged CDD ($\Delta\rho_{\text{avg}}(z)$) plots for different Sn coverages x on the $\text{Ag}(001)$ surface; these results are depicted in Fig. 3.28. The interaction between adsorbate and substrate atoms leads to a redistribution of the surface electron density. The small electronegativity difference between Sn (1.96) and Ag (1.93) results in charge sharing and is responsible for covalent bonding in nature. For lower Sn coverage, it was observed that the charge redistribution is relatively small, but it is found to increase with the coverage. Accumulated electrons (indicated by red lobes) are getting localized on top of the Sn atoms while the top layer Ag atoms are suffering from electron depletion (indicated by blue lobes). Accumulation of electrons near Sn atoms leads to an Sn-dominating orbital character in the band structure. Due to the redistribution of charges at the interface, the surface potential decreases, and as a result the crossing point at \bar{X} gradually shifts downward in energy and the band structure has a linearly dispersive or ‘V-shape’ feature which indicates a Dirac-cone-like behaviour, as observed for the 1 ML case.

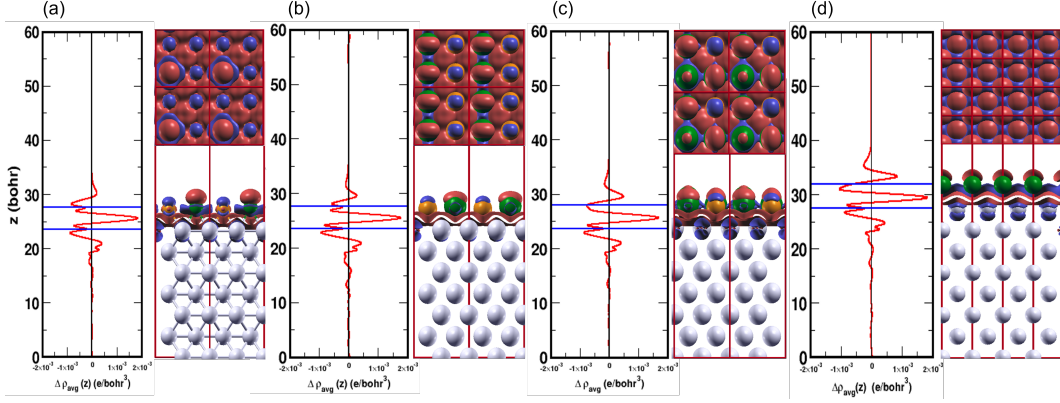


Figure 3.28: 3D charge density difference (CDD) plots $\Delta\rho$ (right Figs. along with side and top views) and planar-averaged CDD plots (left Figs.) for (a) $x = 0.25, p(2 \times 2)$ cell, (b) $x = 0.5, p(2 \times 1)$ cell, (c) $x = 0.75, p(2 \times 2)$ cell, and (d) $x = 1.0, p(1 \times 1)$ cell. Color scheme of the atoms: Sn – green, surface Ag atom – orange, below Ag atom – light gray. Isosurface value for the CDD plots = $\pm 0.001 e/\text{bohr}^3$. Accumulation and depletion of electrons are represented by the red and blue colors, respectively. The horizontal blue lines in each case correspond to the average heights of the top two layers.

3.5.6 Evolution of electrostatic potential with Sn coverage

Next, we want to see the nature of the electrostatic potential in the system slabs, specially in the Sn/Ag interface regions. So, we calculate the electrostatic potential V_{es} , and its planar average taken over the xy plane:

$$V_{es}(z) = \int V_{es}(x, y, z) dx dy, \quad (3.24)$$

where, $V_{es} = V_{bare} + V_H$, is the sum of the bare electron-nucleus potential and Hartree potential. The plots of $V_{es}(z)$ are shown in Fig. 3.29, for (a) clean Ag(001), $p(1 \times 1)$ cell, (b) $x = 0.25, p(2 \times 2)$ cell, (c) $x = 0.5, p(2 \times 2)$ cell, (d) $x = 0.75, p(2 \times 2)$ cell, and (e) $x = 1.0, p(1 \times 1)$ cell.

The potential is oscillating and periodic in the inside region of the slab, and constant in the vacuum region. The vertical black dotted lines represent the average height of the top layer atoms. We observe a sharp change in the potential near the top layer which contains the Sn-Ag layer. For clean Ag(001), this change is very

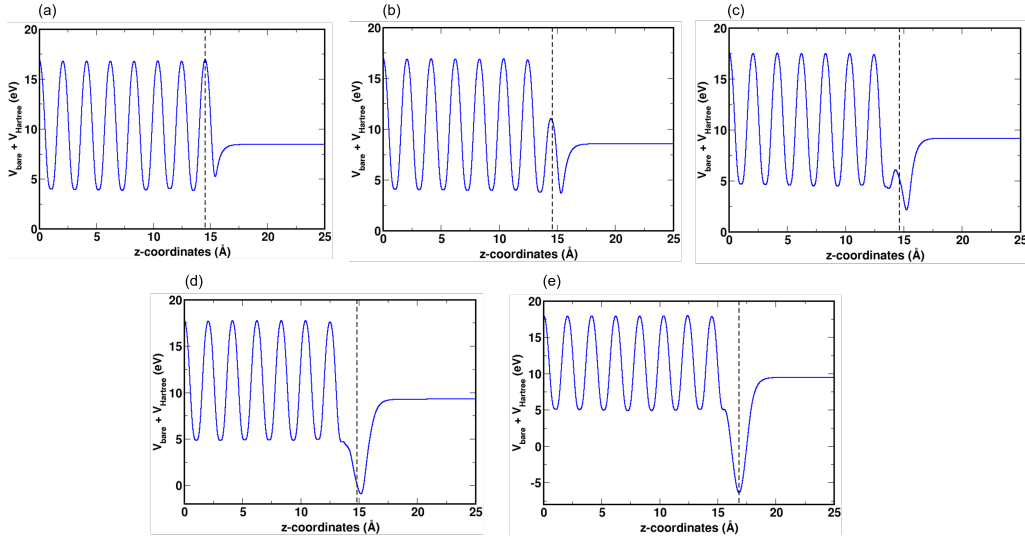


Figure 3.29: Electrostatic potential $V_{bare} + V_{Hartree}$ as a function of z -coordinates of the slabs for (a) clean Ag(001), $p(1 \times 1)$ cell, (b) $x = 0.25$, $p(2 \times 2)$ cell, (c) $x = 0.5$, $p(2 \times 2)$ cell, (d) $x = 0.75$, $p(2 \times 2)$ cell, and (e) $x = 1.0$, $p(1 \times 1)$ cell. The vertical black dotted line represent average height of the top layer in each case. The change in the potential is clearly observed in the Sn/Ag interface region; the potential is decreasing as Sn concentration x is increasing.

minimal, and as the Sn concentration in the top layer increases, this sharp change in the potential becomes prominent. For clean Ag(001), the peak (maximum in potential energy curve) height of the periodic potential at the top layer is same as that of the other inside layers, as well as of the bulk like layers, of the slab. Also, we see one minimum in the planar averaged electrostatic potential energy curve, just above the top layer. For $x = 0.25$, the peak height of the potential at the top layer is decreased, also the depth of the minimum just above this peak is increased a little bit. We see the trend that, as the Sn concentration increases, the height of the peak of the electrostatic potential associated with the top layer decreases, as well as the depth of the minimum just above it increases. Also, as the Sn coverage increases, the position (z -height) of the vertical black dotted line shifts towards this minimum, from the top peak. For $x = 0.75$, the top peak has almost disappeared, and the depth of the minimum above it reaches a negative value. For the full Sn monolayer, i.e., $x = 1.0$, the depth of the minimum is reduced further and reaches a more negative

value, with the black dotted line falling exactly at this depth which represents the height of the Sn monolayer. This continuous decrease of the electrostatic potential with Sn concentration, in the Sn/Ag interface region, causes a shift in the bands associated with the Sn atoms (linearly dispersive V-shape-like bands) downward in energy in the ARPES measurements and in the DFT calculations.

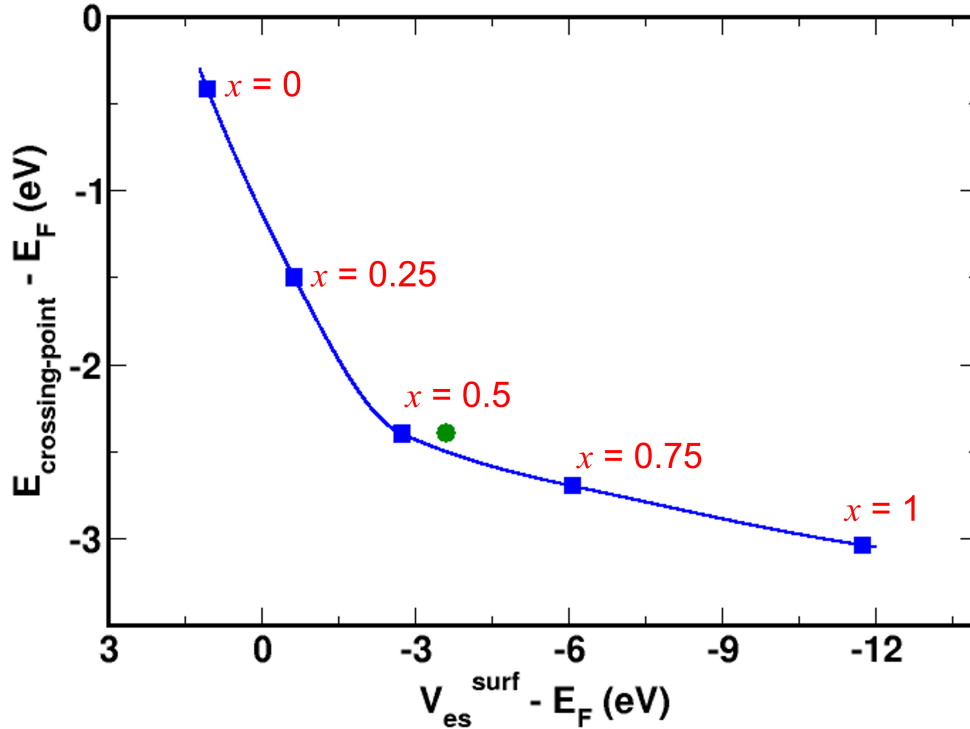


Figure 3.30: Variation of the crossing point below the Fermi level with surface electrostatic potential for different Sn concentration x . Blue filled squares are for the structures for which band structures are calculated, and green filled circle is for $x = 0.5$, $p(1 \times 10)$ cell.

The correlation between the surface electrostatic potential and the energy of the crossing point can be seen in Fig. 3.30. Here, the blue filled squares are for the structures for which band structures are calculated above, and the green filled circle is for $x = 0.5$, $p(1 \times 10)$ cell, which is the structure observed in LEED. We believe that the (unfolded) band structure is primarily sensitive to the surface electrostatic potential, which in turn is primarily sensitive to the concentration of Sn atoms in the surface alloy. For example, at $x = 0.5$, LEED gave $p(1 \times 10)$ unit

cell and our DFT calculations gave $p(2 \times 2)$. So we have calculated the surface electrostatic potential for both the structures; see the green dot and blue square, respectively, at $x = 0.5$ in Fig. 3.30). We see that though the geometry is very different, replacing one structure by the other would not make a significant difference in the behavior of surface potential as a function of x , and hence the position of the crossing point as a function of x . This could be a possible explanation for why we get such good agreement between our DFT calculated unfolded and surface-projected band structures and the ARPES data, even for cases (such as at $x = 0.5$) where DFT and experiment do not seem to agree about the structure of the lowest-energy surface alloy configuration.

3.5.7 Further discussion

During the creation of the surface, atoms of the topmost layer lose some bonds as the lattice symmetry gets broken due to the presence of vacuum on one side. Due to this lack of bonding, the excess charge accumulates at the surface which causes a modification of the surface potential. It is well known that the modified potential due to excess charge gives rise to the surface states at \bar{M} of both Ag(001) and Cu(001) surfaces,^{29;48} in which $d_{x^2-y^2}$ bands are pushed out from the bulk continuum by the Coulomb repulsion of excess sp electrons at the surface. After Sn deposition, when Ag surface atoms make bonds with Sn atoms, the confined charges get spread over the interface and lower the surface potential. The experimentally observed downward shifting of the \bar{M} surface states with Sn adsorption on Ag(001)⁷⁹ is direct evidence of this. Similarly, due to the reduction of surface potential, an interfacial state is formed which gets split off from bulk Ag sp bands. The hybridization between Sn- $5sp$ and Ag- sp bands is responsible for the formation of the interfacial states with bonding-antibonding characters. Due to the existence of the projected band gap region between sp and d bands at \bar{X} ,²⁹ the interfacial state has a larger

amplitude at the Ag-Sn interface at this symmetry point. The extensive dispersion of the S_2 band at lower coverage may suggest that the interfacial states are not localized as metallic ones, but have a more covalent nature and are laterally delocalized.

As the p -block metals have the general electronic configurations of $s^2p^1-s^2p^3$, the filling of the p bands decides the evolution of the electronic structure across the series and the s orbital contribution is expected to be insignificant due to the inner pair effect. In the literature, only a few cases of p -block metals on other substrates have been explored. On noble metal (001) surfaces, the cases of Bi/Ag(001), Pb/Ag(001), and In/Cu(001) are known and we compare the case of Sn/Ag(001) with them for a better understanding of the electronic structure evolution.^{23;80} In the case of a half-filled Bi/Ag(001) system, several Bi induced surface bands were observed near the Fermi surface.²⁸ At the \bar{X} point, a band similar to S_2 is observed for different Bi coverages, although the movement of this band with Bi coverage is opposite.²⁸ For 0.75 ML of Bi coverage, the band position at \bar{X} is found to be lower in energy than that for the 0.5 ML Bi coverage. However, the experimental ARPES results are complicated by the band foldings resulting from the different (4×4) surface orderings. It is not very clear whether any surface alloying or Ag surface segregation occurs in the Bi/Ag system. The observation of a constant Auger signal intensity above 0.8 ML of Bi coverage without the formation of any new structural phases is interesting. For the Pb/Ag(001) system, only the pseudo-hexagonal monolayer case that is commensurate with a $c(6\times 2)$ coincidence cell to the Ag substrate,⁸¹ is studied along the $\bar{\Gamma} - \bar{M}$ direction. Although different Pb bands are observed, the band folding makes it difficult to understand and detailed studies are required, especially along with the $\bar{\Gamma} - \bar{X}$ direction of Ag(001) in the bulk band gap region.

On Cu(001) substrates, there have been extensive studies of the growth of Sn and Indium. In the case of Sn/Cu(001), the focus of the studies has been their atomic structure due to their complex phase diagrams. From a recent ab initio study,⁴⁶

it has been suggested that up to an Sn coverage of 0.5 ML, the Sn goes into a substitutional site making a substitutional surface alloy, beyond which Sn goes to the adatom site, forming a complex surface alloy. The electronic structure of the system has been studied in the $\bar{\Gamma} - \bar{M}$ direction to understand the charge-density-wave (CDW) formation, however with little emphasis on the electronic structure evolution with alloy formation. However, indium on Cu(001) is a relatively well-studied system due to the presence of the CDW phase. For RT deposition, the Indium atoms are incorporated into the surface lattice for low coverages while for higher coverages, surface dealloying occurs with indium atoms forming overlayers.^{23;80} The evolution of the electronic structure of the In/Cu(001) system was studied by ARPES and a band similar to S_2 (see Fig. 3.19) is observed with a higher BE shift with In coverage. Interestingly, the BE of this S_2 -like band with In coverage [see Fig. 13(b) of T. Aruga's paper²³], does get saturated beyond 0.7 ML In coverage, where the de-alloying occurs and no more In goes into the substitutional sites. Comparing this with the behaviour of the Sn on Ag(001) case as shown in Fig. 3.16(b), we do not observe any saturation in the BE of the S_2 band, suggesting that the Sn atoms keep getting substituted into the Ag surface lattice up to the monolayer coverage, in complete agreement with our DFT calculations. This also suggests that the behaviour of the S_2 band intensity at the \bar{X} point (crossing-point) with the coverage of the solute atoms is a good measure of the incorporation (substitution) of the solute atoms into the substrate lattice. This can be understood by the change of the potential experienced by the solute atoms continually by the continuous substitution in the host lattice.

3.6 Conclusions

In summary, our experimental collaborators have deposited Sn atoms on the Ag(001) surface. Our naive expectation was that Sn atoms would wet the Ag surface and form an overlayer, because the surface energy of Sn(001) is less than that of Ag(001), and also the metallic radii of the Sn and Ag atoms are very similar in their respective bulk crystals. However, in contrast to our expectation, very interestingly, Sn-Ag substitutional surface alloys are formed at all values of Sn concentration x considered in our experiments and DFT calculations.

We have found the reason why the formation of Sn-Ag surface alloys is favored over the formation of overlayer or sub-surface structures. We have shown that Sn atoms “become larger” on Ag(001), and they become bigger than the surface Ag atoms which results in the formation of Sn-Ag surface alloy, and helps to relieve tensile surface stress of the Ag(001).

The surface alloys are purely 2D, since no Sn atoms are found in the second or third layer below the surface atomic layer. The surface alloy structures predicted by DFT calculations match quite well with the LEED experiments, but the agreement is not perfect.

We further computed the electronic structure calculations and compared with the APRES data at different values of x . We see very good agreement between theory and experiment at all values of x . This is true even for cases where the structure found by DFT differs from that suggested by LEED, suggesting that the electronic structure is more sensitive to the Sn concentration than the details of the geometric structure of the surface alloy. The main feature of the band structure is two linearly dispersive bands crossing each other and forming a Dirac-like-cone; the upper half of which comes from the Sn orbitals and the lower half of which comes from the Ag orbitals. As x increases, the crossing point downshifts in energy. and finally at

full monolayer (i.e., $x = 1.0$) only the upper half cone exists with a 'V'-shape with complete Sn contribution. The surface potential and the charge redistribution at the interface predominantly determine the characteristics of the band structure.

Bibliography

- [1] M. Bode, S. Heinze, A. Kubetzka, O. Pietzsch, M. Hennefarth, M. Getzlaff, R. Wiesendanger, X. Nie, G. Bihlmayer, and S. Blügel, “Structural, electronic, and magnetic properties of a Mn monolayer on W(110),” *Phys. Rev. B*, vol. 66, no. 1, p. 014425, 2002.
- [2] J. Das *et al.*, “Structure of Cr monolayer on Ag(001): A buried two-dimensional $c(2 \times 2)$ antiferromagnet,” *Phys. Rev. B*, vol. 91, no. 12, p. 125435, 2015.
- [3] J. Das, S. Biswas, K. Ulman, R. Banerjee, G. Gautam, A. K. Kundu, S. Narasimhan, and K. S. Menon, “Electronic structure of a buried two-dimensional antiferromagnetic layer: Experimental and theoretical investigation of Ag/Cr/Ag(001),” *Phys. Rev. B*, vol. 98, no. 7, p. 075137, 2018.
- [4] J. R. Osiecki and R. Uhrberg, “Alloying of Sn in the surface layer of Ag(111),” *Phys. Rev. B*, vol. 87, no. 7, p. 075441, 2013.
- [5] D.-A. Luh, C.-H. Wang, and Y.-W. Yang, “Growth of thin Sn films on Ag(111) studied with low-energy electron diffraction and X-ray photoelectron spectroscopy,” *Thin Solid Films*, vol. 682, pp. 44–49, 2019.
- [6] J. Knudsen, A. U. Nilekar, R. T. Vang, J. Schnadt, E. L. Kunkes, J. A. Dumesic,

- M. Mavrikakis, and F. Besenbacher, “A Cu/Pt near-surface alloy for water-gas shift catalysis,” *J. Am. Chem. Soc.*, vol. 129, no. 20, pp. 6485–6490, 2007.
- [7] S. Zafeiratos, S. Piccinin, and D. Teschner, “Alloys in catalysis: phase separation and surface segregation phenomena in response to the reactive environment,” *Catal. Sci. Technol.*, vol. 2, no. 9, pp. 1787–1801, 2012.
- [8] C. R. Ast, J. Henk, A. Ernst, L. Moreschini, M. C. Falub, D. Pacilé, P. Bruno, K. Kern, and M. Grioni, “Giant spin splitting through surface alloying,” *Phys. Rev. Lett.*, vol. 98, no. 18, p. 186807, 2007.
- [9] J. Tersoff, “Surface-confined alloy formation in immiscible systems,” *Phys. Rev. Lett.*, vol. 74, no. 3, p. 434, 1995.
- [10] B. E. Koel, A. Sellidj, and M. Paffett, “Ultrathin films of Pd on Au(111): evidence for surface alloy formation,” *Phys. Rev. B*, vol. 46, no. 12, p. 7846, 1992.
- [11] S. Mehendale, Y. Girard, V. Repain, C. Chacon, J. Lagoute, S. Rousset, M. Marathe, and S. Narasimhan, “Ordered surface alloy of bulk-immiscible components stabilized by magnetism,” *Phys. Rev. Lett.*, vol. 105, no. 5, p. 056101, 2010.
- [12] L. P. Nielsen, F. Besenbacher, I. Stensgaard, E. Laegsgaard, C. Engdahl, P. Stoltze, K. W. Jacobsen, and J. K. Nørskov, “Initial growth of Au on Ni(110): Surface alloying of immiscible metals,” *Phys. Rev. Lett.*, vol. 71, no. 5, p. 754, 1993.
- [13] C. Nagl, E. Platzgummer, O. Haller, M. Schmid, and P. Varga, “Surface alloying and superstructures of Pb on Cu(100),” *Surf. Sci.*, vol. 331, pp. 831–837, 1995.

- [14] H. Röder, R. Schuster, H. Brune, and K. Kern, “Monolayer-confined mixing at the Ag-Pt(111) interface,” *Phys. Rev. Lett.*, vol. 71, no. 13, p. 2086, 1993.
- [15] M. M. Biener, J. Biener, R. Schalek, and C. M. Friend, “Surface alloying of immiscible metals: Mo on Au(111) studied by STM,” *Surf. Sci.*, vol. 594, no. 1-3, pp. 221–230, 2005.
- [16] V. Fiorentini, M. Methfessel, and M. Scheffler, “Reconstruction mechanism of fcc transition metal (001) surfaces,” *Phys. Rev. Lett.*, vol. 71, no. 7, p. 1051, 1993.
- [17] M. Marathe, *Structural, Magnetic and Electronic Properties of Surface alloys and Interfaces: A First Principles Study*. JNCASR, 2013.
- [18] S. Oppo, V. Fiorentini, and M. Scheffler, “Theory of adsorption and surfactant effect of Sb on Ag(111),” *Phys. Rev. Lett.*, vol. 71, no. 15, p. 2437, 1993.
- [19] U. Mizutani, “The hume-rothery rules for structurally complex alloy phases,” in *Surface Properties and Engineering of Complex Intermetallics*, pp. 323–399, World Scientific, 2010.
- [20] T. Egami and Y. Waseda, “Atomic size effect on the formability of metallic glasses,” *J. Non-Cryst. Solids*, vol. 64, no. 1-2, pp. 113–134, 1984.
- [21] W. Hume-Rothery, *Researches on the nature, properties, and conditions of formation of intermetallic compounds, with special reference to certain compounds of tin*. PhD thesis, University of London, 1926.
- [22] E. Bauer, “Phänomenologische theorie der kristallabscheidung an oberflächen. ii,” *Zeitschrift für Kristallographie-Crystalline Materials*, vol. 110, no. 1-6, pp. 395–431, 1958.

- [23] T. Aruga, “Surface Peierls transition on Cu(001) covered with heavier p-block metals,” *Surf. Sci. Rep.*, vol. 61, no. 6, pp. 283–302, 2006.
- [24] L. Moreschini, A. Bendounan, I. Gierz, C. Ast, H. Mirhosseini, H. Höchst, K. Kern, J. Henk, A. Ernst, S. Ostanin, *et al.*, “Assessing the atomic contribution to the Rashba spin-orbit splitting in surface alloys: Sb/Ag(111),” *Phys. Rev. B*, vol. 79, no. 7, p. 075424, 2009.
- [25] E. Krasovskii, “Spin-orbit coupling at surfaces and 2D materials,” *J. Phys. Condens. Matter*, vol. 27, no. 49, p. 493001, 2015.
- [26] K. Miyamoto, A. Kimura, K. Kuroda, T. Okuda, K. Shimada, H. Namatame, M. Taniguchi, and M. Donath, “Spin-polarized Dirac-cone-like surface state with d character at W(110),” *Phys. Rev. Lett.*, vol. 108, no. 6, p. 066808, 2012.
- [27] O. M. Magnussen, J. Hageböck, J. Hotlos, and R. J. Behm, “In situ scanning tunnelling microscopy observations of a disorder-order phase transition in hydrogensulfate adlayers on Au(111),” *Faraday Discuss*, vol. 94, pp. 329–338, 1992.
- [28] T. Nakagawa *et al.*, “Evolution of geometric and electronic structure at the Bi/Ag(001) interface,” *Phys. Rev. B*, vol. 72, no. 16, p. 165405, 2005.
- [29] T. Nakagawa *et al.*, “Evolution of geometric and electronic structure in ultrathin films on Cu(001),” *Phys. Rev. B*, vol. 66, no. 8, p. 085402, 2002.
- [30] W. H. Rothery, C. W. Haworth, and R. E. Smallman, *The structure of metals and alloys*. London, Metals and Metallurgy Trust of the Institute of Metals and the Institution of Metallurgists., 1969.
- [31] https://www.webelements.com/tin/atom_sizes.html.
- [32] https://www.webelements.com/silver/atom_sizes.html.

- [33] <https://www.webelements.com/tin/electronegativity.html>.
- [34] <https://www.webelements.com/silver/electronegativity.html>.
- [35] S. Chada, R. Fournelle, W. Laub, and D. Shangguan, “Copper substrate dissolution in eutectic Sn-Ag solder and its effect on microstructure,” *J. Electron. Mater.*, vol. 29, no. 10, pp. 1214–1221, 2000.
- [36] J. Li, P. Agyakwa, and C. Johnson, “Kinetics of Ag₃Sn growth in Ag–Sn–Ag system during transient liquid phase soldering process,” *Acta Mater.*, vol. 58, no. 9, pp. 3429–3443, 2010.
- [37] M. Marathe, M. Imam, and S. Narasimhan, “Elastic and chemical contributions to the stability of magnetic surface alloys on Ru(0001),” *Phys. Rev. B*, vol. 79, no. 8, p. 085413, 2009.
- [38] W. Tyson and W. Miller, “Surface free energies of solid metals: Estimation from liquid surface tension measurements,” *Surf. Sci.*, vol. 62, no. 1, pp. 267–276, 1977.
- [39] H. Erschbaumer, A. Freeman, C. Fu, and R. Podloucky, “Surface states, electronic structure and surface energy of the Ag(001) surface,” *Surf. Sci.*, vol. 243, no. 1-3, pp. 317–322, 1991.
- [40] S. Overbury and Y. S. Ku, “Formation of stable, two-dimensional alloy-surface phases: Sn on Cu(111), Ni(111), and Pt(111),” *Phys. Rev. B*, vol. 46, no. 12, p. 7868, 1992.
- [41] M. Maniraj, D. Jungkenn, W. Shi, S. Emmerich, L. Lyu, J. Kollamana, Z. Wei, B. Yan, M. Cinchetti, S. Mathias, *et al.*, “Structure and electronic properties of the $(3 \times 3) R 30^\circ$ SnAu₂/Au(111) surface alloy,” *Phys. Rev. B*, vol. 98, no. 20, p. 205419, 2018.

- [42] Y. Li, L. Jiang, and B. Koel, “Surface alloy formation and the structure of $c(2 \times 2)$ -Sn/Ni(100) determined by low-energy alkali-ion scattering,” *Phys. Rev. B*, vol. 49, no. 4, p. 2813, 1994.
- [43] M. T. Paffett, A. D. Logan, R. J. Simonson, and B. E. Koel, “A multitechnique surface science examination of Sn deposition on Pt(100),” *Surf. Sci.*, vol. 250, no. 1-3, pp. 123–138, 1991.
- [44] M.-G. Barthès and C. Pariset, “A low energy electron diffraction-Auger electron spectroscopy study of alloy formation during the adsorption of tin on (100) and (111) Au,” *Thin Solid Films*, vol. 77, no. 4, pp. 305–312, 1981.
- [45] C. Argile and G. Rhead, “Growth of metal monolayers and ultrathin films on copper: Simple and bimetallic layers of lead and tin,” *Thin Solid Films*, vol. 87, no. 3, pp. 265–275, 1982.
- [46] P. Machain, J. E. Gayone, J. D. Fuhr, and H. Ascolani, “Non-alloy/alloy transitions in the Sn/Cu(001) system: An STM, LEED and DFT study,” *Appl. Surf. Sci.*, vol. 422, pp. 838–846, 2017.
- [47] J.-H. Lee, J. Yun, T. Lee, and A. Soon, “Ab initio surface phase diagram of Sn/Cu(001): reconciling experiments with theory,” *Phys. Rev. Appl.*, vol. 8, no. 3, p. 034010, 2017.
- [48] S. Chakraborty and K. S. R. Menon, “Growth and structural evolution of Sn on Ag(001): Epitaxial monolayer to thick alloy film,” *J. Vac. Sci. Technol.*, vol. 34, no. 4, p. 041513, 2016.
- [49] S. Mahatha and K. S. Menon, “Angle-resolved photoemission spectroscopic facility for surface,” *Current Science*, vol. 98, no. 6, 2010.

-
- [50] A. Goldmann and E. Bartels, “High-resolution study of the \bar{M} surface state on Ag(100),” *Surf. Sci.*, vol. 122, no. 2, pp. L629–L634, 1982.
- [51] P. Giannozzi, S. Baroni, N. Bonini, M. Calandra, R. Car, C. Cavazzoni, D. Ceresoli, G. L. Chiarotti, M. Cococcioni, I. Dabo, *et al.*, “QUANTUM ESPRESSO: a modular and open-source software project for quantum simulations of materials,” *J. Phys. Condens. Matter*, vol. 21, no. 39, p. 395502, 2009.
- [52] J. P. Perdew, K. Burke, and M. Ernzerhof, “Generalized gradient approximation made simple,” *Phys. Rev. Lett.*, vol. 77, no. 18, p. 3865, 1996.
- [53] D. Vanderbilt, “Soft self-consistent pseudopotentials in a generalized eigenvalue formalism,” *Phys. Rev. B*, vol. 41, no. 11, p. 7892, 1990.
- [54] L. Bengtsson, “Dipole correction for surface supercell calculations,” *Phys. Rev. B*, vol. 59, no. 19, p. 12301, 1999.
- [55] R. Fletcher, “Practical methods of optimization john wiley & sons,” *New York*, vol. 80, p. 4, 1987.
- [56] H. J. Monkhorst and J. D. Pack, “Special points for Brillouin-zone integrations,” *Phys. Rev. B*, vol. 13, no. 12, p. 5188, 1976.
- [57] N. Marzari, D. Vanderbilt, A. De Vita, and M. Payne, “Thermal contraction and disordering of the Al(110) surface,” *Phys. Rev. Lett.*, vol. 82, no. 16, p. 3296, 1999.
- [58] W. Ku, T. Berlijn, C.-C. Lee, *et al.*, “Unfolding first-principles band structures,” *Phys. Rev. Lett.*, vol. 104, no. 21, p. 216401, 2010.
- [59] G. Cipriani *et al.*, “Adsorption of atomic oxygen on Ag(001): a study based on density-functional theory,” *Surf. Sci.*, vol. 501, no. 3, pp. 182–190, 2002.

-
- [60] G. Bozzolo and J. Ferrante, “Determination of parameters of a method for predicting alloy properties,” *Phys. Rev. B*, vol. 46, no. 13, p. 8600, 1992.
- [61] C. Lian and S. Meng, “Dirac cone pairs in silicene induced by interface Si-Ag hybridization: a first-principles effective band study,” *Phys. Rev. B*, vol. 95, no. 24, p. 245409, 2017.
- [62] T. Dargam, R. Capaz, and B. Koiller, “Disorder and size effects in the envelope-function approximation,” *Phys. Rev. B*, vol. 56, no. 15, p. 9625, 1997.
- [63] T. B. Boykin and G. Klimeck, “Practical application of zone-folding concepts in tight-binding calculations,” *Phys. Rev. B*, vol. 71, no. 11, p. 115215, 2005.
- [64] P. V. Medeiros, S. Stafström, and J. Björk, “Effects of extrinsic and intrinsic perturbations on the electronic structure of graphene: Retaining an effective primitive cell band structure by band unfolding,” *Phys. Rev. B*, vol. 89, no. 4, p. 041407, 2014.
- [65] M. Gajdoš, A. Eichler, and J. Hafner, “Ab initio density functional study of O on the Ag(001) surface,” *Surf. Sci.*, vol. 531, no. 3, pp. 272–286, 2003.
- [66] H. Li, J. Quinn, Y. Li, D. Tian, F. Jona, and P. Marcus, “Multilayer relaxation of clean Ag{001},” *Phys. Rev. B*, vol. 43, no. 9, p. 7305, 1991.
- [67] K. Kádas, Z. Nabi, S. Kwon, L. Vitos, R. Ahuja, B. Johansson, and J. Kollár, “Surface relaxation and surface stress of 4d transition metals,” *Surf. Sci.*, vol. 600, no. 2, pp. 395–402, 2006.
- [68] S. Kwon, Z. Nabi, K. Kádas, L. Vitos, J. Kollár, B. Johansson, and R. Ahuja, “Surface energy and stress release by layer relaxation,” *Phys. Rev. B*, vol. 72, no. 23, p. 235423, 2005.

- [69] L. Vitos, A. Ruban, H. L. Skriver, and J. Kollár, “The surface energy of metals,” *Surf. Sci.*, vol. 411, no. 1-2, pp. 186–202, 1998.
- [70] M. S. Daw, S. M. Foiles, and M. I. Baskes, “The embedded-atom method: a review of theory and applications,” *Mater Sci Eng*, vol. 9, no. 7-8, pp. 251–310, 1993.
- [71] R. Pushpa, P. Ghosh, S. Narasimhan, and S. de Gironcoli, “Effective coordination as a predictor of adsorption energies: A model study of NO on Rh(100) and Rh/MgO(100) surfaces,” *Phys. Rev. B*, vol. 79, no. 16, p. 165406, 2009.
- [72] P. Ghosh, R. Pushpa, S. de Gironcoli, and S. Narasimhan, “Effective coordination number: A simple indicator of activation energies for NO dissociation on Rh(100) surfaces,” *Phys. Rev. B*, vol. 80, no. 23, p. 233406, 2009.
- [73] R. Pentcheva and M. Scheffler, “Initial adsorption of Co on Cu(001): A first-principles investigation,” *Phys. Rev. B*, vol. 65, no. 15, p. 155418, 2002.
- [74] L.-J. Chen and R. Wu, “Structural and electronic properties of an ordered alloy surface: rippling and bonding in $c(2 \times 2)$ -SnNi(001),” *Surf. Sci.*, vol. 345, no. 3, pp. L34–L38, 1996.
- [75] D. Li, H. Xiao, X. Zu, and H. Dong, “First-principles study of Sn adsorption on Ni(100),(110) and (111) surfaces,” *Mater. Sci. Eng. A*, vol. 460, pp. 50–57, 2007.
- [76] M. Walker, M. Brown, M. Draxler, M. Dowsett, C. F. McConville, T. Noakes, and P. Bailey, “Structural analysis of the Cu(100)- $p(2 \times 2)$ -Sn surface using low and medium energy ion scattering spectroscopies,” *Phys. Rev. B*, vol. 83, no. 8, p. 085424, 2011.

-
- [77] Y. Nara, K. Yaji, T. Iimori, K. Nakatsuji, and F. Komori, “STM observation of surface phases of Sn/Cu(001),” *Surf. Sci.*, vol. 601, no. 22, pp. 5170–5172, 2007.
- [78] E. Hansen, T. Miller, and T.-C. Chiang, “Overlayer test of surface photoemission effect in Cu(100),” *Phys. Rev. Lett.*, vol. 78, no. 14, p. 2807, 1997.
- [79] S. Chakraborty and K. S. R. Menon, “LEED and photoemission study of growth and structural evolution of Sn on Ag(001),” *Vacuum*, vol. 125, pp. 106–112, 2016.
- [80] S. Hatta, C. Walker, O. Sakata, H. Okuyama, and T. Aruga, “Structure analysis of Cu(001)-c(4 × 4)-In by surface X-ray diffraction,” *Surf. Sci.*, vol. 565, no. 2-3, pp. 144–150, 2004.
- [81] A. Crepaldi *et al.*, “Interplay between electronic and structural properties in the Pb/Ag(100) interface,” *J. Phys. Condens. Matter*, vol. 27, no. 45, p. 455502, 2015.

Chapter 4

Structural, Electronic and Vibrational Properties of CsPbX₃ and Fe-doped CsPbX₃ (X = Br, Cl)

Nothing in life is to be feared, it is only to be understood. Now is the time to understand more, so that we may fear less.

Marie Curie

In this chapter, we study the electronic, photoluminescence and optical properties of pristine CsPbBr₃ and CsPbCl₃, and Fe-doped CsPbBr₃ and CsPbCl₃. This is collaborative work with the group of Prof. Ranjani Viswanatha, New Chemistry Unit, JNCASR, Bangalore. They were able to successfully dope Fe atoms in CsPbBr₃ and CsPbCl₃ nanocrystals. They measured the photoluminescence of the Fe-doped systems, and compared this with the pristine systems. They also did some optical measurements of the pristine CsPbBr₃ and CsPbCl₃ perovskite materials. We have modelled the pristine CsPbX₃ systems along with the Fe-doped CsPbX₃ systems (X

= Br, Cl) at the atomic scale and performed DFT calculations to make insights on structural, electronic, electronic and optical properties.

4.1 Introduction

Perovskite materials have attracted enormous attention due to the very large number of compounds whose crystals form in the perovskite structures, and the fact that their various physical and chemical properties are often of interest for various applications. Perovskite materials have the formula ABX_3 , where A is an organic or inorganic cation such as methylammonium (MA^+ , $CH_3NH_3^+$), formamidinium (FA^+ , $CH_3(NH_2)_2^+$), Cs^+ etc., B is a metal ion such as Pb^{2+} , Sn^{2+} , Bi^{2+} , and X is an anion like halide (F^- , Cl^- , Br^- and I^-) or oxide (O^{2-}). Halide perovskites have recently received a lot of attraction due to their potential applications in devices such as photovoltaic cells,¹ solid-state planar perovskite solar cells,² etc. Halide perovskites have achieved high quantum efficiencies of over 8% in the visible and near infrared regions.³⁻⁵ Very recently, single-junction solar cells made of an organic-inorganic hybrid halide perovskite showed a record efficiency of 23.3%, which is almost comparable to those of the conventional photovoltaics that use materials such as GaAs, CdTe, Si and CuInGaSe. Halide perovskites can also be used as lasers and they have achieved high quality factors.⁶ Perovskite photo-detectors and X-ray detectors have shown high sensitivity with low noise.^{7;8} All these potential applications arise from the excellent electronic and optoelectronic properties of the halide perovskites. Changing the composition of the halide ions in the halide perovskites, the band gap can be tuned and as a result, one can obtain better properties such as increased photoluminescence quantum yield (PLQY) and better stability. However, this compositional engineering has a few limitations: intrinsic structural phase transition and weak stability against moisture, high temperature and light.⁹⁻¹¹

Doping of foreign atoms into the halide perovskite lattice is a more effective way of tuning the electronic and optoelectronic properties of the pristine systems. A low doping percentage is enough to change the properties of the pristine systems hugely and such low percentage doping does not change the crystal structures of the pristine systems. The doping strategy can lead to more optimized and better optoelectronic properties for the technological applications of the halide perovskites. Over the years, many metal ions such as Mn^{2+} , K^+ , Bi^{3+} , Rb^+ , Ce^{3+} , Tb^{3+} , Yb^{3+} , etc. have been doped into the lattices of halide perovskites. This doping strategy changes and improves many of the properties of the pristine systems. To give a few examples, doped halide perovskites can have larger stability, higher PLQY, reduced defect state densities, new emission characteristics etc., which leads to outstanding optoelectronic properties compared to the pristine counterparts.¹²⁻¹⁶ However, there still remain some topics that are not well understood yet, e.g., it is not well understood whether dopants are incorporated into the matrices of the halide perovskites or they remain at the surface. Also, how and why do the dopant atoms change the properties of a pristine system?

Transition metal dopants in perovskite crystals can tune the electronic and optical properties of the pristine systems and could also introduce magnetism in the halide perovskites, which could have applications in spintronics devices.¹⁷⁻¹⁹ Because of the synthesis challenges, very few magnetic dopants have been successfully incorporated into the bulk lattices of the halide perovskites till now. The most common is Mn^{2+} , which gives dual emission: the host's band edge emission and Mn $d-d$ emission.^{13;20;21} For example, Mn-doped CsPbCl_3 nanocrystals (NCs) display band edge emission at 402 nm, and Mn $d-d$ yellow emission (${}^4\text{T}_1 - {}^6\text{A}_1$) at 586 nm (~ 2.1 eV). Due to the spin-forbidden nature, the lifetime of this emission is very high (1.6 ms). For magnetic dopants in the II-VI semiconductors, there is strong exchange interaction between the charge carrier of the host and the d electrons of the

transition metal (e.g., Mn), which drives the excitation energy transfer and creates coupled electronic states between the exciton and the dopant.^{22;23} This results in long-lifetime dopant luminescence and magnetically coupled excitons.^{24–27} In lead halide perovskites, the high tolerance for trap states favors exciton energy transfer to the transition metal d states and hence $d-d$ emission. Another example is Ni^{2+} , which increases PLQY in the halide perovskites NCs.^{28–30}

One of the less studied transition metal dopants is Fe; it is abundant in the earth, environmentally friendly and cheap in price. It was recently found that Fe doping in II-VI semiconductor quantum dots (QDs) results in a magneto-optical Stark effect which has potential applications in spintronics devices.³¹ Fe^{3+} doping in CsPbBr_3 and CsPbCl_3 microwires results in the enhancement of the non-linear absorption coefficient by one order of magnitude, compared to other halide perovskite NCs, which suggests that Fe helps in the two-photon absorption process.³² It has been predicted theoretically that upon Fe doping in CsPbBr_3 , the efficiency of CO_2 conversion into CH_4 increases,³³ which has been further experimentally proved.³⁴ Fe acts as a luminescence quencher for II-VI semiconductors,^{35;36} but the effects of Fe on the optical and electronic properties of halide perovskites are not well understood till date. Also, the effect of magnetism of the Fe dopants on the halide perovskites is less understood. Therefore, a detailed investigation of electronic and optical properties of Fe-doped halide perovskites is highly desirable.

In this chapter, we have carried out theoretical investigations on the structural, magnetic and electronic properties of CsPbBr_3 and CsPbCl_3 upon Fe doping, using DFT calculations. We first look into the effects on the structural properties of Fe incorporation into the lattices of CsPbBr_3 and CsPbCl_3 . We also look into the magnetic properties of the Fe-doped systems. Next, we examine the electronic structure of pristine CsPbBr_3 and CsPbCl_3 and compare the results with those for Fe-doped CsPbBr_3 and CsPbCl_3 . We also suggest a possible reason for the photoluminescence

(PL) quenching upon Fe doping in CsPbBr_3 and CsPbCl_3 . Finally we look into the vibrational properties of the Fe-doped CsPbBr_3 and CsPbCl_3 to try and understand why the PL intensity completely dies, at higher Fe concentration, in one material, but remains constant at a finite value in the other material.

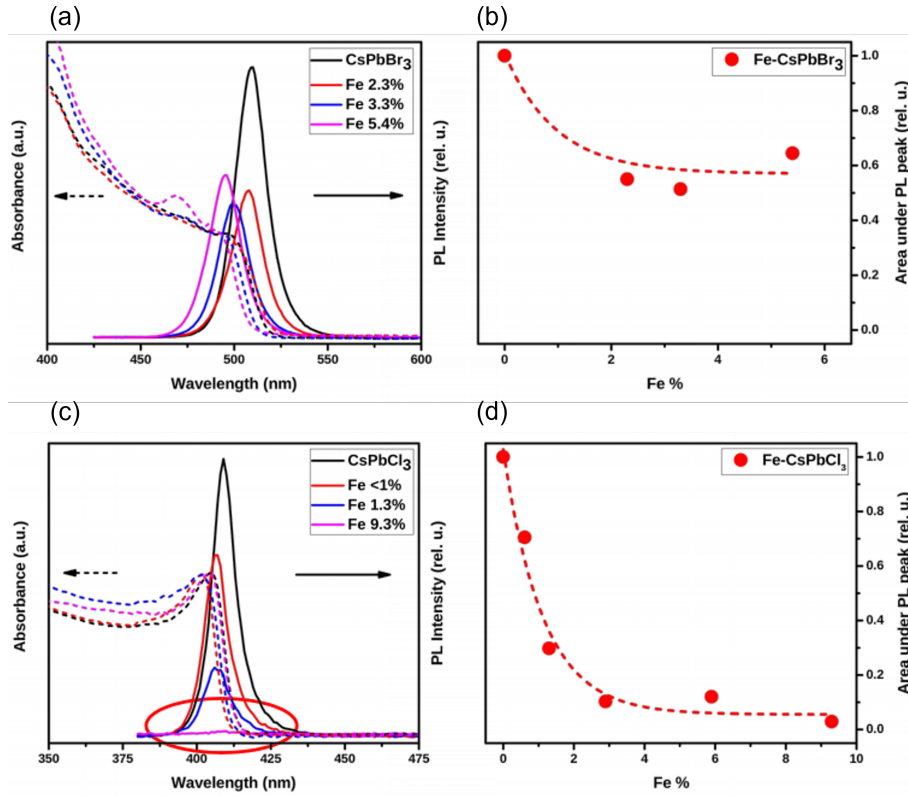


Figure 4.1: Experimental photoluminescence (PL) spectra of pristine CsPbX_3 and Fe-doped CsPbX_3 systems ($X = \text{Br}, \text{Cl}$). (a) and (c) show the change in the PL intensity and absorbance with increasing Fe concentration for Fe-doped CsPbBr_3 and Fe-doped CsPbCl_3 , respectively. (b) and (d) show change in the area under the PL curve with Fe concentration. *This figure is taken from Saptarshi Chakraborty's (NCU, JNCASR) Ph.D thesis and used with permission.*

4.2 Experimental motivation

Our experimental collaborators (PhD student Saptarshi Chakraborty and Prof. Ranjani Viswanatha at JNCASR) investigated the change in the electronic structure of some perovskite quantum dots (QDs) due to the presence of isoelectronic dopants.

They were able to synthesise nanocrystals (NCs) of CsPbBr_3 , CsPbCl_3 , Fe-doped CsPbBr_3 and Fe-doped CsPbCl_3 using a colloidal method. They investigated the structural and optical properties of the NCs using X-ray absorption fine structure (XAFS) spectroscopy and steady-state absorption and emission spectroscopy. Fig. 4.1 shows the measured PL intensity of pristine CsPbBr_3 , CsPbCl_3 and Fe-doped CsPbBr_3 , Fe-doped CsPbCl_3 , with different Fe concentrations. Fig. 4.1(a) and (c) show PL intensity and absorbance of pristine systems and Fe-doped systems. Fig. 4.1(b) and (d) show the variation of area under the PL curve with Fe concentration, for both Fe-doped CsPbBr_3 and Fe-doped CsPbCl_3 , respectively. It was seen in the experiments that upon Fe doping in the pristine CsPbBr_3 and CsPbCl_3 NCs, the PLQY is reduced. The PL spectra and PLQY behave differently for Fe-doped CsPbBr_3 and Fe-doped CsPbCl_3 . They observed that as the Fe concentration increases, the PL intensity decreases drastically and is completely quenched at around 9% Fe concentration for Fe-doped CsPbCl_3 . However, for Fe-doped CsPbBr_3 , though the PL intensity reduces with respect to pristine CsPbBr_3 with increasing Fe concentration, the PL intensity is not quenched completely and remains constant at a finite value for Fe concentrations beyond 2%.

Based on the above described experimental observations we ask the following questions: (i) why is the PL intensity reduced upon Fe doping in both CsPbBr_3 and CsPbCl_3 crystals, and (ii) why is the behaviour different in Fe-doped CsPbBr_3 and Fe-doped CsPbCl_3 at higher Fe concentrations?

4.3 Computational details

DFT calculations were performed using the Quantum ESPRESSO software package.^{37;38} The Kohn-Sham wavefunctions and the corresponding charge densities were expanded in plane-wave basis sets having cutoffs of 40 Ry and 400 Ry, respectively.

Exchange-correlation interactions were treated using the Perdew-Burke-Ernzerhof form of the Generalized Gradient Approximation (PBE-GGA).³⁹ The interactions between valence electrons and ionic cores were described using ultrasoft pseudopotentials.⁴⁰

The pristine CsPbBr₃ and CsPbCl₃ crystals were modelled with five-atom cubic unit cells, forming perovskite structures. In the perovskite unit cells, we have a Pb-Br₆ or Pb-Cl₆ octahedral environment in which one Pb atom is surrounded by six Br/Cl atoms. For the Fe-doped systems we considered $2 \times 2 \times 2$ supercells in which either one Pb atom was substituted by one Fe atom to make 12.5% Fe-doped systems, or two Pb atoms were substituted by two Fe atoms to make 25% Fe-doped systems. For the pristine systems we have optimized the lattice parameters; due to the symmetry of the systems, all forces on atoms were zero. For the Fe-doped systems, all the cell parameters and atomic coordinates were relaxed using the Broyden-Fletcher-Goldfarb-Shanno (BFGS) algorithm^{41–44}, until all components of the forces on all atoms were less than 0.001 Ry/Bohr. Brillouin zone sampling was done using an $8 \times 8 \times 8$ Monkhorst-Pack k-point mesh for the primitive unit cells and $4 \times 4 \times 4$ for the supercells.⁴⁵ Marzari-Vanderbilt cold smearing of width 0.005 Ry was used to improve convergence. Since there are heavy elements like Pb and Br, we have taken into account the spin-orbit effects using fully relativistic pseudopotentials.

The vibrational properties of Fe-doped CsPbBr₃ and Fe-doped CsPbCl₃ are calculated in their optimized geometries, by calculating the dynamical matrices using Density Functional Perturbation Theory (DFPT), as implemented in ‘PHONON’ package³⁷ of Quantum ESPRESSO. We have used a $2 \times 2 \times 2$ q-point mesh for these calculations. Scalar-relativistic ultrasoft pseudopotentials are used for the DFPT calculations of phonons. The threshold for self-consistency of DFPT calculation was chosen to be 10^{-14} .

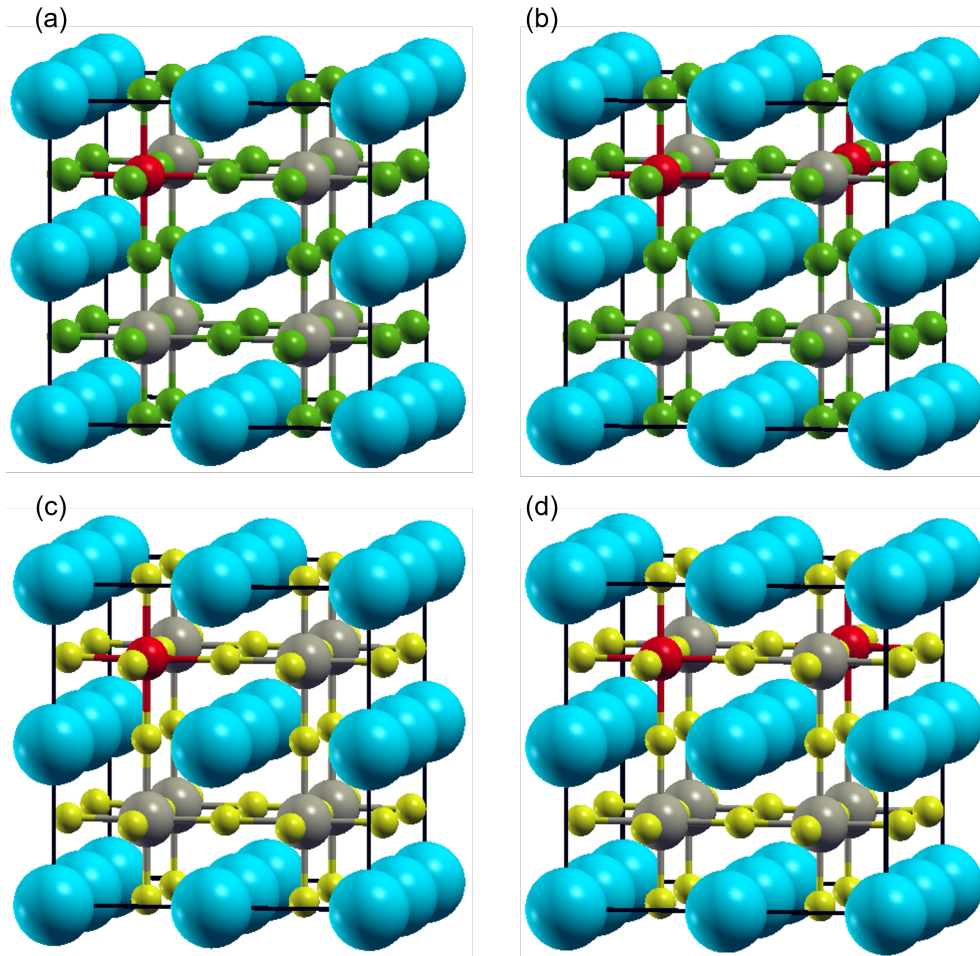


Figure 4.2: Systems studied in our DFT calculations: (a) 12.5% Fe-doped CsPbBr_3 , (b) 25% Fe-doped CsPbBr_3 , (c) 12.5% Fe-doped CsPbCl_3 , and (d) 25% Fe-doped CsPbCl_3 . A $2 \times 2 \times 2$ supercell contains 8 Cs, 7(6) Pb, 1(2) Fe and 24 Br/Cl atoms for 12.5%(25%) Fe concentrations. Only the lowest energy structures are shown at 25% Fe concentration in which two Fe atoms are 2nd NN or face-diagonal. Atomic color code: Cyan – Cs, Gray – Pb, Green – Br, Yellow – Cl, Red – Fe.

4.4 Systems under study

Though the experiments were performed on NCs and not bulk crystals, the size of the NCs is very large (few tens of nm). We have therefore performed theoretical calculations using density functional theory (DFT) by taking the bulk structures of the pristine and Fe-doped perovskite materials. We have used DFT for the electronic structure calculations and density functional perturbation theory (DFPT) for the

vibrational properties of the crystalline solids. We took cubic crystals of CsPbBr₃ and CsPbCl₃ perovskites which consist of 1 Cs atom, 1 Pb atom and 3 Br/Cl atoms in the primitive unit cell. For the Fe-doped systems, we considered $2 \times 2 \times 2$ supercells in which one Pb atom was substituted by one Fe atom to make 12.5% Fe-doped systems and 2 Pb atoms were substituted by 2 Fe atoms to make 25% Fe-doped systems. Fig. 4.2 shows the structures of 12.5% and 25% Fe-doped CsPbBr₃ and Fe-doped CsPbCl₃ in the $2 \times 2 \times 2$ supercells. Various inequivalent ways of positioning these two substituent atoms in the supercell are possible; this point is discussed further below. Though in the experiments the Fe concentration was less than 13%, we have considered higher concentrations in our calculations to avoid the use of larger supercells which would be computationally costly. We note also that the only difference found in the experimental PL spectra of Fe-doped CsPbBr₃ and Fe-doped CsPbCl₃ was at higher Fe concentrations.

4.5 Results and discussion

4.5.1 Lattice parameters of CsPbX₃ and Fe-doped CsPbX₃ (X = Br, Cl)

We have calculated the optimized lattice constant of pristine CsPbBr₃ as 6.01 Å, which is in excellent agreement with a previous theoretical value of 6.00 Å,⁴⁶ but larger than our experimental value of 5.85 Å for the CsPbBr₃ NC and an earlier experimental value of 5.87 Å⁴⁷ for bulk CsPbBr₃. Our optimized lattice constant for CsPbCl₃ is 5.74 Å which is in excellent agreement with a previous theoretical value of 5.73 Å⁴⁶ but larger than our experimental value of 5.62 Å for the CsPbCl₃ NC and an earlier experimental value of 5.61 Å⁴⁷ for bulk CsPbCl₃. The difference in the lattice parameters between theory and experiment is presumably an example

of the well known tendency of the GGA to overestimate lattice constants.

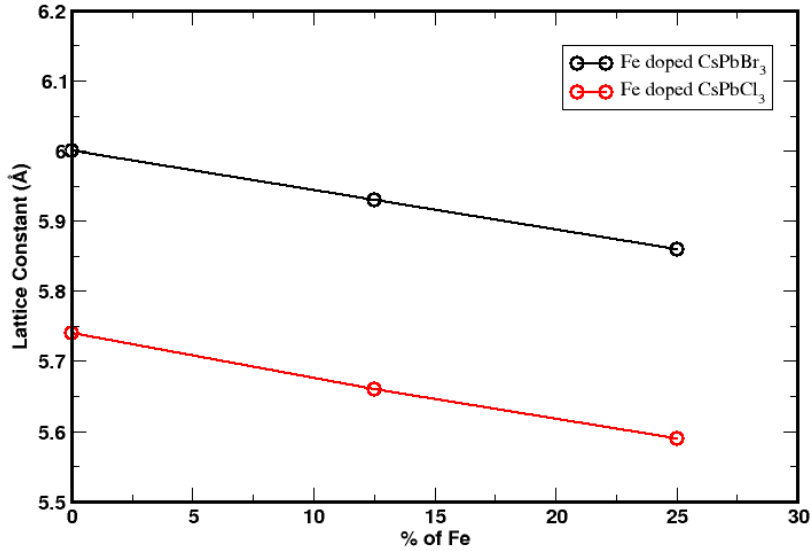


Figure 4.3: Lattice constants of pristine CsPbBr₃ and Fe-doped CsPbBr₃ (black circles), and of CsPbCl₃ and Fe-doped CsPbCl₃ (red circles). Black and red lines are linear fits to the data.

Next, we consider Fe doping in the pristine systems. We have taken $2 \times 2 \times 2$ supercells of CsPbBr₃ and CsPbCl₃ and substitute one or two Pb atoms by one or two Fe atoms to get 12.5% and 25% Fe-doped systems. Upon Fe doping into the systems, all the atomic coordinates as well as the cell parameters are relaxed to find the ground state structures.

For 12.5% Fe-doped CsPbBr₃ and Fe-doped CsPbCl₃, only one nonequivalent structure is possible – all the eight Pb sites are identical for a Fe atom. However, for 25% Fe-doped CsPbBr₃ and Fe-doped CsPbCl₃, there are three nonequivalent structures are possible - (i) two Fe atoms can occupy nearest-neighbor Fe sites, i.e., they sit side by side at a distance equal to the lattice parameter of CsPbCl₃, (ii) two Fe atoms can occupy next-neighbor Fe sites, i.e., they sit along the diagonals of a square at a distance $\sqrt{2}$ times lattice constant of CsPbCl₃, and (iii) two Fe atoms

Fe-Fe arrangement	ΔE for FM (meV)	ΔE for AFM (meV)
1st NN	364	333
2nd NN	0	71
3rd NN	387	379

Table 4.1: DFT energetics of different structures of Fe-doped CsPbBr₃, for 25% Fe concentration. In the different structures, the two Fe atoms in the unit cells are at different distances from each other; they also differ in their relative magnetic ordering. ΔE_{ads} denotes the energy of a given configuration with respect to the lowest energy configuration.

Fe-Fe arrangement	ΔE for FM (meV)	ΔE for AFM (meV)
1st NN	397	384
2nd NN	0	36
3rd NN	329	330

Table 4.2: DFT energetics of different structures of Fe-doped CsPbCl₃, for 25% Fe concentration. In the different structures, the two Fe atoms in the unit cells are at different distances from each other; they also differ in their relative magnetic ordering. ΔE_{ads} denotes the energy of a given configuration with respect to the lowest energy configuration.

can occupy next-nearest-neighbor Fe sites, i.e., they sit along the body diagonals of a cube at a distance $\sqrt{3}$ times lattice constant of CsPbCl₃. We have considered all these configurations of Fe doping and optimized the lattice parameters. Tables 4.1 and 4.2 show the DFT calculated energetics of different configurations which differ in the relative position of the two Fe dopant atoms, i.e., they are at different distances from each other [such as first nearest neighbor (NN) or adjacent, second NN or face-diagonal and third NN or body-diagonal], and also have different magnetic ordering with respect to each other [the two Fe atoms have ferromagnetic (FM) ordering or anti-ferromagnetic (AFM) ordering] for 25% Fe-doped CsPbBr₃ and 25% Fe-doped CsPbCl₃, respectively. We see that for both the systems, the lowest energy configuration is when the two Fe atoms are second NN or face-diagonal, having FM ordering. All the further calculations are done for these lowest energy configurations

only.

The calculated lattice parameters of 12.5% and 25% Fe-doped CsPbBr₃ are 5.899 Å and 5.802 Å, respectively. Similarly, the calculated lattice parameters of 12.5% and 25% Fe-doped CsPbCl₃ are 5.629 Å and 5.538 Å, respectively. We see a gradual decrease in the lattice constant upon increasing the Fe concentration. This is due to the smaller size of a Fe atom than a Pb atom. We also find a linear relationship between the lattice constant and Fe concentration, as shown in Fig. 4.3.

4.5.2 Stability of pristine CsPbX₃ and Fe-doped CsPbX₃ (X = Br, Cl)

Though all-inorganic halide perovskites have gained tremendous attention due to their potential applications, they have some problems: they are thermally unstable, and are also unstable with respect to oxidation and moisture. Doping of foreign atoms such as transition metal ions into the matrix of the pristine systems provides better stability to the systems.

We will first check whether Fe-doping makes any improvement on the stability of CsPbBr₃ and CsPbCl₃. For this, we calculate the formation energy of pristine and Fe-doped systems.

The formation energy of pristine CsPbX₃ (X = Br, Cl) is given by,

$$\Delta H = \frac{1}{N} [E_{CsPbX_3} - \mu_{Cs} - \mu_{Pb} - 3\mu_X]. \quad (4.1)$$

The formation energy of Fe-doped CsPbX₃ (X = Br, Cl) is given by,

$$\Delta H = \frac{1}{N} [E_{Fe-CsPbX_3} - \mu_{Cs} - (1-x)\mu_{Pb} - 3\mu_X - x\mu_{Fe}], \quad (4.2)$$

where, E_{CsPbX_3} and $E_{Fe-CsPbX_3}$ are the total energy of pristine and Fe-doped systems, μ 's are the chemical potentials of the atoms and are taken as the total energy

of isolated atoms, x is the dopant Fe concentration. There is no universal rule for how to choose of chemical potentials of the elements, in the above equations. Some authors use the total energies of the isolated atoms (as we have done), others use the bulk atom energy, and yet others use many other reference systems (depending on the method of synthesis) to calculate the single atom's energy.

System	Formation energy (eV)
CsPbBr ₃	-2.31
12.5% Fe-CsPbBr ₃	-2.37
25% Fe-CsPbBr ₃	-2.44
CsPbCl ₃	-2.62
12.5% Fe-CsPbCl ₃	-2.69
25% Fe-CsPbCl ₃	-2.77

Table 4.3: Calculated formation energies of pristine and Fe-doped systems.

Table 4.3 shows the calculated formation energy of pristine CsPbX₃ and Fe-doped CsPbX₃ (X = Br, Cl) systems. We see that formation energy becomes more negative upon Fe doping for both Fe-doped CsPbBr₃ CsPbCl₃. This means Fe doping increases the stability with respect to the pristine counterparts. Also, we see that stability increases with increasing Fe concentration. Another point is that the chloride systems are more stable than the bromide systems, even after Fe doping.

4.5.3 Electronic structure of pristine CsPbBr₃ and CsPbCl₃

The electronic structure of pristine CsPbBr₃ is shown in Fig. 4.4. The band structure and orbital projected density of states (PDOS) confirm that there is a finite gap in this material which indicates that this material is a semiconductor. We have done calculations both without spin-orbit coupling (SOC) and with SOC, and compared the results. Our PBE-GGA calculated band gap of CsPbBr₃, without SOC, is 1.79 eV; this is in excellent agreement with a previous DFT calculated value of 1.79 eV⁴⁶ and smaller than the experimental gap of 2.36 eV⁴⁸ for bulk CsPbBr₃, and

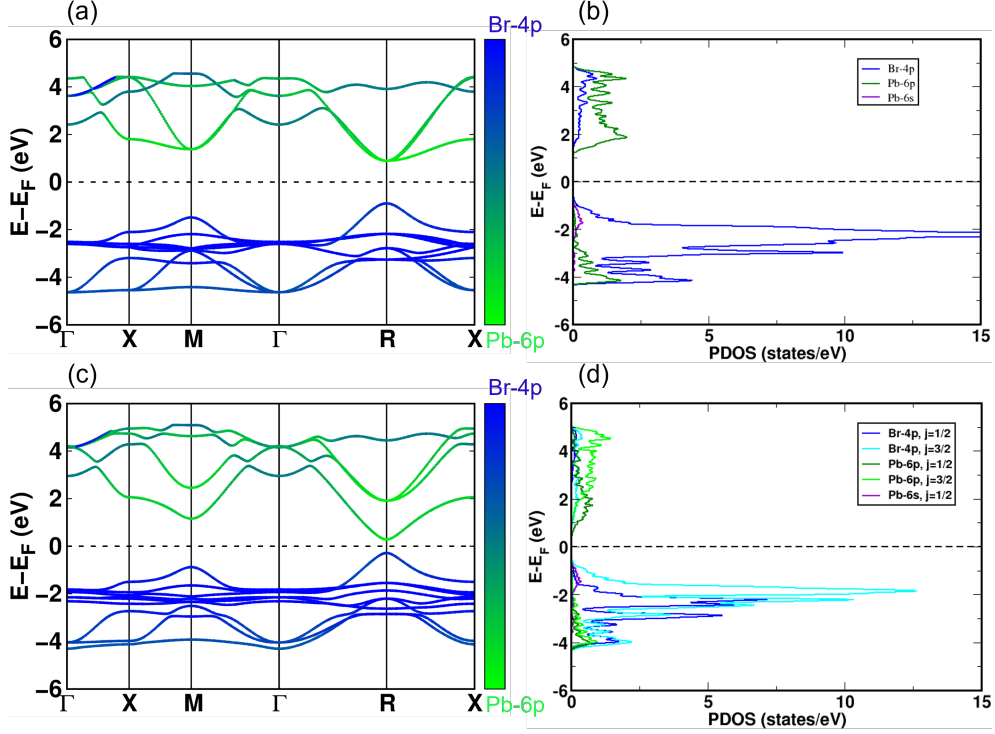


Figure 4.4: Electronic structure of pristine CsPbBr₃. Panels (a) and (b) show the orbital-projected band structure and projected density of states (PDOS), respectively, of CsPbBr₃, without spin-orbit coupling (SOC). Panels (c) and (d) show the orbital-projected band structure and PDOS, respectively, of CsPbBr₃, with SOC. The PDOS confirms that the main contributions come from Pb-6p and Br-4p orbitals, we have projected the band structures onto these orbitals and shown the relative contributions from these two orbitals according to the color scale. Orbital contributions in the band structure plots: Green - Pb-6p and Blue - Br-4p.

our experimental gap of 2.42 eV for the CsPbBr₃ NCs. This underestimation in the calculated value for band gap is due to the use of PBE-GGA. We have projected the Kohn-Sham wave functions onto the individual atomic orbitals for band structure and density of states calculations. The projected density of states (PDOS) tells us that the valence bands mainly arise from Br-4p orbitals and the conduction bands mainly arise from Pb-6p orbitals. Hence, we have projected the band structure onto these two orbitals and compared the orbital contributions as shown by the two-color band structures in Fig. 4.4(a) and (c). We see that both valence band maximum (VBM) and conduction band minimum (CBM) lie at the *R* point of the Brillouin

zone (BZ), giving CsPbBr₃ as a direct gap semiconductor. Upon the inclusion of SOC, some degenerate bands split, both in the conduction and valence states. There is no splitting in VBM as this has mostly Br character, and Br is a light element. In contrast, the CBM splits as this is due to heavy Pb element, which results in a decrease in the band gap. The value of the band gap in the presence of SOC is 0.567 eV. This value matches well with a previous PBE-GGA calculated value of 0.61 eV.⁴⁹ The PDOS is shown with each j resolved in Fig. 4.4(d). We observe significant splitting in the Pb-6p states into $j_{1/2}$ and $j_{3/2}$ energy levels.

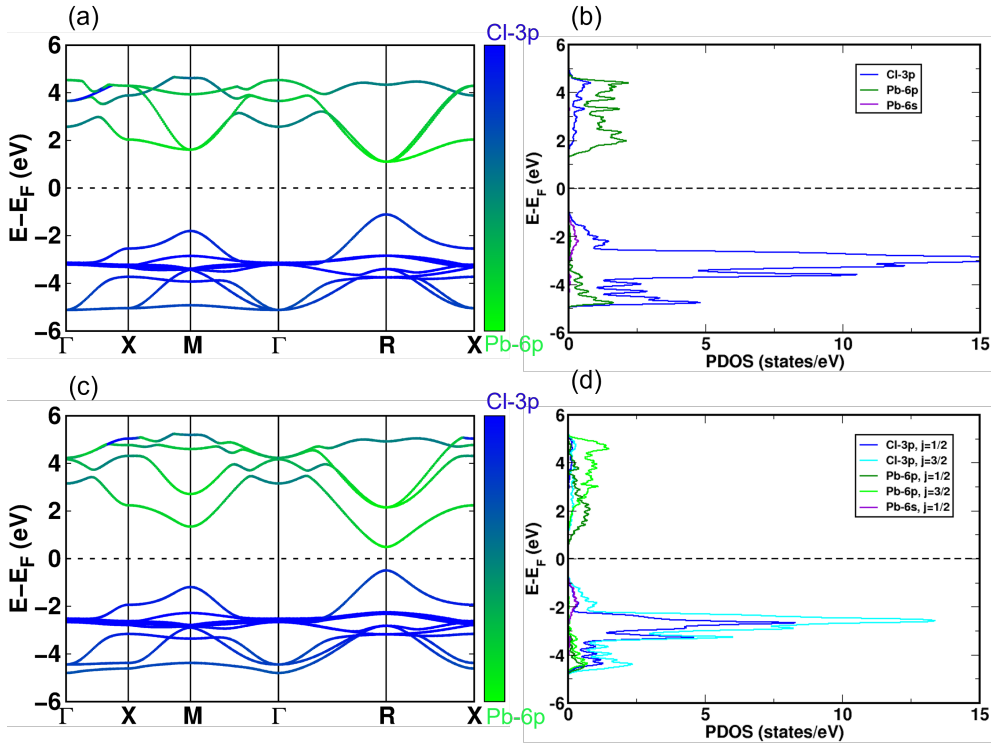


Figure 4.5: Electronic structure of pristine CsPbCl₃. (a) and (b) are projected band structure and PDOS, respectively, of CsPbCl₃, without spin-orbit coupling (SOC). (c) and (d) are the same of CsPbCl₃, with SOC. PDOS confirms that the main contributions come from Pb-6p and Cl-3p orbitals, we have projected the band structures onto these orbitals and shown a comparison according to the color scale. Orbital contributions in the band structures plots: Green - Pb-6p and Blue - Cl-3p.

The band structure and PDOS of CsPbCl₃ are shown in Fig. 4.5, without and

with SOC. This is also a semiconductor with a calculated gap of 2.22 eV in our PBE-GGA calculation, without SOC; this is in excellent agreement with a previous DFT calculated value of 2.21 eV and smaller than the experimental gap of 3.0 eV⁴⁸ for bulk CsPbCl₃, and our experimental gap of 3.0 eV for CsPbCl₃ NCs. Similar to the case of CsPbBr₃, the valence and conduction bands are mainly contributed by Cl-3*p* and Pb-6*p* orbitals, respectively. CsPbCl₃ is also a direct gap semiconductor with VBM and CBM both lying at the *R* point of the BZ. The two-color projected band structures show the relative contributions of Pb-6*p* and Cl-3*p* orbitals. Upon the inclusion of SOC, splitting is observed in both valence and conduction bands. However, similar to the case of CsPbBr₃, the VBM does not split as its main contributions come from the relatively light Cl atoms. However, the CBM at the *R* point splits, as its main contributions are from the heavy Pb atoms; it moves downward in energy, which decreases the band gap. The value of the SOC induced gap is 0.985 eV.

4.5.4 Spin-polarization of Fe-doped CsPbBr₃ and Fe-doped CsPbCl₃

Pristine CsPbBr₃ and CsPbCl₃ are non-magnetic materials. When we do the substitutional doping of the Fe atoms, as Fe atoms have very large magnetic moments, this makes the Fe-doped CsPbBr₃ and Fe-doped CsPbCl₃ magnetic or spin-polarized. For all the Fe-doped systems considered here, the DFT calculated total magnetization is 4.00 μ_B per Fe atom per unit cell. For 12.5% Fe-doped CsPbBr₃, the value of the magnetic moment on each Fe atom is 3.57 μ_B and that on each adjacent Br atom is 0.05 μ_B . For 25% Fe-doped CsPbBr₃, the moment on each Fe atoms is 3.55 μ_B and that on each adjacent Br atom is 0.08 μ_B . For Fe-doped CsPbCl₃, the moment on each Fe atom is 3.62 μ_B and that on each adjacent Cl atom is 0.05 μ_B . For 25% Fe-doped CsPbCl₃, the moment on each Fe atom is 3.60 μ_B and that on

each adjacent Cl atom is $0.08 \mu_B$.

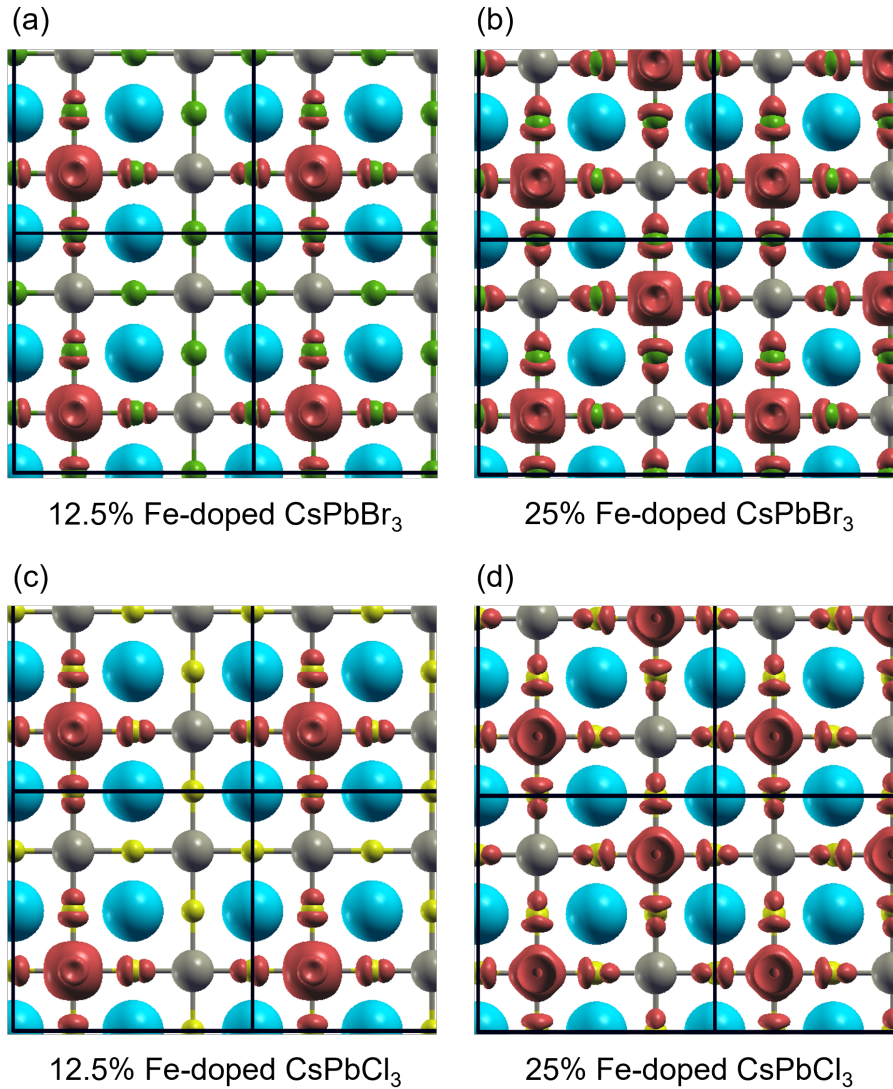


Figure 4.6: Isosurfaces of the spin-polarization density or magnetization density $[m(\mathbf{r}) = n^\uparrow(\mathbf{r}) - n^\downarrow(\mathbf{r})]$ of Fe-doped CsPbBr₃ for (a) 12.5% and (b) 25% Fe concentration, and of Fe-doped CsPbCl₃ for (c) 12.5% and (d) 25% Fe concentration. Red and blue lobes represent $m(\mathbf{r}) > 0$ and $m(\mathbf{r}) < 0$, respectively. We note strong magnetic moments on Fe atoms, plus small magnetic moments on the Br/Cl atoms adjacent to the Fe atoms. Isovalue used = $\pm 0.001 \text{ e/bohr}^3$. We do not see any blue lobes at this isovalue.

Fig. 4.6 shows the spin-polarization density (or magnetization density) for the Fe-doped systems, where the magnetization density is given by, $m(\mathbf{r}) = n^\uparrow(\mathbf{r}) - n^\downarrow(\mathbf{r})$; here $n^\uparrow(\mathbf{r})$ and $n^\downarrow(\mathbf{r})$ are the electronic densities for up and down spins, respectively.

Red lobes correspond to $m(\mathbf{r}) > 0$, indicating that the majority spins are up spins at that location in space, and blue lobes correspond to $m(\mathbf{r}) < 0$, indicating the majority spins are down spins at that location in space. The isovalue used for the magnetization density plots is $+/- 0.001 \text{ e/bohr}^3$. The size of the lobe surrounding an atom is an indication of the magnitude of the magnetic moment on that atom. We clearly see high magnetic moments on the Fe atoms, along with small moments on the adjacent Br/Cl atoms, consistent with the previous paragraph. In these plots, we see only red lobes, we do not see any blue lobes, which means $m(\mathbf{r}) > 0$ everywhere in space, indicating all the spins are aligned in the same direction, making the systems ferromagnetic. The values of the magnetic moments on Cs and Pb atoms are negligible, also the moments on the Br/Cl atoms which are far away from the Fe atoms are also negligible.

4.5.5 Electronic structure of Fe-doped CsPbBr₃ and Fe-doped CsPbCl₃

Next, we considered the effect of the incorporation of the Fe atoms in CsPbBr₃ and CsPbCl₃. For that, we have considered substitutional doping of Fe atoms in place of the Pb atoms in the unit cell of CsPbBr₃ and CsPbCl₃. Though in the experiments, Fe-doping concentrations were always less than 13%, we have taken $2 \times 2 \times 2$ supercells to reduce computational costs; we therefore substitute one/two Pb atoms by one/two Fe atoms to achieve a 12.5%/25% Fe-doping concentrations in our DFT calculations.

We have done both without SOC (scalar-relativistic) and with SOC (fully-relativistic) calculations. The projected density of states (PDOS) plots for Fe-doped CsPbBr₃ are shown in Fig. 4.7. Fig. 4.8 shows the orbital projected band structure of Fe-doped CsPbBr₃. Fig. 4.9 shows the PDOS of Fe-doped CsPbCl₃ and Fig. 4.10 shows

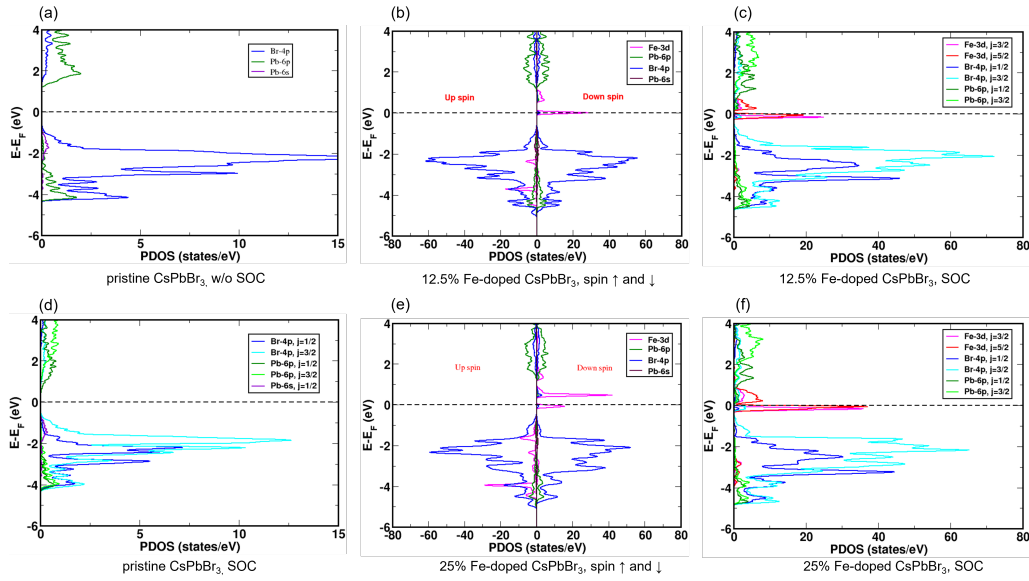


Figure 4.7: Orbital projected density of states (PDOS) of Fe-doped CsPbBr₃ and comparison with the PDOS of pristine CsPbBr₃. (a) and (d) are PDOS of pristine CsPbBr₃ without SOC and with SOC, respectively. PDOS of 12.5% Fe-doped CsPbBr₃ is shown in (b) without SOC, for spin up and down, and (c) with SOC. PDOS of 25% Fe-doped CsPbBr₃ is shown in (e) without SOC, for spin up and down, and (f) with SOC. The main contributions come from three orbitals: Fe-3*d*, Br-4*p* and Pb-6*p*.

the orbital projected band structure of Fe-doped CsPbCl₃. These figures contain results for 12.5% and 25% Fe concentrations, without SOC and with SOC. Both Fe-doped CsPbBr₃ and Fe-doped CsPbCl₃ show very similar electronic structure. For better comparison, the PDOS plots also contain the PDOS of the respective pristine systems.

After Fe doping, similar to the pristine systems, the valence bands are mainly contributed by Br-4*p* (for Fe-doped CsPbBr₃) or Cl-3*p* (for Fe-doped CsPbCl₃) orbitals and the conduction bands are mainly contributed by Pb-6*p* orbitals [see Fig. 4.7(b)-(d) and 4.9(b)-(d)]. Upon Fe doping, the main change we notice is the appearance of Fe-3*d* states in both Fe-doped CsPbBr₃ and Fe-doped CsPbCl₃, in the middle of the band gap region of the respective pristine systems. Near the Fermi level, the main contributions come from three atomic orbitals: Fe-3*d*, Br-4*p*

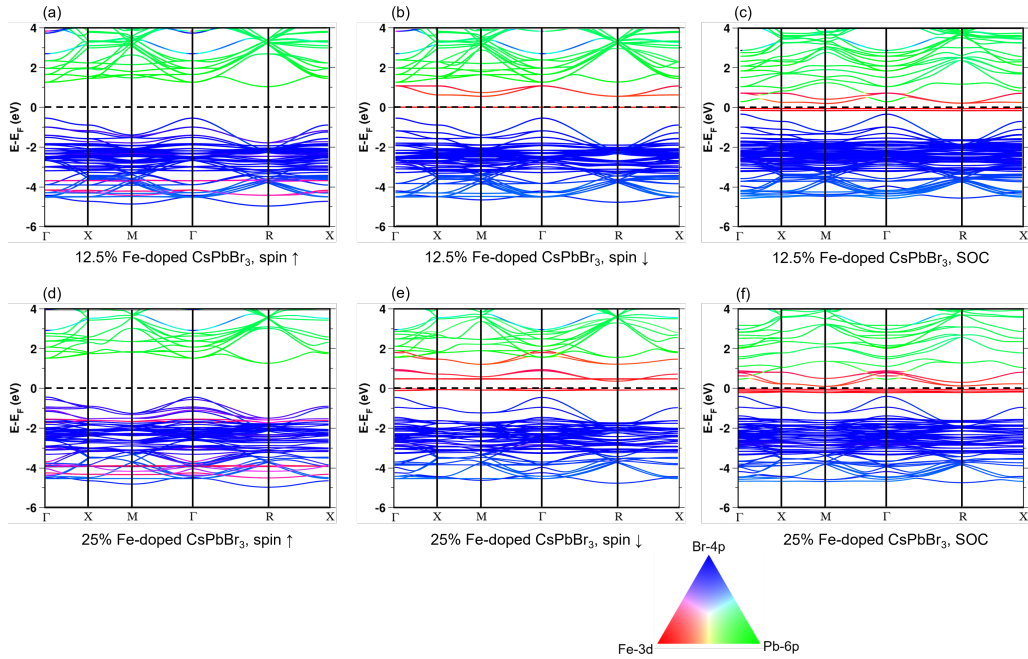


Figure 4.8: Orbital projected band structure of Fe-doped CsPbBr_3 . At 12.5% Fe concentration, (a), (b) are without SOC, for spin up and down, respectively, and (c) is with SOC. At 25% Fe concentration, (d), (e) are without SOC, for spin up and down, respectively, and (f) is with SOC. The bands are projected onto three atomic orbitals, which have the most contributions near the Fermi level, as shown in the three-color triangle - red: Fe-3d, blue: Br-4p and green: Pb-6p. The intermediate colors indicate the extent of mixing of these orbital contributions.

or Cl-3p and Pb-6p. That is why the bands are projected onto these three orbitals, the relative contributions are shown by three-color plots as shown in Fig. 4.8 and 4.10, where red, blue and green represent contribution of Fe-3d, Br-4p or Cl-3p and Pb-6p states, respectively. Intermediate colors represent the degree of mixing or hybridization of the orbitals.

Doping by the magnetic Fe atoms makes the Fe-doped systems magnetic. When SOC is not included, near the Fermi level, there are no spin up states which crosses the Fermi level. However, there are some Fe-3d spin down states which cross the Fermi level 4.7(b), (e) and 4.9(b), (e). This suggests that both Fe-doped CsPbBr_3 and Fe-doped CsPbCl_3 are half-metallic, i.e., one spin channel can conduct and the other spin channel is insulating, making these materials useful for spintronics devices.

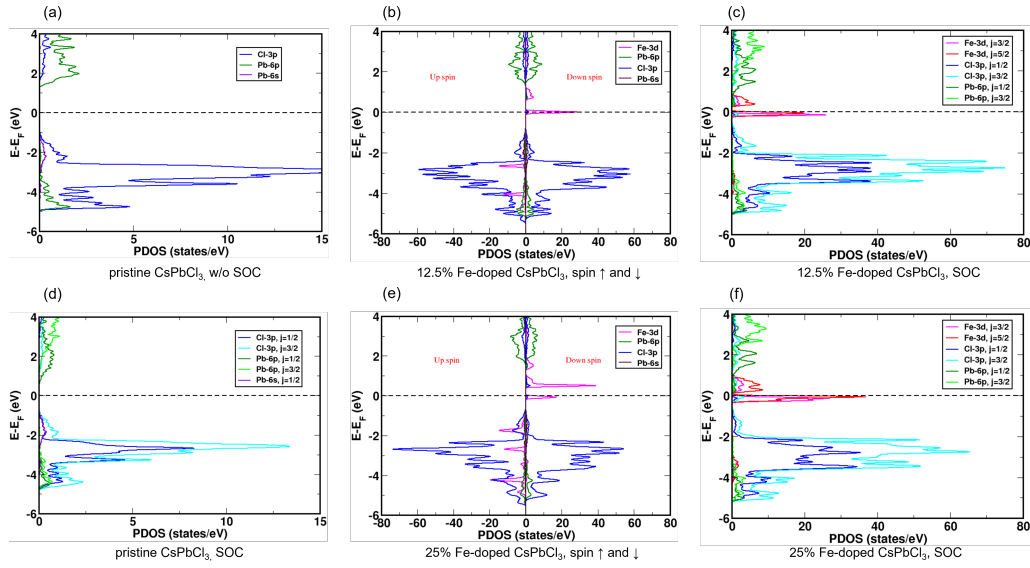


Figure 4.9: Orbital projected density of states (PDOS) of Fe-doped CsPbCl_3 and comparison with the PDOS of pristine CsPbCl_3 . (a) and (d) are PDOS of pristine CsPbCl_3 without SOC and with SOC, respectively. PDOS of 12.5% Fe-doped CsPbCl_3 is shown in (b) without SOC, for spin up and down, and (c) with SOC. PDOS of 25% Fe-doped CsPbCl_3 is shown in (e) without SOC, for spin up and down, and (f) with SOC. The main contributions come from three orbitals: Fe-3d, Cl-3p and Pb-6p.

In both the Fe-doped systems, two types of Fe-3d states arise: one consists of very flat and localized Fe-3d states, in the mid gap region and the other is broadly dispersive and more extended Fe-3d states very close to the conduction bands hybridizing with the Pb-6p states. When SOC is incorporated, the splitting of the Br-4p or Cl-3p valence states is less, whereas since SOC is higher for the heavy Pb elements, making a large splitting of the Pb-6p states in the conduction band into $j = 1/2$ and $j = 3/2$ states. The SOC induced splitting is shown according to the j -values of the orbitals (j is a good quantum number when SOC is included) in the PODS plots [see Fig. 4.7 and 4.9]. Pb-6p, $j = 1/2$ states shift downward in energy which leads to stronger hybridization with the Fe-3d states. This hybridization is also clear in the orbital projected band structures [see Fig. 4.8 and 4.10].

When a photon of band-edge energy is incident on the pristine systems, an electron makes a transition from the Br-4p or Cl-3p valence band to the Pb-6p

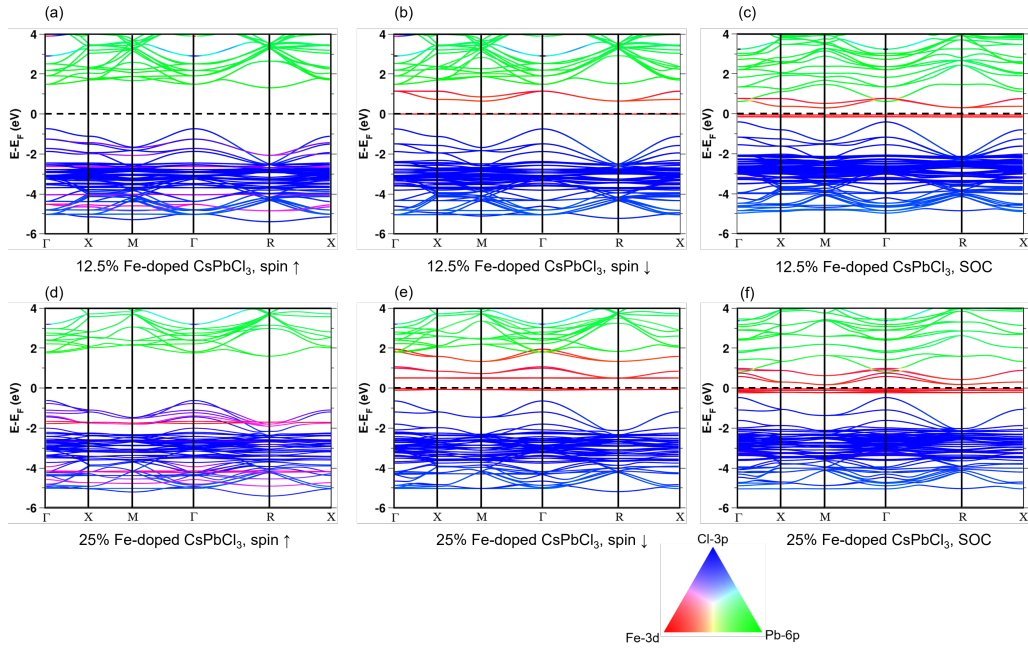


Figure 4.10: Orbital projected band structure of Fe-doped CsPbCl_3 . At 12.5% Fe concentration, (a), (b) are without SOC, for spin up and down, respectively, and (c) is with SOC. At 25% Fe concentration, (d), (e) are without SOC, for spin up and down, respectively, and (f) is with SOC. The bands are projected onto 3 atomic orbitals, which have the most contributions near the Fermi level, as shown in the three-color triangle - red: Fe-3d, blue: Cl-3p and green: Pb-6p. The intermediate colors correspond to mixing of the orbital contributions.

conduction band. This leads to the formation of a bound state between the electron in the conduction band and the newly born hole in the valence band. This bound electron-hole pair is called an exciton. To release its excitation energy, the excited electron then comes back to the valence band and recombines with the hole, resulting in the emission of a photon of band-edge energy and high photoluminescence (PL) i.e., the excitation energy of the electrons is converted into photons of the same energy. This is known as radiative recombination. This leads to a very high PL intensity for the pristine systems [see Fig. 4.1].

As already mentioned, in both Fe-doped CsPbBr_3 and Fe-doped CsPbCl_3 , Fe-3d states arise in the mid gap region and hybridize with Pb-6p conduction bands. As a result, the excited electrons in the conduction bands do not directly recombine

with the hole in the valence bands, instead, they get trapped by the mid-gap Fe-3d states. This transition from the Pb-6p states in the conduction band to the Fe-3d mid gap states is not photon-emitting or not radiative, unlike in the pristine systems. Rather the excitation energy of the electrons is converted into the lattice thermal vibrational energy i.e., phonons. Since no photon is emitted in this process, this is called a non-radiative process, and this is the reason for the reduction in the PL intensity in the Fe-doped systems as observed in the measurements (recall Fig. 4.1). So, this explains why the PL intensity is less in the Fe-doped systems than in the pristine systems.

Another point is that the sharp Dirac-delta like nature of the Fe-3d states in the mid gap region (as shown in the PDOS plots, see Fig. 4.7 and 4.9) hints that there should be some Fe-3d flat bands in the mid gap region; this is reflected in the three-color projected band structure plots [see Fig. 4.8 and 4.10], where we see some completely non-dispersive flat Fe-3d bands in the mid gap region. The effective mass of the trapped electrons in the flat bands is extremely large. So, once the excited electrons get trapped by these flat Fe-3d bands, it is very difficult for them to return back to the conduction bands or combine with a hole in the valence bands. These flat bands also lie away from both valence and conduction bands, hence the flat bands act like deep trap states. This increases the non-radiative decay and hence results in PL quenching.

We also observe that as the Fe concentration increases, the density of the Fe-3d energy levels in the mid-gap region increases, as clear in the DFT calculated three-color band structure plots in Fig. 4.8 and 4.10, as well as from the peak heights in the PDOS plots in Fig. 4.7 and 4.9, which results in an increase in the non-radiative decay process from the Pb-6p conduction bands to the Fe-3d mid-gap levels. So, the PL intensity is quenched more as the Fe concentration increases (see Fig. 4.1), consistent with the experimental observations.

Since the electronic structure is similar in both Fe-doped CsPbBr₃ and Fe-doped CsPbCl₃ systems, one would expect, based on the above arguments, that the PL quenching should increase with increasing Fe concentration and the PL intensity should finally be completely quenched, in both the systems. However, this is not the case, we will next try to understand this.

4.5.6 Vibrational properties of Fe-doped CsPbBr₃ and Fe-doped CsPbCl₃

As the electronic structure is similar in both Fe-doped CsPbBr₃ and Fe-doped CsPbCl₃ systems, one might expect that the PL quenching should increase with increasing Fe concentration and then finally the PL should be completely quenched, in both the systems. However, as discussed above, experiments show a difference between the behavior of Fe-doped CsPbBr₃ and Fe-doped CsPbCl₃. At around 3% Fe concentration, the PL intensity reduces to zero for the Fe-doped CsPbCl₃, whereas for Fe-doped CsPbBr₃ the PL intensity does not go zero, rather it remains constant at some finite value as the Fe concentration increases (see Fig. 4.1). This discrepancy leads us to calculate the vibrational properties of the Fe-doped CsPbBr₃ and Fe-doped CsPbCl₃.

We wish to see whether the behaviour of vibrational properties is different in both the systems. There might possibly be different vibrational behaviour of the two lattices; it might happen that in one lattice, the excitation energy of the electrons is converted to the lattice vibrational energy to a greater extent than in the other lattice, due to different electron-phonon (EPC) coupling strengths in the two materials. X. Gong et al.,⁵⁰ explained the dramatically different PLQY in PhC₂ and C₄ crystals by showing different electron-phonon coupling strengths in these

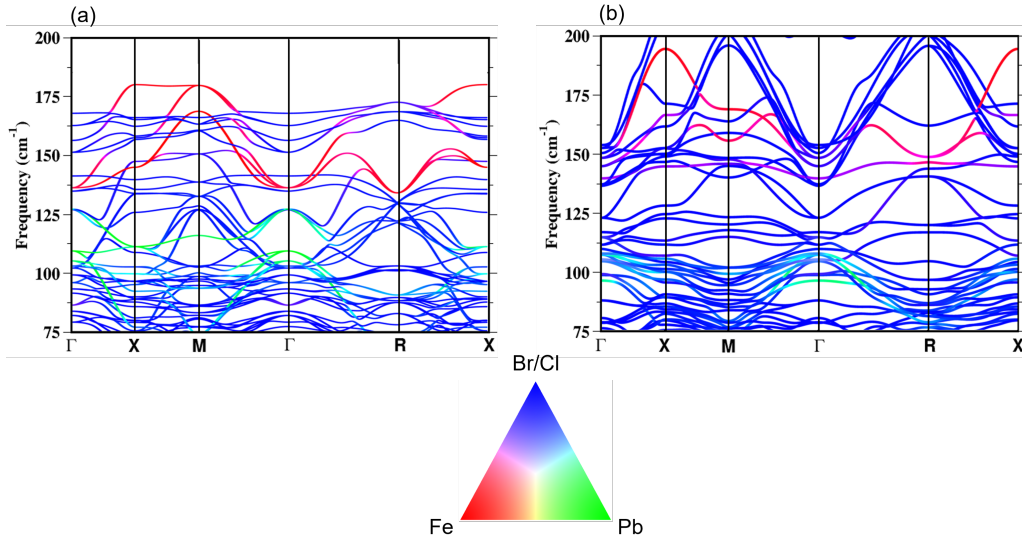


Figure 4.11: Phonon dispersion along with atomic contributions, calculated without SOC for 12.5% Fe-doped systems. (a) and (b) are for Fe-doped CsPbBr₃ and Fe-doped CsPbCl₃, respectively. The phonon branches are colored according to the weights of the atomic contributions. Color code: Red – Fe, Blue – Br/Cl and Green – Pb, as shown in the triangle. The intermediate colors correspond to the mixing of the atomic contributions.

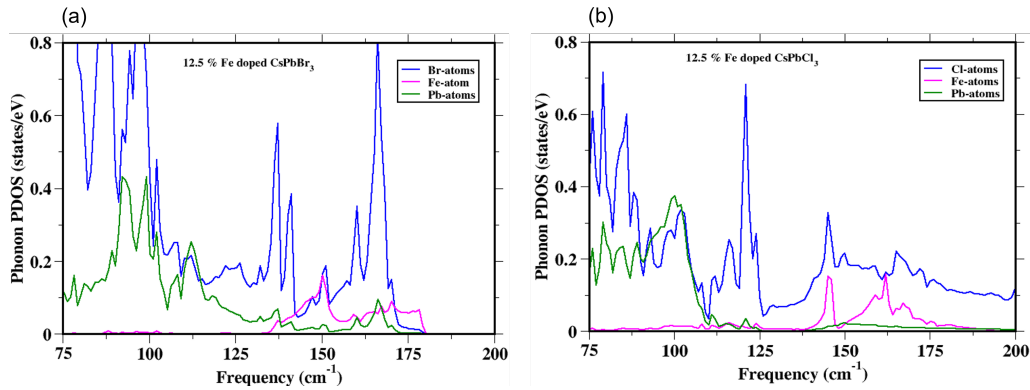


Figure 4.12: Phonon or vibrational density of states along with atomic contributions, calculated without SOC for 12.5% Fe-doped systems. (a) and (b) are for Fe-doped CsPbBr₃ and Fe-doped CsPbCl₃, respectively. Color code: Magenta – Fe, Blue – Br/Cl and Green – Pb.

two materials, though the trap densities are comparable and similar in the two materials. This paper calculated the EPC coupling strength from the full widths at half maxima FWHMs of the temperature dependent PL spectra, and fitting this data with a model. There are also other papers which also calculate the EPC using

the above mentioned approach.^{51;52}

We first calculate the vibrational properties i.e., phonon dispersion (Fig. 4.11]) and the phonon density of states [see Fig. 4.12], along with the atomic contributions to them. The vibrational properties are calculated using density functional perturbation theory (DFPT) and only for the 12.5% doped systems, and for reasons of computational cost, SOC is not included in the phonon calculations.

The phonon dispersion with atomic contributions and atom projected phonon partial density of states are shown in Fig. 4.11 and 4.12, in the frequency range of Fe atoms' contributions (for both the Fe-doped systems, Fe atoms vibrate in the frequency range 135 cm^{-1} to 180 cm^{-1}) as we are interested to see the effect of Fe in the pristine systems. We observe that there is significant vibrational coupling between Fe and Br atoms for Fe-doped CsPbBr_3 , and Fe and Cl atoms for Fe-doped CsPbCl_3 . The contribution of Pb atoms in the frequency range of Fe atoms' contribution is very small. Being a heavy element, Pb atoms contribute primarily to phonons below 110 cm^{-1} in frequency. Also, Cl atoms, being a light element, contribute to vibrations even at 200 cm^{-1} at which Br atoms' Ph-PDOS vanishes, since Br atoms are heavier than Cl atoms. So, Fe-Br or Fe-Cl vibrational couplings are observed in the frequency range 135 cm^{-1} to 180 cm^{-1} and this range is almost the same in both the materials. Next, we calculate the value of electron-phonon coupling in the following.

4.5.7 Origin of different photoluminescence behaviour in Fe-doped CsPbBr_3 and Fe-doped CsPbCl_3 : Explanation from electron-phonon coupling

Though the electronic structures and trap states are similar in both Fe-doped CsPbBr_3 and Fe-doped CsPbCl_3 , the experiments show different PL behaviours

in these materials; at higher Fe concentration, the PL intensity completely died for Fe-doped CsPbCl₃, while it remained finite for Fe-doped CsPbBr₃. We speculate that this arises from the fact that in one material (Fe-doped CsPbCl₃) the conversion of electronic excitation energy into lattice vibrational energy is more effective than in the other material (Fe-doped CsPbBr₃), which results in increased non-radiative transitions in Fe-doped CsPbCl₃ leading to complete quenching of photoluminescence in it. So, we next attempt to calculate electron-phonon coupling (EPC) strengths in these two Fe-doped systems.

To estimate the strength of the electron phonon coupling, we follow previous authors by first computing the deformation potential, which is a measure of EPC.⁵⁰ The deformation potential (D) is defined as the change in electronic band energy due to small atomic displacements (e.g., due to application of strain) and is given by,

$$D = \frac{\Delta E}{\Delta l/l_0} \quad (4.3)$$

where, ΔE is the change in band energy due to small strain Δl , and l_0 is the optimized lattice parameter of the concerned unit cell. Here, we apply strain of -1% and $+1\%$ in the unit cells of both Fe-doped CsPbBr₃ and Fe-doped CsPbCl₃. We have calculated the electronic band structure with no strain (i.e., with the optimized lattice parameter), and with -1% and $+1\%$ applied strain.

Figs. 4.13(a) and (b) each contain three superimposed band structures (i.e., all the band structures calculated with no strain and strain are shown in the same plot) calculated with different strains (i.e., -1% (blue bands), 0% (black bands) and $+1\%$ (red bands)), for 12.5% Fe-doped CsPbBr₃ and 12.5% Fe-doped CsPbCl₃, respectively. Notice that, to enable an appropriate comparison and to identify the changes due to strain, here all bands are shifted in energy with respect to the

corresponding Cs-5s core level, which is assumed to be unaffected by strain.

In Fig. 4.13, black, red and blue lines correspond to the bands due to 0%, +1% and -1% strains, respectively. A closer look helps us to notice that mainly Fe-3d mid gap levels and the valence band maximum (VBM) change significantly with strain as the red and blue lines are not falling on the black lines and are quite perceptibly shifted with respect to the black lines, for both Fe-doped CsPbBr₃ and Fe-doped CsPbCl₃. The changes in the conduction band minima (CBM) are not so large. However, a more zoomed-in view tells that the change in VBM and CBM is a little higher for Fe-doped CsPbCl₃ than that in Fe-doped CsPbBr₃; these changes we will quantify below.

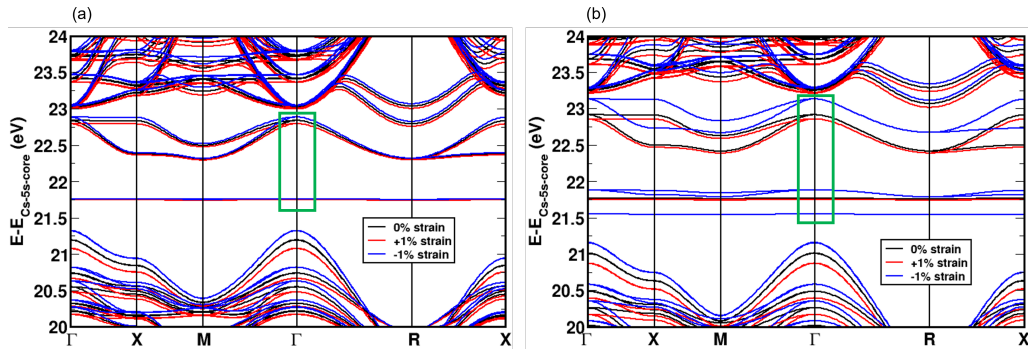


Figure 4.13: Electronic band structure of (a) 12.5% Fe-doped CsPbBr₃ and (b) 12.5% Fe-doped CsPbCl₃, with different applied strains. For comparison, all the band structures with three different strain values are shown in the same plot. Black, red and blue lines correspond to bands due to 0%, +1% and -1% strain.

We notice that the Fe-3d levels in the mid gap region are very sensitive to the applied strain. In fact, for Fe-doped CsPbCl₃, the triply degenerate Fe-3d flat bands split into two flat bands for -1% strain. The other less dispersive Fe-3d mid gap states are also changed hugely due to -1% strain. Though Fe-3d mid gap levels change for Fe-doped CsPbBr₃ also, however, this is not so large in compared to the large change (in fact large splitting) in Fe-doped CsPbCl₃. For simple comparison, we have drawn a green rectangle in each panel of Fig. 4.13, to demarcate the region we wish to focus on. We observe a very large splitting and shifting in Fe-3d mid gap

levels for Fe-doped CsPbCl₃, while the change in electronic band energy is not so large for Fe-doped CsPbBr₃.

Next, we quantify the change in the electron band energy due to applied strain, i.e., calculate the deformation potential D ⁵³ using Eq. 4.3.

We calculate the change in electronic energy at some points of the band structure due to applied strain. We consider a few points in some bands: (i) VBM at the Γ point, (ii) CBM at the R point, (iii) maximum and minimum of Fe-3d flat bands, and (iv) maximum and minimum of Fe-3d less dispersive bands. We have considered these bands as they are important for band edge transition induced photoluminescence and trapping of electrons. Different colors correspond to different points of bands in the band structure as mentioned above and full lines are for 12.5% Fe-doped CsPbBr₃ and dashed lines are for 12.5% Fe-doped CsPbCl₃.

First we calculate the change in electronic band energy of the above mentioned bands at the above mentioned points, and then compute the average. Our calculations gives $D = 3.71$ eV for 12.5% Fe-doped CsPbBr₃ and $D = 10.55$ eV for 12.5% Fe-doped CsPbCl₃. This implies $D_{Fe-CsPbCl_3}$ is 2.84 times larger than $D_{Fe-CsPbBr_3}$.

To calculate the electron-phonon coupling matrix element, we also need to know the elastic constant C_{11} . Here we will make the assumption that the value of this elastic constant for the Fe-doped systems can be approximated by that for the pristine systems, which we believe to be a valid assumption since in the experimental systems, the Fe concentration is small. So, we have calculated the elastic constant C_{11} of pristine CsPbBr₃ and pristine CsPbCl₃ using the following two equations for cubic systems:⁵⁴

$$\Delta E = 3V(C_{11} - C_{12})e_1^2 + O(e_1^3), \quad (4.4)$$

and,⁵⁴

$$3B = C_{11} + 2C_{12}, \quad (4.5)$$

where ΔE is the difference in total energy of a strained system with respect to the unstrained system, V is the optimized volume of the unit cell, e_1 is applied strain, and B is bulk modulus of the system. We have considered some geometries in which the unit cells of CsPbBr₃ and CsPbCl₃ are strained with tensile and compressive strain, by increasing and decreasing the lattice constant such that the volume remain constant at the optimized volume V . Then we fit the ΔE vs e_1 curve with a 3rd order polynomial, which become mostly parabola as the 3rd order contribution is very less. By extracting the fitting parameters we obtain $C_{11} - C_{12}$ as given in Eq. 4.4. Also, bulk modulus of CsPbBr₃ and CsPbCl₃ have been calculated and thus we obtain $C_{11} + 2C_{12}$ as given in Eq. 4.5. By solving Eqn. 4.4 and 4.5 we obtain $C_{11} = 42.42$ GPa for CsPbBr₃ and $C_{11} = 49.15$ GPa for CsPbCl₃.

Now, for an electron making a transition from initial state \mathbf{k} to the final state \mathbf{k}' via interaction with phonons created by lattice vibration, the transition probability is given by the matrix element:⁵⁵

$$|M|^2 = \frac{k_B T D^2}{V C_{11}}, \quad (4.6)$$

where k_B is the Boltzmann constant, T is the temperature, V is the volume of crystal, C_{11} is the elastic constant. D is the deformation potential already computed above. That is, the transition probability is proportional to the square of the deformation potential and inversely proportional to the elastic constant.⁵⁵ Since this transition probability from state \mathbf{k} to state \mathbf{k}' is occurring via interaction with phonons, this is a measure of electron-phonon coupling in the system. So, the electron phonon coupling (EPC) $\propto D^2/C_{11}$.

We have calculated the value of the transition matrix element $|M|^2$ using Eq. 4.6.

We have taken $T = 300$ K i.e., room temperature, and V has been taken as unit cell volumes of CsPbBr_3 and CsPbCl_3 . Our calculation gives: $|M|^2 = 2.1 \times 10^{-45}$ for CsPbBr_3 and $|M|^2 = 17 \times 10^{-45}$ for CsPbCl_3 , both in SI units.

So, we see that, $|M|^2$ or EPC is 8.1 times larger in Fe-doped CsPbCl_3 than that in Fe-doped CsPbBr_3 . This larger EPC in Fe-doped CsPbCl_3 is responsible for larger non-radiative recombination in this system than in Fe-doped CsPbBr_3 . This leads to complete quenching of photoluminescence in Fe-doped CsPbCl_3 at higher Fe concentrations.

4.6 Summary and conclusions

In conclusion, experiments showed photoluminescence (PL) quenching upon Fe doping in CsPbBr_3 and CsPbCl_3 nanocrystals. However, at higher Fe concentration, PL quenching is different for these two materials: in Fe-doped CsPbBr_3 PL intensity remains finite at a constant value and in Fe-doped CsPbCl_3 PL was completely quenched.

We have performed DFT calculations on the pristine and Fe-doped materials, with 12.5% and 25% Fe concentrations. We find that Fe doping increases the stability of these materials. However, upon computing the band structure, we find that Fe doping results in the appearance of Fe-3d states in the mid gap region of the pristine systems, for both Fe-doped CsPbBr_3 and Fe-doped CsPbCl_3 . As a result, excited electrons are trapped by the Fe-3d levels. This non-radiative recombination reduces the PL intensity in the Fe-doped systems with respect to the pristine systems. The density of Fe-3d states in the mid-gap region increases with increasing Fe concentration, and as a result, more and more excited electrons get trapped in these states, which explains why the photoluminescence intensity decreases with increasing Fe concentration. However, the very similar electronic structure in the two Fe-doped

halide perovskites cannot explain different PL behaviour.

We have calculated the electron-phonon coupling (EPC) in these systems via the deformation potential D . The calculated value of D for Fe-doped CsPbCl₃ is much larger than that in Fe-doped CsPbBr₃, as is the value of the electron-phonon coupling matrix element M . This indicates that the conversion of electronic excitation energy into lattice vibrational energy is much larger for Fe-doped CsPbCl₃ than for CsPbBr₃, leading to complete quenching of PL in the latter system at higher Fe concentrations.

Our results show that though Fe doping confers additional stability, this comes at the cost of PL quenching. The degree of PL quenching depends on the particular halide, due to different strengths of electron-phonon coupling.

Bibliography

- [1] A. Kojima, K. Teshima, Y. Shirai, and T. Miyasaka, “Organometal halide perovskites as visible-light sensitizers for photovoltaic cells,” *J. Am. Chem. Soc.*, vol. 131, no. 17, pp. 6050–6051, 2009.
- [2] M. Liu, M. B. Johnston, and H. J. Snaith, “Efficient planar heterojunction perovskite solar cells by vapour deposition,” *Nature*, vol. 501, no. 7467, pp. 395–398, 2013.
- [3] H. Cho, S.-H. Jeong, M.-H. Park, Y.-H. Kim, C. Wolf, C.-L. Lee, J. H. Heo, A. Sadhanala, N. Myoung, S. Yoo, *et al.*, “Overcoming the electroluminescence efficiency limitations of perovskite light-emitting diodes,” *Science*, vol. 350, no. 6265, pp. 1222–1225, 2015.
- [4] N. Wang, L. Cheng, R. Ge, S. Zhang, Y. Miao, W. Zou, C. Yi, Y. Sun, Y. Cao, R. Yang, *et al.*, “Perovskite light-emitting diodes based on solution-processed self-organized multiple quantum wells,” *Nat. Photon*, vol. 10, no. 11, pp. 699–704, 2016.
- [5] Z. Xiao, R. A. Kerner, L. Zhao, N. L. Tran, K. M. Lee, T.-W. Koh, G. D. Scholes, and B. P. Rand, “Efficient perovskite light-emitting diodes featuring nanometre-sized crystallites,” *Nat. Photon.*, vol. 11, no. 2, pp. 108–115, 2017.

- [6] H. Zhu, Y. Fu, F. Meng, X. Wu, Z. Gong, Q. Ding, M. V. Gustafsson, M. T. Trinh, S. Jin, and X. Zhu, “Lead halide perovskite nanowire lasers with low lasing thresholds and high quality factors,” *Nat. Mater.*, vol. 14, no. 6, pp. 636–642, 2015.
- [7] C. Bao, Z. Chen, Y. Fang, H. Wei, Y. Deng, X. Xiao, L. Li, and J. Huang, “Low-noise and large-linear-dynamic-range photodetectors based on hybrid-perovskite thin-single-crystals,” *Adv. Mater.*, vol. 29, no. 39, p. 1703209, 2017.
- [8] H. Wei, Y. Fang, P. Mulligan, W. Chuirazzi, H.-H. Fang, C. Wang, B. R. Ecker, Y. Gao, M. A. Loi, L. Cao, *et al.*, “Sensitive x-ray detectors made of methylammonium lead tribromide perovskite single crystals,” *Nat. Photon.*, vol. 10, no. 5, pp. 333–339, 2016.
- [9] Q. Wang, M. Lyu, M. Zhang, J.-H. Yun, H. Chen, and L. Wang, “Transition from the tetragonal to cubic phase of organohalide perovskite: the role of chlorine in crystal formation of $\text{CH}_3\text{NH}_3\text{PbI}_3$ on TiO_2 substrates,” *J. Phys. Chem. Lett.*, vol. 6, no. 21, pp. 4379–4384, 2015.
- [10] M. Kulbak, S. Gupta, N. Kedem, I. Levine, T. Bendikov, G. Hodes, and D. Cahen, “Cesium enhances long-term stability of lead bromide perovskite-based solar cells,” *J. Phys. Chem. Lett.*, vol. 7, no. 1, pp. 167–172, 2016.
- [11] X. Zheng, C. Wu, S. K. Jha, Z. Li, K. Zhu, and S. Priya, “Improved phase stability of formamidinium lead triiodide perovskite by strain relaxation,” *ACS Energy Lett.*, vol. 1, no. 5, pp. 1014–1020, 2016.
- [12] D. Parobek, B. J. Roman, Y. Dong, H. Jin, E. Lee, M. Sheldon, and D. H. Son, “Exciton-to-dopant energy transfer in Mn-doped cesium lead halide perovskite nanocrystals,” *Nano Lett.*, vol. 16, no. 12, pp. 7376–7380, 2016.

-
- [13] W. Liu, Q. Lin, H. Li, K. Wu, I. Robel, J. M. Pietryga, and V. I. Klimov, “Mn²⁺-doped lead halide perovskite nanocrystals with dual-color emission controlled by halide content,” *J. Am. Chem. Soc.*, vol. 138, no. 45, pp. 14954–14961, 2016.
- [14] Y. Hu, T. Qiu, F. Bai, X. Miao, and S. Zhang, “Enhancing moisture-tolerance and photovoltaic performances of FAPbI₃ by bismuth incorporation,” *J. Mater. Chem.*, vol. 5, no. 48, pp. 25258–25265, 2017.
- [15] D. Bai, J. Zhang, Z. Jin, H. Bian, K. Wang, H. Wang, L. Liang, Q. Wang, and S. F. Liu, “Interstitial Mn²⁺-driven high-aspect-ratio grain growth for low-trap-density microcrystalline films for record efficiency CsPbI₂Br solar cells,” *ACS Energy Lett.*, vol. 3, no. 4, pp. 970–978, 2018.
- [16] J.-S. Yao, J. Ge, B.-N. Han, K.-H. Wang, H.-B. Yao, H.-L. Yu, J.-H. Li, B.-S. Zhu, J.-Z. Song, C. Chen, *et al.*, “Ce³⁺-doping to modulate photoluminescence kinetics for efficient CsPbBr₃ nanocrystals based light-emitting diodes,” *J. Am. Chem. Soc.*, vol. 140, no. 10, pp. 3626–3634, 2018.
- [17] A. Amo, T. Liew, C. Adrados, R. Houdré, E. Giacobino, A. Kavokin, and A. Bramati, “Exciton–polariton spin switches,” *Nat. Photon.*, vol. 4, no. 6, pp. 361–366, 2010.
- [18] N. Pradhan, S. Das Adhikari, A. Nag, and D. D. Sarma, “Luminescence, plasmonic, and magnetic properties of doped semiconductor nanocrystals,” *Angew. Chem. Int. Ed.*, vol. 56, no. 25, pp. 7038–7054, 2017.
- [19] R. Fainblat, C. J. Barrows, and D. R. Gamelin, “Single magnetic impurities in colloidal quantum dots and magic-size clusters,” *Chem. Mater.*, vol. 29, no. 19, pp. 8023–8036, 2017.

- [20] S. Das Adhikari, S. K. Dutta, A. Dutta, A. K. Guria, and N. Pradhan, “Chemically tailoring the dopant emission in manganese-doped CsPbCl₃ perovskite nanocrystals,” *Angew. Chem*, vol. 129, no. 30, pp. 8872–8876, 2017.
- [21] S. Das Adhikari, A. K. Guria, and N. Pradhan, “Insights of doping and the photoluminescence properties of Mn-doped perovskite nanocrystals,” *J. Phys. Chem. Lett*, vol. 10, no. 9, pp. 2250–2257, 2019.
- [22] H.-Y. Chen and D. H. Son, “Energy and charge transfer dynamics in doped semiconductor nanocrystals,” *Isr. J. Chem.*, vol. 52, no. 11-12, pp. 1016–1026, 2012.
- [23] R. Beaulac, P. I. Archer, S. T. Ochsenein, and D. R. Gamelin, “Mn²⁺-doped CdSe quantum dots: new inorganic materials for spin-electronics and spin-photonics,” *Adv. Funct. Mater.*, vol. 18, no. 24, pp. 3873–3891, 2008.
- [24] H. Yang, P. H. Holloway, and B. B. Ratna, “Photoluminescent and electroluminescent properties of Mn-doped ZnS nanocrystals,” *J. Appl. Phys.*, vol. 93, no. 1, pp. 586–592, 2003.
- [25] G. Couston, T. Gacoin, and J. Boilot, “Synthesis and Photoluminescence of Cd_{1-x}Mn_xS(x≤5) Nanocrystals,” *J. Phys. Chem. B*, vol. 102, no. 27, pp. 5257–5260, 1998.
- [26] P. I. Archer, S. A. Santangelo, and D. R. Gamelin, “Direct observation of *sp*–*d* exchange interactions in colloidal Mn²⁺- and Co²⁺-doped CdSe quantum dots,” *Nano Lett.*, vol. 7, no. 4, pp. 1037–1043, 2007.
- [27] D. J. Norris, N. Yao, F. T. Charnock, and T. A. Kennedy, “High-quality manganese-doped ZnSe nanocrystals,” *Nano Lett.*, vol. 1, no. 1, pp. 3–7, 2001.

- [28] Z. J. Yong, S. Q. Guo, J. P. Ma, J. Y. Zhang, Z. Y. Li, Y. M. Chen, B. B. Zhang, Y. Zhou, J. Shu, J.-L. Gu, *et al.*, “Doping-enhanced short-range order of perovskite nanocrystals for near-unity violet luminescence quantum yield,” *J. Am. Chem. Soc.*, vol. 140, no. 31, pp. 9942–9951, 2018.
- [29] A. Shapiro, M. W. Heindl, F. Horani, M.-H. Dahan, J. Tang, Y. Amouyal, and E. Lifshitz, “Significance of Ni doping in CsPbX₃ nanocrystals via postsynthesis cation–anion coexchange,” *J. Phys. Chem. C*, vol. 123, no. 40, pp. 24979–24987, 2019.
- [30] G. Pan, X. Bai, W. Xu, X. Chen, Y. Zhai, J. Zhu, H. Shao, N. Ding, L. Xu, B. Dong, *et al.*, “Bright Blue Light Emission of Ni²⁺ Ion-Doped CsPbCl_xBr_{3-x} Perovskite Quantum Dots Enabling Efficient Light-Emitting Devices,” *ACS Appl. Mater. Interfaces*, vol. 12, no. 12, pp. 14195–14202, 2020.
- [31] M. Makkar, L. Dheer, A. Singh, L. Moretti, M. Maiuri, S. Ghosh, G. Cerullo, U. V. Waghmare, and R. Viswanatha, “Magneto-optical Stark effect in Fe-doped CdS nanocrystals,” *Nano Lett.*, vol. 21, no. 9, pp. 3798–3804, 2021.
- [32] S. Zou, G. Yang, T. Yang, D. Zhao, Z. Gan, W. Chen, H. Zhong, X. Wen, B. Jia, and B. Zou, “Template-free synthesis of high-yield Fe-doped cesium lead halide perovskite ultralong microwires with enhanced two-photon absorption,” *J. Phys. Chem. Lett.*, vol. 9, no. 17, pp. 4878–4885, 2018.
- [33] C. Tang, C. Chen, W. Xu, and L. Xu, “Design of doped cesium lead halide perovskite as a photo-catalytic CO₂ reduction catalyst,” *J. Mater. Chem. A*, vol. 7, no. 12, pp. 6911–6919, 2019.
- [34] S. Shyamal, S. K. Dutta, and N. Pradhan, “Doping iron in CsPbBr₃ perovskite nanocrystals for efficient and product selective CO₂ reduction,” *J. Phys. Chem. Lett.*, vol. 10, no. 24, pp. 7965–7969, 2019.

-
- [35] P. Borse, N. Deshmukh, R. Shinde, S. Kulkarni, *et al.*, “Luminescence quenching in ZnS nanoparticles due to Fe and Ni doping,” *J. Mater. Sci.*, vol. 34, no. 24, pp. 6087–6093, 1999.
- [36] P. Piotrowski and W. Pacuski, “Photoluminescence of CdTe quantum wells doped with cobalt and iron,” *J. Lumin.*, vol. 221, p. 117047, 2020.
- [37] P. Giannozzi, S. Baroni, N. Bonini, M. Calandra, R. Car, C. Cavazzoni, D. Ceresoli, G. L. Chiarotti, M. Cococcioni, I. Dabo, *et al.*, “QUANTUM ESPRESSO: a modular and open-source software project for quantum simulations of materials,” *J. Phys.: Condens. Matter*, vol. 21, no. 39, p. 395502, 2009.
- [38] P. Giannozzi, O. Andreussi, T. Brumme, O. Bunau, M. B. Nardelli, M. Calandra, R. Car, C. Cavazzoni, D. Ceresoli, M. Cococcioni, *et al.*, “Advanced capabilities for materials modelling with QUANTUM ESPRESSO,” *J. Phys.: Condens. Matter*, vol. 29, no. 46, p. 465901, 2017.
- [39] J. P. Perdew, K. Burke, and M. Ernzerhof, “Generalized gradient approximation made simple,” *Phys. Rev. Lett.*, vol. 77, no. 18, p. 3865, 1996.
- [40] D. Vanderbilt, “Soft self-consistent pseudopotentials in a generalized eigenvalue formalism,” *Phys. Rev. B*, vol. 41, no. 11, p. 7892, 1990.
- [41] C. G. Broyden, J. E. Dennis Jr, and J. J. Moré, “On the local and superlinear convergence of quasi-newton methods,” *IMA J. Appl. Math.*, vol. 12, no. 3, pp. 223–245, 1973.
- [42] R. Fletcher, “A new approach to variable metric algorithms,” *Comput. J.*, vol. 13, no. 3, pp. 317–322, 1970.

-
- [43] D. Goldfarb, “A family of variable-metric methods derived by variational means,” *Math. Comput.*, vol. 24, no. 109, pp. 23–26, 1970.
- [44] D. F. Shanno, “Conditioning of quasi-Newton methods for function minimization,” *Math. Comput.*, vol. 24, no. 111, pp. 647–656, 1970.
- [45] H. J. Monkhorst and J. D. Pack, “Special points for Brillouin-zone integrations,” *Phys. Rev. B*, vol. 13, no. 12, p. 5188, 1976.
- [46] C. Grote, B. Ehrlich, and R. F. Berger, “Tuning the near-gap electronic structure of tin-halide and lead-halide perovskites via changes in atomic layering,” *Phys. Rev. B*, vol. 90, no. 20, p. 205202, 2014.
- [47] G. S. Rohrer, *Structure and bonding in crystalline materials*. Cambridge University Press, 2001.
- [48] K. Gesi, K. Ozawa, and S. Hirotsu, “Effect of hydrostatic pressure on the structural phase transitions in CsPbCl₃ and CsPbBr₃,” *J. Phys. Soc. Japan.*, vol. 38, no. 2, pp. 463–466, 1975.
- [49] H. M. Ghaithan, Z. A. Alahmed, S. M. Qaid, M. Hezam, and A. S. Aldwayyan, “Density functional study of cubic, tetragonal, and orthorhombic CsPbBr₃ perovskite,” *ACS Omega*, vol. 5, no. 13, pp. 7468–7480, 2020.
- [50] X. Gong, O. Voznyy, A. Jain, W. Liu, R. Sabatini, Z. Piontkowski, G. Walters, G. Bappi, S. Nokhrin, O. Bushuyev, *et al.*, “Electron–phonon interaction in efficient perovskite blue emitters,” *Nat. Mater.*, vol. 17, no. 6, pp. 550–556, 2018.
- [51] J. Meng, Z. Lan, W. Lin, M. Liang, X. Zou, Q. Zhao, H. Geng, I. E. Castelli, S. E. Canton, T. Pullerits, *et al.*, “Optimizing the quasi-equilibrium state of hot carriers in all-inorganic lead halide perovskite nanocrystals through Mn

- doping: fundamental dynamics and device perspectives,” *Chem. Sci.*, vol. 13, no. 6, pp. 1734–1745, 2022.
- [52] A. D. Wright, C. Verdi, R. L. Milot, G. E. Eperon, M. A. Pérez-Osorio, H. J. Snaith, F. Giustino, M. B. Johnston, and L. M. Herz, “Electron–phonon coupling in hybrid lead halide perovskites,” *Nat. Commun.*, vol. 7, no. 1, pp. 1–9, 2016.
- [53] T. Zhao, W. Shi, J. Xi, D. Wang, and Z. Shuai, “Intrinsic and extrinsic charge transport in $\text{CH}_3\text{NH}_3\text{PbI}_3$ perovskites predicted from first-principles,” *Sci. rep.*, vol. 6, no. 1, p. 19968, 2016.
- [54] M. Mehl, J. Osburn, D. Papaconstantopoulos, and B. Klein, “Structural properties of ordered high-melting-temperature intermetallic alloys from first-principles total-energy calculations,” *Phys. Rev. B*, vol. 41, no. 15, p. 10311, 1990.
- [55] J. Bardeen and W. Shockley, “Deformation potentials and mobilities in non-polar crystals,” *Phys. Rev.*, vol. 80, no. 1, p. 72, 1950.

Chapter 5

Optical properties of CsPbX₃ and Fe-doped CsPbX₃ (X = Br, Cl)

Dreams are something you have to believe in. I almost gave up on mine. To all of you out there, please keep your dreams alive.

Ke Huy Quan

In this chapter, we study the optical properties of CsPbBr₃ and CsPbCl₃. This work was done in collaboration with the experimental groups of Prof. Ranjani Viswanatha (PhD student - Saptarshi Chakraborty), New Chemistry Unit, JNCASR, Bangalore and Prof. Bivas Saha (PhD student – Krishna C. Maurya), Chemistry and Physics of Materials Unit, JNCASR, Bangalore. They performed photoluminescence (PL) and optical properties measurements. We have done first-principles density functional theory calculations to study the optical properties of these materials.

5.1 Introduction

All-inorganic cesium lead halide perovskite (CsPbX_3 , $X = \text{Cl, Br, I}$) nanocrystals (NCs) have received significant attention due to their potential applications in photovoltaic and optoelectronic devices such as solar cells, light-emitting diodes (LEDs), photodetectors, low-threshold optically pumped lasers, field-effect transistors, lasers and memristors.^{1–8} They show outstanding photophysical properties such as high photoluminescence quantum yield (PLQY), short exciton life times, narrow emission bandwidth, etc. By changing the halide species one can obtain light emission throughout the whole visible region.^{9;10} For example, NCs of CsPbCl_3 give emission at ~ 406 nm, i.e., a blue emission which has potential applications in lasers, light-emitting diodes, ultraviolet (UV) or high energy photodetectors and displays.^{11–15} As CsPbCl_3 NCs are excellent in UV light absorption they can be used in transparent optoelectronic devices. These NCs can also host rare-earth or transition metal ions which give stability to the pristine systems and are very important in fundamental science as well as in applications: excitons can transfer energy to these ions which further gives emission in visible or near infrared (IR) region. Mn^{2+} -doped CsPbCl_3 NCs can convert ‘wasted’ energy in the UV region into usable visible light, which increases the power conversion efficiency (PCE) of solar cells.^{16;17}

For traditional semiconductor solar cells, such as silicon solar cells, it took more than twenty years to achieve PCE of $\sim 20\%$, while for halide perovskite solar cells, the PCE has been improved from 3.81% to $\sim 20\%$ within a few years.^{18–21} All-inorganic perovskite materials are better than organic-inorganic halide perovskite in the sense that they possess greater stability, are better able to deal with oxygen and moisture, have higher melting points ($> 500^\circ\text{C}$), and have better photostability. Also, NCs of all-inorganic perovskites possess a very high PLQY, with emission in the whole visible region [see Fig. 5.1], with narrow line widths (12 – 40 nm).

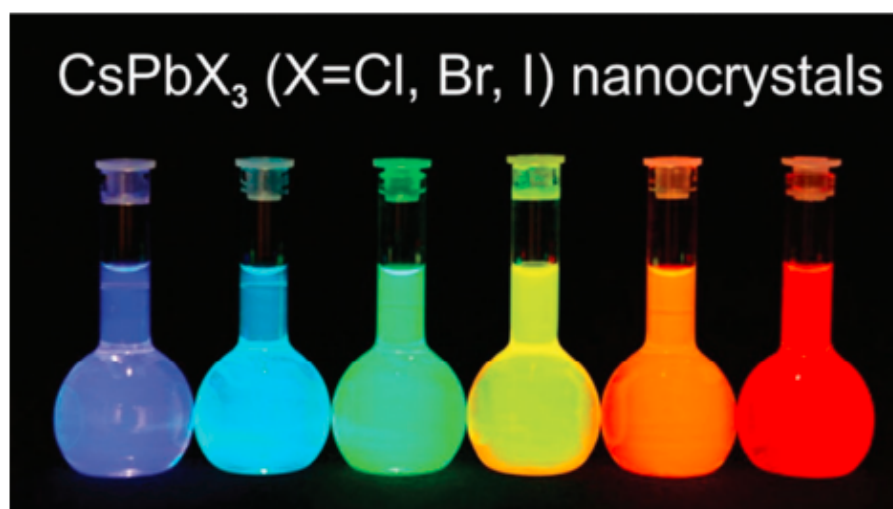


Figure 5.1: All-inorganic perovskite NCs show emission throughout the whole visible region. Used with permission from Ref. 1. Further permission related to the material excerpted should be directed to the ACS.

These properties make the all-inorganic perovskites ideal candidates for optoelectronic applications.²² Within a very short period of time, all-inorganic perovskites have become very popular because of their better photoluminescence and electroluminescence properties, compared to the conventional cadmium based chalcogenide NCs. In particular, they can be used to make next generation LEDs with high efficiency and high tunability.

All-inorganic halide perovskite show PLQY as high as $\sim 90\%$ with tunable PL wavelength from near UV to near IR region. By varying the halide from chloride to iodide, one can go from longer to shorter wavelengths of emission, with CsPbBr₃ emitting in the green region of the spectrum.

However, the air-stability and thermal-stability of these halide perovskites is still an issue. Several authors have suggested that doping these materials with a metal can increase the stability.^{23;24} It is not clear, however, whether or not this will impact the optical properties. This is the issue we will explore in this chapter. We are particularly interested in substituting (partly) the toxic element Pb.

5.2 Experimental motivation

Our experimental collaborators from the group of Prof. Ranjani Viswanatha, New Chemistry Unit, JNCASR, Bangalore and Prof. Bivas Saha, Chemistry and Physics of Materials Unit, JNCASR have studied the optical properties of CsPbBr₃ and CsPbCl₃. In particular, they have attempted to determine the possible optical transitions in these perovskite materials using ellipsometry experiments. They have found the absorption peaks corresponding to the band edge transitions of CsPbBr₃ and CsPbCl₃. In addition, the ellipsometry measurements can probe some more transitions besides the band edge transitions. These transitions are excited state transitions from the valence band maxima of the two materials.

Ellipsometry is an experimental technique to measure the change in the polarization of light as it reflects or transmits from a material. The linearly polarized light is incident on and is reflected from the sample, and becomes elliptically polarized light upon reflection. Ellipsometry measures the change in the polarization of light in terms of an amplitude ratio Ψ and phase difference Δ . From these two quantities Ψ and Δ , one can obtain frequency dependent fundamental optical constants, such as the complex index of refraction and complex dielectric function of a material: $\tilde{\epsilon}(\omega) = \epsilon_1(\omega) + i\epsilon_2(\omega)$, where ϵ_1 is the real part of the dielectric function and ϵ_2 is the imaginary part. These quantities ϵ_1 and ϵ_2 are measured as a function of the photon energy (which is proportional to the frequency of the electric field of the incoming electromagnetic wave) of the incoming light. As the absorption of a material is directly proportional to its ϵ_2 , so this also produces absorption spectra of the concerned materials. The peaks in the ϵ_2 spectra or the minimum of the $\frac{d^2\epsilon_2}{dE^2}$ spectra gives the possible optical transitions in CsPbBr₃ and CsPbCl₃.

Our main aims in this chapter are to (i) find the origin of these optical transitions i.e., identify the states which are responsible for these transitions, and (ii) compare

the experimentally measured values of ϵ_1 and ϵ_2 (obtained from the ellipsometry data) with the results obtained from our first-principles density functional theory (DFT) calculations.

5.3 Computational details

All calculations have been performed using density functional theory (DFT) as implemented in the Quantum ESPRESSO package.^{25;26} The interactions between the valence electrons and ionic cores were described using norm-conserving pseudopotentials.²⁷ The exchange correlation functional was treated using a Generalized Gradient Approximation of the Perdew-Burke-Ernzerhof (PBE-GGA) form.²⁸ The Kohn-Sham wavefunctions and the corresponding charge densities were expanded in plane-wave basis sets having cut-offs of 80 Ry and 320 Ry, respectively. Brillouin zone sampling was done using an $8 \times 8 \times 8$ Monkhorst-Pack mesh,²⁹ along with Marzari-Vanderbilt cold smearing of width 0.001 Ry.³⁰ The pristine CsPbBr₃ and CsPbCl₃ crystals were modelled with cubic unit cells containing five atoms, forming perovskite structures.

The optical properties of CsPbBr₃ and CsPbCl₃ have been calculated using the **epsilon.x** post-processing routine that is a part of the Quantum ESPRESSO package.^{25;26} The imaginary part of the dielectric tensor ϵ_2 , has been calculated using the Drude-Lorentz model, using the formula:³¹

$$\epsilon_{2\alpha,\beta} = \frac{8\pi e^2}{\Omega N_{\mathbf{k}} m^2} \sum_{n \in V} \sum_{n' \in C} \sum_{\mathbf{k}} \frac{\hat{M}_{\alpha,\beta}}{E_{\mathbf{k},n'} - E_{\mathbf{k},n}} \times \frac{\Gamma \omega f(E_{\mathbf{k},n})}{[(\omega_{\mathbf{k},n'} - \omega_{\mathbf{k},n})^2 - \omega^2]^2 + \Gamma^2 \omega^2}, \quad (5.1)$$

where α, β run over the Cartesian directions x, y, z . Ω is the volume of the unit cell, n and n' index the valence (V) and conduction bands (C) respectively, \mathbf{k} indexes

the wave-vectors sampled in the Brillouin zone, $N_{\mathbf{k}}$ is the total number of such \mathbf{k} -points, ω is the frequency, $E_{\mathbf{k},\mathbf{n}}$ are the Kohn-Sham eigenvalues, $E_{\mathbf{k},\mathbf{n}'} - E_{\mathbf{k},\mathbf{n}}$ are the transition energies, e and m are the electronic charge and mass, respectively, of the electron, Γ is the interband broadening parameter, and $f(E_{\mathbf{k},\mathbf{n}})$ is the Fermi-Dirac distribution function that accounts for the occupation of the bands. Here, $\hat{M}_{\alpha,\beta}$ are the squared matrix elements of the momentum operator. We note that only direct transitions are considered, and contributions from the non-local part of the pseudopotential are neglected. The value of the interband broadening parameter Γ was set to 0.2 eV (in order to identify the peaks due to individual transitions) or 0.4 eV (to compare with the experimental data).

5.4 Systems under study

We have taken pristine CsPbBr₃ and CsPbCl₃ in the cubic structures containing five atoms in their respective unit cells. We note that though, at a temperature of 0 K, previous authors have found some octahedral distortions from the cubic perovskite structures, these distortions disappear at room temperature.³² As the experiments we wish to compare with were carried out at room temperature, we do not consider these octahedral distortions in our calculations. We have computed the electronic structure (band structure) and also the optical properties calculations. Finally we have identified the possible optical transitions measured experimentally in these materials.

5.5 Results and discussion

5.5.1 Optical properties of pristine CsPbBr₃ and CsPbCl₃

The electronic band structures of CsPbBr₃ and CsPbCl₃ are shown in Figs. 5.2(b) and 5.3(b), respectively. Our PBE-GGA calculations indicate a direct band gap at the R point, equal to 1.79 eV for CsPbBr₃ and 2.22 eV for CsPbCl₃. In Table 5.1, we compare our results for the band gap, with previously calculated values,^{33;34} as well as experimentally measured values.³⁵ It can be seen that while our results are in good agreement with earlier GGA values, the band gaps are underestimated with respect to experimental values, which is a well-known shortcoming of DFT within the GGA.

Material	E_g (ours) (eV)	E_g (previous) (eV)	E_g (expt) (eV)
CsPbBr ₃	1.79	1.76 (PBE-GGA) ³³	2.30 ³⁵
CsPbCl ₃	2.22	2.20 (PBE-GGA) ³⁴	3.00 ³⁵

Table 5.1: Band gap E_g of CsPbBr₃ and CsPbCl₃. Comparison between our calculated values, previously calculated values and experimentally measured values.

From ellipsometry measurements, we have extracted the spectrum of $\epsilon_2(E)$ for both CsPbBr₃ and CsPbCl₃ [see red curves in Figs. 1(b) and 2(b)]. The critical points in the spectra for CsPbBr₃ and CsPbCl₃ are identified as the minima of the corresponding $\frac{d^2\epsilon_2}{dE^2}$ curves.

Accordingly, we have found three critical points for CsPbBr₃ and four critical points for CsPbCl₃ in the energy range 0 – 7 eV. These are marked as E_a , E_b , E_c and E_d in Figs. 5.2(b) and 5.3(b). The critical points for CsPbBr₃ are $E_a = 2.55$ eV, $E_b = 3.25$ eV and $E_c = 4.56$ eV, and for CsPbCl₃ are $E_a = 3.10$ eV, $E_b = 3.42$ eV, $E_c = 4.53$ eV and $E_d = 5.56$ eV. We note that the minimum corresponding to

E_b for CsPbBr₃ is rather broad and flat, and there is therefore a particularly large error bar associated with the reported value of 3.25 eV.

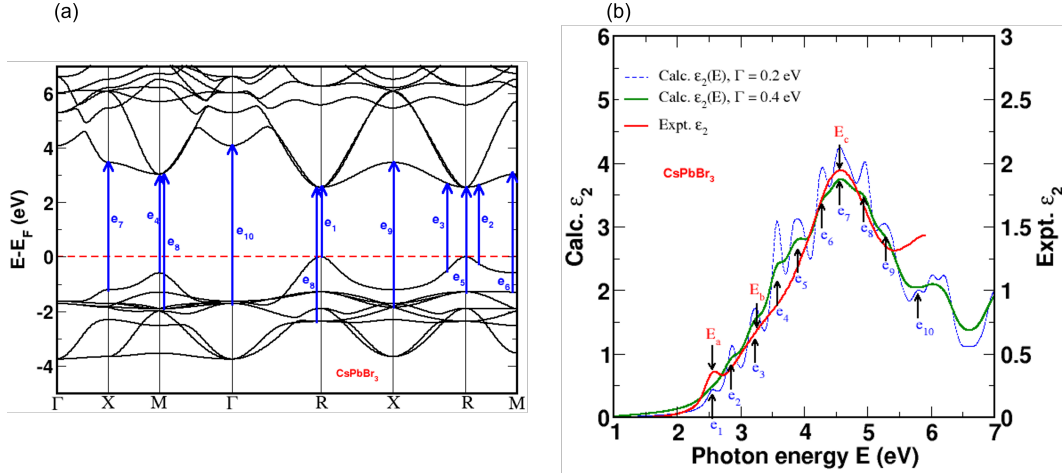


Figure 5.2: (a) Calculated band structure of CsPbBr₃. Scissor correction of 0.76 eV has been applied to the conduction bands. The vertical blue arrows indicate direct transitions that have been identified with the peaks in the dotted blue curves in (b). (b) Imaginary part of the dielectric function ϵ_2 from ellipsometry measurements (red curve) and DFT calculations (blue and green curves) for CsPbBr₃. The dotted blue and solid green curves were computed using broadening parameters $\Gamma = 0.2$ eV and 0.4 eV, respectively.

We have also computed the imaginary part of the dielectric function ϵ_2 using DFT, to compare with the ellipsometry data. We actually want to identify a one-to-one correspondence behind the creation of each peak in the ϵ_2 spectra with the possible transitions in the corresponding band structure of the relevant. ϵ_2 is calculated with two different values of the interband broadening parameter $\Gamma = 0.2$ eV and 0.4 eV. These are shown as, respectively, the dotted blue and solid green curves in Figs. 5.2(b) and 5.3(b).

The first peak of the experimental ϵ_2 spectrum [red curves in Figs. 5.2(b) and 5.3(b)] is the first critical point E_a , and is found at 2.55 eV for CsPbBr₃ and 3.10 eV for CsPbCl₃. These correspond to the band-edge excitonic absorption peak for the corresponding material. We recall that our theoretically calculated values of the band gap are 1.79 eV for CsPbBr₃ and 2.22 eV for CsPbCl₃. To account for the

Label of Expt. peak	Transition energy (eV) (Expt.)	Label of Calc. peak	Identified transitions (Calc.)	Transition energy (eV) (Calc.)	Orbitals involved
E_a	2.55	e ₁	R → R	2.55	Br-4p → Pb-6p
—	—	e ₂	$C_a \rightarrow C_a$	2.86	Br-4p → Pb-6p
E_b	3.25	e ₃	$C_b \rightarrow C_b$	3.23	Br-4p → Pb-6p
—	—	e ₄	M → M	3.56	Br-4p → Pb-6p
—	—	e ₅	$R_2 \rightarrow R$	3.89	Br-4p → Pb-6p
—	—	e ₆	$M_2 \rightarrow R$	4.28	Br-4p → Pb-6p
E_c	4.56	e ₇	X → X	4.56	Br-4p → Pb-6p
—	—	e ₈	$R_4 \rightarrow R, M_3 \rightarrow M$	4.95	Br-4p → Pb-6p
—	—	e ₉	$X_3 \rightarrow X, X_4 \rightarrow X$	5.26	Br-4p → Pb-6p
—	—	e ₁₀	$\Gamma \rightarrow \Gamma$	5.80	Br-4p → Cs-6s

Table 5.2: Identified optical transitions from calculation for CsPbBr₃ and comparison with ellipsometry measurements. The values of the transitions energies are written and compared between calculation and experiment. The orbitals involved in the transitions are also mentioned. All the theoretical values are shifted up with 0.76 eV.

DFT underestimation of the band gap, we match the first peaks of ϵ_2 as measured experimentally and calculated from DFT, by shifting up the theoretically calculated spectra by an amount Δ ,³⁶ we note that this corresponds to applying a ‘scissors correction’ Δ to the conduction bands, which is a standard procedure in the field. The values of this shift are $\Delta_{CsPbBr_3} = 0.76$ eV and $\Delta_{CsPbCl_3} = 0.88$ eV. We note that our values for E_a are slightly higher than those reported by previous authors;^{37;38} we attribute this slight discrepancy to the small size of the nanocrystals of CsPbBr₃ and CsPbCl₃ used in our experiments.

By looking at Fig. 5.2(b), we see that for CsPbBr₃ we have excellent agreement between the experimentally measured spectrum (red curve) and the theoretically computed values (green curve), for both the shape and the width of the curve, though the calculated values appear to be larger than the theoretical values in magnitude by a factor of ~ 2 . In contrast, for CsPbCl₃ [see Fig. 5.3(b)] the magnitude of ϵ_2 agrees well between experiment and theory; however, the width of the overall spectrum appears to be overestimated in the calculations, with a notable red shift.

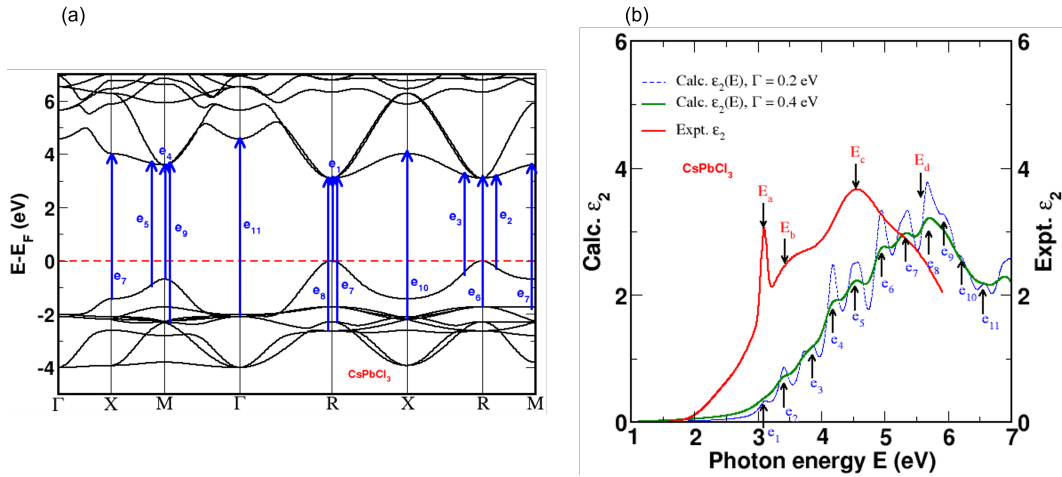


Figure 5.3: (a) Calculated band structure of CsPbCl_3 . Scissor correction of 0.88 eV has been applied to the conduction bands. The vertical blue arrows indicate direct transitions that have been identified with the peaks in the dotted blue curves in (b). (b) Imaginary part of the dielectric function ϵ_2 from ellipsometry measurements (red curve) and DFT calculations (blue and green curves) for CsPbCl_3 . The dotted blue and solid green curves were computed using broadening parameters $\Gamma = 0.2$ eV and 0.4 eV, respectively.

Due to the small value of the broadening parameter Γ used to compute $\epsilon_2(E)$ in the blue dotted curves in Figs. 5.2(b) and 5.3(b), one can see that the spectrum is composed of individual peaks, and one can identify each peak as arising from specific transitions in the band structure. These transitions are indicated by the blue arrows in Figs. 5.2(a) and 5.3(a), and the corresponding peaks are labeled in Figs. 5.2(b) and 5.3(b). We note that not all the peaks observed in the theoretically computed dotted blue curves are experimentally resolved as critical points in the spectrum of ϵ_2 .

In Table 5.2 and Table 5.3, we have listed (for CsPbBr_3 and CsPbCl_3 , respectively) the energies of the theoretically computed peaks as well as the experimentally determined critical points. By comparing the two, we can assign the transitions responsible for the experimentally determined critical points. Accordingly, for CsPbBr_3 , we make the following assignments: E_a : $R \rightarrow R$, E_b : $C_b \rightarrow C_b$, and E_c : $X \rightarrow X$. As mentioned above, there is considerable uncertainty in the value of

E_b and it is therefore also possible that it arises from $M \rightarrow M$ transitions, as has been claimed by previous authors.³⁷ Similarly, for CsPbCl₃, we tentatively assign $E_a: R \rightarrow R$, $E_b: C_a \rightarrow C_a$, $E_c: C_c \rightarrow C_c$ and $E_d: R_4 \rightarrow R$. We note that the points C_a , C_b and C_c are not high symmetry points in the Brillouin zone, but correspond to points [see Figs. 5.2(a) and 5.3(a)] where the band structure has inflection points.

Label of Expt. peak	Transition energy (eV) (Expt.)	Label of Calc. peak	Identified transitions (Calc.)	Transition energy (eV) (Calc.)	Orbitals involved
E_a	3.10	e ₁	R \rightarrow R	3.1	Cl-3p \rightarrow Pb-6p
E_b	3.42	e ₂	$C_a \rightarrow C_a$	3.41	Cl-3p \rightarrow Pb-6p
—	—	e ₃	$C_b \rightarrow C_b$	3.73	Cl-3p \rightarrow Pb-6p
—	—	e ₄	M \rightarrow M	4.18	Cl-3p \rightarrow Pb-6p
E_c	4.53	e ₅	$C_c \rightarrow C_c$	4.57	Cl-3p \rightarrow Pb-6p
—	—	e ₆	R ₂ \rightarrow R	4.94	Cl-3p \rightarrow Pb-6p
—	—	e ₇	R ₃ \rightarrow R, M ₂ \rightarrow M, X \rightarrow X	5.35	Cl-3p \rightarrow Pb-6p
E_d	5.56	e ₈	R ₄ \rightarrow R	5.67	Cl-3p \rightarrow Pb-6p
—	—	e ₉	M ₃ \rightarrow M	5.91	Cl-3p \rightarrow Pb-6p
—	—	e ₁₀	X ₂ \rightarrow X	6.21	Cl-3p \rightarrow Pb-6p
—	—	e ₁₁	$\Gamma \rightarrow \Gamma$	6.57	Cl-3p \rightarrow Cs-6s

Table 5.3: Identified optical transitions from calculation for CsPbCl₃ and comparison with ellipsometry measurements. The values of the transitions energies are written and compared between calculation and experiment. The orbitals involved in the transitions are also mentioned. All the theoretical values are shifted up with 0.88 eV.

We have projected the Kohn-Sham wavefunctions onto the atomic orbitals to get information about the contribution from various atomic orbitals to the valence and conduction band states in different parts of the Brillouin zone. We find that the highest states in the valence bands in CsPbBr₃ (CsPbCl₃) have contributions primarily from the Br-4*p* (Cl-3*p*) orbitals. In contrast, the lowest states in the conduction band mainly arise from the Pb-6*p* states, throughout the Brillouin zone (BZ), except in the vicinity of the zone-center Γ , where Cs-6*s* orbitals contribute more. Thus, the orbital involvement in all the direct transitions is Br-4*p* (Cl-3*p*) \rightarrow Pb-6*p* for all k-points, except at the Γ point where a Br-4*p* (Cl-3*p*) \rightarrow Cs-6*s*

transition takes place.

5.5.2 Comparison between CsPbBr₃ and CsPbCl₃: Experiment vs. Calculations

Figs. 5.2(b) tells us that, for CsPbBr₃, the calculated $\epsilon_2(\omega)$ spectra are in excellent agreement with the ellipsometry data, at least regarding the shape of the curve, though there is a discrepancy in the absolute values. Fig. 5.3(b) tells, in contrast, for CsPbCl₃ the shape and width of the spectrum does not match well when one compares experiment and calculation (though the absolute values match very well between our calculation and experiment). In this section, we provide a possible explanation for why there is this discrepancy for CsPbCl₃ but not for CsPbBr₃.

Our calculations are done using DFT which is a 0 K theory, and ellipsometry measurements are done at room temperature (RT), ~ 300 K. As each peak in the $\epsilon_2(\omega)$ spectrum corresponds to one transition between valence and conduction bands in the respective band structures, the origin of deviation in the $\epsilon_2(\omega)$ spectrum for CsPbCl₃ must come from inability to capture exact band energies in our (zero-temperature) calculations.

We want to check if the electronic band energies change with temperature. At RT, thermal energy creates a large number of phonons. A large electron-phonon coupling can result in a significant change in the band energy with temperature. This was something we had looked at in the previous chapter when calculating the deformation potential D .

However, to try to understand the results obtained in this chapter, it does not suffice to compute the change in energy of an individual state in a band n with wavevector \mathbf{k} . Instead we have to look at differences in two steps: (i) first we have to look at how the energy of a given transition changes, by looking, for a fixed \mathbf{k} ,

at how the energy of the transition from bands $n \rightarrow n'$ changes, by looking at the change in band energies of the states (n, \mathbf{k}) and (n', \mathbf{k}) ; (ii) how the shape of $\epsilon_2(\omega)$ changes, for example by looking at W , the difference in energy in ω_{BE} and ω_{pk} , which are the energies of the band edge transition and peak transition, respectively.

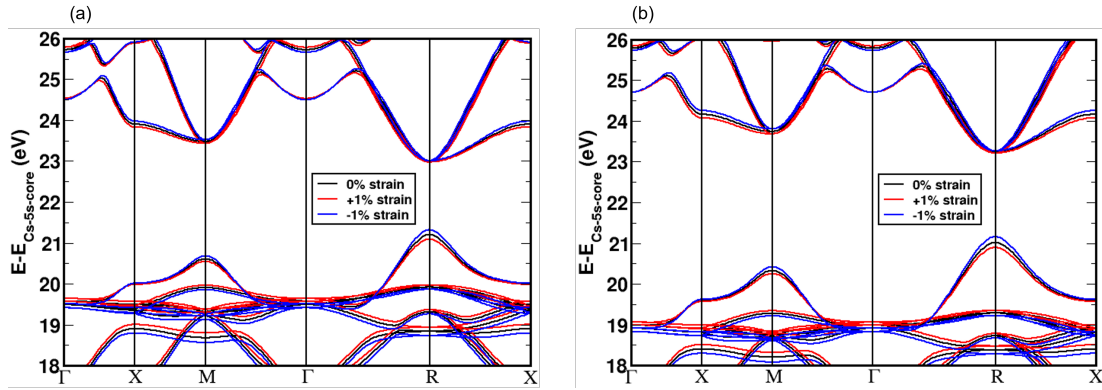


Figure 5.4: Calculated band structure of (a) CsPbBr₃ and (b) CsPbCl₃ for -1% (blue bands), 0% (black bands) and $+1\%$ (red bands) strain.

To estimate the temperature difference of these quantities, we will look at the electron-phonon coupling for these states, which in turn we will estimate (as in the previous chapter) by computing their response to a strain applied to the crystal.

Fig. 5.4 shows the band structures calculated with 0% strain (black bands), -1% strain (blue bands) and $+1\%$ strain (red bands) for both CsPbBr₃ and CsPbCl₃. Here, for an appropriate comparison, all bands have been shifted with respect to the Cs-5s core level for each system, which is expected to be relatively insensitive to strain.

In Table 5.4 we present our results obtained by analyzing the shifts in band energies with strain (shown in Fig. 5.4). We note that for both CsPbBr₃ and CsPbCl₃, the band edge energy ω_{BE} corresponds to a transition from the valence band maximum (VBM) to the conduction band minimum (CBM) at the R point. This is the transition labeled e_1 in both Fig. 5.2 and Fig. 5.3. The peak energy ω_{pk} corresponds to the e_7 transition (at the X point) for CsPbBr₃ and the e_8 transition (at the R

System	Strain ($\Delta l/l_0$)	Band edge ω_{BE} (eV)	Peak ω_{pk} (eV)	$W = \omega_{pk} - \omega_{BE}$ (eV)
CsPbBr ₃	-1%	1.686	3.960	2.274
	0%	1.791	3.907	2.116
	+1%	1.885	3.850	1.965
δ	—	—	—	15.45
CsPbCl ₃	-1%	2.105	4.984	2.879
	0%	2.218	4.858	2.640
	+1%	2.317	4.731	2.420
δ	—	—	—	22.95

Table 5.4: Variation in the transition energies corresponding to the band edge (ω_{BE}) and peak (ω_{pk}) in $\epsilon_2(\omega)$ with applied strain, for both CsPbBr₃ and CsPbCl₃. W is the difference in energy between the peak and band edge transitions, and δ (defined in the text) is a measure of electron-phonon coupling.

point) for CsPbCl₃. We note that the values listed in this table are the ‘bare’ values obtained from DFT and have not been shifted to align the experimental and computed band edge energies, unlike the values listed in Tables 5.2 and 5.3. These values are all listed at zero strain, and at isotropic strains of +1% and -1%.

We have also listed the values of the width $W = \omega_{pk} - \omega_{BE}$. Now, in analogy with the deformation potential, we define:

$$\delta = \frac{\Delta W}{\Delta l/l_0}. \quad (5.2)$$

δ is a measure of how strongly the shape (width) of $\epsilon_2(\omega)$ is affected by electron-phonon interactions, and hence temperature. We find that $\delta = 22.95$ for CsPbCl₃ and $\delta = 15.45$ for CsPbBr₃. Thus, the effect of electron-phonon couplings (and hence temperature) on the width of $\epsilon_2(\omega)$ is almost one-and-a-half times larger for CsPbCl₃ than for CsPbBr₃. We note that with this rather simple treatment of electron-phonon coupling, one may expect to get a qualitative trend but not quantitative

accuracy. We believe our results can explain why there is a considerable mismatch in the experimental and computed widths of the broad peak in $\epsilon_2(\omega)$ for CsPbCl₃ but not for CsPbBr₃. We also note that several authors who have computed optical spectra for similar systems have noted that in addition to a lateral shift, they also have to apply an overall broadening/narrowing to their computed spectra to obtain a match with experiment. We suggest that strong electron-phonon coupling may be at least a part of the reason for this.

5.5.3 Comparison of dielectric function: pristine and Fe-doped CsPbX₃ (X = Br, Cl)

For optoelectronic applications of Fe-doped CsPbBr₃ and Fe-doped CsPbCl₃, we need to know the optical performance of these materials. For this, we have to look how these materials interact when they are illuminated. The frequency dependent (frequency of the incoming electromagnetic wave) imaginary part ($\epsilon_2(\omega)$) of dielectric function is a very important quantity to measure the optical properties of a material. These properties are a measure of how the electrons within a material interact with the photons of the incoming electromagnetic wave, when the material is illuminated. The equations for calculating $\epsilon_2(\omega)$ are given in the ‘Methods and Formalism’ chapter of this thesis.

Figs. 5.5(a) and (b) show the imaginary part of the frequency dependent dielectric function $\epsilon_2(\omega)$ for pristine CsPbBr₃, 12.5% Fe-doped CsPbBr₃ and CsPbCl₃, 12.5% Fe-doped CsPbCl₃, respectively. We note that the calculated $\epsilon_2(\omega)$ spectra capture all the direct transitions, with crystal momentum conserved i.e., no phonons are involved in the process.

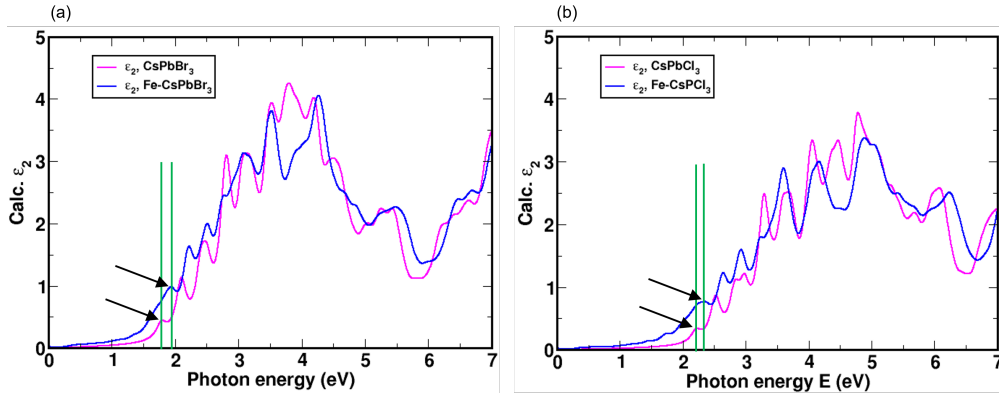


Figure 5.5: Calculated imaginary part (ϵ_2) of frequency dependent dielectric function for (a) CsPbBr₃, 12.5% Fe-doped CsPbBr₃ and (b) CsPbCl₃, 12.5% Fe-doped CsPbCl₃. Color code of curves: magenta – pristine systems and blue – Fe-doped systems. Green vertical lines and black arrows represent the first peak in ϵ_2 spectra for all the systems.

For 12.5% Fe-doped CsPbBr₃ and 25% Fe-doped CsPbBr₃ the calculated direct band gaps at the Γ point are 1.82 eV and 2.00 eV, respectively, while for pristine CsPbBr₃ the calculated band gap was 1.79 eV. Also for 12.5% Fe-doped CsPbCl₃ and 25% Fe-doped CsPbCl₃ the calculated direct band gaps at the Γ point are 2.24 eV and 2.41 eV, respectively, while for pristine CsPbCl₃ the calculated band gap was 2.22 eV. So, the band gap (excluding the Fe-induced mid gap states) increases upon Fe-doping and it is increasing with increasing Fe concentration. Band gap increase indicates decrease in wavelength of photoluminescence and therefore there is a ‘blue shift’ upon Fe-doping. The first peak of the $\epsilon_2(\omega)$ spectrum corresponds to the lowest energy band edge transition in the band structure. We see that upon Fe doping the first peak in the $\epsilon_2(\omega)$ spectrum is shifted a little upward in energy, for both bromide and chloride systems, as shown by green vertical lines and black arrows in Fig. 5.5(a) and (b). This is due to the fact that the direct band gap increases upon Fe-doping with respect to pristine systems, for both the materials. This small blue shift in photoluminescence upon Fe doping is consistent with the experimental observations [see Fig. 4.1 in the previous chapter].

5.6 Conclusions

In summary, our experimental collaborators have done ellipsometry measurements of pristine CsPbBr₃ and pristine CsPbCl₃ and identified the band edge transitions as well as some higher energy excited state optical transitions from the peaks obtained in the $\epsilon_2(\omega)$ spectra.

We have calculated the electronic band structures of pristine CsPbBr₃ and CsPbCl₃. As the optical transitions depend on the momentum matrix elements and the density of the final states given by the Fermi's golden rule, we further calculated the frequency dependent imaginary part of the dielectric function $\epsilon_2(\omega)$ which captures these things together. As GGA calculations underestimate the band gap, the calculated $\epsilon_2(\omega)$ spectra has to be shifted (for both CsPbBr₃ and CsPbCl₃) upward in energy to match the first peak (i.e., the band edge transition) of the calculated spectra with the experimental spectra.

The calculated spectra is compared with the experiment and the band edge transition as well as the higher energy optical transitions are identified. Overall, for CsPbBr₃ $\epsilon_2(\omega)$ the spectrum matches very well with the experiment. The calculation overestimates the peak energy for CsPbCl₃. We suggest that the reason for this disagreement is a strong electron-phonon coupling in CsPbCl₃, resulting in a large change in the energies of some electronic transitions with temperature.

The $\epsilon_2(\omega)$ spectra has been calculated for Fe-doped CsPbBr₃ and Fe-doped CsPbCl₃ also and compared with the pristine systems. We see that the band gap increases upon Fe doping which causes a blue shift with respect to the emission and absorption of the pristine systems.

Bibliography

- [1] L. Protesescu, S. Yakunin, M. I. Bodnarchuk, F. Krieg, R. Caputo, C. H. Hendon, R. X. Yang, A. Walsh, and M. V. Kovalenko, “Nanocrystals of cesium lead halide perovskites (CsPbX_3 , X= Cl, Br, and I): novel optoelectronic materials showing bright emission with wide color gamut,” *Nano. Lett.*, vol. 15, no. 6, pp. 3692–3696, 2015.
- [2] J. M. Ball and A. Petrozza, “Defects in perovskite-halides and their effects in solar cells,” *Nat. Energy*, vol. 1, no. 11, pp. 1–13, 2016.
- [3] Q. Wang, X. Zhang, Z. Jin, J. Zhang, Z. Gao, Y. Li, and S. F. Liu, “Energy-down-shift CsPbCl_3 : Mn quantum dots for boosting the efficiency and stability of perovskite solar cells,” *ACS Energy Lett.*, vol. 2, no. 7, pp. 1479–1486, 2017.
- [4] S. Das Adhikari, S. K. Dutta, A. Dutta, A. K. Guria, and N. Pradhan, “Chemically tailoring the dopant emission in manganese-doped CsPbCl_3 perovskite nanocrystals,” *Angew. Chem.*, vol. 129, no. 30, pp. 8872–8876, 2017.
- [5] X. Hu, X. Zhang, L. Liang, J. Bao, S. Li, W. Yang, and Y. Xie, “High-performance flexible broadband photodetector based on organolead halide perovskite,” *Adv. Funct. Mater.*, vol. 24, no. 46, pp. 7373–7380, 2014.

- [6] C. Gu and J.-S. Lee, “Flexible hybrid organic–inorganic perovskite memory,” *ACS Nano*, vol. 10, no. 5, pp. 5413–5418, 2016.
- [7] Z.-K. Tan, R. S. Moghaddam, M. L. Lai, P. Docampo, R. Higler, F. Deschler, M. Price, A. Sadhanala, L. M. Pazos, D. Credgington, *et al.*, “Bright light-emitting diodes based on organometal halide perovskite,” *Nat. Nanotechnol.*, vol. 9, no. 9, pp. 687–692, 2014.
- [8] H. Zhu, Y. Fu, F. Meng, X. Wu, Z. Gong, Q. Ding, M. V. Gustafsson, M. T. Trinh, S. Jin, and X. Zhu, “Lead halide perovskite nanowire lasers with low lasing thresholds and high quality factors,” *Nat. Mater.*, vol. 14, no. 6, pp. 636–642, 2015.
- [9] C. H. Kang, I. Dursun, G. Liu, L. Sinatra, X. Sun, M. Kong, J. Pan, P. Maity, E.-N. Ooi, T. K. Ng, *et al.*, “High-speed colour-converting photodetector with all-inorganic CsPbBr₃ perovskite nanocrystals for ultraviolet light communication,” *Light Sci. Appl.*, vol. 8, no. 1, p. 94, 2019.
- [10] G. Almeida, I. Infante, and L. Manna, “Resurfacing halide perovskite nanocrystals,” *Science*, vol. 364, no. 6443, pp. 833–834, 2019.
- [11] T. Fang, F. Zhang, S. Yuan, H. Zeng, and J. Song, “Recent advances and prospects toward blue perovskite materials and light-emitting diodes,” *InfoMat*, vol. 1, no. 2, pp. 211–233, 2019.
- [12] J. Ma, J. A. McLeod, L.-Y. Chang, C.-W. Pao, B.-H. Lin, X.-Y. Li, Z. Wang, J. Chen, T.-K. Sham, and L. Liu, “Increasing photoluminescence yield of CsPbCl₃ nanocrystals by heterovalent doping with Pr³⁺,” *Mater. Res. Bull.*, vol. 129, p. 110907, 2020.
- [13] P. Gui, H. Zhou, F. Yao, Z. Song, B. Li, and G. Fang, “Space-confined

- growth of individual wide bandgap single crystal CsPbCl₃ microplatelet for near-ultraviolet photodetection,” *Small*, vol. 15, no. 39, p. 1902618, 2019.
- [14] S. Chu, S. Pan, and G. Li, “Trap state passivation and photoactivation in wide band gap inorganic perovskite semiconductors,” *Phys. Chem. Chem. Phys.*, vol. 20, no. 39, pp. 25476–25481, 2018.
- [15] S. Abe, J. J. Joos, L. I. Martin, Z. Hens, and P. F. Smet, “Hybrid remote quantum dot/powder phosphor designs for display backlights,” *Light Sci. Appl.*, vol. 6, no. 6, pp. e16271–e16271, 2017.
- [16] J. Zhang, Q. Wang, X. Zhang, J. Jiang, Z. Gao, Z. Jin, and S. F. Liu, “High-performance transparent ultraviolet photodetectors based on inorganic perovskite CsPbCl₃ nanocrystals,” *RSC Adv.*, vol. 7, no. 58, pp. 36722–36727, 2017.
- [17] B. Chen, P. N. Rudd, S. Yang, Y. Yuan, and J. Huang, “Imperfections and their passivation in halide perovskite solar cells,” *Chem Soc Rev*, vol. 48, no. 14, pp. 3842–3867, 2019.
- [18] A. Kojima, K. Teshima, Y. Shirai, and T. Miyasaka, “Organometal halide perovskites as visible-light sensitizers for photovoltaic cells,” *J. Am. Chem. Soc.*, vol. 131, no. 17, pp. 6050–6051, 2009.
- [19] N. J. Jeon, J. H. Noh, W. S. Yang, Y. C. Kim, S. Ryu, J. Seo, and S. I. Seok, “Compositional engineering of perovskite materials for high-performance solar cells,” *Nature*, vol. 517, no. 7535, pp. 476–480, 2015.
- [20] K.-G. Lim, S. Ahn, Y.-H. Kim, Y. Qi, and T.-W. Lee, “Universal energy level tailoring of self-organized hole extraction layers in organic solar cells and organic–inorganic hybrid perovskite solar cells,” *Energy Environ. Sci.*, vol. 9, no. 3, pp. 932–939, 2016.

- [21] H. Kim, K.-G. Lim, and T.-W. Lee, “Planar heterojunction organometal halide perovskite solar cells: roles of interfacial layers,” *Energy Environ. Sci.*, vol. 9, no. 1, pp. 12–30, 2016.
- [22] C. C. Stoumpos, C. D. Malliakas, J. A. Peters, Z. Liu, M. Sebastian, J. Im, T. C. Chasapis, A. C. Wibowo, D. Y. Chung, A. J. Freeman, *et al.*, “Crystal growth of the perovskite semiconductor CsPbBr₃: a new material for high-energy radiation detection,” *Cryst. Growth Des.*, vol. 13, no. 7, pp. 2722–2727, 2013.
- [23] B. Roose, K. C. Gödel, S. Pathak, A. Sadhanala, J. P. C. Baena, B. D. Wilts, H. J. Snaith, U. Wiesner, M. Grätzel, U. Steiner, *et al.*, “Enhanced efficiency and stability of perovskite solar cells through Nd-doping of mesostructured TiO₂,” *Adv. Energy Mater.*, vol. 6, no. 2, p. 1501868, 2016.
- [24] G. Wang, M. Lei, J. Liu, Q. He, and W. Zhang, “Improving the Stability and Optoelectronic Properties of All Inorganic Less-Pb Perovskites by B-Site Doping for High-Performance Inorganic Perovskite Solar Cells,” *Solar RRL*, vol. 4, no. 12, p. 2000528, 2020.
- [25] P. Giannozzi, S. Baroni, N. Bonini, M. Calandra, R. Car, C. Cavazzoni, D. Ceresoli, G. L. Chiarotti, M. Cococcioni, I. Dabo, *et al.*, “QUANTUM ESPRESSO: a modular and open-source software project for quantum simulations of materials,” *J. of Phys.: Condens. Matter*, vol. 21, no. 39, p. 395502, 2009.
- [26] P. Giannozzi, O. Andreussi, T. Brumme, O. Bunau, M. B. Nardelli, M. Calandra, R. Car, C. Cavazzoni, D. Ceresoli, M. Cococcioni, *et al.*, “Advanced capabilities for materials modelling with Quantum ESPRESSO,” *J. of Phys.: Condens. Matter*, vol. 29, no. 46, p. 465901, 2017.

-
- [27] D. Hamann, “Optimized norm-conserving vanderbilt pseudopotentials,” *Phys. Rev. B*, vol. 88, no. 8, p. 085117, 2013.
- [28] J. P. Perdew, K. Burke, and M. Ernzerhof, “Generalized gradient approximation made simple,” *Phys. Rev. Lett.*, vol. 77, no. 18, p. 3865, 1996.
- [29] H. J. Monkhorst and J. D. Pack, “Special points for brillouin-zone integrations,” *Phys. Rev. B*, vol. 13, no. 12, p. 5188, 1976.
- [30] N. Marzari, D. Vanderbilt, A. De Vita, and M. Payne, “Thermal contraction and disordering of the Al(110) surface,” *Phys. Rev. Lett.*, vol. 82, no. 16, p. 3296, 1999.
- [31] H. Ehrenreich and H. Philipp, “Optical properties of Ag and Cu,” *Phys. Rev.*, vol. 128, no. 4, p. 1622, 1962.
- [32] P. Guo, Y. Xia, J. Gong, C. C. Stoumpos, K. M. McCall, G. C. Alexander, Z. Ma, H. Zhou, D. J. Gosztola, J. B. Ketterson, *et al.*, “Polar fluctuations in metal halide perovskites uncovered by acoustic phonon anomalies,” *ACS Energy Lett.*, vol. 2, no. 10, pp. 2463–2469, 2017.
- [33] H. M. Ghaithan, Z. A. Alahmed, S. M. Qaid, M. Hezam, and A. S. Aldwayyan, “Density functional study of cubic, tetragonal, and orthorhombic CsPbBr₃ perovskite,” *ACS Omega*, vol. 5, no. 13, pp. 7468–7480, 2020.
- [34] M. Kholil, M. Bhuiyan, M. A. Rahman, M. Ali, and M. Aftabuzzaman, “Effects of Fe doping on the visible light absorption and bandgap tuning of lead-free (CsSnCl₃) and lead halide (CsPbCl₃) perovskites for optoelectronic applications,” *AIP Adv.*, vol. 11, no. 3, p. 035229, 2021.
- [35] K. Heidrich, W. Schäfer, M. Schreiber, J. Söchtig, G. Trendel, J. Treusch, T. Grandke, and H. Stolz, “Electronic structure, photoemission spectra, and

- vacuum-ultraviolet optical spectra of CsPbCl₃ and CsPbBr₃,” *Phys. Rev. B*, vol. 24, no. 10, p. 5642, 1981.
- [36] F. Zheng, J. Tao, and A. M. Rappe, “Frequency-dependent dielectric function of semiconductors with application to physisorption,” *Phys. Rev. B*, vol. 95, no. 3, p. 035203, 2017.
- [37] X. Chen, Y. Wang, J. Song, X. Li, J. Xu, H. Zeng, and H. Sun, “Temperature dependent reflectance and ellipsometry studies on a CsPbBr₃ single crystal,” *J. Phys. Chem. C*, vol. 123, no. 16, pp. 10564–10570, 2019.
- [38] M. Zhao, Y. Shi, J. Dai, and J. Lian, “Ellipsometric study of the complex optical constants of a CsPbBr₃ perovskite thin film,” *J. Mater. Chem. C*, vol. 6, no. 39, pp. 10450–10455, 2018.

Chapter 6

Electronic Properties of Two Dimensional Electron Gas at LVO/KTO Interface

If you are receptive and humble,
Mathematics will lead you by the
hand.

Paul A. M. Dirac

In this chapter, we study the electronic properties of the two dimensional electron gas (2DEG) formed at the interface of LaVO_3 and KTaO_3 . These materials are commonly referred to as LVO and KTO, respectively, and the interface formed by them is referred to as LVO/KTO. The work presented in this chapter was performed in collaboration with the experimental group of Prof. Suvankar Chakraverty, INST, Mohali, who experimentally created an LVO/KTO interface, and studied its properties. We have performed first-principles density functional theory calculations on this system, to gain insight into the electronic properties of the 2DEG formed at the LVO/KTO interface.

6.1 Introduction

A two-dimensional electron gas (2DEG) refers to a system of electrons confined within a two-dimensional plane, typically at the interface between two different insulators or two semiconductors or one insulator and one semiconductor. In such systems, electrons are free to move in two dimensions but are tightly confined in the third dimension.

This confinement along the third direction leads to the quantization of electronic energy levels along that direction. The spacing between the electronic energy levels in the third direction is greater than the thermal energy $k_B T$, where k_B is Boltzmann's constant and T is the temperature, so that thermal energy alone cannot lead to the motion of the electrons along the third dimension, and the wavefunction has the form of standing wave along the third dimension.

The most commonly observed 2DEGs are found at interfaces in metal oxide semiconductor field effect transistors (MOSFETs). In MOSFETs, the electrons are extremely confined to the vicinity of the interface between a semiconductor (eg., Si) and metal oxide (which is an insulator, e.g., SiO_2) by an externally applied positive gate voltage. At low temperatures, only the lowest electronic energy level along the direction perpendicular to the interface is occupied, and hence the motion of the electrons perpendicular to the interface is ignored. However, the electrons can freely move parallel to the interface, thus forming a 2DEG.

Already, two Nobel prizes have been awarded in the field of 2DEG research: one in 1985 to Klaus von Klitzing for the discovery of the Integer Quantum Hall effect, and the other in 1998 to Daniel Tsui, Horst Störmer and Robert Laughlin for the discovery of the Fractional Quantum Hall effect.

Oxide materials exhibit many diverse properties like magnetism, ferroelectricity,

superconductivity, etc.¹ When two or more oxides are combined to form heterostructures, a rich variety of phenomena emerges.^{2;3} These oxide heterostructures can be made experimentally by recently developed thin film deposition techniques such as pulsed laser deposition and molecular beam epitaxy.

Transition metal oxide heterostructures are very famous and fundamentally important for diverse emergent properties. This vast range of emergent properties includes magnetism, half-metallic behavior, multiferroicity, high temperature superconductivity, optical and electrical effects, quantum oscillations in conductivity and colossal magnetoresistance.⁴⁻¹³

In 2004, Ohtomo and Hwang observed electronic conduction or a metallic phase, for the first time, at the interface of two insulator perovskites, LaAlO_3 and SrTiO_3 .¹⁴ Since then, the $\text{LaAlO}_3/\text{SrTiO}_3$ interface, commonly referred to as LAO/STO, has become very well known, and has been extensively studied for the past two decades.^{15;16} In this system, a metallic phase emerges at the interface of the two materials, while the individual bulk components LAO and STO are insulators. It is observed that the metallic phase is confined to a region within a few nanometers of the interface, and thus this can be treated as a two-dimensional electron gas (2DEG).¹⁷ The 2DEG has a very high charge carrier density of $\sim 10^{13} \text{ cm}^{-2}$ and large mobility of $\sim 10^3 \text{ cm}^2 \text{ V}^{-1} \text{ s}^{-1}$ which makes it of great interest for applications in nanoelectronics, e.g., oxide field-effect transistors.¹⁸⁻²¹

The LAO/STO interface also shows some fascinating emergent properties such as magnetism, superconductivity, quantum Hall effect, coexistence of ferromagnetism and superconductivity, photoconductivity, resistance switching, Shubnikov-de Haas oscillations, etc.^{4;10;12;20;22-28}

Further, the charge carrier density and hence the conductivity of the 2DEG at the interface can be tuned by means of an applied electric field and/or electromagnetic radiation.^{12;20;24;29} The charge carrier density increases as the light illumination

increases. Even after switching off the light, this increased conductivity remains for several days; this is known as ‘persistent photoconductivity’.^{29–31} In addition to LAO/STO, this phenomenon has also been observed in other interfaces, e.g., LTO/STO (LTO = LaTiO₃).

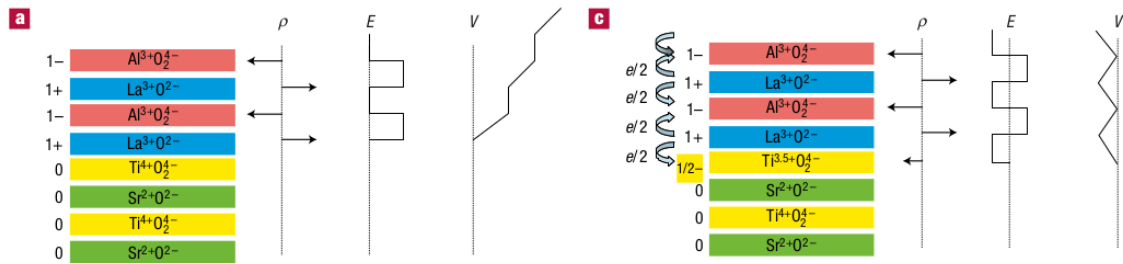


Figure 6.1: (a) The unreconstructed interface has neutral (001) planes in SrTiO₃, but the (001) planes in LaAlO₃ have alternating net charges (ρ). If the interface plane is LaO/TiO₂, this produces a non-negative electric field (E), leading in turn to an electric potential (V) that diverges with thickness. (c) The divergence catastrophe at the LaO/TiO₂ interface can be avoided if half an electron is added to the last Ti layer. This produces an interface dipole that causes the electric field to oscillate about zero and the potential remains finite. The upper free surface is not shown, but in this simple model the uppermost AlO₂ layer would be missing half an electron, which would bring the electric field and potential back to zero at the upper surface. Reprinted with permission from Ref. 15.

A spin-polarized 2DEG has been found at the interface of two non-magnetic materials LAO and STO.⁸ Magnetism emerges at the cost of exchange splitting of the Ti-3d conduction electrons; this is confirmed by first-principles calculations of LAO/STO.^{32:33} First principles calculations have also found spin polarization at the LaTiO₃/SrTiO₃ interface.³⁴ These findings are of interest for possible applications in spintronics.³⁵ Standard electronic devices such as transistors and diodes carry information using the charge degrees of freedom of electrons; carrying information using instead (or in addition) spin degrees of freedom could have different advantages such as low power cost, better energy efficiency, and new devices can be constructed like spin transistors.³⁶

An enormous amount of work, both experimental and theoretical, has been done

in the past two decades, on 2DEGs at oxide interfaces. However, the origin of 2DEGs in many oxide interface systems is not very clear: many mechanisms have been proposed, and there is still an ongoing debate. Two mechanisms have become particularly popular.^{37;38} The most popular mechanism, arguably, is known as ‘electronic reconstruction’ due to ‘polar catastrophe’.¹⁵ This mechanism is shown in Fig. 6.1. In oxide interfaces such as $\text{LaMO}_3/\text{SrTiO}_3$ ($M = \text{metal atom}$), along the (001) direction, the LaMO_3 is comprised of alternating LaO and MO_2 planes. If we consider formal ionic charges, this consists of alternating $(\text{LaO})^{+1}$ and $(\text{MO})^{-1}$ charged planes. In contrast, SrTiO_3 consists of alternating $(\text{SrO})^0$ and TiO^0 neutral layers. This causes a finite polarization inside LaMO_3 . Therefore, when a LaMO_3 film is grown on a TiO_2 terminated $\text{SrTiO}_3(001)$ surface, a polarization discontinuity exists at the interface region which increases the electrostatic potential as the LaMO_3 film thickness increases. Thus there exists a potential divergence, this is called the ‘polar catastrophe’. This makes the system unstable. To eliminate the polar catastrophe, $\frac{1}{2}$ electron is transferred, from the surface of LaMO_3 to the $\text{LaMO}_3/\text{SrTiO}_3$ interface, thereby eliminating the divergence of potential. This mechanism is known as ‘electronic reconstruction’ due to ‘polar catastrophe’.

Another well accepted mechanism for 2DEG formation at the interface of two semiconductors is ‘modulation doping’, shown in Fig. 6.2. In modulation doping, the conduction electrons (holes) are spatially separated from their donor (acceptor) impurity ions.³⁹ Suppose there is an interface formed between a wider band gap semiconductor and narrower band gap semiconductor and the wider gap semiconductor is doped with some donor (acceptor) impurity ions. In this case the band alignment is such that that the conduction band minimum of the wider gap semiconductor is above the conduction band minimum of the narrower gap semiconductor and this conduction band minimum is crossing the Fermi level at the interfacial region. Due to these relative conduction band offsets, the electrons (holes) donated by

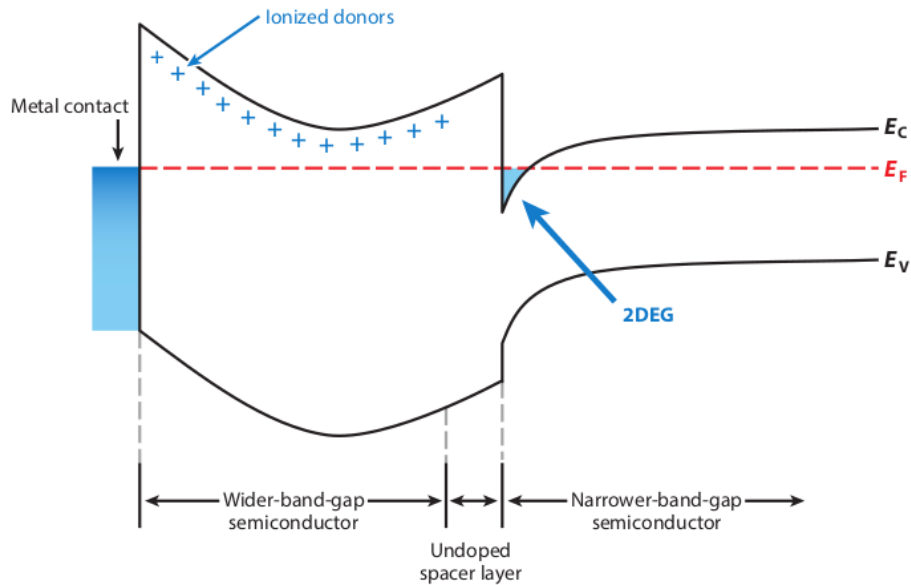


Figure 6.2: Principle of modulation doping. Electrons from the donors in the material with the higher-conduction band edge transfer into the conduction band of the semiconductor on the other side of the interface, creating a 2DEG. The electrons are spatially separated from their donors, and ionized impurity scattering is thus reduced. E_C and E_V denote the conduction band edge and valence band edge, respectively, and E_F denotes the Fermi level. Reprinted with permission from Ref. 38.

their donors (acceptors) are transferred to the partially occupied conduction band of the narrower gap semiconductor at the interface. The transferred electrons (holes) will not go away from the interface as they will remain attracted by their corresponding donors (acceptors), thus creating a 2DEG at the interface. Due to this spatial separation between electrons (holes) and their donors (acceptors), the scattering or trapping is dramatically reduced, which increases the mobility of the 2DEG. One example of a system where one observes 2DEG formation by modulation doping is AlGaAs/GaAs heterostructures having extremely high carrier mobility of $3 \times 10^7 \text{ cm}^2 \text{ V}^{-1} \text{ s}^{-1}$.^{40;41} This method has very important device applications such as in high-electron-mobility transistors (HEMTs).^{42;43}

There are other mechanisms suggested in the literature, for 2DEG formation at the interface of two insulating perovskites, such as oxygen vacancies^{44–46} and cation

intermixing⁴⁷⁻⁴⁹.

Charge transfer can also happen at the interfaces of $\text{LaMO}_3/\text{SrTiO}_3$ superlattice, if the LaMO_3 is nonstoichiometric i.e., LaMO_3 is terminated with LaO layers on both sides. For this case, an ‘extra’ electron is introduced into the system due to the uncompensated ionic charge on the additional $(\text{LaO})^{+1}$ monolayer, a mechanism which is equivalent to electron doping.⁵⁰

As already mentioned above, the most studied system in the perovskite oxide 2DEG community is $\text{LaAlO}_3/\text{SrTiO}_3$ (LAO/STO). This is an example of a polar/non-polar interface as LAO is a polar material and STO is a non-polar material. Considering 2DEG formation at the interface of two band insulators perovskite oxides, 2DEG is discovered for the first time at this interface and from then this system is being studied even till now, over two decades of fascinating research. The formation of 2DEG at LAO/STO is ‘electronic reconstruction’ due to polar catastrophe, as described above. LAO/STO is an example of polar/non-polar interface, where LAO is a polar material as it consists of alternating charged $(\text{LaO})^+$ and $(\text{AlO}_2)^-$ layers and STO is a non-polar material as it consists of alternating neutral $(\text{SrO})^0$ and $(\text{TiO}_2)^0$ layers. At the $(\text{LaO})^+ / (\text{TiO}_2)^0$ interface, $\frac{1}{2}$ electrons are transferred from the charged $(\text{LaO})^+$ layer to the neutral $(\text{TiO}_2)^0$ layer at the interface, to avoid the polar discontinuity and hence polar catastrophe. These transferred electrons then partially occupy the Ti-3d orbitals of STO and create conduction at the interface.¹⁵

It has also been observed that for less than 4 unit cells (u.c.) of LAO film thickness, the LAO/STO interface remains insulating. So there exists a critical film thickness of 4 u.c. above which the conducting nature starts at this interface.²⁰ Theoretical studies have shown that this critical thickness for forming a 2DEG at the interface is strongly related to the polar distortions or electric polarization in the LAO film.^{51;52} M. Behtash et al.,⁵² have shown that the polarization strength

decreases as the thickness increases for LAO. When the LAO film thickness is below 5 u.c., the polarization strength within the LAO is strong enough to cancel the polar catastrophe induced electron transfer. At the 5 u.c. LAO thickness, the polarization is sufficiently weak that polar catastrophe induced electron transfer can only be partially opposed and thus a few electrons will be transferred to the interface which forms the metallic states. The calculated interfacial charge carrier density is $1.6 \times 10^{13} \text{ cm}^{-2}$, which is well consistent with the experimental value of $1-2 \times 10^{13} \text{ cm}^{-2}$.^{20;53-56}

2DEGs can also be formed at non-polar/non-polar interfaces. We have seen above that the electronic reconstruction due to polar catastrophe can be the origin of 2DEG formation at the polar/non-polar LAO/STO interface. Electronic reconstruction due to polar catastrophe can also be the reason of forming 2DEG at the non-polar/non-polar interfaces. One such example is $\text{CaZrO}_3/\text{SrTiO}_3$,^{57;58} in which both CaZrO_3 and SrTiO_3 consist of neutral layers and hence there is no polar discontinuity at the interface. Chen et al. have found a 2DEG at the $\text{CaZrO}_3/\text{SrTiO}_3$ interface for the first time.⁵⁷ S. Nazir et al.⁵⁸ performed first-principles calculations and showed that the compressive strain due to lattice mismatch between CaZrO_3 and SrTiO_3 can induce a strong polarization in CaZrO_3 and the $\text{CaZrO}_3/\text{SrTiO}_3$ heterostructure shows an insulator to metal transition as the CaZrO_3 thickness increases. This is in agreement with the experimental observations.⁵⁷

So, we have given examples of 2DEG formation at polar/non-polar (e.g., LAO/STO) and non-polar/non-polar interfaces (e.g., $\text{CaZrO}_3/\text{SrTiO}_3$). The third possibility is the polar-polar interfaces, in which both the film and substrate are polar materials. Examples of such heterostructure systems are $\text{LaAlO}_3/\text{KNbO}_3$, $\text{LaAlO}_3/\text{KTaO}_3$, $\text{LaAlO}_3/\text{NaNbO}_3$, $\text{LaAlO}_3/\text{NaTaO}_3$ etc.^{59;60} For polar/polar heterostructure systems, when the interface consists of two donor layers (i.e., cation layers), e.g.,

a $(\text{LaO})^+ / (\text{TaO}_2)^+$ interface in $\text{LaAlO}_3 / \text{KTaO}_3$, both the donor layers could donate electrons to the interface and we could have a higher interfacial charge carrier density compared to the polar/non-polar and non-polar/non-polar interfaces, as in polar/non-polar interfaces there is only one donor layer. Similarly, if the interface consists of two acceptor layers (i.e., anion layers), then they could donate holes to the interface, thus leading to the creation of a two dimensional hole gas (2DHG).

Here, the reason people choose Nb and Ta based perovskites as the substrate materials is that Nb-4*d* and Ta-5*d* states are less localized than Ti-3*d* states, which increases the carrier mobility in these materials compared to STO based interfaces. Also, Nb and Ta have larger spin-orbit coupling than Ti, which can give rise to interesting physics. Zou et al.,⁶¹ have successfully created polar/polar $\text{LaTiO}_3 / \text{KTaO}_3$ heterostructures in which LaTiO_3 is a Mott insulator and KTaO_3 is a band insulator. They observed a higher interfacial charge carrier density and carrier mobility than in the widely studied LAO/STO interface.

Recently, people got interested in KTaO_3 (KTO) based heterostructure interfaces due to several reasons: (i) KTO has Ta-5*d* electrons which are less localized than the Ti-3*d* electrons of SrTiO_3 . This increases the mobility of the 2DEG formed at the KTO based heterointerfaces,⁶² and (ii) KTO has a very high spin-orbit coupling which is one order of magnitude larger than in STO. This can lead to interesting spin-orbit physics and potential applications in spin-electronic devices.^{62;63} Only a very few KTO based heterostructures have been found which can host a 2DEG at their interfaces, such as $\text{LaTiO}_3 / \text{KTaO}_3$, $\text{LaVO}_3 / \text{KTaO}_3$ and EuO / KTO .^{61–64}

Research on 2DEGs is important with respect to fundamental physics and also has tremendous potential applications. Superconductivity has also been observed at the LAO/STO interface.^{10;23;65} Many potential and diverse applications have been reported for 2DEGs. For example, the 2DEG at the LAO/STO interface can be used for sensors⁶⁶, field-effect transistors^{20;21}, thermoelectrics^{67;68}, solar cells^{69;70},

nanophotodetectors⁷¹ etc. The photoconductivity of 2DEGs has a lot of potential applications such as optical switches, photodetectors, holographic memory etc.^{29;71-73}

6.2 Experimental motivation

Our experimental collaborators in the group of Prof. Suvankar Chakraverty, INST, Mohali have grown thin film of LVO on a TaO₂-terminated KTO(001) substrate using pulsed laser deposition, at 600 °C substrate temperature.⁶² They have prepared different samples of different LVO thickness. Atomic force microscopy (AFM) confirms that the KTO(001) substrate is single terminated or TaO₂ terminated.⁷⁴ X-ray diffraction (XRD), reflection high-energy electron diffraction (RHEED) and X-ray photoemission (XPS) measurements confirm that a high quality LVO thin film is grown epitaxially on the KTO substrate.⁶²

Our experimental collaborators measured the temperature dependent two-dimensional (2D) electrical resistivity (ρ_{2D}) for conduction parallel to the LVO/KTO interface, using the standard four-probe method.⁶² These results are shown in Fig. 6.3. The resistivity is found to increase with increasing temperature, which confirms that the interface behaves like a metal and is a two-dimensional electron gas (2DEG) as the conduction electrons are confined near the interface. Also, the $I - V$ characteristics show linear behaviour which also confirms the ohmic or metallic nature of the interface. It is very clear from Fig.6.3 that, for 2 monolayer (ML) LVO film thickness, the value of resistivity is very large and also the resistivity decreases with increasing temperature, hence interface becomes insulating. The interface is found to be insulating below 3 ML film thickness, and conductive above 3 ML film thickness. Fig. 6.3 shows ρ_{2D} vs T , we see that all the samples having LVO film thickness greater than 3 ML are conducting at room temperature (RT), and they are conducting down to 1.8 K. As the resistivity increases with increasing temperature, it indicates the

metallic behaviour of the interface.

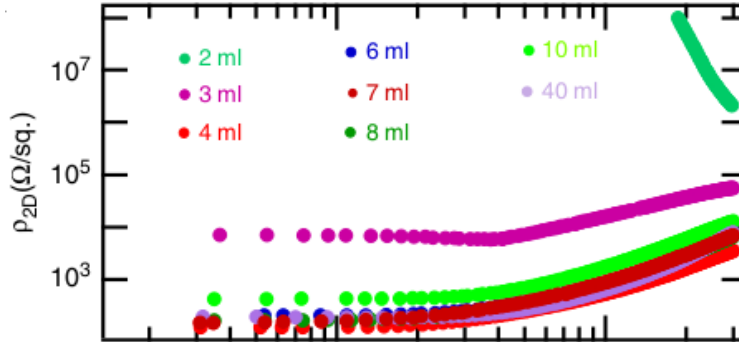


Figure 6.3: Measured two-dimensional resistivity vs temperature for LVO/KTO interface using four-probe method. Reprinted with permission from Ref. 62.

They performed Hall measurements and measured the charge carrier density and carrier mobility, at 300 K and 1.8 K. They observed that once the LVO/KTO interface becomes conducting, the carrier density and mobility are independent of the LVO film thickness. This is compatible with the ‘electronic reconstruction’ mechanism of the 2DEG formation, where once the critical film thickness has been achieved to avoid the ‘polar catastrophe’, increasing the film thickness does not add further carriers to the interface. They obtained a high carrier mobility of $\sim 600 \text{ cm}^2 \text{ V}^{-1} \text{ s}^{-1}$ at 1.8 K. The obtained carrier density at the LVO/KTO interface is $1 \times 10^{14} \text{ cm}^{-2}$.⁷⁴ This interfacial charge carrier density is one order of magnitude higher than that of the polar/non-polar (e.g., LAO/STO) interfaces.

They have also studied the effect of light and electric field on the electrical conductivity of the 2DEG formed at the LVO/KTO interface.⁷⁴ The interface shows ‘persistent photoconductivity’. They observed that the conductivity increases under light illumination.

We want to theoretically study the electronic properties of the LVO/KTO interface and gain further insights into this system using first-principles DFT calculations.

6.3 Systems studied

We have considered several systems in our first-principles DFT calculations. KTO has the perovskite structure and it is cubic at all temperatures. Fig. 6.4 shows the cubic crystal structure of KTO. We have shown a $2 \times 2 \times 2$ supercell in this figure. However, the calculations have been performed using the $1 \times 1 \times 1$ primitive unit cell.

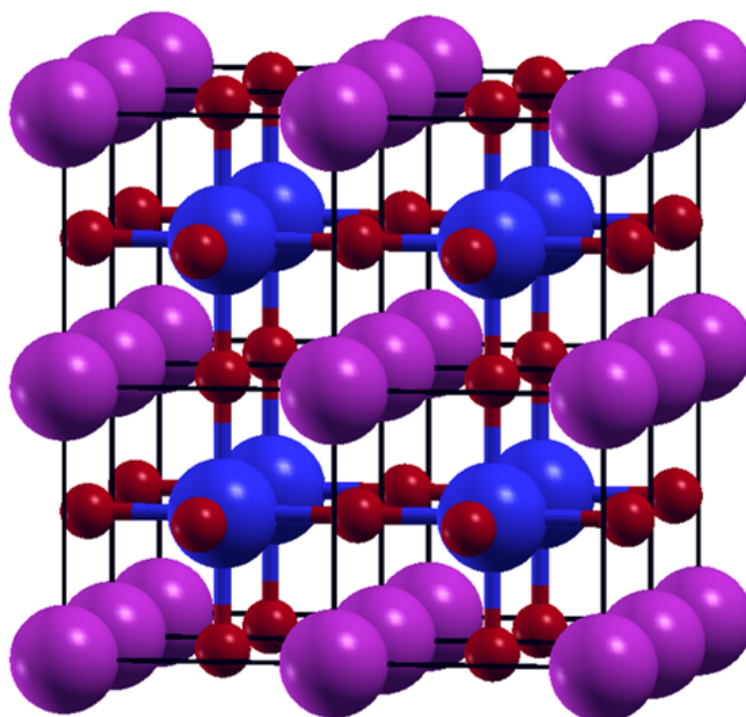


Figure 6.4: Cubic crystal structure of bulk KTaO_3 . It has the perovskite structure in which each Ta atom is surrounded by six O atoms forming an TaO_6 Octahedron. Here, a $2 \times 2 \times 2$ supercell is shown. The primitive unit cell contains five atoms: one K, one Ta and three O atoms. Atomic color code: magenta: K, blue: Ta, red: O.

Bulk LVO possesses a monoclinic crystal structure below 140 K, with C-type antiferromagnetic ordering (C-AFM). Above 140 K, LVO is non-magnetic (NM) and it has an orthorhombic structure. In our calculations we have considered the room temperature (RT) orthorhombic phase, as shown in Fig. 6.5(a). We have also considered a hypothetical tetragonal structure of bulk LVO. This is considered because

the LVO layers have been found experimentally to have a tetragonal structure when grown on the KTO(001) substrate. The tetragonal structure of LVO is shown in Fig. 6.5(b).

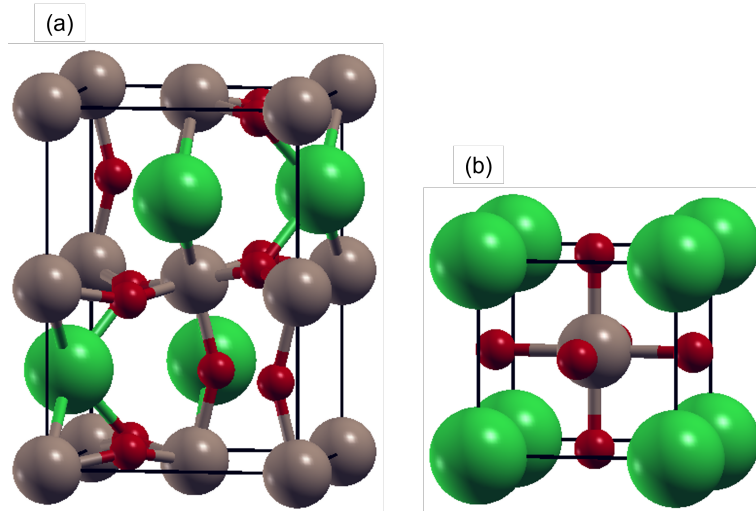


Figure 6.5: Structure of bulk LaVO_3 : (a) orthorhombic and (b) tetragonal. The orthorhombic structure can be derived from the cubic structure by introducing a pattern of alternating distortions in the VO_6 octahedra. The primitive unit cell of (a) contains a total of 20 atoms: four La, four V and twelve O atoms. The primitive unit cell of (b) contains five atoms: one La, one V and three O. Atomic color code: green: La, brown: V, red: O.

Next, we have considered a TaO_2 terminated KTO(001) surface as shown in Fig. 6.6(a). To form this surface, we have taken a nine-layer KTO(001) surface slab. The bulk-truncated slab contains 4.5 unit cells of KTO. The width of the vacuum region (introduced to obtain artificial periodicity along the z direction) is greater than 15 \AA .

Next, we have done atomistic modelling of the LVO/KTO interface, using two different kinds of systems: (i) an infinitely repeating LVO/KTO superlattice (no vacuum region introduced along z). Note that in this system, each supercell contains two LVO/KTO interfaces. (b) by including a vacuum along the z -direction, the system we are effectively studying consists of a KTO slab and a LVO slab with a single interface between them (one interface per supercell). The thicknesses

of the LVO film and KTO substrate are varied. Fig. 6.6(b) and 6.6(c) show the $(\text{LVO})_{4.5}/(\text{KTO})_{4.5}$ superlattice and the slab model, respectively. Here 4.5 means that the system is comprised of 4.5 unit cells (u.c.) i.e., 9 atomic layers. As found in the experiment, we have considered a TaO_2 terminated KTO(001) substrate and a LaO terminated LVO film. Thus at the interface we have adjacent LaO and TaO_2 layers.

6.4 Computational details

We have performed spin polarized density functional theory (DFT) calculations as implemented in the Quantum ESPRESSO (QE) software package.^{75;76} Exchange-correlation interactions are treated using the Perdew-Burke-Ernzerhof form of the Generalized Gradient Approximation (PBE-GGA).⁷⁷ The interactions between valence electrons and ionic cores are described by ultrasoft pseudopotentials.⁷⁸

In the systems studied in this chapter, i.e., LVO, KTO bulk, KTO(001) surface and LVO/KTO interface, there exist strongly localized V-3*d* and Ta-5*d* orbitals which need correction for the strong electron-electron correlation using Hubbard U (and J) parameters. We have done DFT+ U calculations to capture the strong localization and correct for the self-interaction error of the V-3*d* and Ta-5*d* orbitals. We have used two different variants of these calculations. For geometry optimization we have used the DFT+ U method of Cococcioni and de Gironcoli,⁷⁹ (keyword: `lda_plus_u_kind = 0` in QE-6.5), which uses only the Hubbard U parameter, where U is the onsite Coulomb repulsion. In the rest of this chapter we will refer to this as the C-dG method with atomic projection. This is the only DFT+ U option available in QE for geometry optimization calculations. For electronic structure calculations, we have used the rotationally invariant scheme of Liechtenstein et al.⁸⁰ (keyword: `lda_plus_u_kind = 1` in QE-6.5), which uses Hubbard U and J parameters, where

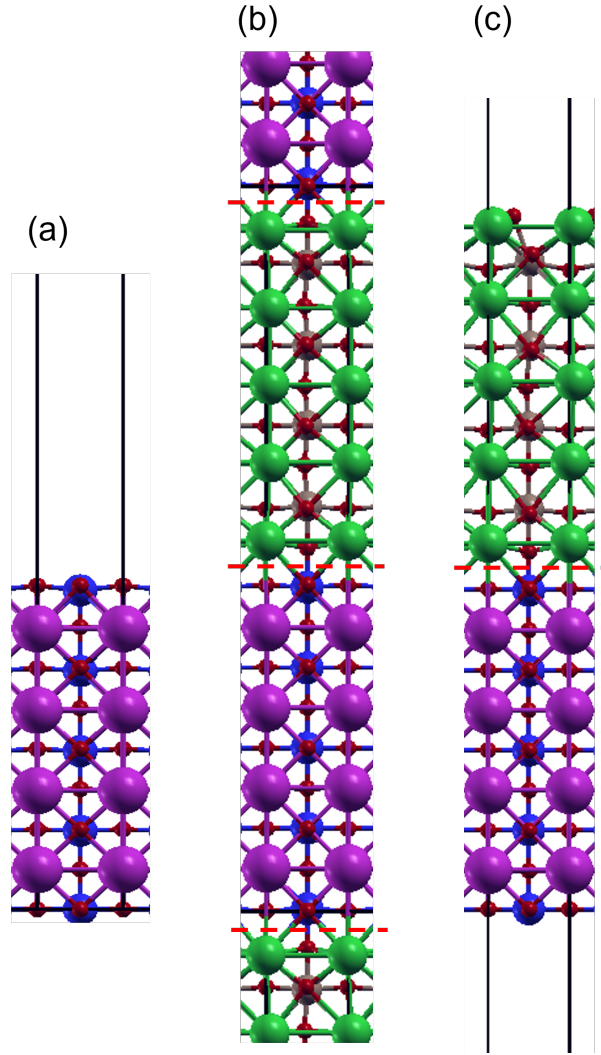


Figure 6.6: Optimized structure of (a) 9-layers KTO(001) slab with TaO₂ termination, (b) LVO/KTO interface in the superlattice model, and (c) LVO/KTO interface with vacuum. The horizontal red dashed lines indicate the locations of the interfaces. (b) contains two interfaces per unit cell and (c) contains only one interface per unit cell. Atomic color code: green: La, brown: V, red: O, magenta: K, blue: Ta.

J is the onsite exchange interaction. In the rest of this chapter we will call this as L method, with ortho-atomic projection. This rotationally invariant scheme is used in addition to the C-dG method as spin-orbit coupling (SOC) calculations are possible in QE only with this option. We have also used the ortho-atomic projection as it is claimed to give better results for electronic structure,⁸¹ than the atomic projection.

The values of U and J parameters for $V-3d$ states are chosen so that it matches correct experimental band gap in its RT orthorhombic phase. This is discussed under electronic structure of bulk orthorhombic LVO. Hubbard U parameter for $Ta-5d$ orbital is chosen from the literature.⁵⁹

The Kohn-Sham wave functions and the corresponding charge densities are expanded in plane-wave basis sets having cutoffs of 40 Ry and 400 Ry, respectively. Brillouin zone sampling is done using a Monkhorst-Pack mesh.⁸² We have used an $8 \times 8 \times 8$ k-mesh for bulk cubic KTO, $8 \times 8 \times 6$ k-mesh for bulk orthorhombic LVO, $8 \times 8 \times 8$ k-mesh for bulk tetragonal LVO, and an $8 \times 8 \times 1$ k-mesh for the KTO(001) surface and LVO/KTO interface models. For metallic systems, convergence is improved using Marzari-Vanderbilt cold smearing⁸³ of width of 0.005 Ry.

For SOC, we have used fully relativistic pseudopotentials for all the atoms.

For bulk LVO and KTO, all atoms are allowed to relax. For the KTO(001) surface, the bottom two layers of the slab are kept fixed at the bulk coordinates and all other layers are allowed to relax. For LVO/KTO superlattice model all the atoms as well as the supercell parameter along the z direction are allowed to relax, and for LVO/KTO interface with vacuum, only the bottommost layer is kept fixed and all other layers are allowed to relax. For geometry optimization, we use the Broyden-Fletcher-Goldfarb-Shanno (BFGS) algorithm⁸⁴, until all components of the forces on all atoms are less than 0.001 Ry/Bohr.

6.5 Results and discussion

Before examining the electronic properties of the LVO/KTO interface, we first study the structural and electronic properties of the constituents, i.e., cubic KTO, KTO(001) surface, orthorhombic LVO and tetragonal LVO. This will help us in understanding the structural and electronic properties, as well as emergent properties,

if there are any, of the LVO/KTO interface.

6.5.1 Constituent: Bulk KTO

Structural properties of bulk KTO

KTO possesses the cubic perovskite structure, as shown in Fig. 6.4 above, at all temperatures. In this system, each Ta cation is coordinated by six O anions to form the TO_6 octahedra, while the K cation has 12 nearest neighbour O anions. The coordination number of each O anion is 2, coordinated by two Ta atoms. Our PBE-GGA calculated lattice constant = 4.011 Å, which is very close to the experimental value of 3.989 Å and previous theoretical values, as shown in Table 6.1. The calculated bulk modulus is also compared with previous theoretical and experimental results and tabulated in Table 6.1.

Property	Our calc. (PBE-GGA)	Previous calculations	Expt
a_0	4.011 Å	4.031 Å (PBE-GGA) ⁸⁵ 4.028 Å (PBE-GGA) ⁸⁷ 3.989 Å (PBEsol-GGA) ⁸⁵ 3.950 Å (LDA) ⁸⁹	3.988 Å ⁸⁶ 3.989 Å ⁸⁸
B_0	190.7 GPa	183.51 GPa (PBE-GGA) ⁸⁵ 200.07 GPa (PBEsol-GGA) ⁸⁵ 224.85 GPa (LDA) ⁸⁹	218 GPa ⁹⁰

Table 6.1: Our PBE-GGA calculated optimized lattice constant (a_0) and bulk modulus (B_0) of bulk KTO. The values are compared against previous calculations with different functionals and with experiments.

Electronic structure of bulk KTO

Next, we calculate the electronic structure of cubic KTO. The band structure and orbital projected density of states (PDOS) of bulk KTO are calculated both without and with spin-orbit coupling (SOC). Fig. 6.7 show the band structure and PDOS

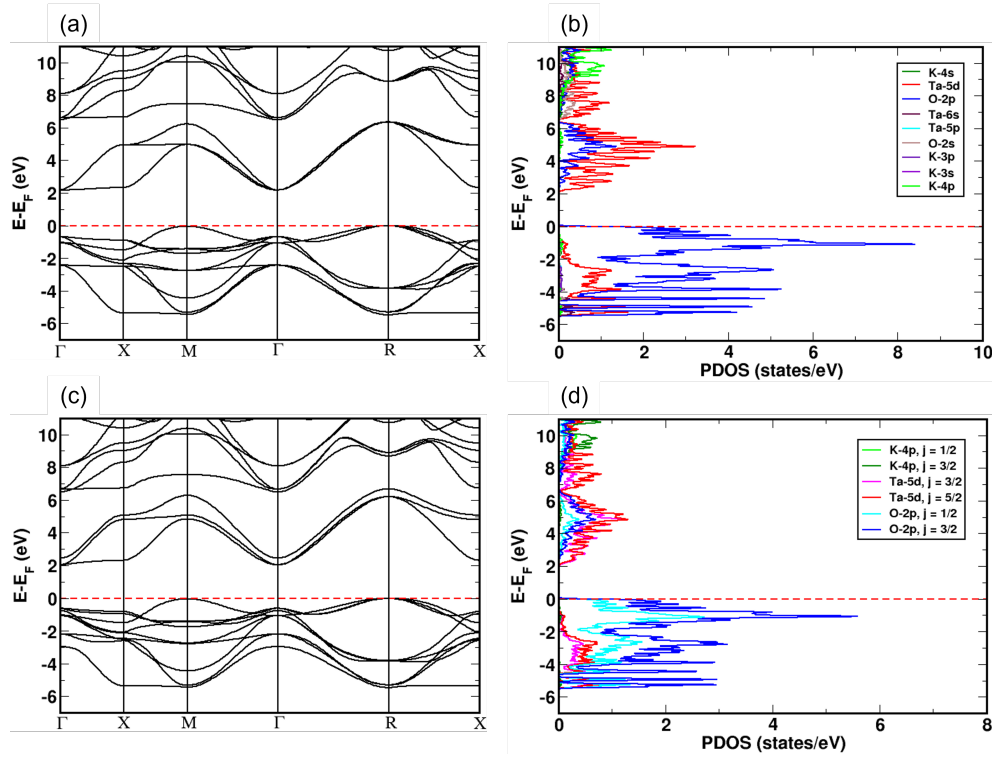


Figure 6.7: (a) Electronic band structure and (b) projected density of states (PDOS) of bulk KTO without spin-orbit coupling (SOC). (c) Electronic band structure and (d) PDOS of bulk KTO with SOC. The corresponding colors of the orbital projected DOS are shown in the insets of (b) and (d). The calculated $R-\Gamma$ indirect band gap is = 2.18 eV without SOC, and 2.04 eV with SOC. In each case, the Fermi level is set at the valence band maximum (VBM) and is indicated by the red dashed lines.

without and with SOC. We see that cubic KTO is an insulator as there is no state which crosses the Fermi level. Our PBE-GGA calculated band gap is 2.18 eV (without SOC), which matches excellently with previous theoretical results [see Table 6.2]. However, this value is lower than the experimental value of 3.60 eV⁹¹, which is a well known shortcoming of DFT calculations performed using GGA exchange-correlation. The band dispersion also agrees well with previous theoretical results.⁸⁵ Hybrid functionals and GW approximation methods correctly reproduce the experimental band gap; however, we have not attempted these because of the high experimental cost. Ojha et. al.,⁹² calculated the band gap after including a Hubbard U parameter. Without any Hubbard U , their calculated band gap is 2.05 eV. With $U = 1.35$ eV,

the band gap is 2.10 eV. In other words, the band gap does not improve significantly with GGA+U.

Our calc. band gap E_g (eV)	Previously calculated band gap E_g (eV)	Experimental band gap E_g (eV)
2.18 (PBE-GGA)	2.05 (PBE-GGA) ⁹² 2.15 (PBE-GGA) ⁸⁵ 2.14 (PBEsol-GGA) ⁸⁵ 2.10 (PBE-GGA+U) ⁹² 2.16 (LDA) ⁸⁹ 3.61 (HSE06) ⁹³ 3.60 (HSE06) ⁹² 3.57 (GW) ⁹⁴	3.60 ⁹¹

Table 6.2: Our PBE-GGA calculated band gap of bulk KTaO_3 . The value is compared against other calculated values with different functionals and methods, and also with the experiment. As usual, GGA underestimates the band gap.

Fig. 6.7(a) show that the valence band maximum (VBM) lies at the R point in the Brillouin zone (we note that the energies are almost degenerate at the M and R points) and the conduction band minimum (CBM) lies at the Γ point. So, bulk KTO has an indirect band gap. Examining the PDOS in Fig. 6.7(b) indicates that the valence bands are mainly contributed by the O-2 p orbitals, with less contribution from the Ta-5 d states. This hybridization confirms the covalent bonding between O and Ta atoms. The conduction bands are mainly contributed by the Ta-5 d states with less contribution from O-2 p orbitals. The contributions coming from the other atomic orbitals are very small.

As there is the heavy atom Ta present in this system, we include spin-orbit coupling (SOC) to see the effect on the band structure of KTO. Upon the inclusion of SOC, KTO remains an indirect band gap insulator, with the VBM remaining at the R point and the CBM remaining at the Γ point. As the valence bands are dominated by O-2 p states and the conduction bands are mainly contributed by the Ta-5 d states [see Fig. 6.7(b)], SOC mainly affects the splitting of the states

in the conduction band. The splitting of the states in the valence band is also present, but not as noticeable, due to significant contribution coming from Ta-5d orbitals. Due to splitting of the states, the band gap reduces a little bit, the SOC induced band gap is = 2.04 eV. Here, the important splitting is the splitting of the lowest energy conduction band level at the Γ point [see Fig. 6.7(c)]. The amount of splitting is 417 meV, in our calculations. This value agrees excellently with a previous LDA calculated value of ~ 400 meV.⁹⁵ This SOC induced splitting is one order of magnitude larger than that in STO. This made people interested in studying KTO-based heterostructure as they can show interesting physics as well as spin-electronics applications.

6.5.2 KTO(001) surface

As the LVO/KTO interface is formed by the epitaxial growth of a LVO film on a TaO₂ terminated KTO(001) surface, we next study the KTO(001) surface.

Structural properties of the KTO(001) surface

Fig. 6.6(a) above shows the optimized structure of the KTO(001) surface. To model the KTO(001) surface we have taken a nine-layer-thick (4.5 u.c.) asymmetric slab with TaO₂ surface termination, along with a vacuum with thickness of more than 15 Å. The bottom two layers are kept fixed at the bulk coordinates. All other layers are allowed to relax. We found that the KTO(001) surface is also non-magnetic, as is bulk KTO.

Next we calculate the percentage interlayer relaxation for a few top layers:

$$\Delta_{ij} = \frac{d_{ij} - d_B}{d_B} \times 100, \quad (6.1)$$

where d_{ij} is the separation between the i^{th} and j^{th} layers upon relaxation and d_B

is the bulk separation between layers. The numbering of the layers starts from the topmost layer i.e., d_{12} is the separation between the topmost (first) layer and second layer, d_{23} is the separation between the second and third layers, and so on. The KTO(001) surface slab consists of alternating KO and TaO₂ layers. We have used the average z -coordinate of all the atoms in a layer to calculate d_{ij} and hence Δ_{ij} . We obtain $\Delta_{12} = 2.52\%$, i.e., d_{12} is expanded with respect to d_B by 2.52%. Similarly, d_{23} is expanded by 3.99%, and d_{34} is expanded by 1.43%. In the near-surface layers, we see that the O atoms are a little bit higher in z -height compared to the corresponding Ta or K atoms, depending on whether we are considering a TaO₂ or KO layer; this buckling within a layer is clearly visible in Fig. 6.6(a).

Electronic structure of the KTO(001) surface

Next we calculate the electronic structure of the KTO(001) surface. Fig. 6.8 shows the band structure of the KTO(001) slab, both without and with SOC. The main interesting feature is that there are some bands which cross the Fermi level and hence the KTO(001) surface is metallic, though bulk KTO is insulator. Another important feature is the existence of some parabolic bands crossing the Fermi level, and just above it, centered around the Γ point. These bands might be responsible for the formation of a two-dimensional electron gas (2DEG) at the LVO/KTO interface. Some Rashba type splittings are observed in the band structure upon the inclusion of spin-orbit coupling (SOC) [see Fig. 6.8(b)]. Our calculated band dispersion is consistent with previous calculations.^{96–98}

Fig. 6.9 shows the PDOS of the KTO(001) slab, without SOC. Near the Fermi level, Ta-5*d* orbitals mainly contribute, with a very small contribution from O-2*p* orbitals. This also makes clear that due to the existence of heavy Ta bands, there is large SOC splitting in the conduction bands.

We further show the band structure projected onto each layer of the KTO(001)

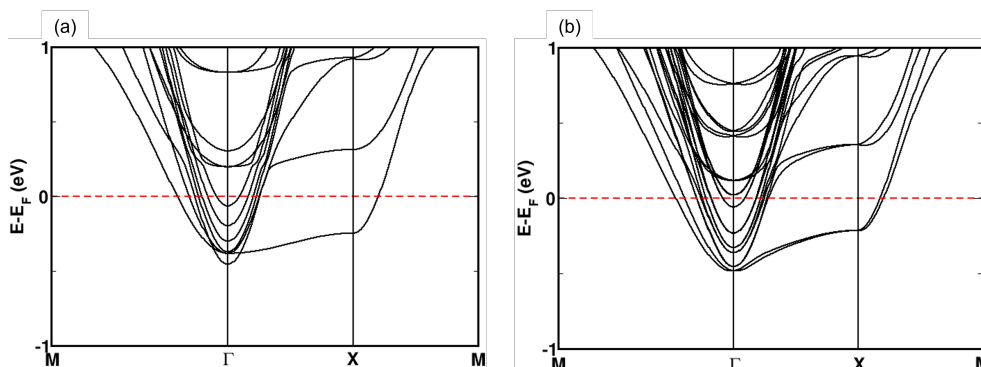


Figure 6.8: Electronic band structure of the KTO(001) surface (a) without SOC and (b) with SOC. The horizontal red dashed line represents the Fermi level in each case.

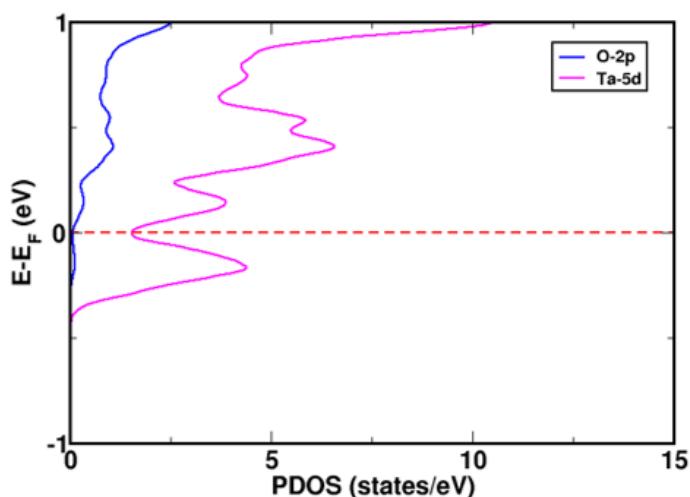


Figure 6.9: PDOS of KTO(001) surface, calculated without SOC. Orbitals on which the wavefunctions are projected are shown in the inset. The horizontal red dashed line represents the Fermi level.

surface slab, to identify the origin of each band layer-wise. Fig. 6.10 shows the projected band structures in which the bands are projected onto all the atomic orbitals of the top TaO₂, third TaO₂, fifth TaO₂ and seventh TaO₂ layer of the KTO(001) surface slab. Contributions from the alternating KO layers of the KTO(001) surface slab are negligibly small, and hence projection onto the KO layers are not shown.

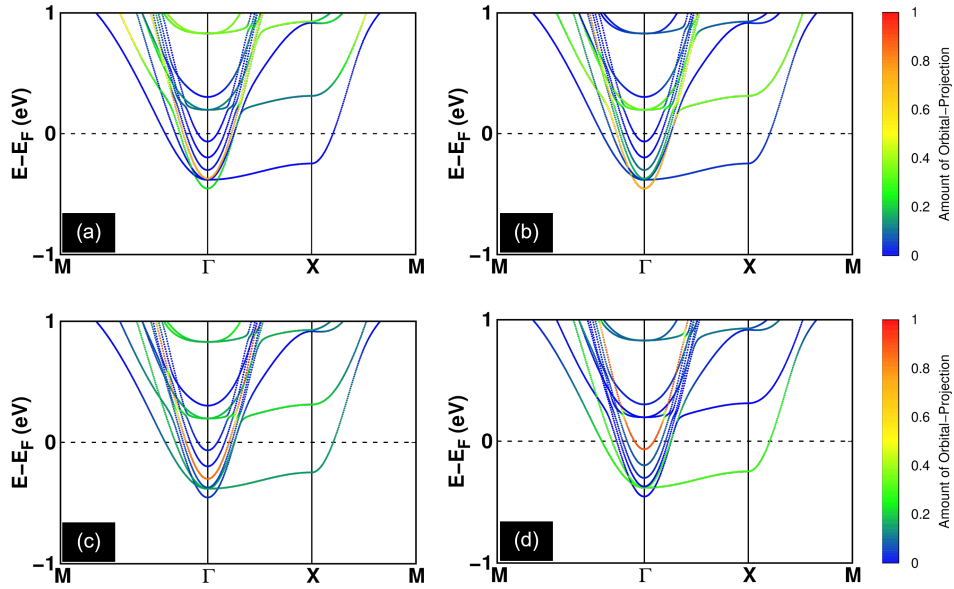


Figure 6.10: Bands are projected on to all atomic orbitals of (a) top TaO₂, (b) 3rd TaO₂, (c) 5th TaO₂ and (d) 7th TaO₂ layer of KTO(001) surface, without SOC. The color scales represent the amount of orbital projection. The horizontal black dashed line represents the Fermi level in each case. The color scales represent the amount of orbital projection, for each layer.

6.5.3 Constituent: Bulk LVO

We have studied bulk LVO in two structures [see Fig. 6.5]. One is the orthorhombic structure, which is the experimentally observed RT phase. The other is the tetragonal phase, the reason for studying this is that this is the structure that grows when LVO is deposited epitaxially on KTO.

Bulk LVO in orthorhombic structure

Structural properties of bulk orthorhombic LVO

Our DFT optimized structure of bulk LVO in RT orthorhombic crystal is shown in Fig. 6.5(a). The orthorhombic LaVO₃ structure can be formed from the $2 \times 2 \times 2$ cubic perovskite, by displacing the V and O atoms from their mean positions. See Fig. 6.11, which show the $2 \times 2 \times 2$ cubic perovskite and the formation of the orthorhombic crystal due to the deformation of the VO₆ octahedra with respect to

the cubic structure. We have optimized the cell parameters and atomic positions in our calculations. The optimized lattice parameters are consistent with previous calculated results and with the experimental values. Table 6.3 shows the comparison of our calculated lattice parameters, calculated with $U = J = 0$, with the previous calculated results and experimental values.

Lattice parameter	Our PBE-GGA DFT calculated value	Previous calculated value ⁹⁹	Expt. value ¹⁰⁰
a	5.547 Å	5.632 Å	5.555 Å
b	5.571 Å	5.614 Å	5.553 Å
c	7.952 Å	7.843 Å	7.848 Å

Table 6.3: Table of lattice parameters of orthorhombic LVO. Our PBE-GGA calculated optimized lattice parameters (here, $U = J = 0$) are compared against previous calculations with different functionals and with experiments.

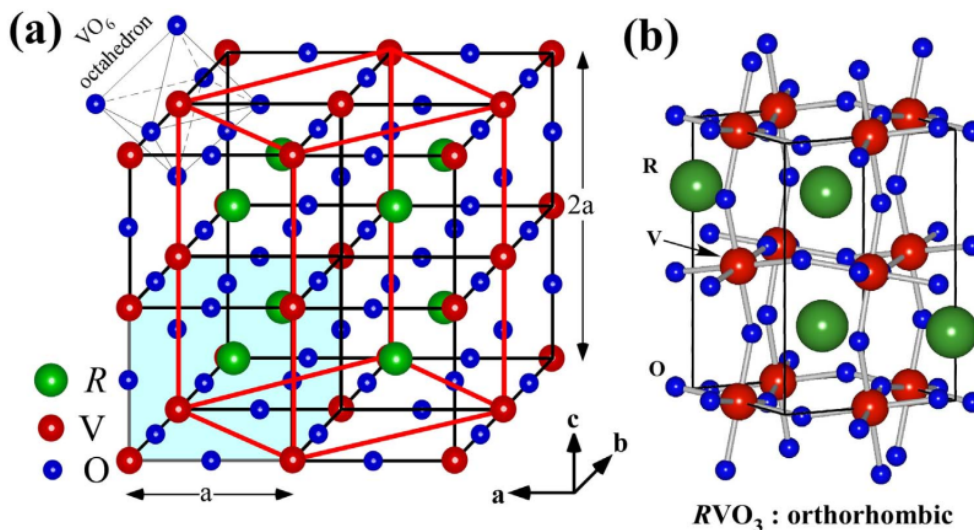


Figure 6.11: (a) Schematic representation of a $2 \times 2 \times 2$ standard perovskite (RVO_3) structure. Each vanadium atom is surrounded by an oxygen octahedron (for simplicity only one oxygen octahedron is shown). Orthorhombic RVO_3 structure is derived from the above $2 \times 2 \times 2$ standard perovskite structure as shown by thick red line. (b) Orthorhombic crystal structure of RVO_3 . Reprinted with permission from Ref. 101.

Electronic structure of bulk orthorhombic LVO

Next, we show the calculated band structure and PDOS of orthorhombic bulk LVO,

both without and with SOC.

LVO is a Mott insulator¹⁰² i.e, under the conventional band theory it emerges as a metal, which does not match with the experimental finding. Actually, orthorhombic LVO has been experimentally determined to have a band gap of 1.1 eV¹⁰². However, there exist strongly localized V-3*d* orbitals and if the strong electron-electron correlation of the V-3*d* electrons are captured correctly, LVO can show the correct insulating behaviour in calculations too.

To correct for the self interaction of the strongly correlated V-3*d* electrons, we have calculated the band structure of bulk orthorhombic LVO with the DFT+*U* method. We have used two different kinds of DFT+*U* methods as implemented in the Quantum ESPRESSO (QE) package: (i) C-dG method⁷⁹ and (ii) L method⁸⁰. These are described in the computational details section above. Fig. 6.12 shows the band structure obtained for different DFT+*U* methods, with different values of Hubbard onsite Coulomb repulsion parameter *U* and onsite Coulomb exchange parameter *J*. In all of these cases, the atomic positions are relaxed with the corresponding *U* value. However, the cell parameters *a*, *b*, and *c* are taken to be the same as those obtained for the *U* = *J* = 0 calculation [See Table 6.3].

Fig. 6.12(a) shows the band structure of bulk orthorhombic LVO without any Hubbard parameters i.e., *U* = 0 here. Band structure shows existence of bands crossing the Fermi level and hence the system turns out as a metal. So, to capture the correct band gap, we show the band structure calculated with both the C-dG method and the L method.

Figs. 6.12(b)-(d) show the band structure calculated with the C-dG method with different *U* values. For *U* = 0 eV, the system is a metal and at smaller *U* values (e.g., *U* = 2.0 eV) the system remains metallic. Upon increasing *U* further, the gap opens up and the band gap E_g increases. However, for the range of *U* values used in our calculations, E_g does not match with the experimental value of 1.1 eV.

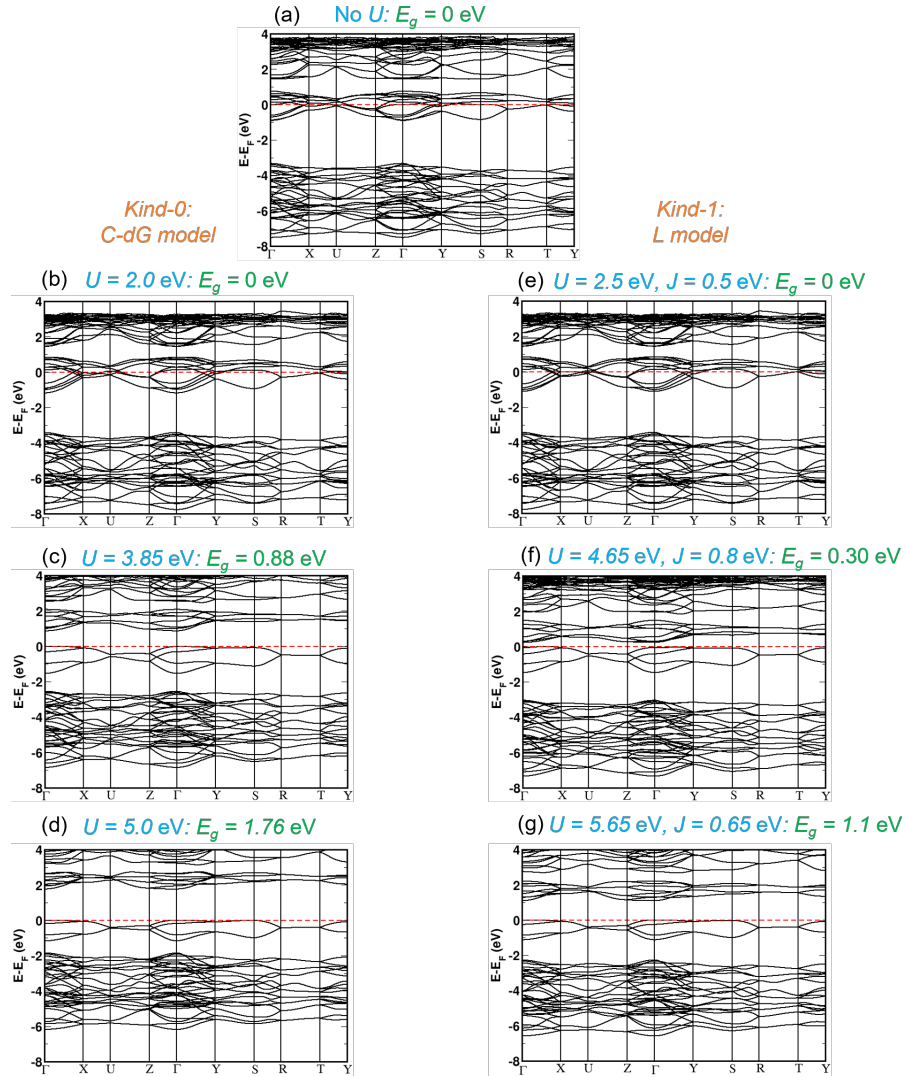


Figure 6.12: Electronic band structure of bulk orthorhombic LVO with DFT+ U calculations. Two types of DFT+ U calculations are used, as implemented in QE: (i) C-dG method⁷⁹, and (ii) L method⁸⁰. Used different combinations of values of U and J parameters to match the experimental band gap of 1.1 eV. The method, values of U and J , and E_g are written at the top of each figure.

Figs. 6.12(e)-(g) show the band structure calculated with the L method with different (U, J) values. To compare with results from the C-dG method, we note that $U_{eff} = U - J$ of the L method is equivalent to the U value of the C-dG method; the values of U and J have been chosen accordingly to facilitate this comparison. For smaller values of (U, J) (e.g., $U = 2.5$ eV and $J = 0.5$ eV), LVO remain a metal. For higher U and J values a gap opens up and E_g increases as U_{eff} increases. We see that

for $U = 5.65$ eV and $J = 0.65$ eV, the calculated $E_g = 1.1$ eV [see Fig. 6.12(g)], which matches with the experimental value of 1.1 eV. Thus an appropriate combination of U and J or ‘correct’ treatment of electron-electron correlation can produce the experimental band gap of orthorhombic LVO. Hence, LVO is a Mott insulator. Note that orthorhombic LVO has a direct gap at the Γ point.

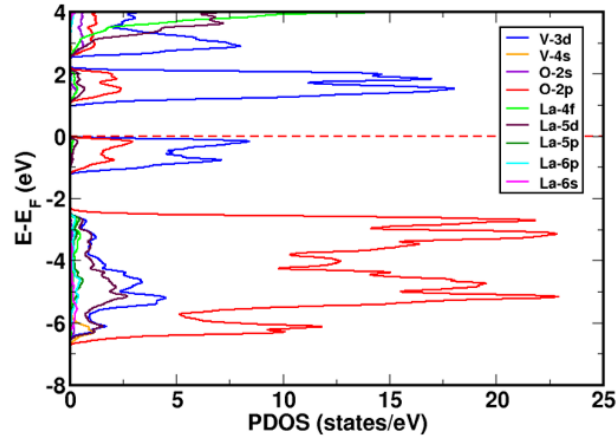


Figure 6.13: PDOS of bulk orthorhombic LVO without SOC. Here we have used DFT+ U with kind = 1 of QE, ortho-atomic projection, $U = 5.65$ eV, $J = 0.65$ eV. The orbitals on which the wave functions are projected on are shown in the inset. The Fermi level is represented by the red dashed line.

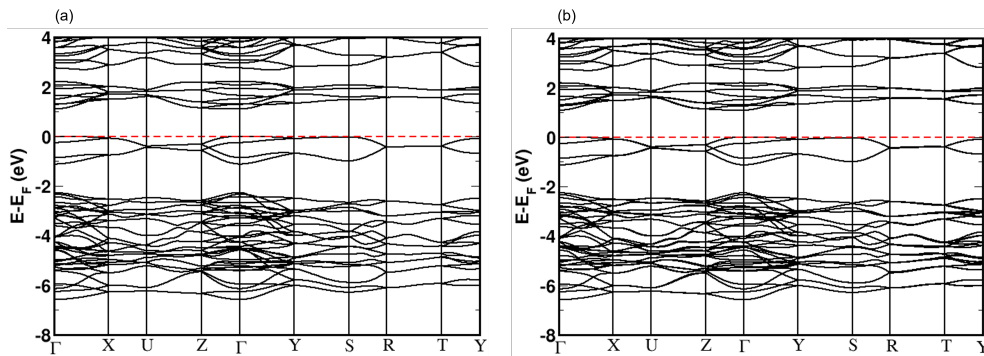


Figure 6.14: Electronic band structure of bulk orthorhombic LVO (a) without SOC and (b) with SOC. Here we have used DFT+ U with kind = 1 of QE, ortho-atomic projection, $U = 5.65$ eV, $J = 0.65$ eV. The Fermi level is set at the VBM and is represented by the red dashed line in each case.

In subsequent calculations presented in this chapter we will use the L method because it allows one to incorporate SOC. All further results presented in this chapter

will be performed with the L method and $U = 5.65$ eV and $J = 0.65$ eV for V-3d orbitals. (However, since geometry optimization has not yet been implemented in the code with the L method, all relaxed structures are first obtained using C-dG model and $U = 5$ eV.

We note that our values for the optimal values of U and J differ slightly from those of previous authors. S. Kumari et al.,¹⁰¹ reported that they found the correct band gap of 1.1 eV at $U = 4.65$ eV and $J = 0.8$ eV.

By examining the band structure shown in Fig. 6.12(g) we see that the system displays electronic features characteristic of a Mott insulator, with the lower Hubbard subband between -1.1 eV to 0 eV, and the upper Hubbard subband between 1.1 eV and 2.2 eV.

We have also calculated the orbital projected density of states (PDOS) as shown in Fig. 6.13. It is observed that the VBM (here lower Hubbard band) and CBM (here upper Hubbard band) are mainly contributed by the V-3d orbitals, with little hybridization with the O-2p orbitals.

As there are heavy La atoms, we incorporate SOC in the system to see the effect on the band structure. We show the band structure without SOC and with SOC side by side in Fig. 6.14(a) and Fig. 6.14(b), respectively, to enable ease of comparison.

We do not see any observable splitting of the valence and conduction bands. This is due to the fact that the orbitals of heavy La atoms do not contribute to these bands [clear from the PDOS of Fig. 6.13]. The bands arising from the heavy La atomic orbitals are expected to be affected by SOC. The band gap does not change upon inclusion of SOC. Very minimal splittings are observed at $E - E_F > 3$ eV where La orbitals contribute. However, these bands are not important for us as they are much higher in energy with respect to the Fermi level.

LVO in tetragonal phase

Structure of bulk tetragonal LVO

Next we have considered a tetragonal structure of bulk LVO. Note that freestanding LVO is not found in this structure. However, this structure can form when the in-plane lattice parameters are strained due to pseudomorphic epitaxial growth on a substrate with a different lattice constant from that of freestanding LVO. Thus, in our case, when LVO is grown on KTO, the LVO layers are found (experimentally) to assume a tetragonal structure, whose in-plane (x and y) lattice parameters are determined by that of the cubic KTO substrate. Fig. 6.5(b) shows the tetragonal structure of bulk LVO, with in-plane lattice parameters determined by KTO ($a = b = 4.011 \text{ \AA} = a_0^{KTO}$). The DFT optimized out-of-plane lattice constant is $c = 3.95 \text{ \AA}$.

Magnetic ground state of bulk tetragonal LVO

Here, since this is a hypothetical bulk structure, we do not have experimental information about the magnetic configuration. Magnetism can arise from the localized V-3d orbitals. We have considered different possible magnetic configurations of LVO in the tetragonal structure: non-magnetic (NM), ferromagnetic (FM), and three different types of antiferromagnetic ordering (A-AFM, C-AFM and G-AFM) [see Fig. 6.15]. We have computed the total energy in these configurations to find the magnetic ground state and hence the magnetic ordering of the V atoms of tetragonal LVO.

In order to consider NM and FM ordering, a unit cell of tetragonal crystal containing five atoms (one formula unit of LVO) is sufficient. However, for the AFM orderings we had to consider supercells: $1 \times 1 \times 2$ supercell (two formula units) for A-AFM, $\sqrt{2} \times \sqrt{2} \times 1$ (two formula units) for C-AFM, and $\sqrt{2} \times \sqrt{2} \times 2$ supercell (four formula units) for G-AFM. So, in order to compare the relative energetics of

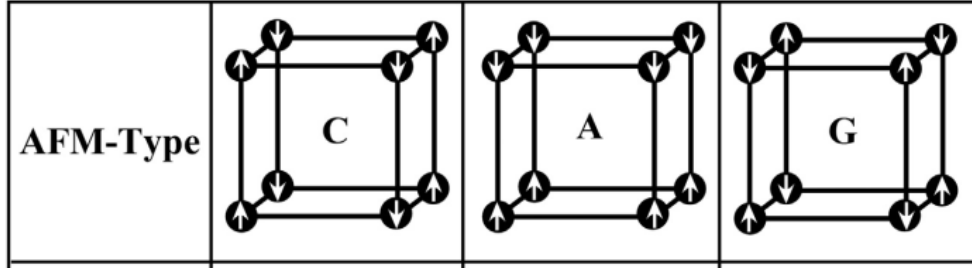


Figure 6.15: Different types of anti ferromagnetic (AFM) orderings. C-AFM means ferromagnetic stacking of antiferromagnetic layers, A-AFM means antiferromagnetic stacking of ferromagnetic layers, and G-AFM means antiferromagnetic stacking of antiferromagnetic layers. Reprinted with permission from Ref. 101.

these different magnetic configurations, we have compared values of the total energy per formula unit (f.u.), as shown in Table 6.4. A-AFM ordering is found to be the lowest energy magnetic configuration over NM, FM, C-AFM and G-AFM ordering. The relative energies of the other magnetic configurations, with respect to the energy of A-AFM, are shown in Table 6.4. For the A-AFM ordering, the value of total magnetization is zero, and the value of absolute magnetization is $4.25 \mu_B/\text{cell}$, with magnetic moments on the V atoms of $\pm 1.97 \mu_B$.

Magnetic ordering of V atoms	ΔE (meV/f.u.)
NM	1692
FM	73
A-AFM	0
C-AFM	143
G-AFM	244

Table 6.4: Comparison of total energy of different magnetic configurations of tetragonal bulk LVO. ΔE is the total energy difference with respect to the lowest energy configuration A-AFM. It is taken per formula unit of LVO to compare the total energies.

Electronic structure of bulk tetragonal LVO

As A-AFM is the magnetic ground state for tetragonal LVO, we further calculate the band structure and PDOS for A-AFM ordering only. Fig. 6.16 shows the band structure and PDOS of tetragonal LVO without SOC. We see that the tetragonal

LVO is also non-metallic like orthorhombic LVO. The states in the valence bands mainly arise from the V-3*d* and O-2*p* orbitals while the lower energy states in the conduction band mainly arise from V-3*d* and La-5*d* orbitals.

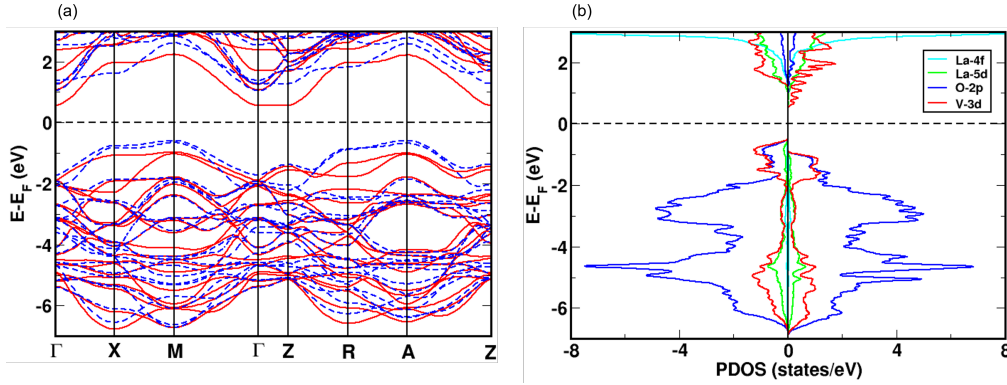


Figure 6.16: (a) Electronic band structure and (b) PDOS of bulk tetragonal LVO calculated without SOC. The atomic orbitals on which the wave functions are projected on are shown in the inset of (b). Black dashed line represents the Fermi level in each case.

6.5.4 LVO/KTO Interface

Now we present the calculated results of the LVO/KTO interface.

Structural properties of LVO/KTO interface

The relaxed structures of systems containing LVO/KTO interfaces are shown for both the superlattice system (periodic along z -direction) and the slab with vacuum (only artificial periodicity along the z -direction due to introduction of the vacuum region) are shown in Fig. 6.6(b) and 6.6(c), respectively. For these systems, the in-plane lattice parameters (a and b) are kept fixed at the optimized lattice parameter of the bulk cubic KTO substrate ($a_0^{KTO} = 4.011$ Å). So, the LVO film is under tensile strain when it is grown on the KTO substrate. However, the strain is small, less than 1%, which makes it possible to successfully grow the LVO film epitaxially and pseudomorphically on the KTO substrate. The out-of-plane lattice constant of

the superlattice and all the atomic positions are allowed to relax. Different thicknesses of the LVO and KTO are considered. Fig. 6.17 shows the structure of a $(\text{LVO})_{4.5}/(\text{KTO})_{8.5}$ superlattice.

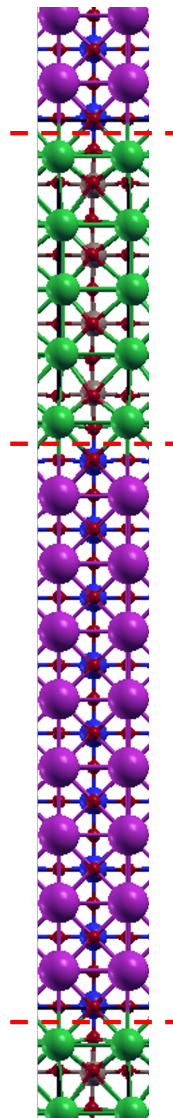


Figure 6.17: Structure of $(\text{LVO})_{4.5}/(\text{KTO})_{8.5}$ superlattice model. The red dashed lines represent the locations of the interfaces. Atomic color code: green: La, brown: V, red: O, magenta: K, blue: Ta.

Further analyzing the structural properties of superlattice, the interlayer relaxations of $(\text{LVO})_{4.5}/(\text{KTO})_{8.5}$ (this symbol means 4.5 unit cells of LVO film is grown

on 8.5 unit cells of KTO substrate) superlattice are plotted in Fig.6.18(a). We observe that, interlayer relaxations mainly occur around the interface region as the most structural reconstruction happens there, and this decays rapidly away from the interface (the black dashed line), on both LVO and KTO sides. Also, LVO undergoes large structural reconstruction, as the amplitude of Δ_{ij} is very large on LVO side compared to the KTO side.

We define the relative displacement or polar distortion as $(z_{cation} - z_{anion})$, where z_{cation} and z_{anion} are the average z -coordinates of the cations and anions in each layer of the relaxed superlattice structure. The calculated relative displacement of cations and anions (polar distortions) for each layer are plotted in Fig.6.18(b).

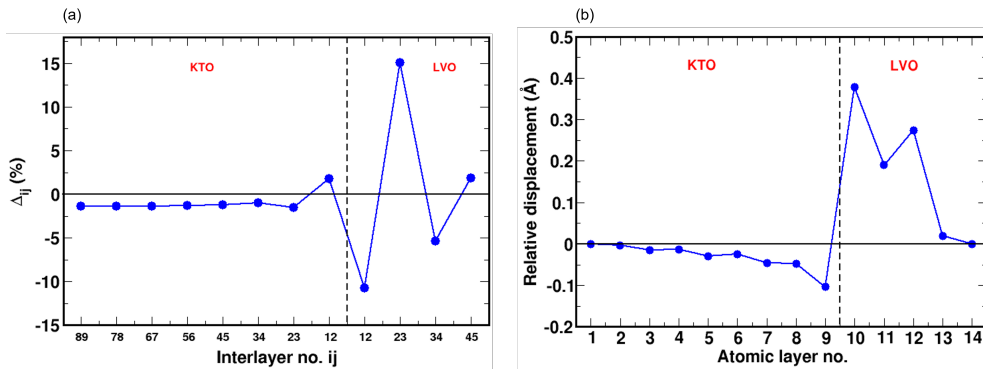


Figure 6.18: (a) Percentage interlayer relaxations Δ_{ij} (%) and (b) relative displacement or polar distortion between cations and anions for each layer of $(\text{LVO})_{4.5}/(\text{KTO})_{8.5}$ superlattice. The black dashed line represent the location of the interface.

We see ferroelectric-like distortions in which positively charged K, Ta, La and V ions and negatively charged O ions are displaced relative to each other, for each layer. This polar distortion creates local electric dipoles. All the electric dipoles created by these polar distortions point in the same direction on LVO and KTO sides. We see that relative displacement is negative on the KTO side and positive on the LVO side. This indicates that the O_2^- anions in each layer (for both LVO and KTO sides) want to come closer to the interface. Hence, the electric dipoles

created in each layer of KTO point in the direction away from the interface. This is also true on LVO side, all the electric dipoles in each layer on LVO side point in the direction away from the interface. Hence polarization vectors are created on KTO and LVO sides which are antiparallel. We observe that the amplitude of the polar distortions is maximum near the interface region and it decreases rapidly as we go away from the interface. Similar behaviour has also been previously observed by S. Okamoto et al.³⁴ for LaTiO₃/SrTiO₃ superlattices.

Magnetic ground state of LVO/KTO interface

Though there exists one previous DFT study of LVO/KTO interfaces, the authors did not consider spin-polarization in their calculations.¹⁰³ However, as there are magnetic V atoms, we believe that one should consider spin-polarization in this system.

So, we calculate the magnetic ground state i.e., the preferred magnetic ordering of the V atoms in the LVO/KTO superlattice. Different magnetic configurations of V atoms in (LVO)_{4.5}/(KTO)_{4.5} superlattice are considered, based on the magnetic moments on the V atoms: NM, FM, A-AFM, C-AFM and G-AFM. The total energies are compared per formula unit for these magnetic configurations, these results are shown in Table 6.5

Magnetic ordering of V atoms	ΔE (meV/f.u.)
NM	6433
FM	21
A-AFM	0
C-AFM	352
G-AFM	459

Table 6.5: Comparison of total energy of different magnetic orderings of V atoms in (LVO)_{4.5}/(KTO)_{4.5} superlattice. ΔE is the total energy difference with respect to the lowest energy configuration A-AFM. It is taken per formula unit of LVO/KTO to compare the total energies.

We see that A-AFM ordering is energetically the most favourable magnetic configuration over NM, FM, C-AFM and G-AFM. Table 6.5 shows the relative energy of the other magnetic configurations with respect to the energy of A-AFM. We recall that for bulk tetragonal LVO also V atoms preferred A-AFM ordering.

We have calculated the magnetization density (or spin-polarization density) given by: $m(\mathbf{r}) = n_{\uparrow}(\mathbf{r}) - n_{\downarrow}(\mathbf{r})$, for the A-AFM ordering. Here, $n_{\uparrow}(\mathbf{r})$ and $n_{\downarrow}(\mathbf{r})$ are the spin-up and spin-down electron densities, respectively, at the point \mathbf{r} in space. Isosurfaces of the magnetization density for A-AFM ordering are shown in Fig. 6.19.

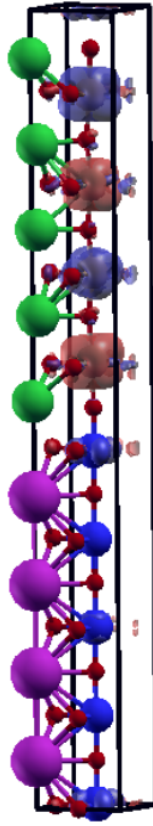


Figure 6.19: Magnetization density of $(\text{LVO})_{4.5}/(\text{KTO})_{4.5}$ superlattice model for A-AFM ordering. Red and blue lobes correspond to excess of spin-up and spin-down electron densities, respectively. Isosurface value = $0.003 \text{ e}/\text{bohr}^3$. Atomic color code: green: La, brown: V, red: O, magenta: K, blue: Ta.

Here, when $m(\mathbf{r}) > 0$, then, $n_{\uparrow}(\mathbf{r}) > n_{\downarrow}(\mathbf{r})$. This means at point \mathbf{r} in space, the spin-up electron density is larger than the spin-down electron density. This is

represented by the red lobes in Fig. 6.19. Similarly, when $m(\mathbf{r}) < 0$, then, $n_{\uparrow}(\mathbf{r}) < n_{\downarrow}(\mathbf{r})$. This means at point \mathbf{r} in space, the spin-down electron density is larger than the spin-up electron density. This is represented by the blue lobes in Fig.6.19. There are alternating red and blue lobes on the V atoms along the z -direction, corresponding to A-AFM ordering, i.e., an antiferromagnetic stacking along the z direction of (in-plane) ferromagnetic layers.

Electronic structure of LVO/KTO interface

Next we show the electronic structure of the LVO/KTO interface. Fig.6.20(a) and (b) show the electronic band structure, without SOC, of $(\text{LVO})_{4.5}/(\text{KTO})_{4.5}$ and $(\text{LVO})_{4.5}/(\text{KTO})_{8.5}$, respectively.

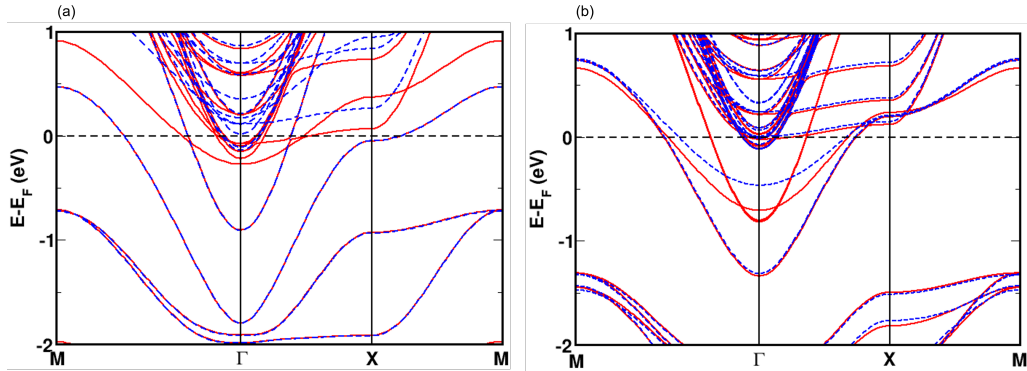


Figure 6.20: Electronic band structure of (a) $(\text{LVO})_{4.5}/(\text{KTO})_{4.5}$ superlattice and (b) $(\text{LVO})_{4.5}/(\text{KTO})_{8.5}$ superlattice. Both are calculated for A-AFM ordering, without SOC. Red lines represent spin up bands and blue dashed lines represent spin down bands. The Fermi level is represented by the black dashed line in each case.

Appearance of many partially occupied bands crossing the Fermi level which indicates that both the $(\text{LVO})_{4.5}/(\text{KTO})_{4.5}$ and $(\text{LVO})_{4.5}/(\text{KTO})_{8.5}$ superlattices are metallic. This is emergence i.e., though the constituents (bulk orthorhombic LVO, bulk tetragonal LVO and bulk cubic KTO) are insulators, the LVO/KTO interface is metallic. There exist many parabolic bands around the Γ point which cross the Fermi level. Parabolic bands correspond to the free electron like behaviour (as

free electrons have parabolic dispersion, $E = \frac{\hbar^2 k^2}{2m}$). These parabolic bands are responsible for the conduction of the 2DEG at the LVO/KTO interface. We also notice that some lower energy partially occupied bands are spin-polarized i.e., spin up bands and spin down bands have different energies. We will show later that these bands are mainly coming from the magnetic V atoms and interfacial Ta atoms which also gain some moments.

Layer-resolved orbital-projected density of states

To get more into the origin of the 2DEG, we plot the layer-resolved PDOS, shown in Fig. 6.21(a). Fig. 6.21(b) shows the corresponding structure of $(\text{LVO})_{4.5}/(\text{KTO})_{8.5}$ superlattice, with the PDOS aligned with the corresponding layer. As the structure is mirror symmetric, we have shown the plots of PDOS only for the layers from the middle layer of KTO part, up to the middle layer of the LVO part. Color code for PDOS: Magenta - Ta-5d, red - O-2p, blue - V-3d and cyan - La-5d orbitals. Full lines represent spin up and dashed lines represent spin down states.

Here, only the states which cross the Fermi level are responsible for the conduction electrons. We see that, at the interface, the conduction or free electrons (which form the 2DEG) arise primarily from from Ta-5d orbitals of the interfacial TaO₂ layer (Ta-5d spin up states). The other TaO₂ layers also contribute to the 2DEG, as the PDOS of these layers also cross the Fermi level, but with less contribution compared to the interfacial TaO₂ layer. Also, different PDOS of spin up and spin down states for the interfacial TaO₂ layer indicates spin polarization. This spin polarization is very minimal for the other TaO₂ layers away from the interface. The KO layers do not have any conduction electrons and thus do not contribute to the 2DEG.

On the LVO side, the PDOS of the VO₂ layers crosses the Fermi level and hence they carry conduction or free electrons which contribute to the 2DEG. The VO₂

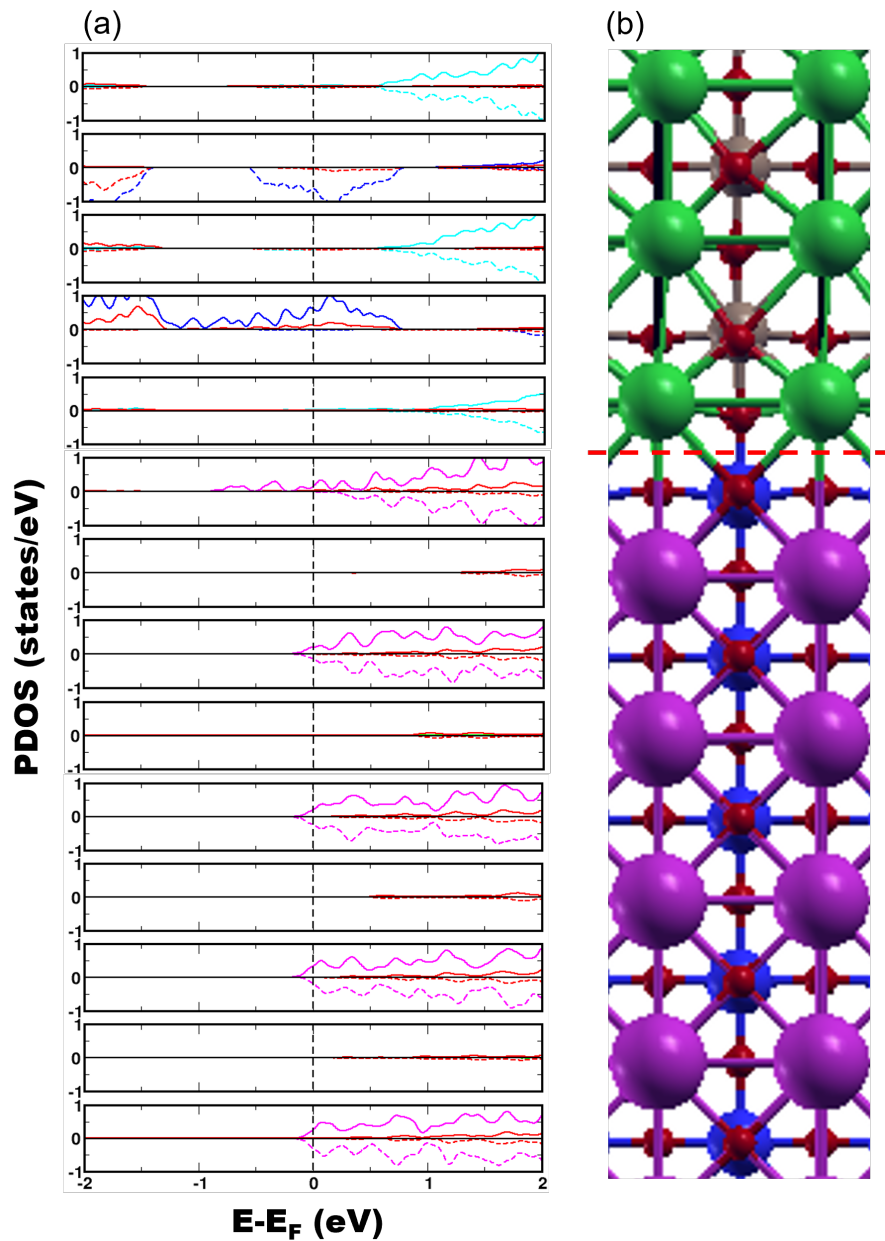


Figure 6.21: (a) Layer-resolved and spin-resolved PDOS of $(\text{LVO})_{4.5}/(\text{KTO})_{8.5}$ superlattice. (b) shows the corresponding structure from the middle of the KTO part to the middle of the LVO part. Color code in (a): magenta - Ta-5d, blue - V-3d, red - O-2p, cyan - La-5d. The full lines represent spin up and the dashed lines represent spin down states.

layer closest to the interface has only spin up states which are partially occupied, and these are mainly coming from the V-3d orbitals with little contribution from the O-2p orbitals. PDOS of the next VO_2 layer also has partially occupied spin down

states which are mainly coming from the V-3*d* orbitals with very little contribution from the O-2*p* orbitals. This again confirms the A-AFM ordering of the V atoms. The LaO layers do not have any free electronic charge.

So, we can say that the metallicity at the LVO/KTO interface is mainly coming from the interfacial TaO₂ layer, and VO₂ layers closer to the interface. The 2DEG is not very sharply confined to the interface, it has tails on both the KTO and LVO sides. However, the tail decays away from the interface. Therefore, we can say that the conduction electrons can move freely in the *xy*-plane, but they are confined within an extremely narrow region perpendicular to the interface. Thus the conduction electrons have a two dimensional nature and form a 2DEG.

We calculate the electron density of the 2DEG by integrating the PDOS from the conduction band minimum up to the Fermi level (i.e., for $-1.33 \text{ eV} \leq E - E_F \leq 0 \text{ eV}$). The calculated interfacial electron density is 5.05×10^{14} electrons/cm², which is reasonably consistent with the experimental value of 1.02×10^{14} electrons/cm².⁶² This value is one order of magnitude higher than that of the polar/non-polar LAO/STO interface.²⁰ This is because we have two donor layers (LaO)⁺ and (TaO₂)⁺ at LVO/KTO interface, whereas LAO/STO has only one donor layer (LaO)⁺ at the interface.

Orbital projected band structure

It is clear from the layer-resolved PDOS [see Fig. 6.21] that mostly Ta-5*d* and V-3*d* states cross the Fermi level and are responsible for the partially occupied bands in the band structure [see Fig. 6.20], with very little contribution from the O-2*p* orbitals. So, the partially occupied bands and hence the 2DEG are completely coming from the TaO₂ and VO₂ layers.

Now, we want to focus on individual bands which cross the Fermi level. We want to see which bands are coming from which atomic orbitals. For this we show bands

projected on Ta-5*d* [see Fig. 6.22] and V-3*d* [see Fig. 6.23] orbitals of each layer of the superlattice.

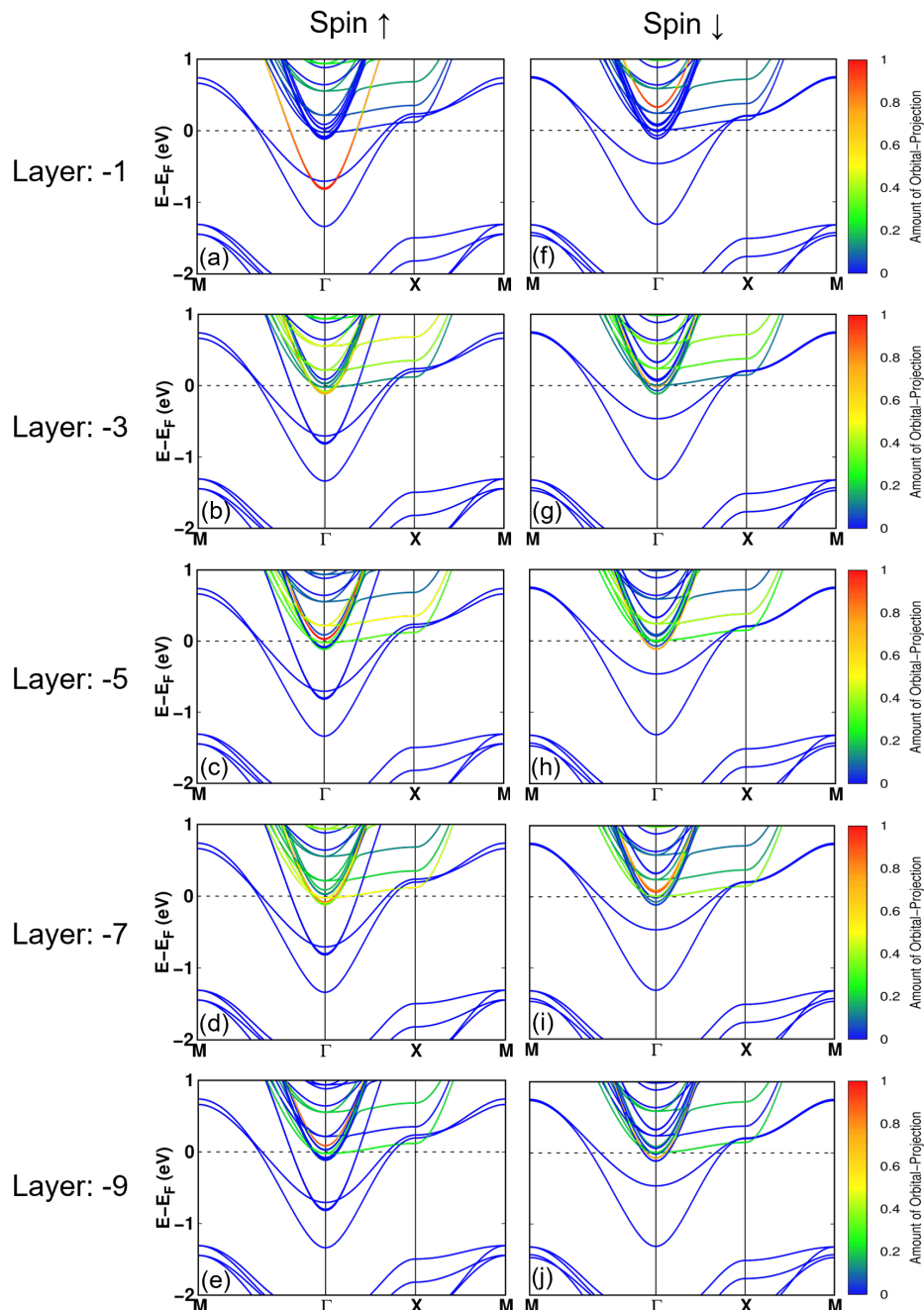


Figure 6.22: (a) Bands are projected on to Ta-5*d* states of each layer of $(\text{LVO})_{4.5}/(\text{KTO})_{8.5}$ superlattice. (a)-(e) are for spin up and (f)-(j) are for spin down bands. Color scales represent the amount of orbital projection.

In Fig. 6.22 and 6.23, the numbering of layers is as before: positive and negative

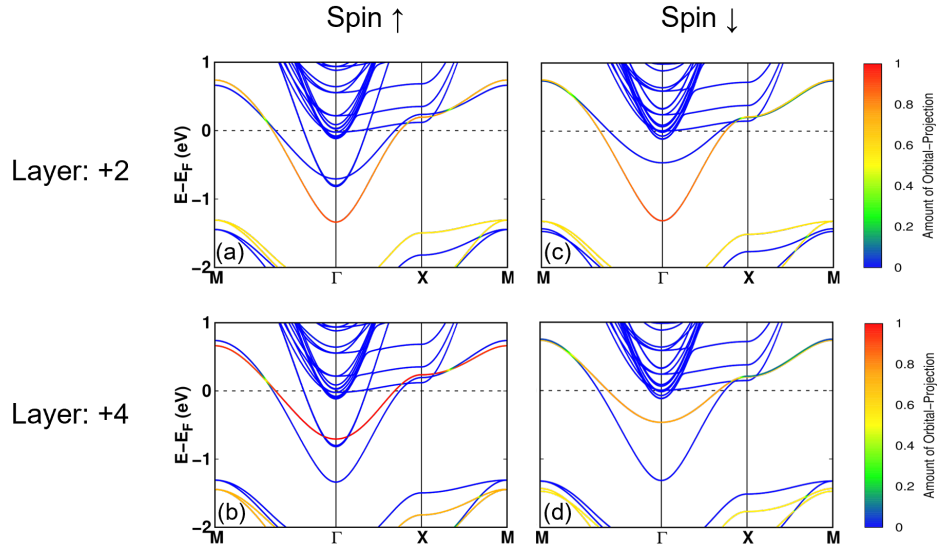


Figure 6.23: (a) Bands are projected on to V-3d states of each layer of $(\text{LVO})_{4.5}/(\text{KTO})_{8.5}$ superlattice. (a)-(b) are for spin up and (c)-(d) are for spin down bands. Color scales represent the amount of orbital projection.

integers for LVO and KTO part, respectively, with increasing magnitude as we go away from the interface. e.g., Layer: -1 combines interfacial TaO_2 layers closest to both the interfaces, Layer: -2 combines next TaO_2 layers from both the interfaces, and so on. As the $(\text{LVO})_{4.5}/(\text{KTO})_{8.5}$ superlattice is mirror symmetric, we get a pair of bands coming from each pair of layers, one from near the interface and the middle of the superlattice unit cell and the other from near the interface at the edge of the superlattice unit cell.

We see that, among the bands crossing the Fermi level, only the bands coming from the interfacial TaO_2 layer, and the two VO_2 layers closest to the interface have lower energy and they are much downward in energy from the Fermi level (around 1 eV below the Fermi level) at the Γ point. We note that these bands completely come from Ta-5d and V-3d orbitals. More specifically, they come from the d_{xy} orbitals, i.e., the conduction electrons can move freely only in the xy -plane, and they have very minimal z -extension. This proves the two-dimensional nature of the electron gas.

The other partially occupied bands barely cross the Fermi level and they all come from the other TaO_2 layers away from the interface. This also confirms that most of the conduction electrons are mainly coming from the interfacial TaO_2 layer and two VO_2 layers closest to the interface.

Electron density of the 2DEG at the interface

We calculate the electron density of 2DEG for each layer of the $(\text{LVO})_{4.5}/(\text{KTO})_{8.5}$ superlattice, by integrating the density of states of each layer for both the majority and minority spin states; a similar procedure has been followed by previous authors for other systems.¹⁰⁴ This layer-resolved and spin-resolved (red circles are for spin up states and blue squares are for spin down states) electronic charge is shown in Fig. 6.24. As the superlattice structure is mirror symmetric, only half the layers are shown. The counting of layers starts from the interface and is represented by positive and negative integers for LVO and KTO part, respectively, as before.

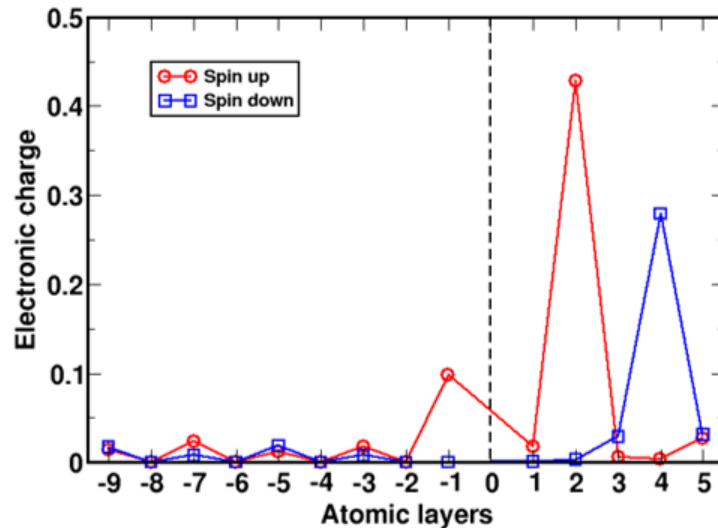


Figure 6.24: Layer-resolved and spin-resolved electronic charge for $(\text{LVO})_{4.5}/(\text{KTO})_{8.5}$ superlattice. Being mirror symmetric, only the layers around the middle interface are shown. Black dashed line represents the position of the middle interface. Counting of layers starts from the interface and represented by positive and negative integers for LVO and KTO part, respectively.

For integration of the PDOS, we have chosen an energy window from the minimum of the partially occupied bands or conduction bands up to the Fermi level,^{104–106} i.e., $-1.337 \text{ eV} \leq E - E_F \leq 0 \text{ eV}$. We notice that the interfacial TaO₂ layer (layer:-1) on the KTO side and the two VO₂ layers closest to the interface (layer:2 and layer:4) on the LVO side have the largest electronic charge. The interfacial TaO₂ layer has 0.62×10^{14} electrons/cm⁻² for spin-up and 0 electrons/cm⁻² for spin-down states. This corresponds to 100% spin polarization for this layer. The VO₂ layer which is closest to the interface has 2.67×10^{14} electrons/cm⁻² for spin-up states and 0 electrons/cm⁻² for spin-down states. The next VO₂ layer has 0 electrons/cm⁻² for spin-up states and 1.74×10^{14} electrons/cm⁻² for spin-down states. This again confirms A-AFM ordering of the V atoms. The VO₂ layers also have 100% spin polarization. Thus we get a layer-wise spin-polarized 2DEG at the LVO/KTO interface. We can say that the electrons accumulate mainly on the interfacial TaO₂ layer and on the two VO₂ layers closest to the interface, with a tail on both the KTO and LVO sides. The 2DEG at LVO/KTO system is mainly coming from the contribution of interfacial TaO₂ layer and the VO₂ layers adjacent to the interface. However, the 2DEG has tail on both LVO and KTO sides with decaying amplitude away from the interface, which means the other TaO₂ and VO₂ layers away from the interface also have minimal contribution to the 2DEG. This is consistent with previous theoretical calculations for other systems,¹⁷ and also with the experimental report that for the LVO/KTO system, the 2DEG is confined to a region of width 10 nm perpendicular to the interface region. All the KO layers on the KTO side and LaO layers on the LVO side do not have significant electronic charge and they do not contribute to the 2DEG. However, the amount of electronic charge decays rapidly away from the interface which indicates the two dimensional nature of the electron gas.

Integrated local density of states (ILDOS)

Next we plot the planar-averaged local density of states (LDOS) integrated in a small energy window from the conduction band minimum up to the Fermi level, known as the integrated LDOS or ILDOS⁹⁷. The ILDOS is defined as,

$$ILDOS = \sum_n \sum_{\mathbf{k}} \int_{\epsilon_{min}}^{\epsilon_{max}} |\psi_{n,\mathbf{k}}(\mathbf{r})|^2 \delta(E - E_{n,\mathbf{k}}) dE, \quad (6.2)$$

where n is the band index, \mathbf{k} is the wave vector in the first Brillouin zone, $[\epsilon_{min}, \epsilon_{max}]$ defines the energy window of integration, $\psi_{n,\mathbf{k}}(\mathbf{r})$ is the wavefunction of band n at \mathbf{k} -point \mathbf{k} , and the delta function counts only the terms for which the energy is a Kohn-Sham eigenvalue. After calculating the *ILDOS*, we average it over the xy -plane. This quantity is plotted in Fig. 6.25.

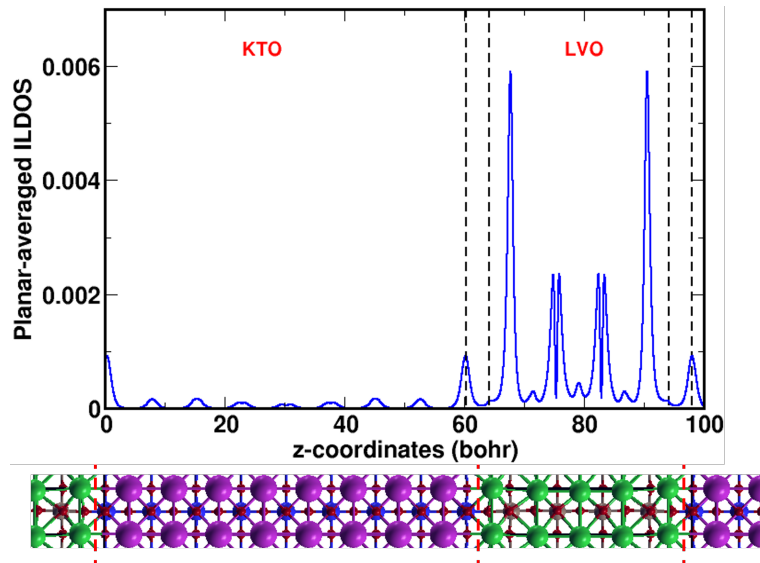


Figure 6.25: Planar-averaged ILDOS for $(\text{LVO})_{4.5}/(\text{KTO})_{8.5}$ superlattice. Black dashed lines represent the position of the interfacial TaO_2 and LaO layers. Structure is also aligned to better understand the peak positions along the z -axis. Atomic color code: green: La, brown: V, red: O, magenta: K, blue: Ta.

Fig. 6.25 shows our results for the *ILDOS* for the $(\text{LVO})_{4.5}/(\text{KTO})_{8.5}$ superlattice. Here, the calculated *ILDOS* tells us the locations of the conduction electrons. The peak of the planar-averaged *ILDOS* reveals that the conduction electrons are

mainly located near the interfacial region, with a very high peak on the VO₂ layers closest to the interface, and smaller peaks on the next VO₂ layers. We also see that on the KTO side, some conduction electrons also reside on the interfacial TaO₂ layer. There is a very small amount of conduction electrons also present in other TaO₂ layers which are away from the interface. The height of the peaks decreases rapidly away from the interface and is almost negligible with respect to the peak heights on VO₂ layers closer to the interface. Thus the electron gas has an essentially two dimensional nature. Away from the interface, 2DEG has a very small tail on both LVO and KTO sides. The electron gas is primarily confined to a width of about 20 bohr (i.e., about 10 nm) about the interface, which is in excellent agreement with the experimental estimate. This result is consistent with the layer-resolved PDOS and layer-resolved electronic charge, as discussed above. We note that this localization would be more clear if we had a thicker LVO region in the superlattice; we plan to confirm this in future calculations.

Planar-averaged charge density difference and charge redistribution

To understand the charge redistribution upon the formation of LVO/KTO interface from the constituents LVO and KTO, we calculate the planar-averaged charge density difference, given by,

$$\Delta\tilde{\rho}(z) = \tilde{\rho}_{SL}(z) - \tilde{\rho}_{subs}(z) - \tilde{\rho}_{film}(z), \quad (6.3)$$

where,

$$\tilde{\rho}_{system}(z) = \frac{1}{S} \int \rho_{system}(x, y, z) dx dy, \quad (6.4)$$

is the planar-averaged charge density taken over the xy plane and S is the surface area of the xy plane of the LVO/KTO superlattice model. Here, $\tilde{\rho}_{SL}(z)$, $\tilde{\rho}_{subs}(z)$

and $\tilde{\rho}_{film}(z)$ correspond to the planar-averaged charge densities of the LVO/KTO superlattice, KTO substrate and LVO film, respectively.

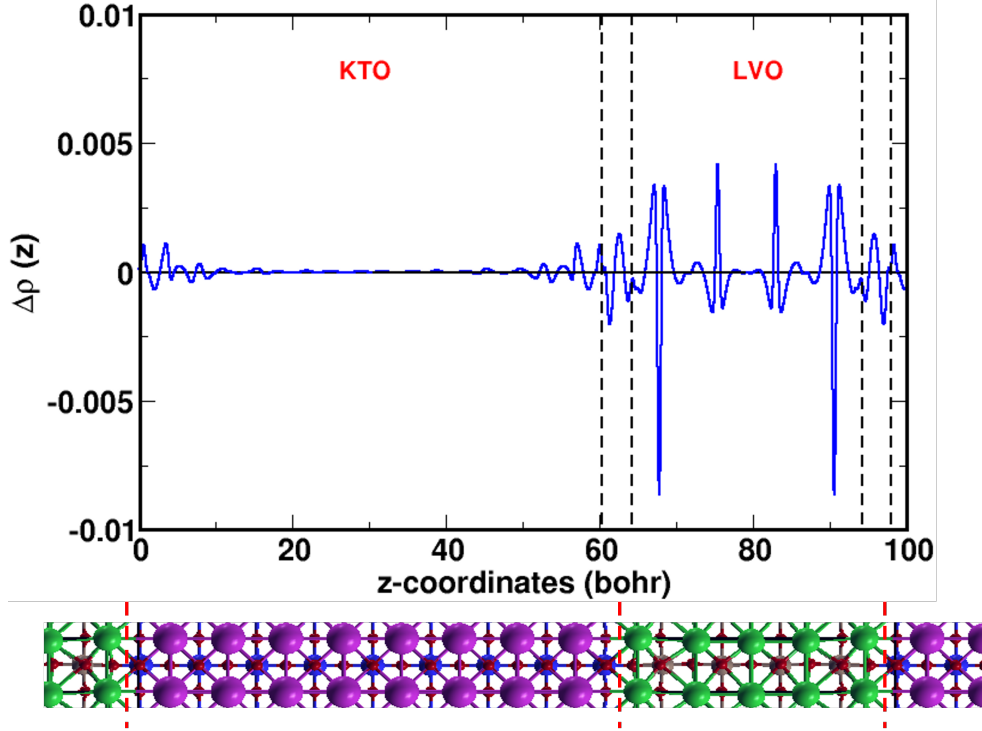


Figure 6.26: Planar-averaged charge density difference $\Delta\tilde{\rho}(z)$ in units of e/bohr^3 for $(\text{LVO})_{4.5}/(\text{KTO})_{8.5}$ superlattice. The vertical black dashed lines represent the interfacial TaO_2 and LaO layers, at the middle and end interfaces of the supercell. The structure is also aligned with the z -coordinates for better understanding. Atomic color code: green: La, brown: V, red: O, magenta: K, blue: Ta.

Fig. 6.26 shows the charge density difference $\Delta\tilde{\rho}(z)$ as a function of the z -coordinate of the $(\text{LVO})_{4.5}/(\text{KTO})_{8.5}$ superlattice, we have also shown the geometric structure below the graph, with the atomic coordinates appropriately aligned with the abscissa of the graph, so as to promote understanding. $\Delta\tilde{\rho}(z)$ is a measure of the charge redistribution upon the formation of the LVO/KTO interface, from the constituents. Large oscillations in the plot of $\Delta\tilde{\rho}(z)$ indicates that charge redistribution mainly occurs around the interface region (indicated by vertical black dashed lines) and on the LVO side. KTO side has smaller oscillations in $\Delta\tilde{\rho}(z)$, compared to the LVO side, which indicates that the KTO side has minimal charge redistribution. On

the KTO side, the oscillations decay very rapidly and become zero after 2 u.c. away from the interface. We can say that there is electronic charge redistribution, i.e., electronic reconstruction is occurring in the LVO/KTO system which is the main mechanism for the origin of the 2DEG at this interface.

Layer-resolved magnetic moments on atoms

We now calculate the magnetic moments on the atoms of each layer. Fig. 6.27 shows magnetic moments on atoms for each layer of $(\text{LVO})_{4.5}/(\text{KTO})_{8.5}$ superlattice. We separately show the spin up and spin down moments, indicated by red and blue circles, respectively.

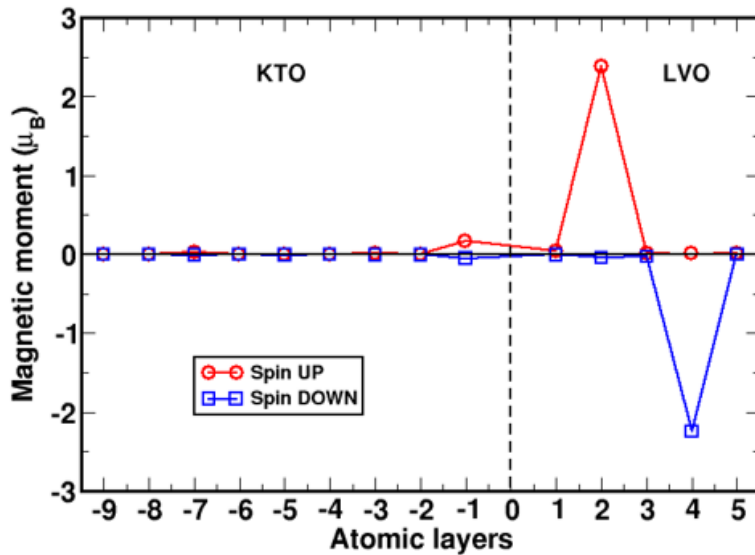


Figure 6.27: Magnetic moments on atoms of each layer for $(\text{LVO})_{4.5}/(\text{KTO})_{8.5}$ superlattice. Red and blue represent spin up and down moments, respectively. Being mirror symmetric, only the layers around the middle interface are shown. Black dashed line represents the position of the middle interface. Counting of layers starts from the interface and represented by positive and negative integers for LVO and KTO part, respectively.

As the superlattice structure is mirror symmetric, only the layers in half the superlattice are shown. The counting of layers starts from the interface and is represented by positive and negative integers for the LVO and KTO parts, respectively, as

before. We see that the VO₂ layers (layer:2 and layer:4 in Fig.6.27) possess very large moments as expected, and alternating VO₂ layers have opposite moments which is basically the effect of A-AFM ordering. For example, layer:2 has only spin up moments and layer:4 contains only spin down moments. Also, interestingly, we see some induced moments on the Ta atoms of the interfacial TaO₂ layer (layer:-1), with small spin up moments on it. The other TaO₂ layers which are further away from the interface do not possess any magnetic moments. This is consistent with the layer-resolved PDOS discussed earlier [see Fig. 6.21 and section-5.4.4].

6.5.5 Conclusions

In conclusion, we have gained insight into the electronic properties of two-dimensional electron gas (2DEG) formed at the interface of a Mott insulator LaVO₃ (LVO) and a band insulator KTaO₃ (KTO), using first-principles DFT calculations.

We have shown that while the constituents (bulk LVO and KTO) are insulators, the LVO/KTO interface becomes metallic and hosts a two-dimensional electron gas. The calculated layer-resolved electronic charge shows that the free charge is mainly located on the interfacial TaO₂ layer and on the VO₂ layers close to the LVO/KTO interface, and the electronic charge decreases away from the interface which proves the two-dimensional nature of the conduction electrons. In agreement with experiments, the width of the 2DEG is found to be about 10 nm.

The 2DEG is spin-polarized due to the strong electron-electron correlations of the localized V-3*d* and Ta-5*d* orbitals. DFT calculations show that in the LVO/KTO superlattice structure, V atoms assume an A-type antiferromagnetic ordering, also the interfacial Ta atoms gain some magnetic moments while other Ta atoms away from the interface are non-magnetic.

We identify ‘electronic reconstruction’ due to polar catastrophe as the origin of the 2DEG at the LVO/KTO interface.

Both atomic layers at the interface, viz., $(\text{LaO})^+$ and $(\text{TaO}_2)^+$, are cationic or donor-like in nature, which increases the electron density at the interface. Our calculated electron density at the interface is, in agreement with experiment, one order higher in magnitude in compared to the two-dimensional electron gas formed at a polar/non-polar interface such as $\text{LaAlO}_3/\text{SrTiO}_3$.

Bibliography

- [1] E. Dagotto, “Complexity in strongly correlated electronic systems,” *Science*, vol. 309, no. 5732, pp. 257–262, 2005.
- [2] Y. Tokura and H. Y. Hwang, “Complex oxides on fire,” *Nat. Mater.*, vol. 7, no. 9, pp. 694–695, 2008.
- [3] J. Reiner, F. Walker, and C. Ahn, “Atomically engineered oxide interfaces,” *Science*, vol. 323, no. 5917, pp. 1018–1019, 2009.
- [4] H. Y. Hwang, Y. Iwasa, M. Kawasaki, B. Keimer, N. Nagaosa, and Y. Tokura, “Emergent phenomena at oxide interfaces,” *Nat. Mater.*, vol. 11, no. 2, pp. 103–113, 2012.
- [5] J. G. Bednorz and K. A. Müller, “Perovskite-type oxides—The new approach to high- T_c superconductivity,” *Rev. of Mod. Phys.*, vol. 60, no. 3, p. 585, 1988.
- [6] K.-I. Kobayashi, T. Kimura, H. Sawada, K. Terakura, and Y. Tokura, “Room-temperature magnetoresistance in an oxide material with an ordered double-perovskite structure,” *Nature*, vol. 395, no. 6703, pp. 677–680, 1998.
- [7] J. Wang, J. Neaton, H. Zheng, V. Nagarajan, S. Ogale, B. Liu, D. Viehland,

- V. Vaithyanathan, D. Schlom, U. Waghmare, *et al.*, “Epitaxial BiFeO₃ multiferroic thin film heterostructures,” *Science*, vol. 299, no. 5613, pp. 1719–1722, 2003.
- [8] A. Brinkman, M. Huijben, M. Van Zalk, J. Huijben, U. Zeitler, J. Maan, W. G. van der Wiel, G. Rijnders, D. H. Blank, and H. Hilgenkamp, “Magnetic effects at the interface between non-magnetic oxides,” *Nat. Mater.*, vol. 6, no. 7, pp. 493–496, 2007.
- [9] C. Liu, X. Yan, D. Jin, Y. Ma, H.-W. Hsiao, Y. Lin, T. M. Bretz-Sullivan, X. Zhou, J. Pearson, B. Fisher, *et al.*, “Two-dimensional superconductivity and anisotropic transport at KTaO₃(111) interfaces,” *Science*, vol. 371, no. 6530, pp. 716–721, 2021.
- [10] J. A. Bert, B. Kalisky, C. Bell, M. Kim, Y. Hikita, H. Y. Hwang, and K. A. Moler, “Direct imaging of the coexistence of ferromagnetism and superconductivity at the LaAlO₃/SrTiO₃ interface,” *Nat. Phys.*, vol. 7, no. 10, pp. 767–771, 2011.
- [11] M. C. Tarun, F. A. Selim, and M. D. McCluskey, “Persistent photoconductivity in strontium titanate,” *Phys. Rev. Lett.*, vol. 111, no. 18, p. 187403, 2013.
- [12] Y. Lei, Y. Li, Y. Chen, Y. Xie, Y. Chen, S. Wang, J. Wang, B. Shen, N. Pryds, H. Hwang, *et al.*, “Visible-light-enhanced gating effect at the LaAlO₃/SrTiO₃ interface,” *Nat. Commun.*, vol. 5, no. 1, p. 5554, 2014.
- [13] Y. Matsubara, K. Takahashi, M. Bahramy, Y. Kozuka, D. Maryenko, J. Falson, A. Tsukazaki, Y. Tokura, and M. Kawasaki, “Observation of the quantum Hall effect in δ -doped SrTiO₃,” *Nat. Commun.*, vol. 7, no. 1, p. 11631, 2016.
- [14] A. Ohtomo and H. Hwang, “A high-mobility electron gas at the

- LaAlO₃/SrTiO₃ heterointerface,” *Nature*, vol. 427, no. 6973, pp. 423–426, 2004.
- [15] N. Nakagawa, H. Y. Hwang, and D. A. Muller, “Why some interfaces cannot be sharp,” *Nat. Mater.*, vol. 5, no. 3, pp. 204–209, 2006.
- [16] Z. S. Popović, S. Satpathy, and R. M. Martin, “Origin of the two-dimensional electron gas carrier density at the LaAlO₃ on SrTiO₃ interface,” *Phys. Rev. Lett.*, vol. 101, no. 25, p. 256801, 2008.
- [17] M. Basletic, J.-L. Maurice, C. Carrétéro, G. Herranz, O. Copie, M. Bibes, É. Jacquet, K. Bouzehouane, S. Fusil, and A. Barthélémy, “Mapping the spatial distribution of charge carriers in LaAlO₃/SrTiO₃ heterostructures,” *Nat. Mater.*, vol. 7, no. 8, pp. 621–625, 2008.
- [18] J. Heber, “Enter the oxides: thin films of oxygen-bearing compounds could have myriad practical applications, finds Joerg Heber, if a few problems can be overcome,” *Nature*, vol. 459, no. 7243, pp. 28–31, 2009.
- [19] R. Ramesh and D. G. Schlom, “Whither oxide electronics?,” *MRS Bulletin*, vol. 33, no. 11, pp. 1006–1014, 2008.
- [20] S. Thiel, G. Hammerl, A. Schmehl, C. W. Schneider, and J. Mannhart, “Tunable quasi-two-dimensional electron gases in oxide heterostructures,” *Science*, vol. 313, no. 5795, pp. 1942–1945, 2006.
- [21] C. Cen, S. Thiel, J. Mannhart, and J. Levy, “Oxide nanoelectronics on demand,” *Science*, vol. 323, no. 5917, pp. 1026–1030, 2009.
- [22] B. Förg, C. Richter, and J. Mannhart, “Field-effect devices utilizing LaAlO₃-SrTiO₃ interfaces,” *Appl. Phys. Lett.*, vol. 100, no. 5, p. 053506, 2012.

- [23] N. Reyren, S. Thiel, A. review, L. F. Kourkoutis, G. Hammerl, C. Richter, C. W. Schneider, T. Kopp, A.-S. Ruetschi, D. Jaccard, *et al.*, “Superconducting interfaces between insulating oxides,” *Science*, vol. 317, no. 5842, pp. 1196–1199, 2007.
- [24] A. Caviglia, S. Gariglio, N. Reyren, D. Jaccard, T. Schneider, M. Gabay, S. Thiel, G. Hammerl, J. Mannhart, and J.-M. Triscone, “Electric field control of the $\text{LaAlO}_3/\text{SrTiO}_3$ interface ground state,” *Nature*, vol. 456, no. 7222, pp. 624–627, 2008.
- [25] A. Caviglia, M. Gabay, S. Gariglio, N. Reyren, C. Cancellieri, and J.-M. Triscone, “Tunable Rashba spin-orbit interaction at oxide interfaces,” *Phys. Rev. Lett.*, vol. 104, no. 12, p. 126803, 2010.
- [26] A. Caviglia, S. Gariglio, C. Cancellieri, B. Sacépé, A. Fete, N. Reyren, M. Gabay, A. Morpurgo, and J.-M. Triscone, “Two-dimensional quantum oscillations of the conductance at $\text{LaAlO}_3/\text{SrTiO}_3$ interfaces,” *Phys. Rev. Lett.*, vol. 105, no. 23, p. 236802, 2010.
- [27] Y. Chen, J. Zhao, J. Sun, N. Pryds, and B. Shen, “Resistance switching at the interface of $\text{LaAlO}_3/\text{SrTiO}_3$,” *Appl. Phys. Lett.*, vol. 97, no. 12, p. 123102, 2010.
- [28] S. J. Allen, B. Jalan, S. Lee, D. G. Ouellette, G. Khalsa, J. Jaroszynski, S. Stemmer, and A. H. MacDonald, “Conduction-band edge and shubnikov-de haas effect in low-electron-density SrTiO_3 ,” *Phys. Rev. B.*, vol. 88, no. 4, p. 045114, 2013.
- [29] A. Tebano, E. Fabbri, D. Pergolesi, G. Balestrino, and E. Traversa, “Room-temperature giant persistent photoconductivity in $\text{SrTiO}_3/\text{LaAlO}_3$ heterostructures,” *Acs Nano*, vol. 6, no. 2, pp. 1278–1283, 2012.

- [30] A. Rastogi, J. Pulikkotil, and R. Budhani, “Enhanced persistent photoconductivity in δ -doped $\text{LaAlO}_3/\text{SrTiO}_3$ heterostructures,” *Phys. Rev. B.*, vol. 89, no. 12, p. 125127, 2014.
- [31] H. Yan, Z. Zhang, S. Wang, L. Ren, M. Li, C. Chen, and K. Jin, “Thickness dependence of photoresponsive properties at SrTiO_3 -based oxide heterointerfaces under different strains,” *J. Mater. Sci.*, vol. 54, pp. 108–115, 2019.
- [32] R. Pentcheva and W. E. Pickett, “Charge localization or itineracy at $\text{LaAlO}_3/\text{SrTiO}_3$ interfaces: Hole polarons, oxygen vacancies, and mobile electrons,” *Phys. Rev. B.*, vol. 74, no. 3, p. 035112, 2006.
- [33] R. Pentcheva and W. E. Pickett, “Correlation-driven charge order at the interface between a mott and a band insulator,” *Phys. Rev. Lett.*, vol. 99, no. 1, p. 016802, 2007.
- [34] S. Okamoto, A. J. Millis, and N. A. Spaldin, “Lattice relaxation in oxide heterostructures: $\text{LaTiO}_3/\text{SrTiO}_3$ superlattices,” *Phys. Rev. Lett.*, vol. 97, no. 5, p. 056802, 2006.
- [35] I. Žutić, J. Fabian, and S. D. Sarma, “Spintronics: Fundamentals and applications,” *Rev. Mod. Phys.*, vol. 76, no. 2, p. 323, 2004.
- [36] S. Datta and B. Das, “Electronic analog of the electro-optic modulator,” *Appl. Phys. Lett.*, vol. 56, no. 7, pp. 665–667, 1990.
- [37] J. Betancourt, T. R. Paudel, E. Y. Tsymlal, and J. Velez, “Spin-polarized two-dimensional electron gas at $\text{GdTiO}_3/\text{SrTiO}_3$ interfaces: Insight from first-principles calculations,” *Phys. Rev. B.*, vol. 96, no. 4, p. 045113, 2017.
- [38] S. Stemmer and S. James Allen, “Two-dimensional electron gases at complex oxide interfaces,” *Annu. Rev. Mater. Res.*, vol. 44, pp. 151–171, 2014.

- [39] R. Dingle, H. Störmer, A. Gossard, and W. Wiegmann, “Electron mobilities in modulation-doped semiconductor heterojunction superlattices,” *Appl. Phys. Lett.*, vol. 33, no. 7, pp. 665–667, 1978.
- [40] J. Eisenstein, K. Cooper, L. Pfeiffer, and K. West, “Insulating and fractional quantum Hall states in the first excited Landau level,” *Phys. Rev. Lett.*, vol. 88, no. 7, p. 076801, 2002.
- [41] V. Umansky, M. Heiblum, Y. Levinson, J. Smet, J. Nübler, and M. Dolev, “MBE growth of ultra-low disorder 2DEG with mobility exceeding 35×10^6 cm²/v s,” *J. Cryst. Growth*, vol. 311, no. 7, pp. 1658–1661, 2009.
- [42] T. Mimura *et al.*, “9 9: Power electronics,” *The Electr. Eng. Handbook*, vol. 19, p. L225, 1980.
- [43] D. Delagebeaudeuf and N. T. Linh, “Metal-(n) AlGaAs-GaAs two-dimensional electron gas FET,” *IEEE Trans. Electron Devices.*, vol. 29, no. 6, pp. 955–960, 1982.
- [44] Z. Zhong, P. Xu, and P. J. Kelly, “Polarity-induced oxygen vacancies at laalo₃/srtio₃ interfaces,” *Phys. Rev. B*, vol. 82, no. 16, p. 165127, 2010.
- [45] Y. Li, S. N. Phattalung, S. Limpijumnong, J. Kim, and J. Yu, “Formation of oxygen vacancies and charge carriers induced in the n-type interface of a LaAlO₃ overlayer on SrTiO₃(001),” *Phys. Rev. B*, vol. 84, no. 24, p. 245307, 2011.
- [46] N. Bristowe, P. Littlewood, and E. Artacho, “Surface defects and conduction in polar oxide heterostructures,” *Phys. Rev. B*, vol. 83, no. 20, p. 205405, 2011.
- [47] P. Willmott, S. Pauli, R. Herger, C. Schlepütz, D. Martoccia, B. Patterson, B. Delley, R. Clarke, D. Kumah, C. Cionca, *et al.*, “Structural basis for the

- conducting interface between LaAlO_3 and SrTiO_3 ,” *Phys. Rev. Lett.*, vol. 99, no. 15, p. 155502, 2007.
- [48] S. A. Chambers, M. H. Engelhard, V. Shutthanandan, Z. Zhu, T. C. Droubay, L. Qiao, P. Sushko, T. Feng, H. D. Lee, T. Gustafsson, *et al.*, “Instability, intermixing and electronic structure at the epitaxial $\text{LaAlO}_3/\text{SrTiO}_3(001)$ heterojunction,” *Surf. Sci. Rep.*, vol. 65, no. 10-12, pp. 317–352, 2010.
- [49] R. Yamamoto, C. Bell, Y. Hikita, H. Y. Hwang, H. Nakamura, T. Kimura, and Y. Wakabayashi, “Structural comparison of n-type and p-type $\text{LaAlO}_3/\text{SrTiO}_3$ interfaces,” *Phys. Rev. Lett.*, vol. 107, no. 3, p. 036104, 2011.
- [50] N. Bristowe, P. Ghosez, P. B. Littlewood, and E. Artacho, “The origin of two-dimensional electron gases at oxide interfaces: insights from theory,” *J. Phys. Condens. Matter.*, vol. 26, no. 14, p. 143201, 2014.
- [51] R. Pentcheva and W. E. Pickett, “Avoiding the polarization catastrophe in LaAlO_3 overlayers on $\text{SrTiO}_3(001)$ through polar distortion,” *Phys. Rev. Lett.*, vol. 102, no. 10, p. 107602, 2009.
- [52] M. Behtash, S. Nazir, Y. Wang, and K. Yang, “Polarization effects on the interfacial conductivity in $\text{LaAlO}_3/\text{SrTiO}_3$ heterostructures: a first-principles study,” *Phys. Chem. Chem. Phys.*, vol. 18, no. 9, pp. 6831–6838, 2016.
- [53] M. Huijben, G. Rijnders, D. H. Blank, S. Bals, S. V. Aert, J. Verbeeck, G. V. Tendeloo, A. Brinkman, and H. Hilgenkamp, “Electronically coupled complementary interfaces between perovskite band insulators,” *Nat. Mater.*, vol. 5, no. 7, pp. 556–560, 2006.
- [54] W. Siemons, G. Koster, H. Yamamoto, W. A. Harrison, G. Lucovsky, T. H. Geballe, D. H. Blank, and M. R. Beasley, “Origin of charge density at LaAlO_3

- on SrTiO₃ heterointerfaces: Possibility of intrinsic doping,” *Phys. Rev. Lett.*, vol. 98, no. 19, p. 196802, 2007.
- [55] A. Annadi, A. Putra, Z. Liu, X. Wang, K. Gopinadhan, Z. Huang, S. Dhar, T. Venkatesan, *et al.*, “Electronic correlation and strain effects at the interfaces between polar and nonpolar complex oxides,” *Phys. Rev. B.*, vol. 86, no. 8, p. 085450, 2012.
- [56] Z. Liu, C. Li, W. Lü, X. Huang, Z. Huang, S. Zeng, X. Qiu, L. Huang, A. Annadi, J. Chen, *et al.*, “Origin of the two-dimensional electron gas at LaAlO₃/SrTiO₃ interfaces: the role of oxygen vacancies and electronic reconstruction,” *Phys. Rev. X.*, vol. 3, no. 2, p. 021010, 2013.
- [57] Y. Chen, F. Trier, T. Kasama, D. V. Christensen, N. Bovet, Z. I. Balogh, H. Li, K. T. S. Thydén, W. Zhang, S. Yazdi, *et al.*, “Creation of high mobility two-dimensional electron gases via strain induced polarization at an otherwise nonpolar complex oxide interface,” *Nano Lett.*, vol. 15, no. 3, pp. 1849–1854, 2015.
- [58] S. Nazir, J. Cheng, and K. Yang, “Creating two-dimensional electron gas in nonpolar/nonpolar oxide interface via polarization discontinuity: First-principles analysis of CaZrO₃/SrTiO₃ heterostructure,” *ACS Appl. Mater. Interfaces.*, vol. 8, no. 1, pp. 390–399, 2016.
- [59] Y. Wang, W. Tang, J. Cheng, M. Behtash, and K. Yang, “Creating two-dimensional electron gas in polar/polar perovskite oxide heterostructures: first-principles characterization of LaAlO₃/A⁺B⁵⁺O₃,” *ACS Appl. Mater. Interfaces.*, vol. 8, no. 21, pp. 13659–13668, 2016.
- [60] L. Fang, C. Chen, Y. Yang, Y. Wu, T. Hu, G. Zhao, Q. Zhu, and W. Ren, “First-principles studies of a two-dimensional electron gas at the interface of

- polar/polar LaAlO₃/KNbO₃ superlattices,” *Phys. Chem. Chem. Phys.*, vol. 21, no. 15, pp. 8046–8053, 2019.
- [61] K. Zou, S. Ismail-Beigi, K. Kisslinger, X. Shen, D. Su, F. Walker, and C. Ahn, “LaTiO₃/KTaO₃ interfaces: A new two-dimensional electron gas system,” *APL Mater.*, vol. 3, no. 3, p. 036104, 2015.
- [62] N. Wadehra, R. Tomar, R. M. Varma, R. Gopal, Y. Singh, S. Dattagupta, and S. Chakraverty, “Planar hall effect and anisotropic magnetoresistance in polar-polar interface of LaVO₃-KTaO₃ with strong spin-orbit coupling,” *Nat. Commun.*, vol. 11, no. 1, p. 874, 2020.
- [63] N. Kumar, N. Wadehra, R. Tomar, S. Dattagupta, S. Kumar, and S. Chakraverty, “Observation of Shubnikov-de Haas Oscillations, Non-trivial Berry Phase, Planar Hall and Anisotropic Magnetoresistance at the conducting interface of EuO-KTaO₃,” *arXiv preprint arXiv:1908.04977*, 2019.
- [64] N. Wadehra and S. Chakraverty, “Electrostatic memory in KTaO₃,” *Appl. Phys. Lett.*, vol. 114, no. 16, 2019.
- [65] L. Li, C. Richter, J. Mannhart, and R. Ashoori, “Coexistence of magnetic order and two-dimensional superconductivity at LaAlO₃/SrTiO₃ interfaces,” *Nat. Phys.*, vol. 7, no. 10, pp. 762–766, 2011.
- [66] Y. Xie, Y. Hikita, C. Bell, and H. Y. Hwang, “Control of electronic conduction at an oxide heterointerface using surface polar adsorbates,” *Nat. Commun.*, vol. 2, no. 1, p. 494, 2011.
- [67] I. Pallecchi, M. Codda, E. G. d’Aglia, D. Marré, A. Review, N. Reyren, S. Gariglio, and J.-M. Triscone, “Seebeck effect in the conducting LaAlO₃/SrTiO₃ interface,” *Phys. Rev. B.*, vol. 81, no. 8, p. 085414, 2010.

- [68] A. Filippetti, P. Delugas, M. Verstraete, I. Pallecchi, A. Gadaleta, D. Marré, D. Li, S. Gariglio, and V. Fiorentini, “Thermopower in oxide heterostructures: The importance of being multiple-band conductors,” *Phys. Rev. B.*, vol. 86, no. 19, p. 195301, 2012.
- [69] E. Assmann, P. Blaha, R. Laskowski, K. Held, S. Okamoto, and G. Sangiovanni, “Oxide heterostructures for efficient solar cells,” *Phys. Rev. Lett.*, vol. 110, no. 7, p. 078701, 2013.
- [70] H. Liang, L. Cheng, X. Zhai, N. Pan, H. Guo, J. Zhao, H. Zhang, L. Li, X. Zhang, X. Wang, *et al.*, “Giant photovoltaic effects driven by residual polar field within unit-cell-scale LaAlO_3 films on SrTiO_3 ,” *Sci. Rep.*, vol. 3, no. 1, p. 1975, 2013.
- [71] P. Irvin, Y. Ma, D. F. Bogorin, C. Cen, C. W. Bark, C. M. Folkman, C.-B. Eom, and J. Levy, “Rewritable nanoscale oxide photodetector,” *Nat. Photon.*, vol. 4, no. 12, pp. 849–852, 2010.
- [72] A. Rastogi, A. Kushwaha, T. Shiyani, A. Gangawar, and R. Budhani, “Electrically tunable optical switching of a mott insulator–band insulator interface,” *Adv. Mater.*, vol. 22, no. 40, pp. 4448–4451, 2010.
- [73] H.-L. Lu, Z.-M. Liao, L. Zhang, W.-T. Yuan, Y. Wang, X.-M. Ma, and D.-P. Yu, “Reversible insulator-metal transition of $\text{LaAlO}_3/\text{SrTiO}_3$ interface for nonvolatile memory,” *Sci. Rep.*, vol. 3, no. 1, p. 2870, 2013.
- [74] S. Goyal, N. Wadehra, and S. Chakraverty, “Tuning the electrical state of 2deg at $\text{LaVO}_3 - \text{KTaO}_3$ interface: effect of light and electrostatic gate,” *Adv. Mater. Interfaces*, vol. 7, no. 16, p. 2000646, 2020.
- [75] P. Giannozzi, S. Baroni, N. Bonini, M. Calandra, R. Car, C. Cavazzoni, D. Ceresoli, G. L. Chiarotti, M. Cococcioni, I. Dabo, *et al.*, “QUANTUM

- ESPRESSO: a modular and open-source software project for quantum simulations of materials,” *J. Condens. Matter Phys.*, vol. 21, no. 39, p. 395502, 2009.
- [76] P. Giannozzi, O. Andreussi, T. Brumme, O. Bunau, M. B. Nardelli, M. Calandra, R. Car, C. Cavazzoni, D. Ceresoli, M. Cococcioni, *et al.*, “Advanced capabilities for materials modelling with quantum ESPRESSO,” *J. Condens. Matter Phys.*, vol. 29, no. 46, p. 465901, 2017.
- [77] J. P. Perdew, K. Burke, and M. Ernzerhof, “Generalized gradient approximation made simple,” *Phys. Rev. Lett.*, vol. 77, no. 18, p. 3865, 1996.
- [78] D. Vanderbilt, “Soft self-consistent pseudopotentials in a generalized eigenvalue formalism,” *Phys. Rev. B.*, vol. 41, no. 11, p. 7892, 1990.
- [79] M. Cococcioni and S. De Gironcoli, “Linear response approach to the calculation of the effective interaction parameters in the lda+ u method,” *Phys. Rev. B.*, vol. 71, no. 3, p. 035105, 2005.
- [80] A. Liechtenstein, V. I. Anisimov, and J. Zaanen, “Density-functional theory and strong interactions: Orbital ordering in Mott-Hubbard insulators,” *Phys. Rev. B.*, vol. 52, no. 8, p. R5467, 1995.
- [81] N. E. Kirchner-Hall, W. Zhao, Y. Xiong, I. Timrov, and I. Dabo, “Extensive benchmarking of DFT+ U calculations for predicting band gaps,” *Appl. Sci.*, vol. 11, no. 5, p. 2395, 2021.
- [82] H. J. Monkhorst and J. D. Pack, “Special points for brillouin-zone integrations,” *Phys. Rev. B.*, vol. 13, no. 12, p. 5188, 1976.
- [83] N. Marzari, D. Vanderbilt, A. De Vita, and M. Payne, “Thermal contraction

- and disordering of the Al(110) surface,” *Phys. Rev. Lett.*, vol. 82, no. 16, p. 3296, 1999.
- [84] R. Fletcher, “Practical methods of optimization john wiley & sons,” *New York*, vol. 80, p. 4, 1987.
- [85] H. Bouafia, S. Hiadsi, B. Abidri, A. Akriche, L. Ghalouci, and B. Sahli, “Structural, elastic, electronic and thermodynamic properties of KTaO_3 and NaTaO_3 : Ab initio investigations,” *Comput. Mater. Sci.*, vol. 75, pp. 1–8, 2013.
- [86] S. Cabuk, H. Akkus, and A. Mamedov, “Electronic and optical properties of KTaO_3 : Ab initio calculation,” *Phys. B: Condens.*, vol. 394, no. 1, pp. 81–85, 2007.
- [87] Y. Wang, Z. Zhang, J. Cheng, Q. Zhang, W. Tang, and K. Yang, “Creating a two-dimensional hole gas in a polar/polar $\text{LaAlO}_3/\text{KTaO}_3$ perovskite heterostructure,” *J. Mater. Chem. C.*, vol. 8, no. 40, pp. 14230–14237, 2020.
- [88] S. Wemple, “Some transport properties of oxygen-deficient single-crystal potassium tantalate (KTaO_3),” *Phys. Rev.*, vol. 137, no. 5A, p. A1575, 1965.
- [89] S. Cabuk, “Ab initio volume-dependent elastic and lattice dynamics properties of KTaO_3 ,” *Phys. Status Solidi B*, vol. 247, no. 1, pp. 93–97, 2010.
- [90] R. Comes and G. Shirane, “Neutron-scattering analysis of the linear-displacement correlations in KTaO_3 ,” *Phys. Rev. B.*, vol. 5, no. 5, p. 1886, 1972.
- [91] G. Jellison Jr, I. Paulauskas, L. Boatner, and D. Singh, “Optical functions of KTaO_3 as determined by spectroscopic ellipsometry and comparison with band structure calculations,” *Phys. Rev. B.*, vol. 74, no. 15, p. 155130, 2006.

- [92] S. K. Ojha, S. K. Gogoi, P. Mandal, S. Kaushik, J. Freeland, M. Jain, and S. Middey, “Oxygen vacancy induced electronic structure modification of KTaO_3 ,” *Phys. Rev. B.*, vol. 103, no. 8, p. 085120, 2021.
- [93] B. Modak and S. K. Ghosh, “An efficient strategy for controlled band gap engineering of KTaO_3 ,” *J. Phys. Chem. C.*, vol. 120, no. 13, pp. 6920–6929, 2016.
- [94] A. Benrekia, N. Benkhattou, A. Nassour, M. Driz, M. Sahnoun, and S. Lebègue, “Structural, electronic and optical properties of cubic SrTiO_3 and KTaO_3 : Ab initio and gw calculations,” *Phys. B: Condens.*, vol. 407, no. 13, pp. 2632–2636, 2012.
- [95] P. King, R. He, T. Eknapakul, P. Buaphet, S.-K. Mo, Y. Kaneko, S. Harashima, Y. Hikita, M. Bahramy, C. Bell, *et al.*, “Subband structure of a two-dimensional electron gas formed at the polar surface of the strong spin-orbit perovskite KTaO_3 ,” *Phys. Rev. Lett.*, vol. 108, no. 11, p. 117602, 2012.
- [96] N. Wu, X.-J. Zhang, and B.-G. Liu, “Strain-enhanced giant Rashba spin splitting in ultrathin KTaO_3 films for spin-polarized photocurrents,” *RSC Adv.*, vol. 10, no. 72, pp. 44088–44095, 2020.
- [97] V. Kumar and N. Ganguli, “Rashba-like spin-orbit interaction and spin texture at the $\text{KTaO}_3(001)$ surface from DFT calculations,” *Phys. Rev. B.*, vol. 106, no. 12, p. 125127, 2022.
- [98] H. Zhang, X. Yan, X. Zhang, S. Wang, C. Xiong, H. Zhang, S. Qi, J. Zhang, F. Han, N. Wu, *et al.*, “Unusual electric and optical tuning of KTaO_3 -based two-dimensional electron gases with 5d orbitals,” *ACS Nano*, vol. 13, no. 1, pp. 609–615, 2019.

- [99] S. Y. Park, A. Kumar, and K. M. Rabe, “Charge-Order-Induced Ferroelectricity in $\text{LaVO}_3/\text{SrVO}_3$ Superlattices,” *Phys. Rev. Lett.*, vol. 118, no. 8, p. 087602, 2017.
- [100] P. Bordet, C. Chaillout, M. Marezio, Q. Huang, A. Santoro, S. Cheong, H. Takagi, C. Oglesby, and B. Batlogg, “Structural aspects of the crystallographic-magnetic transition in LaVO_3 around 140 K,” *J. Solid State Chem.*, vol. 106, no. 2, pp. 253–270, 1993.
- [101] S. Kumari, S. Paul, and S. Raj, “Electronic structure of RVO_3 (R= La and Y): Effect of electron (U) and exchange (J) correlations,” *Solid State Commun.*, vol. 268, pp. 20–25, 2017.
- [102] L. Wang, Y. Li, A. Bera, C. Ma, F. Jin, K. Yuan, W. Yin, A. David, W. Chen, W. Wu, *et al.*, “Device performance of the mott insulator LaVO_3 as a photovoltaic material,” *Physical Review Applied*, vol. 3, no. 6, p. 064015, 2015.
- [103] S. Kakkar and C. Bera, “Rashba spin splitting in two-dimensional electron gas in polar-polar perovskite oxide heterostructure $\text{LaVO}_3/\text{KTaO}_3$: A DFT investigation,” *Phys. E: Low-Dimens. Syst. Nanostructures.*, vol. 144, p. 115394, 2022.
- [104] Y. Wang, M. K. Niranjan, J. D. Burton, J. M. An, K. D. Belashchenko, and E. Y. Tsymbal, “Prediction of a spin-polarized two-dimensional electron gas at the $\text{LaAlO}_3/\text{EuO}(001)$ interface,” *Phys. Rev. B.*, vol. 79, no. 21, p. 212408, 2009.
- [105] V. R. Cooper, “Enhanced carrier mobilities in two-dimensional electron gases at III-III/IV oxide heterostructure interfaces,” *Phys. Rev. B.*, vol. 85, no. 23, p. 235109, 2012.

-
- [106] J. Lee, N. Sai, and A. A. Demkov, “Spin-polarized two-dimensional electron gas through electrostatic doping in LaAlO₃/EuO heterostructures,” *Phys. Rev. B*, vol. 82, no. 23, p. 235305, 2010.

Summary and Future Directions

We have no right to assume that any physical laws exist, or if they have existed up until now, that they will continue to exist in a similar manner in the future.

Max Planck

In this thesis, we performed quantum mechanical simulations using density functional theory (DFT) on a rich variety of systems such as bulk crystals, metal and semiconductor surfaces, surface alloys, pristine and doped halide perovskite materials and heterostructure. We used spin-polarized DFT for magnetic systems, the DFT+ U method for strongly-correlated systems, and relativistic DFT for incorporating spin-orbit coupling. Using these techniques, we studied the structural, electronic, magnetic, optical and vibrational properties of the above mentioned systems

In Chapter 1, we provided a very brief introduction to the problems we studied in this thesis. We discussed the importance of materials science in a historical context, and why it is desirable to use a rational design approach to engineer new materials. The specific systems we have studied are metal surfaces, surface alloys on metal

surfaces, bulk perovskites, transition metal atom doped bulk perovskites, and the interfaces between two perovskite oxide materials. We explained why these systems were worth studying, due to either a fundamental physics point of view, or the possibility of technological applications.

In Chapter 2, we summarized the methods we used in this thesis. We have summarized the basics of density functional theory (DFT) and the computational approaches used when performing DFT calculations. We also discussed the mathematical formalism used to calculate different properties throughout the thesis. For example, we described, in brief, the theory of non spin-polarized and spin-polarized DFT, and the computational approximations made when using DFT for doing simulations of real materials. We also described relativistic DFT, which we used when incorporating spin-orbit coupling in systems containing heavy atoms. Another method that we described was the DFT+ U method, used for a more appropriate treatment of strongly correlated systems. We also described approaches used in this thesis to calculate the optical and vibrational properties of materials.

In Chapter 3, we studied the deposition of Sn atoms on an Ag(001) substrate. This was collaborative work, done together with the experimental group of Prof. K. S. R. Menon, of the Surface Physics and Materials Science Division, SINP, Kolkata. Our theoretical calculations showed that when Sn atoms are deposited on an Ag(001) surface, very interestingly Sn-Ag bimetallic surface alloys are formed for all Sn coverages. This is in contradiction with the naive expectation that Sn atoms would form an overlayer on the Ag(001) surface. We discuss the reasons why these naive expectations are incorrect. Even though the metallic radii of Sn and Ag atoms in their respective bulk structures are very similar, when Sn atoms are deposited on Ag(001), their effective size becomes much larger than that of the Ag surface and bulk atoms. As a result, the incorporation of the large Sn surface atoms within the topmost Ag layer (by the formation of a surface alloy) relieves the tensile surface

stress present in the bare Ag(001) surface. The calculated results were compared against the data from low energy electron diffraction (LEED) experiments. The stable phases predicted by our DFT calculations matched reasonably well with those found in experiment, though there were a few discrepancies.

Then, we calculated the electronic structure of the lowest energy stable structures at each Sn coverage considered in our calculations. The calculated band structures were compared with the angle-resolved photoemission spectroscopy (ARPES) measurements. Overall, we see very good agreement between theory and experiment. Surprisingly, this was found to be true even in cases where the ground state configuration predicted from DFT seemed to differ from that observed in LEED. We believe this is because the main features in the unfolded band structure are primarily sensitive to the surface electrostatic potential, which is relatively insensitive to the actual geometric arrangement of atoms, and depends primarily on the Sn coverage.

An interesting feature in both the experimentally measured and theoretically computed band structure was the existence of a crossing point between two linearly dispersive bands, similar to the Dirac cone in graphene, and a monotonic variation in its energy with the Sn coverage. This variation is attributable to the change in surface electrostatic potential with Sn coverage.

As mentioned above, at some values of Sn coverage x , the lowest energy geometry is different from that observed in the LEED experiments. For example, for $x = 0.5$, the DFT calculated lowest energy structure has a $p(2 \times 2)$ unit cell, while a $p(1 \times 10)$ cell is observed in the LEED experiment. Due to computational feasibility, we were able to perform the band unfolding calculations only for the $p(2 \times 2)$ structure. Though we obtained good agreement with ARPES data, as mentioned above, in future, we would like (if we have adequate computational resources) to perform the computationally expensive band unfolding calculations also for the $p(1 \times 10)$ cell, and provide direct confirmation of our belief that the unfolded band structure is primarily

sensitive to the Sn coverage, and not the details of the atomic arrangement in the surface alloy. It would also be nice to understand why DFT and LEED disagree about the lowest energy structures at some values of x .

In Chapter 4, we studied the structural, electronic and vibrational properties of CsPbBr₃, CsPbCl₃, Fe-doped CsPbBr₃ and Fe-doped CsPbCl₃. This work was done in collaboration with the experimental group of Prof. Ranjani Viswanatha, New Chemistry Unit, JNCASR, Bangalore. They were able to dope Fe atoms successfully into CsPbBr₃ and CsPbCl₃ nanocrystals. They measured the photoluminescence of the Fe-doped systems and compared these results with those obtained from the corresponding pristine systems. They observed that the photoluminescence was considerably quenched or reduced upon Fe doping, compared to the pristine CsPbBr₃ and CsPbCl₃.

We performed DFT calculations to see the effect of Fe doping on these halide perovskites. The electronic structures of the pristine systems and Fe-doped systems were computed and compared. We are able to explain the fundamental origin of photoluminescence quenching in the Fe-doped systems: the introduction of the Fe atoms results in the formation of mid-gap states that trap electrons, resulting in photoluminescence quenching.

We also found that the electron-phonon coupling is much stronger in the chloride than in the bromide systems. This finding explains the greater degree of photoluminescence quenching observed in the former systems, as the stronger electron-phonon coupling results in greater non-radiative losses.

We had calculated the electron-phonon coupling in these systems somewhat indirectly, by calculating the deformation potential, which is obtained by computing the change in electronic eigenvalues when the crystal is subjected to strain.¹ In future, we would like to calculate the electron-phonon coupling strengths for Fe-doped

CsPbBr₃ and Fe-doped CsPbCl₃ more directly, using density functional perturbation theory (DFPT),[give ref here](#) from which we can also get information about the coupling of electrons to optical phonons. This information can then be inserted into the Huang-Rhys factor, which can give us the number of phonons emitted after excited electrons get trapped by the mid-gap Fe-3*d* energy levels. Thus it can provide information about the amount of excitation energy which is getting converted into lattice vibrational energy and we can compare this for Fe-doped CsPbBr₃ and Fe-doped CsPbCl₃.

In Chapter 5, we calculated the optical properties of CsPbX₃ and Fe-doped CsPbX₃ (X = Br, Cl) perovskite materials. Our experimental collaborators in the group of Prof. Ranjani Viswanatha, JNCASR, Bangalore, have done some optical measurements. Other experimental collaborators, in the group of Prof. Bivas Saha, JNCASR, Bangalore, studied optical transitions occurring in CsPbBr₃ and CsPbCl₃ perovskites, using ellipsometry measurements. They measured the frequency dependent optical constants (e.g., the imaginary part of dielectric function $\epsilon_2(\omega)$) by observing the change in polarization of light when it reflects from or is transmitted through CsPbBr₃ and CsPbCl₃.

We calculated the electronic structure and optical properties of CsPbBr₃ and CsPbCl₃ using first principles DFT calculations. We identified the valence states and conduction states involved in the different optical transitions measured in the ellipsometry measurements. We have also identified the atomic orbitals involved in these optical transitions. Further, we have calculated the frequency dependent imaginary part of the dielectric function $\epsilon_2(\omega)$ and compared it with the experimental spectra, for both CsPbBr₃ and CsPbCl₃.

Upon introducing a linear shift in frequency (which is a standard procedure in the field) we found good agreement with experimental data for the CsPbBr₃; the agreement was not as good for CsPbCl₃. Once again, we believe this can be

explained by stronger electron-phonon coupling in the latter system.

We also calculated $\epsilon_2(\omega)$ for Fe-doped systems, and found that there is a little blue shift (increase in band gap) upon Fe doping with respect to the pristine systems, for both Fe-doped CsPbBr₃ and Fe-doped CsPbCl₃.

In future, we would like to repeat these calculations using better functionals such as hybrid functionals, which generally give more accurate values for the band gap and capture better band dispersion, but are computationally more expensive.

In Chapter 6, we studied the electronic properties of the two-dimensional electron gas (2DEG) formed at the LaVO₃/KTaO₃ (LVO/KTO) heterostructure interface. This work was performed in collaboration with the experimental group of Prof. Suvankar Chakraverty, INST, Mohali. They formed the LVO/KTO interface by depositing a thin film of LVO on a TaO₂ terminated KTO(001) substrate, using pulsed laser deposition (PLD). They observed metallicity at the LVO/KTO interface, above 3 monolayer (ML) LVO thickness, upon measuring the two-dimensional (2D) resistivity as a function of temperature. The measured carrier density and carrier mobility, in their experiment, is very high at the LVO/KTO interface.

We first performed electronic structure calculations of the constituents LVO and KTO which were confirmed to be insulating. However, our calculations of the LVO/KTO interface showed a metallic nature, consistent with the experimental observations. The calculated electronic charge was maximum near the interface and decreased away from the interface, which shows the two-dimensional nature of the conduction electrons. We also found that an ‘electronic reconstruction’ is the origin of 2DEG formation at the LVO/KTO interface.

In future, we can calculate the layer-resolved and spin-resolved orbital projected density of states for slab structure of LVO/KTO interface and can show the better picture of ‘electronic reconstruction’ due to polar catastrophe. As there are heavy Ta atoms in the system, we can explore interesting Rashba physics by incorporating

spin-orbit interaction.

For each chapter, we have chosen the problems based on the experimental observations, we have explained them using DFT calculations and provided additional insights into the problems. Though we have tried to understand and provide insights in great detail for all the problems considered, it may happen that this is just the ‘tip of the iceberg’ and thus we can explore many more things which can lead to even more interesting physics.

Bibliography

- [1] T. Zhao, W. Shi, J. Xi, D. Wang, and Z. Shuai, “Intrinsic and extrinsic charge transport in $\text{CH}_3\text{NH}_3\text{PbI}_3$ perovskites predicted from first-principles,” *Sci. rep.*, vol. 6, no. 1, p. 19968, 2016.
- [2] A. D. Wright, C. Verdi, R. L. Milot, G. E. Eperon, M. A. Pérez-Osorio, H. J. Snaith, F. Giustino, M. B. Johnston, and L. M. Herz, “Electron–phonon coupling in hybrid lead halide perovskites,” *Nat. comm.*, vol. 7, no. 1, p. 11755, 2016.